The University Of Sheffield.

Experimental Study and Numerical Modelling of Lithium-ion Battery Thermal Runaway Behaviour

Mohamad Syazarudin Bin Md Said

Supervisor: Dr Yajue Wu

A thesis submitted to the Department of Chemical and Biological Engineering, The University of Sheffield, for the Degree of Doctor of Philosophy (PhD)

February 2018

Abstract

Thermal runaway has been identified as the prevalent failure mode of lithium-ion batteries, which is in most cases, is instigated by applications outside the manufacturer specifications. The intricate exothermic reactions by reactive battery components during thermal runaway are usually accompanied by the release of toxic and flammable gases, which in turn are susceptible to fire and explosion upon exposure to ignition source.

Due to its extensive availability and direct association with our daily life, precise appraisal of the risk involved is imperative. The proliferation of the applications into high-voltage large-capacity emerging areas such as electrified vehicles and stationary energy storage necessitates the understanding of the hazard behaviour at large scale.

The study is aimed at developing a numerical model to predict thermal runaway hazard in a large-capacity battery module. The battery chosen for this study is a cylindrical lithium-ion with lithium cobalt oxide cathode and graphite anode. The model was developed based on thermal kinetic information of the pertinent exothermic reactions as compiled from literature. Battery thermal runaway behaviours under thermally abusive situations and impact-induced short-circuit were predicted. The simulation results indicate that thermal runaway temperature for a full-charged battery falls within the range of 162 ^{o}C – 175 ^{o}C. The induction time and severity of thermal runaway depend on the ambient temperature and the rate of heating process. As the exothermic reactions involved are heat-activated, the temperature of the environment needs to be sufficiently high with considerable amount of exposure period to overcome the activation energy. Prolonged exposure to 150 ^{o}C and below will not result in thermal runaway. Impact-induced short-circuit, on the other hand, inflicts an immediate failure which in turn results in surge of the battery temperature.

The thermal kinetic model was further expanded to include heat transfer modelling to simulate the propagation of thermal runaway in a battery module comprised of nine identical batteries. Two cases were developed where the effects of the location

of failure initiation on thermal runaway propagation were examined. In both cases, thermal runaway propagation was not observed.

Experimental programme was conducted to support and subsequently validate the numerical model. The batteries were tested under both adiabatic and non-adiabatic conditions using Accelerating Rate Calorimeter and oven respectively. The experimental results indicate that thermal runaway temperature for a full-charged battery falls within the range of 163 ^{o}C – 183 ^{o}C. The experimental results indicate that the thermal kinetic model was able to predict thermal runaway temperature as reflected by the agreeable value between both numerical modelling and experimental work, validating the model as a reliable tool for simulation of thermal runaway.

In addition, it was discovered from the experimental tests that the effect of battery electrical capacity on battery thermal runaway is profound. Battery with higher electrical capacity demonstrated a higher tendency to experience thermal runaway with shorter induction time and resulted with a more energetic response, as indicated by higher maximum temperature rise. The effects of increasing the battery mass and total capacity on thermal runaway features were further investigated. Two batteries packed together were more inclined to suffer thermal runaway, as reflected by the shorter induction time. The presence of parallel electrical connection that doubled the total capacity further accelerated thermal runaway in the two batteries.

Destructive impact tests were conducted to simulate the loss of mechanical integrity of the battery structure that might result in internal short-circuit. The impact resulted in immediate energetic thermal runaway and led to a sustained fire. As measured by thermal camera, the impact caused the ejected battery content to reach 845 ^{o}C due to the massive short-circuit. Despite exhibiting a violent response, the heat transfer process to the surrounding batteries was not sufficient to cause thermal runaway propagation in a battery module.

Acknowledgement

I would like to sincerely express my gratitude to my supervisor; Dr Yajue Wu for her guidance and kind assistance throughout my study. Her continuous supervision and insightful suggestions are crucial for the completion of the research work.

I would like to thank the technical staff of the Department of Chemical and Biological Engineering in Buxton Laboratory, Mr David Palmer for being kind and helpful in constructing the experimental rig and providing important technical assistance.

Also, I would like to express my appreciation to Dr Denis Cumming and my colleague Muhammed Abdul Mun'im for their kind assistance with the thermal imaging and high-definition photography.

Special thanks to Peter Bugryniec for his kind assistance and support with the Accelerating Rate Calorimeter.

Finally, I would like to thank Ministry of Higher Education Malaysia and University Putra Malaysia for funding this study, and my family and friends for their support and encouragement.

List of Figures

List of Tables

Abbreviations

ARC	Accelerating rate calorimeter
ATD	Advance Technology Development
BBC	British Broadcasting Corporation
BNEF	Bloomberg New Energy Finance
CPSC	Consumer Product Safety Commission
DEC	Diethyl carbonate
DMC	Dimethyl carbonate
DSC	Differential scanning calorimeter
EC	Ethylene carbonate
EDV	Electric drive vehicles
EUCAR	European Council for Automotive R&D
EV-ARC	Extended volume accelerating rate calorimeter
FTIR	Fourier-Transform Infrared Spectroscopy
HRR	Heat release rate
HWS	Heat-wait-search
ICE	Internal combustion engine
IEC	International Electrotechnical Commission
IEEE	Institute of Electrical and Electronic Engineers
LCO	Lithium cobalt oxide
LFL	Lower flammability limit
LFP	Lithium iron phosphate
LIB	Lithium-ion battery
LMO	Lithium manganese oxide
LTO	Lithium titanate
MCMB	Mesocarbon microbead
NCA	Lithium nickel cobalt aluminium oxide
NiCd	Nickel cadmium

NiMH	Nickel metal hydride
NMC	Lithium nickel manganese
OCV	Open circuit voltage
PC	Polycarbonate
PCC	Phase change composite
PCM	Phase change material
PHRR	Peak heat release rate
PVDF	Polyvinylidene fluoride
QRA	Quantitative risk assessment
REA	Renewable Energy Association
SAE	Society of Automotive Engineers
SBI	Single burning item
SEI	Solid electrolyte interphase
SOC	State of charge
TGA	Thermogravimetric analysis
THC	Total hydrocarbons
TNT	Trinitrotoluene
UL	Underwriter Laboratories
VC	Vinylene carbonate
VSP2	Vent sizing package 2

Nomenclatures

$\dot{m}_{O_2}$	Final oxygen mass flowrate	kg/s
$\dot{m}_{O_2}^0$	Initial oxygen mass flowrate	kg/s
$\dot{m}_e$	Mass flowrate of combustion products	kg/s
$\dot{m}_{fuel}$	Mass flowrate of combusted materials	kg/s
$\dot{q}$	Heat release rate	W
ΔH_{anode}	Anode-solvent reaction enthalpy	J/kg
$\Delta H_{battery}$	Total heat released by battery	kJ
ΔH_c	Heat of combustion	J/kg
$\Delta H_{cathode}$	Cathode breakdown reaction enthalpy	J/kg
$\Delta H_{electrolyte}$	Electrolyte decomposition reaction enthalpy	J/kg
ΔH_{oxygen}	Heat of combustion of oxygen	J/kg
ΔH_{SEI}	SEI decomposition reaction enthalpy	J/kg
ΔH_x	Reaction enthalpy	J/kg
ΔH_{sc}	Amount of electrical energy discharged during short-circuit	J
Δt	Duration of short-circuit	s
A	Frequency factor	s^{-1}
A	Surface area for heat exchange	m^2
a	Specific area of the sample	m^2/g
a_0	Constant of proportionality	m^2/g
A_{anode}	Frequency factor of anode-solvent reaction	s^{-1}
$A_{cathode}$	Frequency factor of cathode breakdown reaction	s^{-1}
$A_{electrolyte}$	Frequency factor of electrolyte decomposition reaction	s^{-1}
A_{SEI}	Frequency factor of SEI decomposition reaction	s^{-1}

C	Battery capacity	Ah
c_{anode}	Dimensionless amount of lithium intercalated within the carbon negative electrode	-
$c_{electrolyte}$	Dimensionless concentration of electrolyte	-
C_i	Capacity of the *i*th cell	-
C_N	Rated battery capacity	Ah
C_p	Specific heat capacity	J/kg.K
$C_{p\ air}$	Specific heat capacity of air	J/kg.K
c_{SEI}	Dimensionless amount of lithium-containing meta-stable species in the SEI	-
c_x	Normalised reactant x concentration	-
E_a	Activation energy	J/mol
E_{anode}	Activation energy of anode-solvent reaction	J/mol
$E_{cathode}$	Activation energy of cathode decomposition reaction	J/mol
$E_{electrolyte}$	Activation energy of electrolyte decomposition reaction	J/mol
E_{SEI}	Activation energy of SEI decomposition reaction	J/mol
h	Heat transfer coefficient	$W/m^2.K$
I	Current	A
k	Rate of reaction	s^{-1}
k_B	Boltzmann's constant	$m^2\ kg\ s^{-2}\ k^{-1}$
K_g	Explosion severity	Pa.m/s
M	Mass	kg
m	Reaction order	-
m_{anode}	Anode-solvent reaction order	-
$m_{cathode}$	Cathode breakdown reaction order	-
$m_{electrolyte}$	Electrolyte decomposition reaction order	-

m_{SEI}	SEI decomposition reaction order	-
m_{TNT}	TNT-equivalent mass	kg
n	Amount of gases	mol
n	Reaction parameter	-
n_0	Initial amount of gases	mol
P	Pressure	Pa
P	Reaction parameter	-
Q	Net rate of heat generation	W
Q_{anode}	Rate of heat generation by reaction between anode and solvent	W
$Q_{cathode}$	Rate of heat generation by cathode breakdown reaction	W
$Q_{convective}$	Rate of convective heat transfer	W
Q_{cr}	Rate of heat generation from chemical reactions	W
$Q_{dissipation}$	Rate of heat transfer from battery to the surrounding	W
$Q_{electrolyte}$	Rate of heat generation by electrolyte decomposition reaction	W
Q_{gen}	Rate of internal heat generation	W
$Q_{radiative}$	Rate of radiative heat transfer	W
Q_{sc}	Rate of heat generation from short-circuit	W
Q_{SEI}	Rate of heat generation by SEI decomposition reaction	W
Q_{TNT}	Explosion energy of TNT	kJ/g
Q_x	Rate of heat generation by chemical reaction x	W
R	Gas constant	$J\ mol^{-1}\ K^{-1}$
R_{anode}	Rate constant of anode-solvent reaction	s^{-1}
R_{can}	Thermal resistance by cell canister	$m^2\ K\ W^{-1}$

$R_{cathode}$	Rate constant of cathode breakdown reaction	s^{-1}
$R_{electrolyte}$	Rate constant of electrolyte decomposition reaction	s^{-1}
R_h	Thermal resistance by convective heat transfer	m^2 K W^{-1}
R_{jr}	Thermal resistance by jellyroll	m^2 K W^{-1}
R_{SEI}	Rate constant of SEI decomposition reaction	s^{-1}
SOC_0	Initial value of SOC	-
SOC_i	SOC of the *i*th cell	-
SOC_M	SOC of the battery module	-
T	Temperature	K
t	Time	s
t_0	Initial time	s
T_{amb}	Ambient temperature	K
V	Battery voltage	V
V	Chamber volume	m^3
W_{anode}	Mass of carbon in anode	kg
$W_{cathode}$	Mass of cathode	kg
$W_{electrolyte}$	Mass of electrolyte	kg
W_x	Mass of reactant x	kg
x_f	Dimensionless amount of lithium content in the metastable SEI	-
x_i	Dimensionless amount of lithium intercalated within the carbon anode	-
z	Dimensionless thickness of SEI layer	-
z_0	Dimensionless initial thickness of SEI layer	-
α	Dimensionless fractional degree of conversion	-
α	Extent of cathode decomposition reaction	-

β	Parameter of autocatalysis	-
ε	Battery surface emissivity	-
η	Coulombic efficiency	-
σ	Stefan-Boltzmann constant	W/m^2K^4
χ	Empirical mass of TNT	-
τ	Time at the point of short-circuit	s

Chemical Compounds

$(CH_2OCO_2Li)_2$	Lithium ethylene dicarbonate
C	Carbon
C_2H_4	Ethylene
C_2H_6	Ethane
C_2HF	Fluoroacetylene
$C_3H_4O_3$	Ethylene carbonate
C_3H_6	Propene
$C_3H_6O_3$	Dimethyl carbonate
$C_4H_6O_3$	Propylene carbonate
CH_2CF_2	Vinylidene difluoride
CH_4	Methane
CO	Carbon monoxide
Co	Cobalt
CO_2	Carbon dioxide
Co_3O_4	Cobalt (II, III) oxide
CoO	Cobalt oxide
CoO_2	Cobalt (II) peroxide
F_2	Fluorine
H_2	Hydrogen
H_2O	Water
HCl	Hydrochloric
HCN	Hydrogen cyanide
HF	Hydrogen fluoride
Li	Lithium
$Li(Ni_{0.45}Mn_{0.45}Co_{0.10})O_2$	Lithium nickel manganese cobalt oxide
$Li(Ni_{0.50}Mn_{0.25}Co_{0.25})O_2$	Lithium nickel manganese cobalt oxide
$Li_{1.1}(Ni_{1/3}Co_{1/3}Mn_{1/3})_{0.9}O_2$	Lithium nickel manganese cobalt oxide

Li_2CO_3	Lithium carbonate
$Li_4Ti_5O_{12}$	Lithium titanate
$LiCoO_2$	Lithium cobalt oxide
$LiCo_xNi_yMn_zO_2$	Lithium cobalt nickel manganese oxide
LiF	Lithium fluoride
$LiFePO_4$	Lithium iron phosphate
$LiMn_2O_4$	Lithium manganese oxide
$LiMn_{3/2}Ni_{1/2}O_4$	Lithium manganese nickel oxide
$LiNi_{0.80}Co_{0.15}Al_{0.05}O_2$	Lithium nickel cobalt aluminium oxide
$LiNi_{0.85}Co_{0.15}O_2$	Lithium nickel cobalt oxide
$LiNiCoAlO_2$	Lithium nickel cobalt aluminium oxide
$LiNiCoMnO_2$	Lithium nickel manganese cobalt oxide
$LiNiCoO_2$	Lithium nickel cobalt oxide
$LiNi_xCo_yMn_zO_2$	Lithium nickel manganese cobalt oxide
$LiPF_6$	Lithium hexafluorophosphate
$Li_x(Ni_{0.80}Co_{0.15}Al_{0.05})O_2$	Lithium nickel cobalt aluminium oxide
Li_xC_6	Lithiated carbon
NO	Nitric oxide
NO_x	Nitrogen oxides
O_2	Oxygen
PF_5	Phosphorus pentafluoride
$POF_2(OH)$	Difltmrophosphoric
POF_3	Phosphoryl fluoride
SO_2	Sulfur dioxide
SO_x	Sulfur oxides

Chapter 1: Introduction

1.1 Background

1.1.1 History of Battery Development

It has been postulated that batteries were invented around 200 B.C. Nowadays, batteries are widely available and play an important role in our daily chores. The use of portable electronic devices and equipment in various areas such as the military, medicine, education, entertainment, aviation and the automotive industry is made possible by the presence of batteries.

In nineteenth and early twentieth centuries, various galvanic pairs were proposed, with nickel cadmium (NiCd), nickel metal hydride (NiMH) and lead acid being the most popular rechargeable batteries. Nowadays, lithium-ion battery (LIB) is substituting conventional batteries in the market. Their superior electrical energy content, long life cycle and low self-discharge properties are highly desirable, which render them as prospective candidates for large-scale and high-capacity applications such as electric vehicles and grid energy storage.

Many battery development projects aim at providing longer runtime for electronic devices, and extending driving range for electric drive vehicles (EDV), which can be achieved by enhancing the energy content (Doughty and Roth, 2012). The demand for compact and lightweight yet powerful batteries has driven the rapid development of LIB. It is reported that the enhancement of specific energy in LIB is occurring at approximately 28% every year. It is projected that future LIB will have 30% - 50% higher energy within the next few years (Doughty and Pesaran, 2012).

The rising interest in renewable and sustainable energy resources incite the application of electrochemical energy storage into large-scale and high-capacity energy storage sectors. Many countries around the world are investing in alternative renewable energy resources, particularly wind and solar power energy plants, which are the most established technologies in this field (Scrosati and Garche, 2010, Wang

et al., 2012). These renewable resources are however, intermittent in nature and continual disruption in supply is expected. Therefore, measures to secure the quality and availability of the power supply is necessary, which can be achieved by using batteries (Vetter and Rohr, 2014). The utilisation of sustainable and renewable energy resources requires a good energy storing system with the ability of discharging the energy upon demand. According to the Renewable Energy Association, as of 2015, 19 out of 32 of the installed energy storage plants in the United Kingdom use batteries for energy storage purposes, where 12 of the projects are based on lithium-ion battery technology. The capacity of the battery-based plants ranges from 5 kW to 50 MW (R.E.A., 2015).

Sustainability issues such as insecurity of fossil fuel supply and emission of greenhouse gases expand the application of batteries into the automotive sector. The transportation sector has been reported to be the main contributor to carbon dioxide emission, which is produced from the combustion process of fossil fuels in the internal combustion engine (ICE) of vehicles. The problem can be alleviated by introducing zero or controlled-emission vehicles, and shifts from conventional vehicles to hybrid and electric vehicles. This course of action will directly reduce the dependence on fossil fuels and consequently diminish the emission of greenhouse gases and criteria pollutants (Bandhauer et al., 2011). The vigorous development of electric drive vehicles relies on the advancement of battery technology, which is the energy carrier in electrified vehicles (Sato, 2001).

The projection made by Bloomberg for battery demand in next few years is shown in Figure 1.1. The demand from consumer electronics and stationary energy storage is expected to increase gradually. The demand from the automotive sector, on the other hand, exhibits an exponential behaviour and within five years, the highest demand will come from this sector due to the electrification of passenger vehicles.

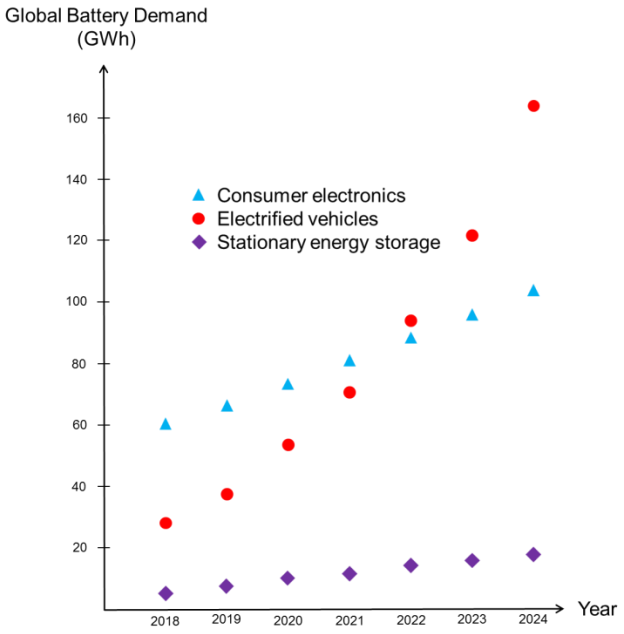

Figure 1.1: Forecast of global battery demand in three main sectors. Adapted from Randall (2017).

The cost of LIB used to be very high, which was close to $1000 per kWh as reported by Väyrynen and Salminen (2012). Market analysis by Bloomberg New Energy Finance (BNEF) reported a 35 percent plunge in LIB prices in 2015 and a 22 percent drop in 2016. According to their projection, the price will decrease another 15 to 20 percent in 2017 (Randall, 2017, Randall, 2016). The forecast of the price range for LIB within next few years, as made by Bloomberg, is presented in Figure 1.2.

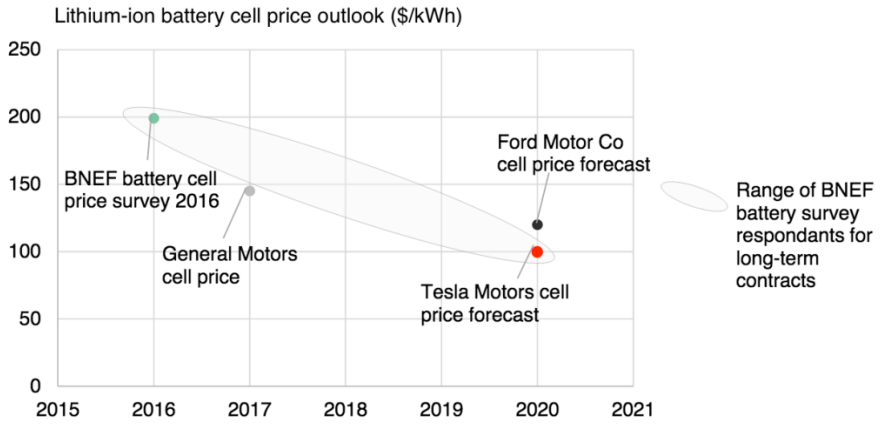

Figure 1.2: Forecast of the lithium-ion battery price (Randall, 2017).

The decrease in the LIB price will in turn reduce the price of electric vehicles. The team projected that the price of electric vehicles will be as competitive as their conventional internal-combustion vehicle counterparts by 2022. Currently, the battery constitutes the largest cost in electric vehicles. The drop in battery cost will make the price of electric cars more affordable and consequently boost market demand.

1.1.2 Fire and Explosion Incidents Associated with Batteries

For the purposes of accident prevention and mitigation of catastrophic failure, batteries are equipped with safety mechanisms at three different stages: cell hardware, system hardware and system software (Lisbona and Snee, 2011). Satisfactory abuse tolerances can be achieved by disposing a substantial amount and typically excessive safety devices (Kim et al., 2007).

Despite the multi-layer safety mechanisms, in addition to the improved inherent safety characteristic of batteries, undesirable incidents are still inevitable. Some of the cases involve profoundly reliable aviation field (Freed, 2014, Wald, 2014, BBCnews, 2013). This situation raises the concern about the safety of this widely available electrochemical energy storage system. In some events, gas was vented (Freed, 2014) and dense smoke was observed (Wald, 2014).

Fire and explosion incidents in relation to batteries, despite being infrequent, have been reported by the media. The recurrence of mishaps tarnishes the reputation of battery manufacturers and taints consumer confidence, which potentially leads to market loss and product withdrawal. Table 1.1 presents some of the fire and explosion incidents associated with batteries that hit automotive, recycling, consumer electronics and aviation sectors.

Table 1.1: List of fire and explosion incidents associated with batteries.

Date / Location	Description	Reference
Aviation		
January 2014 **Tokyo, Japan**	Gas was vented and released from a battery on a Boeing 787 plane parked in Tokyo.	Freed (2014)
July 2011 **Incheon, South Korea**	Freight aircraft of Asiana Airlines crashed into the sea due to the igniting lithium batteries, killing two pilots.	Brett (2011)
3 September 2010 **Dubai, United Arab Emirates**	Freight aircraft of the United Parcel Service crashed near Dubai killing two pilots due to fire on-board. The large quantity of lithium batteries in the cargo was the source of the fire.	Lowy (2010) Garthwaite (2011)
7 January 2013 **Boston, United States**	Heavy smoke and fire were found coming from the front auxiliary power unit battery case in a Boeing 787. Two distinct flames with an approximate length of three inches were observed and loud hissing sound was heard. Attempt to extinguish the flames using dry chemical fire extinguisher was deemed unsuccessful.	Wald (2014) BBCnews (2013) Lowy and Freed (2013)

Consumer Electronics		
23 March 2014 **New Holland, United States**	A battery in a laptop exploded and caused a fire in an apartment in New Holland. The loss was estimated to be $55,000.	LancasterOnline (2014)
21 June 2006 **Japan**	A Dell laptop caught on fire and caused multiple explosions for more than five minutes at a Japanese conference.	Hales (2006)

Recycling		
July 2007 **Preston, United Kingdom**	A fire broke out at a waste treatment plant at Red Scar Industrial Estate, which was caused by ignition of lithium batteries.	HSE (2009)
November 2009 **Trail, British Columbia**	A disastrous fire occurred at a lithium battery recycling facility in Trail. The fire was too volatile and could not be extinguished using water. Blasts like fireworks were heard and projectile shooting from the bunker was observed. A poisonous sulphur dioxide gas plume was released to the atmosphere.	TMTV BCTV (2009) CBCnews (2009)
February 2007 **Thorold, Canada**	Explosions and uncontrollable fire damaged a hazardous waste processing facility in Thorold. It was suggested that this disastrous incident was caused by water ingress into the stored lithium batteries.	Robbins (2007)
14 August 2002 **Clarence, New York, United States**	Shorts between used lithium batteries caused a disastrous fire, burning a total of 68 tonnes of waste. Two-thirds of them were primary lithium batteries.	Robbins (2007)

Automotive		
1 October 2013 **Kent, Washington, United States**	Direct impact of large metallic object into one of the modules in a 16-module battery pack caused fire in a Tesla Model S.	Abada et al. (2016)
17 October 2013 **Merida, Mexico**	Speeding Tesla Model S ended up in crash. The car was engulfed in fire and the car's front end appeared to explode.	Young (2013)

1.1.3 Potential Fire Hazard in Battery Triggers the Recall of Consumer Electronic Products

The number of recorded failures and recalls of batteries is relatively small, compared to the volume of production. It is estimated that the probability for the incidents to occur is less than one in a million cells, and possibly less than one in ten million (Doughty, 2011). The concerns by the manufacturers regarding the battery failure potential and the subsequent fire and explosion hazards have prompted some product recalls from the market. The action is necessary to protect consumers from any potential injuries and to keep the company integrity from disrepute. Information about product recalls in the United States can be found in the United States Consumer Product Safety Commission (CPSC) website.

In 2016, Samsung halted the production of the Galaxy Note 7 and prompted a worldwide recall programme of the model after more than 100 reports of fire and explosion (Lee and Kim, 2016, Cao and Fenner, 2016). The incident maimed the brand image of Samsung: the company lost its spot as the most profitable Android maker to Huawei in the final quarter of 2016, and cost the conglomerate $5 billion of operating profit (Sin, 2016).

In 2014, BBC reported that Panasonic is recalling more than 43,000 laptop and tablet battery packs. The flaw in the manufacturing process contaminated the battery seals with conductive materials, causing them to overheat, and under rare circumstances, to catch fire (Kelion, 2014).

1.1.4 Thermal Runaway in LIB Leads to Fire and Explosion

Most of the disastrous incidents related to LIB are caused by thermal runaway, which has been reported to be the common failure mode. This situation raises the interest in understanding the underlying causes and exploring the prospective techniques to alleviate the problem (Torabi and Esfahanian, 2011). Thermal runaway is triggered by abusive environments such as charging and discharging beyond the specified limit, high temperature operation and subjection to physical impact, which potentially entails induced internal short-circuit (Kim et al., 2008). Abuse tolerance is a daunting technical barrier for LIB as it is related to safety issues. Upon abuse - mechanically, electrically or thermally, the battery exhibits an anomalous temperature hike, which could potentially lead to disastrous shatter of the battery structure (Venugopal, 2001). Additional energy from overcharge activity and external heating exposure is expected to aggravate the severity of thermal runaway consequences (Larsson and Mellander, 2014).

The heat generated from the operation of LIB outside the stability window will induce the heat-activated exothermic reactions inside the battery, which in turn will generate a high amount of heat. The increase in temperature due to exothermic reactions accelerates the reaction kinetics and leads to further temperature rise (Golubkov et al., 2014). In some reactions, the heat is released alongside the emission of flammable and toxic gases. Gases venting is an expected phenomenon during thermal runaway, which is an engineered safety mechanism to prevent internal pressure build up inside the battery beyond its mechanical integrity and consequently lead to catastrophic rupture of the cell casing. High temperature from battery thermal runaway may ignite the flammable gases and combustible part of the battery components, resulting in fire. The vented gases may accumulate within any confined space or enclosure, and under extreme event, the ignition of the accumulated gases may cause explosion.

Higher capacity LIBs inflict more severe consequences during thermal runaway. This is demonstrated by higher energy release by LIBs at higher electrical energy content during induced failure as measured by Lyon and Walters (2016). The impact is expected to be even worse for large scale applications such as automotive and stationary energy storage since a copious amount of batteries with enormous capacity and high voltage are packed together in a single enclosure.

Even though the LIBs produced are of high reliability, which is less than one incident per one million, the number is still very high, especially for the automotive sector. A big number of cells in the energy pack leads to a dramatic increase of the failure rate by almost 1000 times (Eshetu et al., 2013). In addition, the batteries have to endure harsh conditions throughout their lifetime, where exposure to large temperature variations, shock, vibration, as well as high levels of charge and discharge is expected, which make them prone to suffer thermal runaway (Larsson and Mellander, 2014, Doughty and Pesaran, 2012).

Failure of a single cell can lead to cascade failure and complete destruction of the whole battery pack (Lamb et al., 2015, Feng et al., 2015a, Feng et al., 2015b, Spotnitz et al., 2007, Lopez et al., 2015b). The heat generated from the defective cell can propagate to the adjacent cells by convective, radiative and conductive heat transport processes. The heat transferred from the hot cell will heat the neighbouring cells gradually and eventually induce the heat-activated exothermic reactions in those cells, leading to thermal runaway propagation.

1.1.5 Current Techniques in Evaluating LIB Thermal Runaway Hazard

The apprehension of the hazards involved hinders the use of LIBs in applications with zero tolerance for a catastrophic failure. Due to this reason, a numerical indicator of the associated hazard is imperative to provide baseline for understanding the hazards involved and the subsequent safety assessment. In conducting quantified risk assessment (QRA), the information pertaining probability and consequence of the hazard is necessary. The odds of the incidents are established from statistical data and the consequence is the numerical indicator acquired from experimental evaluation or numerical modelling. The output from the quantitative risk assessment can be utilised to establish credible fire and explosion incidents related to battery for the subsequent emergency response and hazard mitigation.

1.1.5.1 Experimental Characterisation of Battery Thermal Runaway

Failure behaviour and thermal hazards of LIBs have been studied by using purpose-built equipment and subjecting them to abusive environments. LIBs are thermally, mechanically and electrically subjected to off-nominal conditions to gain valuable insight into the odds and severity of thermal runaway under various situations.

The oxygen depletion method is a well-established technique and has been used for a long time to provide a numerical indicator of traditional fire hazard. The heat release rate (HRR) is computed based on the Thornton principle, where the fire behaviour is assumed to be directly proportional to the instantaneous rate of oxygen consumption during combustion. This technique however, neglects the amount of heat liberated from Joule heating during short-circuit that might add to total fire hazard posed by LIBs (Ping et al., 2015, Larsson et al., 2014). Moreover, the fire safety concern of LIBs stems from its components where a combination of highly reactive electrodes and flammable organic electrolytes is present. The intrinsic thermal instability of the metallic compounds that form the battery active materials inflicts batteries to self-heat at high temperature, where in most cases, uncontrolled heat release from high rate exothermic decomposition reactions will lead to thermal runaway. In addition, decomposition reaction of positive active materials in the oxidised state releases oxygen. This self-generated oxygen will interfere with the oxygen quantifying process and subsequently reduce the value of measured consumed oxygen (Chen et al., 2015).

Adiabatic calorimetry techniques such as Accelerating Rate Calorimeter (ARC) and VSP2 Calorimeter have been used to explore thermal runaway behaviour of various available lithium-ion battery chemistries under wide range of conditions. In addition, custom-made test rigs are also built by researchers for this purpose. Thermal hazard caused by the thermal instability of the active materials and other components at elevated temperature can be well quantified by slowly inducing the heat-activated exothermic reactions according to the heat-wait-search mode as programmed in the calorimeter. In Vehicle Battery Safety Roadmap Guidance by Doughty and Pesaran (2012), a comparison of chemical instability as measured in self-heating profile by ARC of cylindrical lithium-ion cells fabricated from different cathode materials was presented.

1.1.5.2 Modelling of Thermal Reaction Kinetics for Thermal Runaway Simulation

The behaviour and response of lithium-ion batteries to thermal events can be simulated by modelling thermal decomposition reaction kinetic parameters obtained from thermal stability study of battery components. The breakdown or decomposition of the active materials can be described by specific reaction model, activation energy and pre-exponential factor, which are known as the kinetic triplet. The kinetic study of the active materials that forms the basis for thermal modelling of LIB full cell assembly is provided by Richard and Dahn (1999a) and MacNeil et al. (2000).

In early work by Richard and Dahn (1999c), oven exposure and short-circuit behaviour of LIB was simulated by exploiting thermal kinetic data from self-heating reactions at anode. Later, Hatchard et al. (2001) included autocatalytic exothermic reaction at cathode as part of the heat source term to the model previously developed by Richard and Dahn (1999c). Kim et al. (2007) reproduced work done by Hatchard et al. (2001) and included high temperature electrolyte decomposition reaction that was previously left out. The model was expanded to be three-dimensional using finite volume method to capture heat distribution within the structure and to investigate the effect of battery dimensions. Most of the work pertaining to battery kinetic modelling reported in literature refers to the kinetic model and heat source established by the previously mentioned authors, with some modification to the kinetic parameters to fit the battery chemistries under study.

The information obtained from thermal kinetic modelling enables researchers, developers and manufacturers, among others, to predict the output of thermal runaway without the necessity to perform dangerous, time-consuming and capital-intensive abuse tests (Ping et al., 2014). It is a convenient way to gain insight of unexplored conditions and thermal runaway triggering events, allowing preventative measures to be prepared based on the information.

1.2 Scope and Objectives of the Research

At the moment, most of the works reported in the literature related to thermal runaway study of lithium-ion batteries have been concentrated on the impacts and failure consequences of a single cell. There are limited studies conducted to quantify thermal runaway hazards of lithium-ion batteries beyond singular cell level.

The application of the lithium-ion batteries which previously circulating and contained around small scale electronics is now expanding into emerging markets such as electromobility and stationary energy storage. This situation necessitates for the understanding of the hazard involves in a large scale.

Therefore, this study is aimed at experimental investigation and numerical simulation of thermal runaway behaviour of lithium-ion battery at both singular cell and pack levels.

The objectives of this project include:

1. To identify thermal runaway hazards of lithium-ion battery
2. To establish the techniques of quantifying and characterising lithium-ion battery thermal runaway hazards
3. To establish a thermal kinetic database of thermal decomposition reactions of lithium-ion battery components
4. To develop a numerical model for simulation of lithium-ion battery thermal runaway based on thermal decomposition model of battery components
5. To include heat transfer modelling in the thermal runaway model for simulation of thermal runaway propagation in a battery module
6. To experimentally characterise lithium-ion battery thermal runaway and validate the numerical model
7. To investigate lithium-ion battery thermal runaway behaviour during impact-induced short-circuit

1.3 Research Approach

The research work consists of both numerical modelling and experimental validation. The cell chosen for this study is a 18650 cylindrical lithium-ion with lithium cobalt oxide (LCO) cathode and graphite anode. Thermophysical and kinetic parameters required for thermal runaway modelling are collected from literature.

A numerical model of thermal runaway for a single high-capacity lithium-ion battery is established by modelling the kinetics of thermal decomposition reactions of the battery components. In this work, four thermal reactions are considered. There are two reactions at anode, which are the breakdown of solid electrolyte interphase (SEI), and anode-electrolyte reactions. Meanwhile, both cathode and electrolyte have one reaction. Each of the reaction possesses characteristic thermal decomposition reaction model and parameters. The numerical model is used to predict thermal runaway behaviours of lithium-ion battery under constant high temperature and constant heating rate conditions.

The rapid conversion of electrical energy into heat is incorporated into the thermal kinetic model to simulate thermal runaway behaviour during impact-induced short-circuit. Heat transfer modelling is further included in the short-circuit model to simulate the propagation of thermal runaway in a battery module consists of nine identical batteries.

Experimental programmes are conducted to validate the numerical model. The characteristics of lithium-ion battery thermal runaway are experimentally investigated by using Accelerating Rate Calorimeter and oven. The differences in thermal runaway characteristics from these two approaches are compared. The severity of thermal runaway at different battery capacity and mass is further studied. In addition, destructive impact tests are done to validate the short-circuit model. The propagation of thermal runaway in a 3x3-matrix battery module is examined. Thermal imaging equipment is used to provide thermography of battery core and flames developed during impact tests.

1.4 Layout of the Thesis

Chapter 1 introduces the uprising trend in battery demand for consumer electronics and sustainable renewable energy utilisation. Fire and explosion events associated with batteries are presented, which provide the driving force and steer the direction of this research. The aim and approach of this study are subsequently discussed.

Chapter 2 reviews the fundamental concept of battery used in electrochemical energy storage device and the types of battery chemistry are presented. Safety hazards and modes of battery failure that lead to thermal runaway are discussed.

Chapter 3 reviews the work done in experimental evaluation of battery hazard and modelling of battery behaviour during failure. Thermal analysis and kinetic studies of battery components are discussed as they provide the fundamental base for numerical modelling of battery thermal runaway.

Chapter 4 describes the model developed in this study to simulate battery thermal runaway during failure. Thermal runaway propagation in a battery module is simulated by coupling thermal kinetic and heat transfer modelling.

Chapter 5 describes the experimental programme conducted to validate the model developed in the previous chapter and to provide quantitative information of battery thermal runaway hazards.

Chapter 6 discusses and compares the findings from both numerical modelling and experimental validation work.

Chapter 7 concludes the work done in this thesis and future work for the next stage of the research programme in this area is suggested.

Chapter 2: General Review of Battery and the Associated Safety Hazards

This chapter is aimed at a literature review of the fundamentals of energy storage technology using electrochemical cells, including the basic principle of battery operation and battery chemistries that are widely available. The discussion pertaining to battery safety hazards is highlighted on the rechargeable lithium-ion technology and the concern of fire and explosion hazard in the lithium-ion battery is elaborated. Conditions that lead to battery failure and result in hazardous consequences are identified. Chemical reactions following the battery failure are discussed.

2.1 Classification of Battery

Batteries are energy storage devices based on electrochemical reactions. The chemical energy content in the active materials is converted into electrical energy through electrochemical oxidation-reduction (redox) reactions (Linden, 2001, Väyrynen and Salminen, 2012). Even though there are various chemistries of batteries available, they are all governed by the same fundamental concept to work.

Batteries can be optimised for either power or energy application. Batteries for power application, such as automotive, are designed to deliver high amounts of energy rapidly and therefore draining the energy content within a short time. On the other hand, energy-optimised batteries can be found in computer and electronic applications, where the electrochemical cell is expected to sustain the lifetime of handheld devices (Larsson and Mellander, 2014).

Batteries are available in various geometries – cylindrical, coin and prismatic. The geometry and dimension are governed by international standards, but custom designs are also available for special purposes. Most of the cells are constructed in

accordance with International Electrotechnical Commission (IEC) Standard CEI/IEC 61960. Cylindrical cells are often assigned a five-figure number where the first two digits describe the cell diameter, and the rest represents the cell length in tens of millimetres (Mikolajczak et al., 2011).

2.1.1 Primary and Secondary Battery

Batteries can be classified into two main groups according to their rechargeability (Levy and Bro, 1994).

1. Primary battery

   Primary batteries are not rechargeable and they are discarded once their electrical charge has been spent. Partial charging is possible but this will create hazardous conditions. Most of the primary batteries are the common single-cell cylindrical and flat button batteries.

2. Secondary battery

   Secondary batteries are rechargeable by supplying external power, which will reverse the discharge process. There are two primary functions of rechargeable batteries.

   i. The secondary batteries are used essentially as primary batteries, but with the enhanced ability to be recharged. The batteries are being recharged after drained instead of being discarded. The vast amount of this kind of batteries can be found in portable consumer electronics such as mobile phones, digital cameras, tablets and so on.

   ii. The secondary batteries are used as energy storing devices (Rezvanizaniani et al., 2014). For this application, the batteries are electrically connected to a main energy source. The system stores the excess energy and discharges the energy deposit upon demand.

2.1.2 Main Components of a Battery

The three fundamental components of a cell are anode, cathode and electrolyte.

1. Anode

Anode, which is also known as negative active material, is the reducing fuel electrode. It gives electrons to the external circuit during the redox reaction and undergoes oxidation.

2. Cathode

Cathode, which is also known as positive active material, is the oxidising electrode. It accepts electrons from the external circuit during the redox reaction and undergoes reduction.

3. Electrolyte

Electrolyte provides the medium for charge transfer between anode and cathode within the cell.

2.1.3 Redox Process in Battery during Reversible Chemical-Electrical Energy Conversion

Figure 2.1 illustrates the operation of the cell during charge and discharge. Note that the figure on the right does not apply to the primary cell.

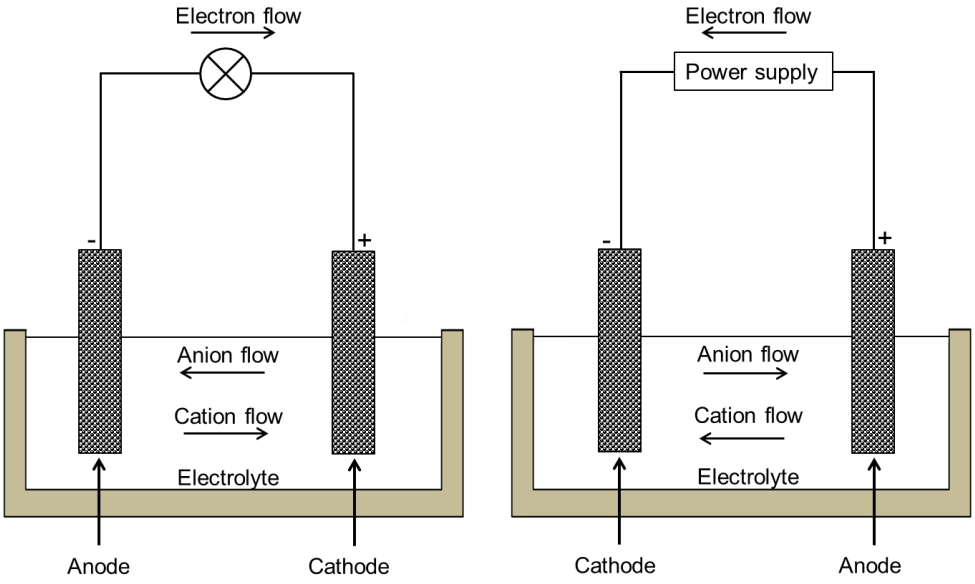

Figure 2.1: Discharge (left) and charge (right) processes in a cell. Adapted from Linden (2001).

During the discharge process (left), which is the conversion of the stored chemical energy into electrical energy, the anode material is being oxidised, releasing electrons that flow to, and accepted by cathode through the load. The cathode is then being reduced. The cations and anions in the electrolyte flow to the cathode and anode respectively and this ion flow, therefore, completes the electric circuit. During the discharge cycle, the anode is negative, and the cathode is positive. The discharge process is illustrated in Figure 2.1 (left).

Charging is a reverse to the discharge process. The process takes place with the supply of external power where the electrical energy is converted into chemical energy and stored in the battery. During the process, the current flows in the opposite direction, from cathode to anode. While charging, the charge at anode and cathode is reversed since it is determined by the reaction that occurs at the electrode. The positive terminal is known as the anode, and the negative terminal is known as the cathode. The charging process is depicted in Figure 2.1 (right).

2.1.4 Capacity and Voltage of Battery

The energy required to drive the electrons is provided by the cell voltage, which is a measure of the tendency of donors to donate electrons and acceptors to accept electrons. The cell voltage is the intrinsic property of active materials in the cell.

The amount of active materials in the cell determines its theoretical capacity, expressed as the number of electrons takes part in the electrochemical reaction. The theoretical capacity is expressed in Coulombs or Ampere-hours (Ah).

The theoretical energy of a cell is the maximum energy that can be delivered, a product of cell theoretical capacity and voltage, and expressed in Watt-hours (Wh) (Armand and Tarascon, 2008).

In practice, the real energy of the cell is much lower than the theoretical due to the following reasons (Linden, 2001).

1. The battery requires many other non-reactive components such as current collector, electrolyte, containers, seals and so on that contribute to the volume and mass of the battery.
2. The battery is not normally discharged fully to zero volts and not charged fully to the theoretical voltage. The former will lessen the delivered capacity, and the latter will lower the average voltage.
3. In normal practice, the stoichiometry balance is not achieved. This situation leads to the excess consumption of one of the active materials and thus reduces the specific energy.

2.2 Terminology in Battery Operation

This section defines some of the important terminology related to the battery operation (MIT Electric Vehicle Team, 2008).

C-rate: A measure of the battery capacity discharge and recharge rate relative to the battery maximum capacity. 1 C implies that the discharge rate will drain the whole capacity of the battery in one hour. For a battery with a capacity of 2.6 Ah, 1 C will discharge the entire 2.6 A in one hour.

State of charge (SOC): An expression of the present battery capacity as a percentage of maximum capacity. It is usually computed from current integration to determine the change in battery capacity over time.

Terminal voltage: The voltage between positive and negative terminals with load applied.

Open-circuit voltage (OCV): The voltage between positive and negative terminals without any load applied.

Cut-off voltage: The minimum voltage allowed and taken as drained state of the battery.

Nominal voltage: The normal voltage of a battery and usually used as a reference voltage.

Capacity: The measure of electrical charge and expressed in Ampere-hours (Ah).

Energy: A measure of total Watt-hours (Wh) available when a battery is discharged at a specified C-rate from 100 percent SOC to cut-off voltage.

Cycle life: The number of charge-discharge cycles of the battery during its lifespan.

Specific energy: Also known as the gravimetric energy. It is the energy per unit mass and expressed in Wh/kg.

Specific power: The power of the battery per unit mass, expressed in W/kg.

Energy density: The energy of the battery per unit volume, expressed in Wh/L.

Power density: The power of the battery per unit volume, expressed in W/L.

Many works related to battery safety investigate the potential hazard at different state of charge (SOC). Therefore, the concept of SOC will be discussed here. A review on the methods to determine SOC has been done by Lu et al. (2013a).

The authors define the SOC as the ratio of the remaining charge of a battery to the total available charge after being charged to the full capacity. The definition is straightforward for single cell but complexity appears as we determine the SOC for a battery module. A battery module with cells parallelly connected is conceptually a high capacity single cell. Due to the self-balancing characteristic of the parallel connection, determination of SOC for the battery module can be treated as for single cell.

The SOC of battery module with series connection, on the other hand, can still be estimated like a single cell. However, it is recommended to make a thorough consideration due to the battery uniformity issue. Provided that the capacity and SOC of each single cells in the battery module are known, the SOC of the module can be calculated as follows.

$$SOC_M = \frac{\sum SOC_i C_i}{\sum C_i} \quad \text{(Eq 2.1)}$$

where SOC_M is the SOC of the battery module, SOC_i and C_i are the SOC and capacity of the *i*th cell respectively. The real SOC of the battery module depends on the real performance and efficiency of the balancing device.

The main challenge in determining SOC of battery module is the measurement or precise estimation of the cell SOC. There are several techniques available for estimation of cell SOC as reviewed by Lu et al. (2013a).

(1) Discharge test method

Despite providing the most reliable data, this method is time-consuming. The procedure involves discharging the battery under controlled discharge rate and temperature. This method is only suitable for research purpose since the battery is fully drained after the discharge and therefore not appropriate for instantaneous estimation of batteries SOC for battery management system (BMS) in vehicles.

(2) Ampere-hour integral (Coulomb counting) method

By using this method, SOC can be mathematically expressed as follows.

$$SOC = SOC_0 - \frac{1}{C_N} \int_{t_0}^{t} \eta I \, dt \qquad \text{(Eq 2.2)}$$

where SOC_0 is the initial value of SOC at time t_0, C_N (Ah) is the rated capacity, η is the Coulombic efficiency, and I (A) is the current. The Coulombic efficiency is taken as 1 during discharge and less than 1 while charging.

(3) Open circuit voltage method

Since the amount of lithium ions in the active materials is commensurate to the open circuit voltage, it is therefore possible to determine SOC from this value. This time-consuming method provides highly precise SOC estimation and involves measuring open circuit voltage at balance state after adequate resting time. Some battery chemistries exhibit hysteretic charge-discharge pattern. Therefore, a careful consideration is necessary when using this technique.

2.3 High Voltage and Large Capacity Battery Pack

In electrochemical energy storage system, the basic unit is the cell, even though the term "battery" is commonly used. The application of batteries is specific; one battery cannot fit all purposes (Väyrynen and Salminen, 2012).

2.3.1 Integration of Individual Cells in Battery System for High Voltage and Large Capacity Applications

In large-scale applications such as automotive sector, the capacity provided by one single cell is not sufficient to satisfy the high energy and power demand. Therefore, it is necessary to build battery packs with a big amount of single cells packed and connected together. A module is assembled by electrically connecting a number of individual cells by either series or parallel or combination of both. A group of modules can be connected and placed together in a single enclosure to form a pack. Battery pack with battery management system, electronic control and other safety mechanisms is known as a system.

The common assembly of cells into a battery system is shown in Figure 2.2.

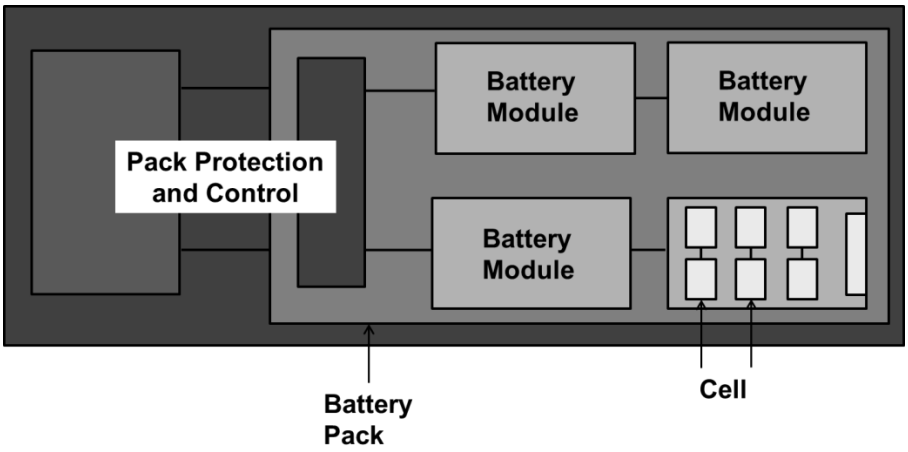

Figure 2.2: Schematic diagram of typical configuration of cells in a battery system for high voltage and large capacity applications. Adapted from Doughty and Pesaran (2012).

2.3.2 Hierarchy in High Voltage and Large Capacity Battery System

The relationship between cell, module, pack and system is described in Figure 2.3, as defined by Väyrynen and Salminen (2012).

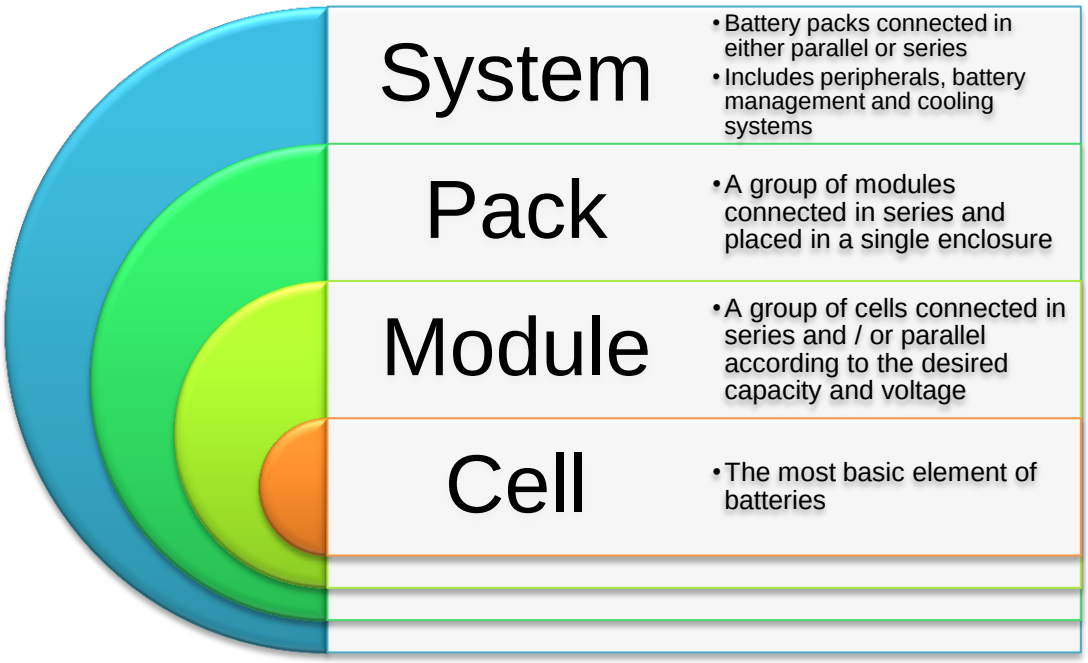

Figure 2.3: The relationship between cell, module, pack and system.

The inter-cells connection in a module is determined according to the required capacity and voltage. The series connection is implemented to achieve higher voltage while the parallel connection is used to acquire higher capacity. In some cases, cells are connected in both series and parallel in order to meet the voltage and capacity requirement. The parallel connection offers better reliability and reduces the impact of degraded cells.

The individual module is equipped with its own battery management system for monitoring of thermal and electrical parameters of the cells. The module level battery management system restricts the number of cells that can be assembled in a module (Saw et al., 2016).

A battery pack is an assembly of battery modules, which is contained within a metallic or plastic container (Saw et al., 2016). The demand for high energy density pack leads to compact design of battery pack with narrow inter-cells spacing (Lopez et al., 2015b).

2.4 Types of Battery Chemistry Available

Plenty galvanic pairs were proposed in the nineteenth and early twentieth centuries, with nickel-cadmium and lead-acid appeared to be the most popular rechargeable batteries (Armand and Tarascon, 2008). Table 2.1 presents some of extensively used batteries and its associate fundamental components.

Table 2.1: Main components of widely available batteries (Levy and Bro, 1994).

Battery	**Anode**	**Cathode**	**Electrolyte**
Zinc / Carbon (Zn/C)	Zinc	Manganese oxide Carbon	Ammonium chloride solutions Zinc chloride solutions
Silver / Zinc (Zn/Ag_2O)	Zinc	Silver oxide	Potassium hydroxide solution Dissolved zinc oxides
Alkaline / Manganese (Zn/MnO_2)	Zinc	Manganese oxide Carbon	Potassium hydroxide solution Dissolved zinc oxides
Lead-Acid (Pb/PbO_2)	Lead Antimony and / or calcium	Lead dioxide Various lead salts	Concentrated sulphuric acid solution
Nickel / Cadmium (NiOOH/Cd)	Cadmium	Hydrated nickel oxide embedded in a porous nickel matrix	Concentrated potassium hydroxide solution

Nickel / Metal Hydride (NiOOH / MH)	Metal hydride	Hydrated nickel oxide embedded in a porous nickel matrix	Concentrated potassium hydroxide solution
Lithium	Metallic lithium	Manganese dioxide	Lithium salt dissolved in organic solvents
Lithium-thionyl chloride	Porous carbon material	Thionyl chloride	Lithium tetrachloroaluminate
Lithium-ion	Lithiated carbon	Lithium transition metal oxide	Lithium salt dissolved in organic solvents

2.5 High Voltage Lithium-Ion Battery (LIB)

Most of the work reported in literature relating to battery safety is concentrated on lithium-ion technology. Hence, the following discussion in this thesis is focussed on lithium-ion battery (LIB), unless stated otherwise.

LIBs are substituting conventional batteries in the market such as NiMH, NiCd, alkaline and lead-acid batteries, and becoming the prospective candidates as energy carrier in electric vehicles and grid energy storage applications. They can offer high voltage (3.6 V), nearly double the conventional batteries (1.2 – 2 V) and high specific energy (240 Wh/kg), up to six times higher than lead-acid battery (40 Wh/kg) (Verma et al., 2010, Väyrynen and Salminen, 2012). In addition, the use of LIB is desirable due to its long life cycle and low self-discharge properties (Jhu et al., 2012). The superior energy content of LIB compared to other rechargeable chemistries is illustrated in Figure 2.4.

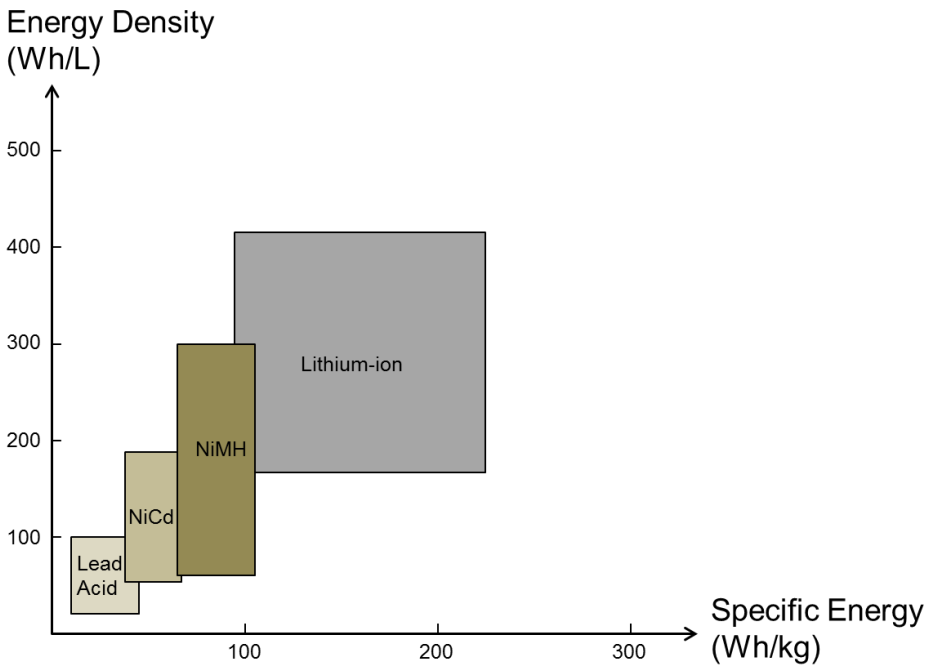

Figure 2.4: Comparison of volumetric and gravimetric energy density of common rechargeable batteries. Adapted from Väyrynen and Salminen (2012).

The high voltage offered by lithium-ion chemistries, which is three times higher than the one offered by NiMH technology, is highly desirable since the number of batteries required to meet the identical voltage requirement can be reduced to one-third. Since cells are commonly connected in series where the failure of a single cell could deactivate the entire module, the reduction in the number of cells in the module entails tremendous improvement to the reliability of the system (Kim et al., 2007).

The development of LIB is a vital milestone in the area of energy storage and conversion (Aurbach et al., 1997). LIB is constructed from carbon anode and transition metal oxide cathode (Doughty and Roth, 2012). Anode and cathode are surrounded by electrolyte but they are electronically isolated by a separator to prevent any internal short-circuit. The separator is semi-permeable to the electrolyte so that the desired ionic conductivity is sustained (Linden, 2001).

2.5.1 Various Chemistries of Lithium-Ion Battery

Rapid development in LIB has been observed with various chemistries having been introduced (Väyrynen and Salminen, 2012). An extensive review of the LIB chemistries has been done by Yang et al. (2006). The first LIB invented is based on lithium cobalt oxide cathode by Sony, which has been commercialised since 1991 and many other chemistries have been developed ever since (Väyrynen and Salminen, 2012). Table 2.2 presents the active materials and voltage range of some commercially available lithium-ion cells.

Table 2.2: Electrode materials and voltage range of various lithium-ion cells (Huria, 2012).

Chemistry	**Commercial name**	**Cathode material**	**Anode material**	**Maximum voltage**	**Nominal voltage**	**Minimum voltage**
Lithium iron phosphate	LFP	$LiFePO_4$	Carbon	3.65	3.3	2.5
Lithium cobalt oxide	LCO	$LiCoO_2$	Carbon	4.2	3.7	2.7
Lithium nickel manganese cobalt oxide	NMC	$LiNiMnCoO_2$	Carbon	4.2	3.6	3.0
Lithium manganese oxide	LMO Spinel	$LiMn_2O_4$	Carbon	4.2	3.7	2.75
Lithium nickel cobalt aluminium oxide	NCA	$LiNiCoAlO_2$	Carbon	4.2	3.6	3.0
Lithium titanate	LTO	$LiCoO_2$ / $LiFePO_4$	$Li_4Ti_5O_{12}$	2.9	2.25	1.5

Some of the battery chemistries employed for commercial electric vehicles are shown in Table 2.3, as compiled by Lu et al. (2013a).

Table 2.3: LIBs used in current electric cars (Lu et al., 2013a).

Vehicle	**Battery Supplier**	**Cathode**	**Anode**
Nissan Leaf EV	Automotive Energy Supply (Nissan NEC JV)	$LiMn_2O_4$	Carbon
Chevrolet Volt	Compact Power (subsidiary of LG Chem)	$LiMn_2O_4$	Carbon
Renault Fluence	Automotive Energy Supply (Nissan NEC JV)	$LiMn_2O_4$	Carbon
Tesla Roadster		$LiNi_{0.8}Co_{0.15}Al_{0.05}O_2$	Carbon
Tesla Model S	Panasonic Energy	Nickel-type	Carbon
BYD E6	BYD	$LiFePO_4$	Carbon
Subaru G4e	Subaru	Lithium-ion Vanadium	Carbon
Honda Fit EV	Toshiba Corporation	$LiCo_xNi_yMn_zO_2$	$Li_4T_5O_{12}$

2.5.2 Lithium Ion Exchange during Reversible Chemical-Electrical Energy Conversion in Lithium-Ion Battery

Electrical work is done in the LIB by the exchange process of lithium ions between anode and cathode that occurs through electrolyte. Upon charging with the supply of external power, lithium ions and electrons will move from cathode to anode through electrolyte and external circuit respectively and therefore complete the electrical network. Ions and electrons flow in a quasi-reversible process with insignificant change in the chemical structure of the cell components (Lyon and Walters, 2016). The flow direction is reversed during discharge. The illustration of this process is given in Figure 2.5. Due to the two-way movement of lithium ions between anode and cathode, LIB is known as the rocking chair or the swing battery (Wang et al., 2012).

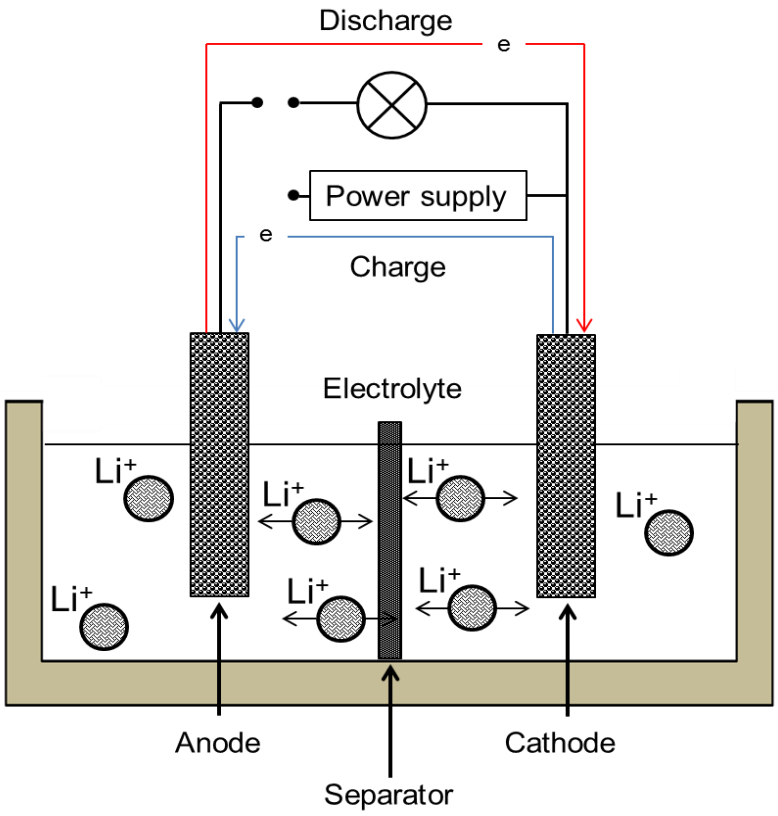

Figure 2.5: Electrons and lithium ions move back and forth between the electrodes during charging and discharge processes. Adapted from Nishi (2001).

For LIB with lithium cobalt oxide cathode, the electrochemical reactions at both cathode and anode during normal operation are shown below. The reactions proceed to the right hand side of the equations during charging and the processes are reversed to the left during discharge.

Cathode: $LiCoO_2 \leftrightarrow xLi^+ + Li_{1-x}CoO_2 + e$ (Eq 2.3)

Anode: $xLi^+ + e + 6C \leftrightarrow Li_xC_6$ (Eq 2.4)

The overall reaction can be expressed in the following equation.

$LiCoO_2 + 6C \leftrightarrow Li_{1-x}CoO_2 + Li_xC_6$ (Eq 2.5)

2.6 Fire and Explosion Hazard of Lithium-Ion Battery

Safety is a crucial feature of any energy storage device, including batteries (Doughty and Roth, 2012). In a review by Goodenough and Kim (2009), safety issues have been identified as the primary challenge in LIB battery development. Due to this reason, progressive development in safety technology is crucial (Ohsaki et al., 2005). While safety mechanisms in the battery might be able to alleviate the safety concerns, they might increase the manufacturing cost and reduce the energy density of the battery.

2.6.1 Source of Fire and Explosion Hazard of Lithium-Ion Battery

As discussed by Larsson and Mellander (2012), the fire hazard in the battery system is a combination of both exothermic reactions and normal fire from combustion of combustible peripherals. This can be expressed as in Eq 2.6.

Battery fire hazard = exothermic reactions + combustible peripherals (Eq 2.6)

1. Exothermic reactions

   Battery is constructed from highly reactive active materials and flammable electrolyte. The reaction of the components with each other releases high amounts of heat when initiated by abusive environments. Some of the reactions are accelerated process and the oxygen required for the combustion is self-produced within the batteries. Consequently, a fire incident due to this problem is difficult to handle. A discussion about the

chemical reactions that take place in batteries during thermal runaway is presented in Section 2.7.3. The first category fire can incite the second category fire.

2. Fire of combustible peripherals

   The second category of fire in the battery system is the traditional fire, which means the fire acquires the oxygen from the environment to sustain the combustion process. This kind of fire can be due to, for instances, fire in plastics, cables and housing of the battery pack.

Batteries are constructed in a unique way where both fuel (anode) and oxidiser (cathode) are placed together in a sealed container (Doughty, 2011). The fire safety concern of LIBs stems from its components where a combination of highly reactive electrodes and flammable organic electrolytes is present. In addition, there is an immense amount of energy stored within the small device.

Under normal operation, the stored chemical energy within the electrochemical cell is converted into electrical energy. However, if the fuel and oxidiser are allowed to react in any undesirable ways, the energy deposit is descended to a high amount of heat and accompanied by the release of toxic and flammable gases under the process called thermal runaway. Thermal runaway is triggered by abusive environments such as charging and discharging beyond the specified limit, high temperature operation and subjection to physical impact, which potentially entails induced internal short-circuit.

The heat generated from the operation of battery outside the stability window will induce the chain of chemical reactions inside the battery, which in turn will generate a high amount of heat. In some reactions, the heat is released concurrently with the emission of flammable and toxic gases. Lu et al. (2013b) reported that the gases generated could cause the pressure inside the cell to surge up to 120 bar.

Gases venting is an expected phenomenon during thermal runaway, which is an engineered safety mechanism to prevent pressure build-up inside the battery beyond its mechanical integrity and consequently lead to catastrophic rupture of the cell

casing. High temperature from battery thermal runaway may ignite the flammable gases and combustible part of the battery components to result in fire. The vented gases may accumulate within any confined space or enclosure, and under extreme events, the ignition of the accumulated gases may cause explosion. A study by Somandepalli et al. (2013) found that the explosion severity of vent gas from the LIB was between those of methane and propane. The team predicted a more severe consequence for overcharged cells.

2.6.2 Hazard Consequence Classification of Battery Safety Tests

The fire event from batteries abuse tests is considered as severe (rated as 5 to 6 out of 7) according to hazards rating schemes developed by various organisations (Ribiere et al., 2012). The description of the hazard level as outlined by European Council for Automotive R&D (EUCAR), Society of Automotive Engineers (SAE) and International Electrotechnical Commission (IEC) is presented in Table 2.4.

Table 2.4: Description of hazard level according to various institutions as compiled by Ribiere et al. (2012).

Overall hazard level	EUCAR description	SAE J2464 description	IEC description	Toxicity issue
0	No effect	No effect	No effect	
1	Passive protection activated	Passive protection activated	Deformation	
2	Defect / damage	Defect / damage	Venting	Yes
3	Leakage (Δmass < 50%)	Minor leakage / venting	Leakage	Yes
4	Venting (Δmass ≥ 50%)	Minor leakage / venting	Leakage	Yes
5	Fire or flame	Rupture	Rupture	Yes
6	Rupture	Fire or flame	Fire	Yes
7	Explosion	Explosion	Explosion	Yes

2.7 Thermal Runaway as Mechanism of Lithium-Ion Battery Failure

The recorded failure and recall of LIB incidents are small in number, compared to the production volume. It is estimated that the probability of the incidents is less than one in a million cells, and possibly less than one in ten million (Doughty, 2011). Most of the reported battery failures are due to thermal runaway (Torabi and Esfahanian, 2011). As previously mentioned, thermal runaway is triggered by operating the battery beyond the design specifications and outside the narrow thermal and electrical stability windows which leads to a surge in battery temperature (Kim et al., 2008).

2.7.1 Initiation of Thermal Runaway by Abusive Conditions and the Propagation in a Battery Pack

Abuse tolerance is a daunting technical barrier for batteries as it is related to safety issues (Kim et al., 2007). Abusive conditions may lead to hazardous situations especially for large systems, which is one of the main reasons deferring commercialisation of LIBs in the transportation sector (Bandhauer et al., 2011).

In general, operating the batteries beyond the stability window leads to heat generation and consequently triggers various chemical reactions in the batteries. Additional energy supply from overcharging and external heating is expected to exacerbate the severity of consequences during the undesirable rapid release of the battery energy deposit (Larsson and Mellander, 2014). Heat and gas generation is a typical response of batteries to abusive environments (Doughty and Roth, 2012).

Charging the batteries beyond the specified maximum voltage and vice versa causes the excess and irreversible extraction of lithium ions from the active materials. This process leads to permanent crystallographic change in both electrodes and results in higher oxidation potential (Doughty and Roth, 2012). The process of lithium ion removal gets harder at almost 100% overcharge due to the increasing cathode resistance and cell impedance. The battery heats up due to the Joule effect and consequently induces the heat-activated reactions (Ohsaki et al., 2005). The same process takes place during short-circuit and thermal abuse. The heat releasing reactions are initiated and being dragged further into thermal runaway by Joule

heating during short-circuit and external thermal energy supply during operation under thermally abusive environments.

The failure of a single cell can lead to cascade failure and complete destruction of the whole battery pack. The heat generated from the defective cell can propagate to the adjacent cells by convective, radiative and conductive heat transport processes. The thermal energy transferred from the hot cell will heat the neighbouring cells gradually and eventually induce the heat-activated exothermic reactions in those cells, leading to detrimental thermal runaway propagation.

Thermal runaway propagation in a battery module has been simulated in a model developed by Spotnitz et al. (2007). The occurrence of the cascade failure in the adjacent cells depends on the relative faulty cell position within the module and heat transfer coefficient. This simulation, however, does not specify the initial mode of failure that leads to this catastrophic event.

Even though there was no validation made for the model developed by Spotnitz et al. (2007), thermal runaway propagation was observed by other researchers such as Feng et al. (2015b) and Lamb et al. (2015). In both studies, thermal runaway was initiated in a single cell by using mechanical nail penetration. Quantification of the heat transfer process through the pole connector, battery shell and fire scorching has been performed by Feng et al. (2015b). The analysis found that the heat transport through the battery shell dominated the heat transfer process. Heat transport due to fire scorching is negligible for thermal runaway propagation but may cause significant damage to the accessories located above the battery module. The same conclusion was drawn in the study by Lamb et al. (2015). The impact of large contact surface between cells appears to be prominent for heat transfer process even though electrical connection is impactful for cells with limited surface area.

2.7.2 Heat Generation and Dissipation in Battery during Thermal Runaway

Battery is a small reactor that operates under different boundary and working conditions and hosts several exothermic reactions. Battery safety is determined by its operating and storage temperature. Battery thermal response to abusive conditions depends on its ability to dissipate heat to the environment.

Poor heat dissipation to the surrounding, along with heat accumulation inside the cells can further accelerate the exothermic reactions between the cell components rather than the desirable electrochemical reactions, leading to detrimental event thermal runaway. Once triggered, there is no way to deter the reactions, and the reactions will proceed to completion.

The process of heat exchange in battery during thermal runaway is illustrated by using Semonov plot in Figure 2.6.

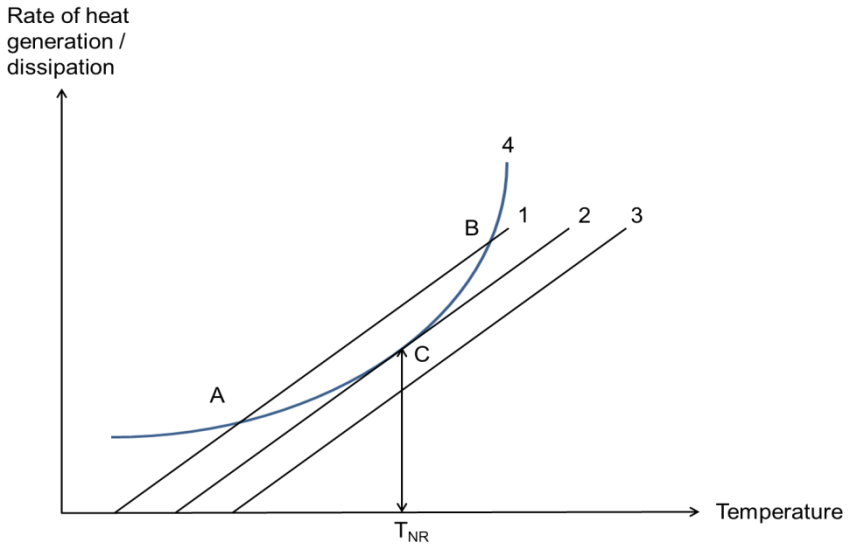

Figure 2.6: Semonov plot for thermal runaway. Adapted from Wang et al. (2012).

Three different heat exchange situations are demonstrated in this discussion. Heat dissipation to the surrounding is represented by three straight lines, Line 1, 2 and 3. The heat dissipation process is assumed to comply with Newton's law of cooling. Meanwhile, the exponential Curve 4 denotes the heat input from external sources,

Joule heating and chemical reactions, assumed to comply with Arrhenius law (Stull, 1977).

In order to provide sufficient cooling for the battery and consequently deterring thermal runaway from occurring, the ambient temperature has to be sufficiently low. This case is depicted in Line 1. The line intercepts Curve 4 at Point A and B where Point A is a stable point. In case of temperature rise or drop, the system will return to the stable point. Meanwhile, Point B is not stable. If the temperature decreases, it will keep falling to reach the stable Point A. If the temperature gets higher than Point B, thermal runaway is expected. In case of Line 2, the battery is experiencing equal heat generation and heat dissipation at the temperature of no return, T_{NR}, which is marked by the tangential point C. Thermal control of the battery temperature is not possible in case where ambient temperature is high to bring about the cooling effect, as represented in Line 3.

2.7.3 Heat-Induced Exothermic Reactions during Thermal Runaway

As previously mentioned in Section 2.6.2, the fire hazard of LIB stems from its components where a combination of highly reactive electrodes and flammable organic electrolytes is present. Due to the complex nature of LIB assembly, there might be numerous sources of heat and exothermic reactions during thermal runaway. These reactions are heat-activated which are instigated by abusive conditions.

According to Tobishima and Yamaki (1999), the heat release during thermal runaway originates from the following exothermic reactions.

1. Positive and negative active materials thermal decomposition
2. Electrolyte thermal decomposition
3. Electrolyte reduction at anode
4. Electrolyte oxidation at cathode
5. Internal short-circuit due to the meltdown of separator

A review by Spotnitz and Franklin (2003) proposed the following heat releasing reactions during abuse testing of LIB.

1. Breakdown of solid electrolyte interphase (SEI)
2. Reaction between intercalated lithium and electrolyte
3. Reaction between fluorinated binder and intercalated lithium
4. Breakdown of electrolyte
5. Decomposition of positive active materials
6. Reaction between metallic lithium, which is formed upon overcharged and electrolyte
7. Reaction between binder and metallic lithium
8. Ohmic resistance, overpotential and entropy change from battery discharge process

Wang et al. (2012) made an additional remark that the listed reactions may not necessarily take place according to the proposed sequence. In fact, some of the reactions are overlapped and difficult to categorise. One of the possible methods for reaction detection is by measuring the heat flow by using calorimetry techniques. This method, however, provides limited information about the species involved in the reactions. Further component identification is necessary for postulation of the chemical reaction mechanism.

Section 2.7.3 describes some of the fundamental reactions in LIB that can potentially cause thermal runaway. The discussion is organised based on the battery main components. The understanding of the reactions involved in thermal runaway is important for improvement of LIB tolerance to abusive conditions (Doughty et al., 2002).

2.7.3.1 Solid Electrolyte Interphase (SEI) Decomposition

The exfoliation of Solid Electrolyte Interphase (SEI) is the first exothermic reaction that occurs during thermal runaway and was discovered by Richard and Dahn (1999a). SEI is a surface film at anode, composed of a variety of salt and solvent reduction products from the first charging process. SEI is made up of metastable ($ROCO_2Li$, ROLi, $(CH_2OCO_2Li)_2$ and polymers) and stable (Li_2CO_3 and LiF)

components. Usually additives such as vinylene carbonate (VC) are added to improve thermal stability of SEI and hence constitutes a portion of SEI composition (Golubkov et al., 2015). The major component is $(CH_2OCO_2Li)_2$, an outstanding passivating agent, which is a reduction product of ethylene carbonate (EC) (Aurbach et al., 1996).

SEI serves as an ionic conductor that allows the transport of lithium ions during the intercalation and deintercalation processes. The film also works as an electronic insulator that prevents further electrolyte decomposition at negative electrode as certain thickness is achieved (Edström et al., 2006). SEI breakdown dictates the thermal response in cell chemistries with little or no oxygen release (Doughty and Roth, 2012).

The breakdown of SEI reaction was discovered by Richard and Dahn (1999a) as they investigated the self-heating behaviour of mesocarbon microbead (MCMB) in 1M $LiPF_6$/EC:DEC (1:2) at varying levels of lithiation using accelerating rate calorimeter (ARC). Identical self-heating peaks were observed at 100 ^oC for all samples irrespective of their degree of lithiation. The peaks appeared from depletion of the reacting species and the subsequent decrease in the rate of self-heating after the highest reaction rate was reached. The equal self-heating curve for all samples indicated that lithium did not take part in the reaction during the peak heat release. It was previously reported that the electrolyte breakdown occurred at 190 ^oC, rendering the reaction to be crossed out from the potential reactions that could possibly explain the observation.

The identical peaks implied that the observation was necessarily instigated by a reactant that was present in approximately the same concentration in all anode samples. Due to the constant concentration of SEI even at varying degree of lithiation, the team proposed that the observation was attributed to the decomposition of the SEI layer.

In separate works, Zhang et al. (1998) conducted a Differential Scanning Calorimetry (DSC) test on Li_xC_6 in $LiPF_6$/EC:DMC (1:1) at different degree of lithiation. Exothermic peaks with identical intensity were observed at approximately 130 ^oC regardless of the lithium content. The same trend was observed by Roth and

Nagasubramanian (2000) on anode of commercial LIB. The exothermic peaks of both charged and partially charged cells were almost identical. In both studies, the authors associated the observation with the breakdown of the passivation layer.

The SEI layer is unstable at high temperature. Physical penetration, overheating and overcharge compel the SEI to decompose. The reaction is exothermic and takes place at temperature between 90 ^{o}C and 120 ^{o}C.

According to Yang et al. (2006), the possible reaction mechanisms during the breakdown are as follows.

$$(CH_2OCO_2Li)_2 \rightarrow Li_2CO_3 + C_2H_4 + CO_2 + 0.5O_2 \quad \text{(Eq 2.7)}$$

$$2Li + (CH_2OCO_2Li)_2 \rightarrow 2Li_2CO_3 + C_2H_4 \quad \text{(Eq 2.8)}$$

According to Richard and Dahn (1999a), the reaction proceeded at a higher temperature to produce a higher self-heating rate while the pattern of identical peaks observed previously remained unchanged. From the curve of ln dT/dt versus 1/T, reaction kinetic of SEI breakdown was determined. The activation energy and the frequency factor of the reaction are determined to be 1.4±10% eV and $1x10^{17}$ min^{-1} respectively.

As the samples stale, the SEI decomposition reaction abates. In a DSC test, Richard and Dahn (1999a) detected a reduction in the intensity of the first exothermic peak near 140 ^{o}C in a sample subjected to extended storage at 60 ^{o}C, which was not observed in a fresh sample. The same pattern was observed by Roth and Nagasubramanian (2000) on the carbon anode of the aged commercial cell. In both studies, the investigators suggested that the ageing process causes partial conversion of metastable SEI into stable species, which is held responsible for the reduced heat intensity.

2.7.3.2 Reaction between Negative Active Materials and Electrolyte

The breakdown of the protective passivating layer exposes the anode surface to the electrolytes and provides an opportunity for the two components to react (Abraham et al., 2006). Electrolytes in LIB usually contain a combination of organic solvents such as ethylene carbonate (EC), propylene carbonate (PC) and dimethyl carbonate (DMC). The presence of different combinations of organic solvents inflicts a variety of reaction products. Intercalated lithium reacts with EC, PC and DMC as follows (Lopez et al., 2015a). All the listed reactions have Li_2CO_3 (one of the SEI components) as a mutual product, in addition to the flammable hydrocarbons.

$$2Li + C_3H_4O_3\ (EC) \rightarrow Li_2CO_3 + C_2H_4 \quad \text{(Eq 2.9)}$$

$$2Li + C_3H_6O_3\ (DMC) \rightarrow Li_2CO_3 + C_2H_6 \quad \text{(Eq 2.10)}$$

$$2Li + C_4H_6O_3\ (PC) \rightarrow Li_2CO_3 + C_3H_6 \quad \text{(Eq 2.11)}$$

The amount of lithium content in the graphite has a profound effect on the reactions. As observed by Wang et al. (2006), the reactions onset temperature exhibited a falling pattern while the amount of heat generated demonstrated an increment as the amount of intercalated lithium increased. In addition, the kinetic of the reactions is determined by the structural form of the solvents in use. Interaction between lithiated carbons and cyclic carbonates recorded a higher onset temperature and a lower heat generation compared to linear carbonates. The strong binding energy of covalent bond in cyclic carbonates entails higher temperature for the reaction to be triggered (Wang et al., 2009). In both studies, the authors presented activation energy and frequency factor of the reaction at each condition under investigation. As concluded by Wang et al. (2011), the ratio of loading in the electrolyte compositions has negligible impact on the reactions. Identical thermal response was observed in all samples at elevated temperature.

2.7.3.3 Fluorinated Binder Reactions

The polyvinylidene fluoride (PVDF) binder is a component of both positive and negative active materials, and can possibly contribute to thermal reactions in a cell. The reaction between intercalated lithium and PVDF occurred at 300 ^{o}C (Biensan et al., 1999).

Pasquier et al. (1998) proposed that lithium and fluorinated binder react according to the following mechanisms, where LiF is the major inorganic product from the reaction.

$$-CH_2-CF_2- + Li \rightarrow LiF + -CH=CF- + 0.5H_2 \quad \text{(Eq 2.12)}$$

$$2Li + RF_2 \rightarrow 2LiF + 0.5R_2 \quad \text{(Eq 2.13)}$$

Thermal analysis by Maleki et al. (1999) and Biensan et al. (1999) found that the reaction between fluorinated binder and lithium is exothermic. According to Roth and Nagasubramanian (2000), higher amount of lithium content in the carbon anode results in higher exotherm. Despite the findings by the investigators, simulation by Spotnitz and Franklin (2003) concluded that the reaction between lithium and fluorinated binder does not play an important role during thermal runaway since the amount of heat liberated from the reaction is relatively low compared to other reactions.

2.7.3.4 Electrolyte Decomposition

Electrolyte in LIBs is a blend of lithium salt, usually $LiPF_6$ and organic solvents. DSC scan of $LiPF_6$ salt by Roth and Nagasubramanian (2000) indicated that the salt decomposed at 195 ^{o}C. In a separate thermogravimetric analysis (TGA), it was found that the mass loss pattern showed a good consistency with the heat flow curve. There were no other thermal reactions observed above the melting point.

The decomposition of the $LiPF_6$ is endothermic and takes place according to the following mechanism.

$$LiPF_6 \rightarrow LiF + PF_5 \quad \text{(Eq 2.14)}$$

The produced PF_5 can further react with water according to the following mechanism.

$$PF_5 + H_2O \rightarrow POF_3 + 2HF \quad \text{(Eq 2.15)}$$

The salt can react with water according to the following chain reactions (Larsson et al., 2014).

$$LiPF_6 + H_2O \rightarrow LiF + POF_3 + 2HF \quad \text{(Eq 2.16)}$$

$$POF_3 + H_2O \rightarrow POF_2(OH) + HF \quad \text{(Eq 2.17)}$$

2.7.3.5 Positive Active Material Decomposition

A selection of positive active materials is available for LIBs. The materials are chosen by manufacturers based on the materials electrochemical and safety performance. The early-commercialised LIBs are based on lithium cobalt oxide ($LiCoO_2$). In general, the positive active material decomposes in the oxidised state to produce oxygen. Excess lithium ions deintercalation from the cathode degrades the electrode stability and consequently promotes oxygen release (Dahn et al., 1994).

The decomposition reaction of the oxide-based cathode materials raises the safety concern of the LIBs. The released oxygen can react exothermically with organic materials within the cell, promoting combustion process and consequently leads to fire. This reaction is the most energetic reaction during thermal runaway (Doughty and Roth, 2012).

For the $LiCoO_2$, the cathode decomposes according to the following mechanisms to produce oxygen (Wang et al., 2012).

$$Li_{0.5}CoO_2 \rightarrow \frac{1}{2}LiCoO_2 + \frac{1}{6}Co_3O_4 + \frac{1}{6}O_2 \quad \text{(Eq 2.18)}$$

$$Co_3O_4 \rightarrow 3CoO + \frac{1}{2}O_2 \quad \text{(Eq 2.19)}$$

$$CoO_2 \rightarrow Co + O_2 \quad \text{(Eq 2.20)}$$

As reported by Roth and Nagasubramanian (2000), fresh $LiCoO_2$ was inert. However, $LiCoO_2$ used for battery assembly exhibited a weak exothermic behaviour over the temperature range of 250 ^oC and 350 ^oC, with reducing intensity and higher onset temperature as the lithium content increased. The team concluded that the lithium removal from the cathode increases the oxidation potential of the electrode and consequently enhances solvent breakdown at the solvent / electrode interface. Thus, thermal stability of the positive active material is not of great concern at a discharged state.

2.8 Summary

It has been identified that hazardous situations are initiated by operating the batteries beyond the manufacturers' specifications, leading to thermal runaway. The heat generated from the abusive situations will induce a chain of chemical reactions inside the battery, which in turn will generate a high amount of heat. In some reactions, the heat is released concurrently with the emission of flammable and toxic gases. High temperature from battery thermal runaway may ignite the flammable gases and combustible parts of the battery components, resulting in fire. The vented gases may accumulate within any confined space or enclosure, and under extreme circumstances, the ignition of the accumulated gases may cause explosion. The transfer of heat from the defective cell to the neighbouring cells will eventually induce the heat-activated exothermic reactions in those cells, leading to thermal runaway propagation and cascade failure of the whole battery pack.

In the next chapter, the work done to evaluate the fire and thermal runaway hazards of lithium-ion battery will be reviewed.

Chapter 3: Literature Review of Evaluation Techniques of Battery Hazards

The hazards posed by LIB have been discussed in Chapter 2. The conditions inflicting catastrophic thermal runaway have been identified. As the applications of LIB are ubiquitous and become increasingly important, precise appraisal of the associated hazards is imperative for hazard quantification. The spur of lithium-ion technology in emerging applications necessitates the understanding of the risk involved.

Batteries are susceptible to standard safety evaluation before being allowed to enter the market. The tests are developed with input from representatives from consumers, authorities, manufacturers and academicians, and are governed by international bodies such as Underwriter Laboratories (UL), Institute of Electrical and Electronic Engineers (IEEE) and International Electrotechnical Commission (IEC) (Mikolajczak et al., 2011, Biensan et al., 1999).

In this chapter, studies done to evaluate LIB thermal hazards are reviewed. The discussion is organised into two main sections, which are experimental and modelling. Due to the diverse nature of the available lithium-ion chemistries and manufacturers that entails significant variation in battery energy and safety performance, an attempt has been made to compile information on the batteries used, particularly active materials, voltage and capacity.

3.1 Experimental Investigation of LIB Hazard

Failure behaviour and thermal hazard of LIB have been studied by using purpose-built equipment and subjecting to abusive environments. Batteries are subjected to thermal, mechanical and electrical off-nominal conditions to gain valuable insight into the probability and severity of thermal runaway under various situations. The hazard of LIB has been studied at both component level and complete cell assembly using various calorimeters.

3.1.1 Hazard Evaluation of LIB under Abusive Environments

Abuse tolerance is a daunting technical barrier for batteries as it is related to safety issues. The operation of batteries outside the design specifications prompts cell heating and concern arises as hazardous situations are created if the temperature exceeds the critical point (von Sacken et al., 1994). Characterisation and evaluation of battery components and full assemblies behaviour under abusive environments are important to provide baseline information on safety and abuse tolerance of a given cell chemistry (Doughty and Roth, 2012).

Abuse testing can be characterised into three main categories: thermal, mechanical, and electrical (Biensan et al., 1999, Tobishima and Yamaki, 1999). Different abusive environments result in different avenues to thermal runaway and distinctive failure behaviour. Some examples of the evaluation techniques are shown in Table 3.1.

Table 3.1: Evaluation techniques of thermal, mechanical and electrical abuse tolerance. Adapted from Biensan et al. (1999) and Tobishima and Yamaki (1999).

Category	**Evaluation techniques**
Mechanical	Crush
	Vacuum
	Nail penetration
	Pressure
	Vibration
	Drop
Electrical	Forced discharge
	Abnormal voltage charging
	Overcharging
	Abnormal current charging
	External short circuit
Thermal	Oil bath
	Fire exposure
	Heating
	Hot plate
	High and low temperature cycling

A survey by Spotnitz and Franklin (2003) identified five prevalent assessment methods to evaluate abuse tolerance of lithium-ion cells.

(1) Short-circuit: A low resistance is connected across the terminals of the battery.
(2) Nail penetration: A nail is forced through the battery at a specified speed. This test is considered as a simulation to internal short-circuit in the cell, which might be caused by defect in the manufacturing process.
(3) Oven: The battery is exposed to a higher temperature from some initial temperature. This test ascertains the cell thermal stability.
(4) Crush: The battery is crushed by using a bar. This assessment is considered as crucial and the survival of cell to this test is mandatory since there is no electronic device can provide protection from crush.
(5) Overcharge: Current is forced through the cell up to some limiting voltage.

A summary of some abusive evaluation tests reported in literature is given in Table 3.2.

Table 3.2: Summary of some prevalent assessments of abuse behaviour conducted by researchers.

Test	**Battery specification**	**Active materials**	**Reference**
Overcharge	EiG ePLB-F007H 3.2 V, 7 Ah EiG ePLB-F007A 3.2 V, 7 Ah European Batteries EBattery 3.2 V, 45 Ah	$LiFePO_4$ cathode and carbon anode	Larsson and Mellander (2014)
	Prismatic battery 0.72 Ah	$LiCoO_2$ cathode and MCMB anode	Belov and Yang (2008)
	Prismatic battery 0.65 Ah	$LiCoO_2$ cathode and graphite anode	Ohsaki et al. (2005)
Crush	ANR26650M1A 3.2 Ah	$LiFePO_4$ cathode	Dubaniewicz and DuCarme (2014)
	Saft MP 174565 4.8 Ah	$LiCoO_2$ cathode	
	4.13 V, 0.720 Ah	Details are not made available by authors	Tobishima and Yamaki (1999)
Oven test	18650 4.3 V, 2.8 Ah	$LiCoO_2$ cathode and graphite anode	Lopez et al. (2015a)

	E-One / Moli Energy ICR 18650 4.2 V, 1.65 Ah	$LiCoO_2$ cathode and carbon anode	Hatchard et al. (2001)
	18650 Samsung 18650 Sanyo 18650 K2 Energy	$LiCoO_2$ cathode $LiCoO_2$ cathode $LiFePO_4$ cathode	Larsson and Mellander (2012)
	4.13 V, 1.270 Ah	Details are not made available by authors	Tobishima and Yamaki (1999)
	NGK battery 3.8 V, 25 Ah	$LiMn_2O_4$ cathode and carbon anode	Kitoh and Nemoto (1999)
Nail penetration	NGK battery 3.8 V, 25 Ah	$LiMn_2O_4$ cathode and carbon anode	Kitoh and Nemoto (1999)
	4.13 V, 0.835 Ah	Details are not made available by authors	Tobishima and Yamaki (1999)
	Panasonic CGR18650CG 2.2 Ah AA Portable Power Corp. model 7035130-10C 3 Ah	$LiCoO_2$ cathode and graphite anode $LiCoO_2$ cathode and graphite anode	Lamb et al. (2015)
	3.8 V, 25 Ah	$LiNi_xCo_yMn_zO_2$ cathode and graphite anode	Feng et al. (2015b)

Short circuit	4.1 V, 1.5 Ah	$LiCoO_2$ cathode and graphite anode	Leising et al. (2001)
	NGK battery 3.8 V, 25 Ah	$LiMn_2O_4$ cathode and carbon anode	Kitoh and Nemoto (1999)

3.1.1.1 Overcharge

As a foreseeable misuse that can possibly arise from failure of the charger or electronic control, the understanding of potential hazards posed by overcharge is important. In a study by Larsson and Mellander (2014), the overcharge behaviour of high-power and high-energy $LiFePO_4$ batteries produced by two different manufacturers was compared. The high-energy and high-power batteries were overcharged at 2 C and 10 C up to 15.3 V respectively. In general, all cells swelled but no thermal runaway was observed. The cells temperature increased from room temperature and reached a moderate temperature between 70 ^{o}C and 80 ^{o}C without any incident, except for a battery from European Batteries that erupted in flames. The fire observed was not reproduced in other batteries and the team believed that the incident was due to the inherited defect from the manufacturing process.

Belov and Yang (2008) investigated the effect of applied current rate on battery temperature. Thermal runaway occurred under all current rates and inflicted the cells to shatter. The increase in applied current rate resulted in lower thermal runaway onset temperature and higher heat generation.

Ohsaki et al. (2005) examined thermal development and gas emission in battery at different state of overcharge. Hydrogen, carbon dioxide, ethane, carbon monoxide, ethylene and methane gases were released from the overcharge reaction and the amount of gases was proportional to the state of overcharge. Carbon monoxide formed the major constituent of the emitted gases at cathode. On the other hand, the biggest portion of the gases released at anode was hydrogen.

3.1.1.2 Crush

Loss of mechanical integrity of the battery structure is a contemplated problem that might arise from heavy load and high impact. Thus, the study of battery response to crush is important to provide an insight into the hazards involved in this situation. Dubaniewicz and DuCarme (2014) conducted crush tests on LIBs in an explosion containment chamber. The chamber was filled with 6.5% CH_4-air to simulate the hazardous conditions in a mining field. The batteries tested in their work were composed of $LiCoO_2$ and $LiFePO_4$ cathode. The cells were crushed using flat plate and plastic wedge and the severity of the failure inflicted by both methods was compared.

$LiCoO_2$ cell crushed using plastic wedge recorded a more perilous behaviour. Thermal runaway inflicted the cell temperature to soar up to 427 ^oC. The ignition of the chamber atmosphere by the crushed cells produced an overpressure up to 676 kPa. On the other hand, as for the $LiCoO_2$ cell crushed using flat plate, thermal runaway was not detected and ignition of the flammable atmosphere was not observed. Crushed $LiFePO_4$ cells using plastic wedge produced no chamber ignition and the overpressure recorded a reading lower than 20 kPa.

Tobishima and Yamaki (1999) conducted a crush test using a 10 mm diameter bar, halving the initial thickness of the batteries. The response of batteries to the invasive test at different charge states was studied. No smoke was released for the cell charged according to its specification. However, fire was observed for overcharged cell.

3.1.1.3 Oven Test

Oven test is a standard evaluation technique to assess battery thermal instability at high ambient temperature. The test provides important information such as activation and maximum temperature of thermal runaway under the specified environment. Lopez et al. (2015a) investigated the effect of different oven temperatures on thermal runaway development in LIB. At temperature of 145 ^oC, the battery temperature recorded a gradual increase and subsequently plateaued at the oven temperature. No thermal runaway was observed. The occurrence of

thermal runaway at oven temperature of 150 and 155 ^{o}C caused the battery temperature to surge and subsequently reduced to and sustained at the preset oven temperature after the completion of the chain reactions. An increase in the oven temperature resulted in a decrease in thermal runaway onset temperature. The same pattern was observed in a work by Hatchard et al. (2001). In both studies, models were developed to describe the thermal behaviour. Data provided by models showed a good agreement with the experimental data and validated the models as a reliable method for temperature prediction.

Larsson and Mellander (2012) examined thermal stability of commercial cylindrical LIBs by continuously heating up the batteries from ambient temperature to the onset of thermal runaway. Temperature spikes were recorded for Sanyo and Samsung batteries and the batteries ignited due to the high reactivity of $LiCoO_2$ cathode. On the other hand, K2 Energy battery, which was based on $LiFePO_4$ cathode, exhibited a mild temperature increase.

Heating test performed by Tobishima and Yamaki (1999) on commercial LIBs found that the batteries survived at 150 ^{o}C but smoked at 155 ^{o}C. In a separate study by Kitoh and Nemoto (1999) at 130 ^{o}C, the battery temperature maintained at the oven temperature for the first 80 minutes and increased to 190 ^{o}C thereafter. Venting was observed, but no ignition. Approximately 40 minutes after the test commenced, an abrupt rise in internal resistance was observed, which was inflicted by short-circuit during separator meltdown.

3.1.1.4 Nail Penetration

The heat liberated from Joule heating during internal short-circuit can trigger heat-activated exothermic reactions and consequently lead to thermal runaway. Therefore, the nail penetration test is performed to simulate an internal short-circuit and to provide an insight of the potential hazards involved during the undesirable electrical conduction. Tobishima and Yamaki (1999) performed a nail test using a nail with 2.5 mm diameter to investigate the effect of battery charge state on the internal short-circuit. Smoke was released from the overcharged cells. Nevertheless,

no smoke was observed from cells charged according to the manufacturer specification.

Kitoh and Nemoto (1999) conducted a stainless steel nail invasion test at 1 mm/s into the central part of a cylindrical battery body. The penetration resulted in venting of electrolyte vapour and hike of temperature up to 380 ^{o}C. Mechanical nail penetration studies were performed by Feng et al. (2015b) and Lamb et al. (2015) on battery modules. Both teams observed the propagation of thermal runaway from the punctured individual cells to the whole batteries in the pack, leading to catastrophic cascade failure of the whole module.

3.1.1.5 Short-circuit

Faulty battery wiring and connection can lead to short-circuit. The severity of the short-circuit event depends on the external short-circuit resistance. High resistance will render as a simple load while low resistance will inflict self-heating of the battery. Leising et al. (2001) observed an increase in the internal temperature of a short-circuited battery up to 132 ^{o}C at external short-circuit resistance of 6 mΩ. The cell gradually cooled down to ambient temperature thereafter. Kitoh and Nemoto (1999) examined the impact of short-circuit resistance on self-heating of LIB with internal resistance of 5 mΩ. No significant temperature hike was observed for short-circuit resistance of 0.2 mΩ due to the immediate cut of short-circuit current by battery current fuse. At 6 mΩ, the battery temperature increased up to 120 ^{o}C and slight venting of electrolyte vapour was observed after 80 s. The battery discharged normally at 11 mΩ and reached maximum temperature of less than 100 ^{o}C.

3.1.2 Study of Thermal Runaway Characteristics in LIB

As previously discussed, fire safety concerns of the LIB stem from its components where a combination of energetic electrodes and flammable organic electrolytes is present, which in turn entails the battery the ability to self-heat. Self-heating at high temperature is an indicator of thermal instability. Calorimeters and reactors are used to drive LIBs into thermal runaway and the resulting failure profiles are comprehensively studied for safety assessment. Hazards originating from the intrinsic reactivity and instability of battery components can be well quantified using those methods. Some of the studies done as reported in literature is summarised in Table 3.3.

Table 3.3: Examples of battery thermal runaway hazard appraisal conducted by researchers using purpose-built equipment.

Equipment	Battery Chemistry and Specifications	Reference
Accelerating Rate Calorimeter	• $LiCoO_2$ cathode and graphite anode • $LiMn_2O_4$ cathode and graphite anode	Mendoza-Hernandez et al. (2015)
	• $LiNi_xCo_yMn_zO_2$ cathode and graphite anode 25 Ah, 3.8 V	Feng et al. (2014)
	• Panasonic CGR18650E 2.55 Ah, 3.7 V • $LiCoO_2$ cathode and graphite anode	Ishikawa et al. (2012)
	• $LiCoO_2$ cathode • Gen2 – $LiNi_{0.80}Co_{0.15}Al_{0.05}O_2$ cathode • Gen3 – $Li_{1.1}(Ni_{1/3}Co_{1/3}Mn_{1/3})_{0.9}O_2$ cathode • $LiMn_2O_4$ cathode • $LiFePO_4$ cathode	Doughty and Pesaran (2012)

	• 18650 Sony cell • $LiCoO_2$ cathode and carbon anode • Gen 1 (Argonne National Laboratory Design) $LiNi_{0.85}Co_{0.15}O_2$ cathode and graphite anode • Gen 2 (Argonne National Laboratory Design) $LiNi_{0.80}Co_{0.15}Al_{0.05}O_2$ cathode and graphite anode	Roth and Doughty (2004)
VSP2 Adiabatic Calorimeter	• Sony SE US18650GR $LiCoO_2$ cathode 2.6 Ah, 3.7 V	Chen et al. (2016)
	• Sanyo UR18650F $LiCoO_2$ cathode 2.6 Ah, 3.7 V • Sony SE US18650GR 2.6 Ah, 3.7 V • Samsung ICR 18650-26D $LiCoO_2$ cathode 2.6 Ah, 3.7 V • LG LGDB218650 $LiCoO_2$ cathode 2.6 Ah, 3.7 V	Jhu et al. (2011a)
	• $LiCoO_2$ cathode 2.6 Ah, 4.2 V • $LiNiCoMnO_2$ 2 Ah, 4.2 V	Jhu et al. (2012)
	• 18650 cell $LiFePO_4$ cathode 1.1 Ah, 3.3 V	Wen et al. (2012)

	• 18650 cell $LiFePO_4$ cathode • 18650 cell $LiCoO_2$ cathode	Lu et al. (2013b)
	• Sanyo UR18650FM $LiCoO_2$ cathode	Jhu et al. (2011b)
C80 Microcalorimeter	• Self-assembled coin cells $LiCoO_2$ cathode and graphite anode	Ping et al. (2014)
Heatable reactor	• $LiFePO_4$ cathode and graphite anode 3.3 V, 1.1 Ah • $Li(Ni_{0.45}Mn_{0.45}Co_{0.10})O_2$ cathode and graphite anode 3.8 V, 1.5 Ah • $LiCoO_2$ / $Li(Ni_{0.50}Mn_{0.25}Co_{0.25})O_2$ cathode and graphite anode 3.8 V, 2.6 Ah	Golubkov et al. (2014)
	• $LiFePO_4$ cathode and graphite anode 1.1 Ah • $Li_x(Ni_{0.80}Co_{0.15}Al_{0.05})O_2$ cathode and graphite anode 3.35 Ah	Golubkov et al. (2015)
Confinement apparatus	• US14500 $LiCoO_2$ cathode 0.58 Ah, 3.7 V • UR14500 $LiCoO_2$ cathode 0.80 Ah, 3.7 V • LC14500 $LiMn_2O_4$ cathode 0.90 Ah, 3.6 V • IFR14500 $LiFePO_4$ cathode 0.90 Ah, 3.2 V	Hsieh et al. (2014)

Combustion chamber	• $LiCoO_2$ cathode and graphite anode 2.1 Ah	Somandepalli et al. (2013)
	• $LiCoO_2$ cathode 2.6 Ah • LiNiCoMn cathode • $LiFePO_4$ cathode	Maloney (2016)

3.1.2.1 Accelerating Rate Calorimetry (ARC)

ARC is an adiabatic calorimeter used to evaluate the self-heating behaviour of batteries at both component and full cell assembly levels. The small size of the standard ARC restricts the work in safety evaluation of large format battery. Recently an expanded version of ARC was introduced by Thermal Hazard Technology, which is known as Extended Volume – ARC (EV-ARC). The new equipment allows the study of hazards of large size batteries (Feng et al., 2014).

The concept of ARC is shown in Figure 3.1. A thermocouple is attached to the sealed battery, which is placed within the calorimeter. A controller is programmed to raise the temperature of the calorimeter to a preset temperature T. The battery heats up due to the heat transport from the heating element. Once the battery temperature approaches the preset temperature T, the temperature of the wall is maintained at T-ε. The small value of ε renders the heat transfer from the battery to the wall negligible and hence sustains the adiabaticity within the bomb.

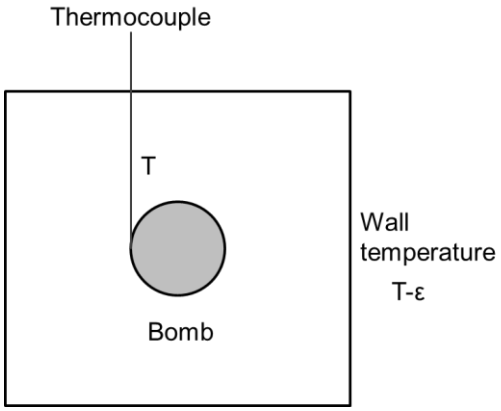

Figure 3.1: Schematic drawing of the adiabatic calorimeter. Adapted from Richard and Dahn (1999a).

The adiabatic self-heating rate of a battery can be measured as a function of time and temperature. From the plots, the onset temperature and the maximum self-heating rate of thermal runaway can be determined (Doughty, 2011). The width of the peak during thermal runaway gives information about the enthalpy of the reaction (Doughty and Roth, 2012).

ARC operates according to the heat-wait-search (HWS) mode which allows determination of the onset temperature of the self-heating profile (Roth and Doughty, 2004). In this mode, the ARC raises the temperature in discrete predetermined steps. Each step raises the temperature and is followed by a waiting period to allow thermal transients to decay and to achieve adiabatic thermal equilibrium between the bomb and the calorimetric jacket (dos Santos et al., 2014). The temperature is increased by another step and the process is repeated if the cell temperature rise does not reach a threshold value, usually 0.02 ^{o}C/min.

If any exothermic reaction takes place, the battery temperature will increase. Subsequently, the ARC shifts to the exotherm mode and the heating process is stopped if the cell temperature increases at a rate equal to or above the threshold value. In order to maintain the adiabaticity of the experimental operation during the exotherm mode, the ARC temperature closely matches the cell temperature, even at high heating rates. During normal operation, the ARC terminates an experiment if the rate falls below the detection limit or endpoint temperature is reached. The algorithm of ARC operation is illustrated in Figure 3.2.

The ARC experiment closely simulates a thermally abusive environment that includes moderately high temperature for relatively long periods of time (Roth and Doughty, 2004). One major disadvantage of ARC is that it is not suitable for investigating endothermic reactions (Golubkov et al., 2014).

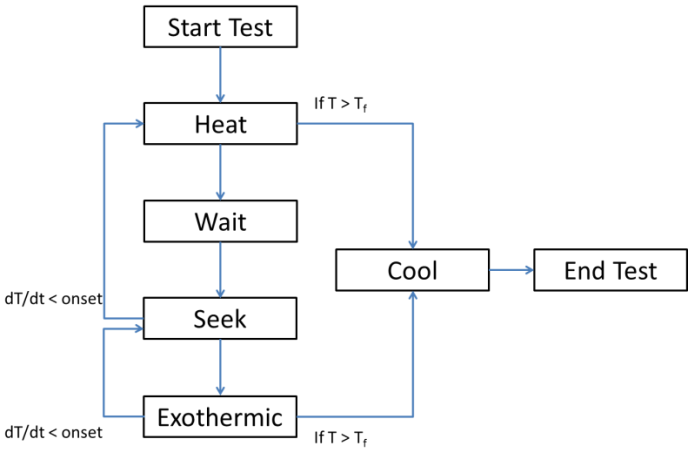

Figure 3.2: Algorithm of ARC operation. Adapted from dos Santos et al. (2014).

Mendoza-Hernandez et al. (2015) compared the effect of charge state on the self-heating behaviour of two different battery chemistries using ARC. The onset of the self-heating temperature decreased as the state of charge increased for $LiCoO_2$-based batteries. $LiMn_2O_4$-based batteries, on the other hand, did not display significant dependency on the charge state. To conclude, $LiCoO_2$ batteries are more reactive and thermally unstable compared to $LiMn_2O_4$ as reflected by higher self-heating rates at all states of charge.

Ishikawa et al. (2012) utilised ARC to examine characteristic of battery thermal runaway at 87% SOC. An abrupt escalation in the battery internal resistance at high temperature caused the open circuit voltage to drop suddenly.

Feng et al. (2014) used ARC to investigate thermal runaway feature of a large format LIB. The battery internal temperature recorded a maximum temperature of 870 ^{o}C, which occurred after the collapse of the separator at 260 ^{o}C. The meltdown of the separator led to internal short-circuit which in turn inflicted the descending of the battery electrical energy into a massive amount of heat.

Roth and Doughty (2004) assessed the thermal abuse response of two advanced battery chemistries developed by United States Department of Energy as part of the Advanced Technology Development (ATD) Program and the findings were compared with commercial Sony 18650 cells. In general, all batteries recorded a higher self-heating rate at higher state of charge. Sony battery, which is based on

$LiCoO_2$ cathode, demonstrated the highest thermal instability among the trio and its behaviour at lower temperature is comparable to the Gen2 cells. An ageing process renders the batteries more thermally stable as the batteries capacity gradually deteriorates with time.

Doughty and Pesaran (2012) reported self-heating behaviour of LIBs and safety performance of five different cathode materials was compared. $LiCoO_2$ battery recorded the lowest onset temperature, highest maximum self-heating rate and widest temperature range, implying that this chemistry is the least thermally stable compared to others.

3.1.2.2 VSP2 Adiabatic Calorimeter

The functions of this equipment are almost similar to ARC (Feng et al., 2014). This equipment has been used by Jhu's group for investigation of thermal and explosion hazard of different LIBs under various conditions (Wen et al., 2012, Jhu et al., 2012, Jhu et al., 2011b, Jhu et al., 2011a).

Chen et al. (2016) characterised thermal runaway features of LIBs at varying SOC using VSP2 calorimeter. Half-charged and higher batteries demonstrated two apparent phases during failure: (1) thermal runaway stage and (2) thermal explosion stage. Activation energy and pre-exponential factor as per Arrhenius relationship at both stages were determined. Temperature increment and the associated energy release at both phases were established. The self-heating behaviour of Stage 1 was mathematically reproduced by using the kinetic parameters and pseudo-zero order reaction model with a reasonable agreement with the experimental data. TNT-equivalent of the total heat released was determined according to the following equation.

$$m_{TNT} = \frac{\chi \Delta H_{battery}}{Q_{TNT}^{1/3}} \quad \text{(Eq 3.1)}$$

where m_{TNT} (g) is the TNT-equivalent mass, χ is the empirical mass of TNT, $\Delta H_{battery}$ (kJ) is the total heat released by battery and Q_{TNT} (kJ/g) is the explosion energy of TNT, usually taken as 4.602 kJ/g.

Jhu et al. (2011a) investigated thermal and self-heating profile of commercial 18650 cylindrical LIBs with $LiCoO_2$ cathode produced by four worldwide consumer battery producers at two different voltages. Activation energy and pre-exponential factor of the failure process were established by using Arrhenius equation.

Jhu et al. (2012) replicated the same test procedures to compare different positive active materials in commercial cylindrical LIBs while the voltage were kept identical. The cathodes of concern were $LiCoO_2$ and $LiNiCoMnO_2$. $LiCoO_2$ chemistry exhibited higher temperature and self-heating rate with lower onset temperature. Activation energy and frequency factor of both chemistries were calculated by Arrhenius relationship using the self-heating profiles.

Jhu et al. (2011b) compared thermal hazard of Sanyo batteries at half and full charge. A battery with 100% SOC posed a bigger hazard as reflected by lower onset temperature, and higher temperature and pressure profiles. Wen et al. (2012) investigated thermal runaway features of full-charged and overcharged 18650 cylindrical $LiFePO_4$ LIBs. Overcharged battery exhibited a more violent behaviour during failure as reflected by lower onset temperature and higher temperature and pressure profiles.

Lu et al. (2013b) examined thermal hazard features of LIB under full-charged and storage state. The cells were composed of $LiFePO_4$ and $LiCoO_2$ cathode materials. Thermal response was more reactive under full-charged condition for both chemistries. Under both storage state and full-charged condition, violent response was observed for $LiCoO_2$ chemistry. The team calculated the TNT equivalent and found that LIBs with $LiCoO_2$ cathode poses a greater hazard than $LiFePO_4$.

3.1.2.3 C80 Microcalorimeter

While some of the calorimetry instruments are unable to detect heat-absorbing reactions, C80 Microcalorimeter comes with the ability to detect endothermic reactions and thus providing information on instantaneous change of heat flow. The detection of both heat releasing and absorbing reactions is better presented using this equipment. The sensitivity of the machine is 0.1 μW and the adiabatic condition sustains the constant temperature stability of the system with deviation of ±0.1 ^{o}C.

Ping et al. (2014) performed thermal analysis of in situ self-assembled coin cells with varying mass of components using C80 Microcalorimeter. The heat flow curves obtained from the test were mathematically deconvoluted to separate the overlapping peaks. Kinetics of the individual peaks were determined and the associated chemical reactions that took place were discussed.

3.1.2.4 Combustion Chamber

Somandepalli et al. (2013) investigated combustion characteristic of gases vented by LIBs during thermal runaway. Composition of hydrogen, carbon monoxide, carbon dioxide and various hydrocarbons at 50%, 100% and 150% SOC was determined. The vented gas was subsequently ignited using a 100 J chemical ignitor in a 20 L combustion chamber. The peak overpressure and the rate of pressure change over a range of gas-air ratio were established. The explosion severity was then calculated by using the following equation.

$$K_g = \frac{dP}{dt} V^{\frac{1}{3}} \quad \text{(Eq 3.2)}$$

where K_g (Pa.m/s) is the explosion severity, dP/dt (Pa/s) is the rate of pressure change and V (m^3) is the chamber volume.

The explosion severity of vented gas at 100% SOC is 65 m-bar/s, which is between methane and propane. The team predicts a more severe consequence at overcharge conditions.

Maloney (2016) quantified various gases emitted during thermal runaway. Volume and concentration of gases released (total hydrocarbons, hydrogen and carbon monoxide) were established at varying charge states and compared between three batteries. Correlation between lower flammability limit (LFL) of gases released by $LiCoO_2$ cells and SOC was determined. The gases were ignited in a 21.7 L combustion chamber to investigate the pressure rise from the combustion of gases emitted by full-charged and half-charged batteries at varying gas-air ratio.

3.1.2.5 Heatable Reactor

Golubkov et al. (2014) built a custom-designed test rig to conduct unrestricted thermal runaway experiments where heaters were used to induce thermal runaway in the LIBs. The reactor was equipped with ten thermocouples for temperature measurement of battery surface, sleeve heater and reactor interior. A pressure transmitter was attached on top of the reactor to measure the reactor internal pressure.

The team studied thermal stability of commercial lithium-ion batteries. Three positive active materials were considered: $LiFePO_4$, $Li(Ni0._{45}Mn_{0.45}Co_{0.10})O_2$ and a blend of $LiCoO_2$ and $Li(Ni_{0.50}Mn_{0.25}Co_{0.25})O_2$. Thermal runaway of the batteries was characterised by maximum, runaway and onset temperature. Three apparent stages were observed: (1) heat up, (2) quasi-exponential and (3) rapid thermal runaway. The amount of gases vented during thermal runaway was calculated according to the ideal gas law.

$$n= \frac{PV}{RT} - n_0 \qquad \text{(Eq 3.3)}$$

where n (mol) is the amount of gases, P (Pa) is the reactor internal pressure, R (J mol^{-1} K^{-1}) is the gas constant and T (K) is the gas temperature, and n_0 (mol) is the initial amount of gases inside the reactor.

The cell with $LiFePO_4$ demonstrated the least reactive response to thermal abuse, and recorded the lowest temperature rise, self-heating rate and amount of gases released while the blended cathode exhibited the most reactive response. The release of H_2, CO, CO_2, CH_4, C_2H_4 and C_2H_6 gases was detected using gas chromatography technique. Possible chemical reactions leading to the gas generation were discussed accordingly.

In another study, Golubkov et al. (2015) investigated the severity of thermal runaway at varying SOC ranging from 0 to 150%. The study focused on LIBs with $LiFePO_4$ and $Li(Ni_{0}._{45}Mn_{0.45}Co_{0.10})O_2$ cathode. The information on effect of SOC on thermal runaway onset and maximum temperature was established. In addition, the amount of vented gases and its composition at different SOC were determined.

3.1.2.6 Confinement Apparatus

Hsieh et al. (2014) constructed a custom-designed confinement equipment to simulate pseudo-adiabatic condition. The equipment, with internal vessel volume of 100 mL, was equipped with pressure transducer and temperature detector to monitor thermal runaway trajectory. Hsieh et al. (2014) compared thermal hazard characteristics of commercial 14500 LIBs composed of three different cathode materials: $LiCoO_2$, $LiFePO_4$ and $LiMn_2O_4$. $LiCoO_2$ exhibited the most severe behaviour as indicated by highest pressure and temperature profiles during failure, followed by $LiMn_2O_4$ and $LiFePO_4$.

3.1.3 Study of LIB Fire Characteristics during Fire Events

As part of safety management, a full appraisal of fire hazard caused by lithium-ion technology is necessary. Fire occurrence is possible due to the presence of combustible materials and flammable electrolytes as parts of the battery assembly, in addition to the reactive electrode materials. Heat release rate (HRR), particularly peak heat release rate (PHRR) is the utmost important parameter in fire safety evaluation.

The advantage of using heat release rate as a quantitative indicator of fire hazard is that the knowledge about chemical compositions and combustion chemistry of the materials is not necessary (Biteau et al., 2008).

There are three methods to calculate the heat release rate.

1. Mass loss

The knowledge about the heat of combustion is necessary for this method. The main challenge for this method is the uncertainty about the completion of the combustion reaction. The heat release rate can be calculated as follows.

$$\dot{q} = \Delta H_c \, \dot{m}_{fuel} \qquad \text{(Eq 3.4)}$$

where $\dot{q}$ (W) is the heat release rate, ΔH_c (J/kg) is the heat of combustion and $\dot{m}_{fuel}$ (kg/s) is the mass flowrate of the combusted material.

2. Convective calorimetry

It is necessary to conduct energy balance in order to employ this method. The knowledge about heat loss term is required. The heat release rate can be calculated as follows.

$$\dot{q} = \dot{m}_e \, C_{p_{air}} \, \Delta T \qquad \text{(Eq 3.5)}$$

where $\dot{q}$ (W) is the heat release rate, $\dot{m}_e$ (kg/s) is the mass flow rate of combustion products, $C_{p_{air}}$ (J/kg.K) is specific heat capacity of air and ΔT (K) is the change in temperature.

3. Species based calorimetry

This technique is based on species concentration, and it is necessary to conduct mass balance in a closed system in order to calculate the heat release rate. The most prevalent technique is based on oxygen mass balance, which has been proven an accurate technique for predicting the heat release rate of polymers, fuels and other chemicals.

According to the Thornton principle, the amount of heat liberated during combustion is proportionate to the amount of oxygen consumed during the process, regardless of the materials or fuels combusted, where complete combustion of 1 kg of oxygen will release 13.1 MJ heat. The cone calorimeter, also known as an oxygen calorimeter is an example of equipment based on this principle. Based on the oxygen depletion method, the heat release rate during any fire event can be calculated by the following equation.

$$\dot{q} = \Delta H_{oxygen} \left(\dot{m}_{O_2}^{0} - \dot{m}_{O_2} \right) \quad \text{(Eq 3.6)}$$

where $\dot{q}$ (W) is the heat release rate, ΔH_{oxygen} (J/kg) is the heat of combustion of oxygen, $\dot{m}_{O_2}^{0}$ (kg/s) is the initial oxygen mass flow rate and $\dot{m}_{O_2}$ (kg/s) is the final oxygen mass flow rate. This equation however will overestimate the heat release rate since most of the combustion process is not complete. A correction factor is necessary to take into account the formation of soot and carbon monoxide.

Even though the measurement of heat release rate according to the oxygen consumption method is a well-established and accepted technique in the fire calorimetry field, Ping et al. (2015) and Larsson et al. (2014) pointed out that the use of this method for quantifying fire hazards of LIBs will impose some inaccuracies. In the event of battery fire, the melting or burning of the separator will lead to short-circuit. The oxygen depletion method is unable to enumerate the amount of thermal energy liberated from Joule heating. Moreover, as discussed in Section 2.7.3.5, the decomposition reaction of positive active material in the oxidised state releases oxygen. This self-generated oxygen will interfere with the oxygen measurement process and subsequently reduce the value of measured consumed oxygen.

Ribiere et al. (2012) estimated that the maximum amount of heat released by the erratic electrical discharge is approximately one-tenth of the total energy hold by full-charged batteries. They therefore concluded that the oxygen depletion technique is acceptable for HRR estimation.

Work done by Chen et al. (2015) discovered that ignoring the effect of internally generated oxygen introduced significant error. In their work, fire development of $LiCoO_2$ and $LiFePO_4$ 18650 cells were compared using fire calorimeter. Lower heat release rate was observed for $LiCoO_2$, implying safer or less reactive response to fire, which is conflicting to previous studies. This observation can be explained by the neglected additional internally self-generated oxygen gas at positive active material. The team corrected the HRR computation by measuring the amount of oxygen gas evolved and subsequently recalculated the associated HRR.

Some of the studies done related to fire hazard are shown in Table 3.4. The experimental rigs used for fire hazard study might have varying names, nevertheless, all the equipment in use principally comprises of two main components, which are the sample ignition and gas detection systems.

Table 3.4: Examples of some battery fire hazard evaluation conducted by researchers.

Reference	**Equipment**	**Battery Specification**	**Battery Active Materials**
Chen et al. (2015)	Fire Calorimeter	Samsung ICR18650-26FM	$LiCoO_2$ cathode and graphite anode
		Sony US18650FT	$LiFePO_4$ cathode and graphite anode
Ribiere et al. (2012)	Tewarson Calorimeter	Pouch 2.9 Ah, 4.1 V	$LiMn_2O_4$ cathode and graphite anode
Larsson et al. (2014)	Single Burning Item	EiG ePLB-F007A 35 Ah, 3.2 V	$LiFePO_4$ cathode and carbon anode
		K2 LFP26650EV 28.8 Ah, 3.2 V	$LiFePO_4$ cathode and carbon anode
		Lenovo laptop battery pack 33.6 Ah, 3.7 V	$LiCoO_2$ cathode
Fu et al. (2015)	Cone Calorimeter	Sanyo UR18650FM 2.6 Ah	$LiCoO_2$ cathode and graphite anode
Ping et al. (2015)	Full-Scale Burning Apparatus	10 Ah	$LiFePO_4$ cathode and graphite anode

3.1.3.1 Single Burning Item

Larsson et al. (2014) studied the burning behaviour of LIB modules during fire tests, comparing two types of positive active material: $LiFePO_4$ (pouch) and cobalt-based (laptop battery pack) using Single Burning Item (SBI). Batteries were ignited using a propane burner. A gas analysis system was equipped to provide in situ measurement of CO, CO_2, HF, POF_3 and O_2 release.

HRR information of the fire event was established in compliance to oxygen consumption method and was corrected for CO_2 generation. HRR spikes were observed in full-charged EiG modules. Broad HRR peak was observed for half-charged and completely drained EiG modules with decreasing magnitude as the SOC decreased. Higher amount of HF release was recorded at lower SOC. Sprinkling water mist into the flame accelerated the rate of HF release while the total emission remained unchanged.

3.1.3.2 Tewarson Calorimeter

In Tewarson calorimeter, batteries are ignited under controlled conditions at the lower part of the equipment. Infrared heaters are used to apply external heat flux to the combustion chamber, providing thermal aggression comparable to a fire event. The fuel-deprived ignition method is desirable in such a way that there is no gas release from the combusted fuel that otherwise will interfere with gases emitted by the batteries under testing. Flammable gases produced from the batteries are ignited using a pilot-flame located at 30 mm above the batteries. Combustion gases are analysed in situ to measure the amount of total hydrocarbons (THC) by using flame ionisation detector, oxygen by using paramagnetic analyser, soot by using optical measurement and carbon dioxide and carbon monoxide by using Fourier-Transform Infrared Spectroscopy (FTIR). Supplementary FTIR is used to give information on standard toxic gases such as SOx, NOx, HCN, hydrogen halides and aldehydes (Ribiere et al., 2012).

Ribiere et al. (2012) performed calorimetry tests at varying SOC to quantify thermal and toxic hazards associated with battery combustion. The team found that peak HRR and reaction rate increased with increasing SOC. The process shifted toward incomplete combustion at higher SOC, as indicated by higher amount of total hydrocarbons and carbon monoxide release.

The heat of combustion of the batteries calculated from the integration of heat release rate was in good agreement with the summation of combustion heat of battery components. The total mass loss recorded an identical reading at all SOC, which was believed to be caused by the combustion of organic and polymeric components of the battery. Exfoliated copper foil was observed and aluminium droplets were noticed at the end of the test. From the observations, it can be deduced that the maximum temperature reached during the combustion process ranges from 600 ^{o}C to 1083 ^{o}C. No organic and polymeric compounds will be able to sustain that temperature and will obviously be combusted.

In general, NO, HF and HCl exhibited almost identical emission patterns. As the SOC increased, the peak gas concentration increased but the production period shortened. SO_2 recorded the highest peak concentration compared to NO, HF and HCl for full-charged cells, but became negligible at 50% and 0% SOC due to the inadequate heat release rate.

3.1.3.3 Cone Calorimeter

Fu et al. (2015) used the cone calorimeter to investigate fire hazard of LIBs at varying SOC and incident heat flux. Heat was radiated to the batteries by the cone heater. The calorimeter was equipped with gas analysers to measure carbon monoxide, carbon dioxide and oxygen gases release. Three apparent stages were identified during fire development: (1) smouldering, (2) sustainable flame and (3) explosion. Peak HRR was higher for higher incident flux and SOC. At a constant heat flux, time to ignition and explosion increased as SOC decreased. Gas analysis found that CO and CO_2 production increased with the state of charge.

The HRR was calculated using two techniques: oxygen depletion and mass loss methods. In general, the HRR curves calculated by both methods are almost

identical with minor inconsistency. The biggest discrepancy between the two methods was observed during transition from Stage 2 to Stage 3.

3.1.3.4 Full-Scale Burning Apparatus

A full-scale burning test was performed by Ping et al. (2015) on large format 50 Ah $LiFePO_4$ / graphite battery module. A 3 kW radiation heater was used to ignite the batteries and a gas analysis system was equipped to provide in situ measurement of CO, CO_2 and O_2 release.

A series of jet flames and stable combustion was observed, in addition to initial battery expansion, and abatement and extinguishment of the flame at the end. Moreover, three distinctive stages were observed from the mass loss profiles: (1) thermal decomposition of the packaging, (2) fierce burning of the ejected gases and (3) abatement and the subsequent fire extinguishment. The maximum flame temperature reached 1500 ^{o}C in the region of 100 mm from the battery surface, which imposed a serious fire hazard since the flame temperature was very high even at a great distance.

3.1.3.5 Fire Calorimeter

Chen et al. (2015) used a fire calorimeter to observe fire development of LIBs at varying SOC. Batteries were heated by using a 2 kW coiled electric heater. The rig was equipped with gas analyser and electronic scale to measure the amount of gases released and mass loss respectively.

Based on their analysis, the authors classified combustion phenomena of LIB into four stages: (1) continuous and self-heating, (2) first flame ejection and stable combustion, (3) second flame ejection and stable combustion and (4) flame weakening and extinguish. Measurement of HRR was conducted according to the oxygen consumption method and the value was corrected to take the amount of oxygen liberated by cathode materials into account. The team calculated the amount of oxygen released and assumed the quantity to be directly proportional to the SOC. $LiCoO_2$ battery posed a higher explosion risk than $LiFePO_4$ as indicated by six-fold higher of oxygen release amount.

3.2 Modelling of Battery Thermal Runaway

Modelling is an important tool in research and development of batteries. A good model allows the prediction of battery thermal behaviour under various operating conditions without the necessity to conduct experimental works that are time-consuming, resource intensive and dangerous, while providing a clear understanding of the underlying fundamental processes. Calorimetry-based simplified model is one of the possible approaches for this purpose. This technique requires information from thermal analysis of the cell components, which are characterised by reaction rate equations using Arrhenius expression (Doughty et al., 2002). The common equipment employed for thermal and kinetic analysis of battery components are accelerating rate calorimetry (ARC) and differential scanning calorimetry (DSC).

3.2.1 Calorimetry and Kinetic Study

Extracting kinetic models during thermal analysis is a crucial stage in investigation of chemical reactions. The models can serve for thermal hazard quantification and the subsequent risk assessment. It is therefore important to extract precise models so that the succeeding analysis is reliable (Kossoy and Koludarova, 1995).

The ARC is an adiabatic calorimeter specifically developed for the evaluation of thermal hazard kinetic. The use of ARC enables determination of kinetic aspects of temperature and pressure associated with chemical reactions and heat of reaction (Townsend and Tou, 1980). The analysis of experimental results will provide important parameters for kinetic modelling.

For a thermal-induced reaction, the reactant conversion into product can be described by the following ordinary differential equation.

$$\frac{d\alpha}{dt} = k(T)\, f(\alpha) \qquad \text{(Eq 3.7)}$$

The rate constant k follows the Arrhenius relationship as follows.

$$k(T) = A\, e^{-\frac{E_a}{RT}} \qquad \text{(Eq 3.8)}$$

where k (s^{-1}) is the reaction rate, α is the fractional degree of conversion, f(α) is the reaction model, E_a (J/mol) is the reaction activation energy, t (s) is the time, R (J mol^{-1} K^{-1}) is the gas constant, T (K) is the temperature and A (s^{-1}) is the frequency factor.

Common reaction models employed for description of solid thermal composition is presented in Table 3.5. The determination of the kinetic triplet, f(α), E_a and A is crucial for accurate description of the reaction kinetic.

Table 3.5: Reaction models that are usually applied to describe thermal decomposition of solids (MacNeil and Dahn, 2001).

Reaction model	$\boldsymbol{\frac{d\alpha}{dt}} =$	$\boldsymbol{k\alpha^m(1-\alpha)^n(-\ln(1-\alpha))^P}$		
		m	n	P
One-dimensional diffusion	$k\alpha^{-1}$	-1	0	0
	$k\alpha$	1	0	0
Power law	$k\alpha^{\frac{1}{2}}$	1/2	0	0
Power law	$k\alpha^{\frac{2}{3}}$	2/3	0	0
Power law	$k\alpha^{\frac{3}{4}}$	3/4	0	0
Zero order	k	0	0	0
Contracting cylinder	$k(1-\alpha)^{\frac{1}{2}}$	0	0.5	0
Contracting sphere	$k(1-\alpha)^{\frac{2}{3}}$	0	2/3	0
First order (nth order)	$k(1-\alpha)$	0	1	0
Second order (nth order)	$k(1-\alpha)^2$	0	2	0
Avrami-Erofeev	$k(1-\alpha)(-\ln(1-\alpha))^{\frac{1}{2}}$	0	1	1/2

Avrami-Erofeev	$k(1-\alpha)(-\ln(1-\alpha))^{\frac{2}{3}}$	0	1	2/3
Avrami-Erofeev	$k(1-\alpha)(-\ln(1-\alpha))^{\frac{3}{4}}$	0	1	3/4
Autocatalytic	$k\alpha(1-\alpha)$	1	1	0
Two-dimensional diffusion	$k(-\ln(1-\alpha))^{-1}$	0	0	-1
Diffusion controlled	$k(1-(1-\alpha)^{\frac{1}{3}})^{-1}(1-\alpha)^{\frac{2}{3}}$	-	-	-
Diffusion controlled	$k((1-\alpha)^{\frac{1}{3}}-1)^{-1}$	-	-	-

In general, thermal decomposition of solid can be mathematically described by the following universal equation.

$$\frac{d\alpha}{dt} = k\,\alpha^m\,(1-\alpha)^n\,(-\ln(1-\alpha))^P \qquad \text{(Eq 3.9)}$$

where α is the fractional degree of conversion, t (s) is the time, k (s^{-1}) is the rate constant, m, n and P are the dimensionless reaction parameters.

The information pertaining to reaction model, activation energy and frequency factor can be used to mathematically describe the reaction progress. The suitability of the kinetic information for prediction of any parameter can be determined by least square analysis (MacNeil and Dahn, 2001).

3.2.2 Thermal Analysis of Battery Active Materials and Thermal Reaction Kinetic Modelling

Numerous works are reported in literature regarding the thermal stability analysis of battery components using calorimetry technique. The study however is of comparative nature and detailed kinetic fundamental analysis has been left out. The works discussed in this section form the foundation for the simulation of battery thermal behaviour, which will be discussed in Section 3.3.

Chemical reactions behind thermal runaway have been discussed in Section 2.7.3. Early work in thermal reaction kinetic modelling of battery components was pioneered by Richard and Dahn (1999b). A mathematical model was developed to describe the conversion of metastable SEI to stable SEI and the sequential reaction between lithium-intercalated anode and electrolyte by manipulating the kinetic data obtained from ARC results in their previous work. The model was able to reproduce the self-heating and heat flow profiles obtained from ARC and DSC measurement respectively with reasonable accuracy. The kinetic study conducted by Richard and Dahn (1999b) has become a primary reference in kinetic modelling for simulation of battery behaviour under thermally or electrically abusive conditions.

The self-heating rate of anode material during the adiabatic ARC test can be expressed as follows.

$$\frac{dT}{dt} = \frac{\Delta H_{SEI}}{C_p}\left|\frac{dx_f}{dt}\right| + \frac{\Delta H_{anode}}{C_p}\left|\frac{dx_i}{dt}\right| \qquad \text{(Eq 3.10)}$$

where ΔH_{SEI} (J/g) is the reaction enthalpy of SEI decomposition, ΔH_{anode} (J/g) is the reaction enthalpy of secondary SEI formation, C_p (J/g.K) is the specific heat capacity of the whole ARC sample, T (K) is the temperature, t (s) is the time, x_f is the fractional lithium content in the metastable SEI and x_i is fractional amount of lithium within the carbon anode.

x_f is the lithium content in the metastable SEI and the temporal change of the concentration during the conversion process to stable SEI can be expressed as follows.

$$\frac{dx_f}{dt} = -A_{SEI}\exp^{-\frac{E_{SEI}}{k_B T}} x_f^{\,m} \qquad \text{(Eq 3.11)}$$

where A_{SEI} (min^{-1}) is the frequency factor, E_{SEI} (eV) is the activation energy, m is the reaction order for this reaction, T (K) is the temperature and k_B is the Boltzmann constant. A_{SEI} is 1.25 x 10^{17}/min, E_{SEI} is 1.4 eV and m is taken as 0.5.

x_i is the amount of lithium intercalated within the carbon anode and the temporal change of the concentration during the formation of secondary SEI can be expressed as follows.

$$\frac{dx_i}{dt} = -A_{anode} \exp^{-\frac{E_{anode}}{k_B T}} x_i^m \exp^{-\frac{z}{z_0}} \frac{a}{a_0} \quad \text{(Eq 3.12)}$$

where A_{anode} (min^{-1}) is the frequency factor, E_{anode} (eV) is the activation energy, m is the reaction order, a (m^2/g) is the specific area of the sample, a_0 (m^2/g) is the constant of proportionality, z (m^{-2}) is the amount of lithium in SEI per unit surface area, z_0 (m^{-2}) is the initial amount of lithium in SEI per unit surface area, T (K) is the temperature and k_B (m^2 kg s^{-2} k^{-1}) is the Boltzmann constant. A_{anode} is 1 x 10^8/min, E_{anode} is 0.8 eV and m is taken as 1.

The growing secondary SEI layer from the reaction between electrolyte and intercalated lithium in the carbon anode retards the transport process of lithium through the layer and consequently impedes the consumption rate of intercalated lithium. This tunnelling factor which diminishes exponentially with length is included in the temporal expression of lithium content as $\exp(-z/z_0)$ where z is the amount of lithium in SEI per unit surface area and its temporal change is expressed as follows.

$$\frac{dz}{dt} = A_{anode} \exp^{-\frac{E_{anode}}{k_B T}} x_i^m \exp^{-\frac{z}{z_0}} \quad \text{(Eq 3.13)}$$

where A_{anode} (min^{-1}) is the frequency factor, E_{anode} (eV) is the activation energy, m is the reaction order, z (m^{-2}) is the amount of lithium in SEI per unit surface area, z_0 (m^{-2}) is the initial amount of lithium in SEI per unit surface area, T (K) is the temperature and k_B (m^2 kg s^{-2} k^{-1}) is the Boltzmann constant. A_{anode} is 1 x 10^8/min, E_{anode} is 0.8 eV and m is taken as 1. Note that the change in z in Eq 3.13 is the reverse of change of x_i in Eq 3.12.

MacNeil et al. (2000) conducted a study on interaction between $LiCoO_2$ and electrolyte using ARC but the identification of the chemical reactions involved was not made. It was found that the reaction is autocatalytic, which means the presence of reaction products catalyses and therefore accelerates the reaction process.

The simple reaction that describes the autocatalytic process is shown below.

$$B \xrightarrow{A} A + P \quad \text{(Eq 3.14)}$$

In this example, product A produced as the reaction progress accelerates the reaction rate. The reaction rate is reduced as the amount of reactant B is depleted. The differential equation that describes the autocatalytic process is shown as follows.

$$\frac{d\alpha}{dt} = k\,(1-\alpha)\,(\beta+\alpha) \qquad \text{(Eq 3.15)}$$

where β is the parameter of autocatalysis, k (s^{-1}) is the rate of reaction as expressed according to Arrhenius equation, t (s) is the time and α is the dimensionless fractional degree of conversion. A low value of β implies a strong autocatalytic behaviour. Fine-tuning the kinetic parameters for curve-fitting purposes demonstrated that a decrease in β would result in an increase in initial slope of the self-heating behaviour, producing large curvature in the profile.

3.3 Simulation of Battery Thermal Behaviour during Failure by Modelling Thermal Reaction Kinetics of Battery Components

The temperature profile of LIBs under abusive conditions can be simulated by utilising the kinetic data of the battery components while the details of the chemical reactions involved remain unknown. A few models have been developed by investigators to predict thermal behaviour of batteries during failure by modelling the thermal decomposition reaction kinetic at component level. Some of the work is compiled in Table 3.6.

Despite various chemical reactions studied during thermal runaway, most of the developed models only consider reactions at active materials. The intricate nature of the chemical reactions involved at battery components can be described by a single thermal kinetic data set. The thermal kinetic study of the active materials that forms the basis for battery thermal modelling has been described in Section 3.2.2.

Table 3.6: Examples of modelling work based on kinetic study of battery active materials as reported in literature.

Reference	**Battery Specifications**	**Battery Active Materials**
Richard and Dahn (1999c)	Cylindrical IMR18650 provided by NEC Moli Energy 1.35 Ah, 4.2 V	$LiMn_2O_4$ cathode
Hatchard et al. (2001)	Cylindrical 18650 provided by E-One / Moli Energy 1.65 Ah, 4.2 V	$LiCoO_2$ cathode and graphite anode
Kim et al. (2007)	Cylindrical 18650 Cylindrical 50900	Graphite anode and $LiCoO_2$ cathode Graphite anode and $LiCoO_2$ cathode
Feng et al. (2015a)	25 Ah, 3.8 V	$LiNi_xCo_yMn_zO_2$ cathode and graphite anode
Lee et al. (2015)	Cylindrical 2.5 Ah Prismatic 2.43 Ah Polymer 3.43 Ah	Graphite anode and $LiNiCoAlO_2$ cathode Graphite anode and $LiCoO_2$ cathode Graphite anode and $LiCoO_2$ cathode
Coman et al. (2016)	3.8 V, 2.6 Ah	$LiCoO_2$ / $Li(Ni_{0.50}Mn_{0.25}Co_{0.25})O_2$ cathode and graphite anode
Lopez et al. (2015a)	Cylindrical 18650 (2.8 Ah, 4.3 V) Prismatic (5.3 Ah, 4.2 V)	Graphite anode and $LiCoO_2$ cathode Graphite anode and $LiMn_{3/2}Ni_{1/2}O_4$ cathode

Spotnitz and Franklin (2003)	Not available	$LiMn_2O_4$ cathode $LiNiCoO_2$ cathode
Kim et al. (2014)	Cylindrical 18650	Graphite anode and $LiCoO_2$ cathode
	LEV50	Graphite anode and $LiCoO_2$ cathode

Richard and Dahn (1999c) simulated thermal behaviour of NEC Moli Energy LIB under constant high temperature and short-circuit conditions. The team considered heat source from SEI breakdown and new SEI formation reactions in their work. The result was in good agreement with the experimental data.

Hatchard et al. (2001) developed a one-dimensional model to simulate battery temperature profile under constant temperature thermal abuse testing. The team considered heat generation from SEI decomposition and included anode and cathode interactions with solvent as part of the battery heat sources. The model required detail information on the thermophysical properties and thermal reaction kinetics of the battery active materials. In addition, the developed model can capture the effect of surface emissivity, geometry, cathode material and anode surface area on battery thermal profile. The model managed to predict quantitative and qualitative behaviour of battery under high temperature thermal abuse, with some discrepancies.

According to the authors, the deviation in the predicted thermal runaway onset time was caused by ignoring the Joule-Thompson effect during electrolyte vapour release through the safety vent in the model development work. Meanwhile, the authors provided two explanations for the discrepancy in the maximum temperature reached. First, the kinetic parameters of the reactions at cathode used in the model, which has been reported by MacNeil et al. (2000) are incomplete, where only the first exothermic peak has been modelled and included in the simulation. Second, high temperature exothermic decompositions have not been included.

Kim et al. (2007) expanded the work done by Hatchard et al. (2001) into three-dimension using the finite volume method and included the high temperature

electrolyte decomposition reaction in the model. Thermal mass-specific heating rates of the chemical reactions at different oven temperatures were explored. The heat distribution within the structure was captured and the effect of battery dimension was investigated. In addition, the team simulated an induced localised heating event to study the propagation of thermal abuse reaction inside a cylindrical cell with 50 mm diameter and 90 mm height. Kim's group acknowledged extensive computer resources as the main hurdle for three-dimensional modelling. No experimental validation was provided.

Spotnitz and Franklin (2003) developed a model to predict battery thermal behaviour during oven, overcharge, short-circuit, crush and nail tests. The chemistries of concern were lithium-ion with $LiMn_2O_4$ and $LiNiCoO_2$ cathode. The simulation predicted temperature profile of the battery and the amount of heat generated from various chemical reactions. No experimental validation was provided.

While most of the modelling work utilises kinetic information reported by Hatchard et al. (2001), a group of researchers from Samsung SDI Co. Ltd. presented their own kinetic parameters for simulation of self-heating behaviour and thermal profile of three different LIBs (Lee et al., 2015). The modelling of self-heating profile dropped the electrolyte reaction from part of the heat source during thermal runaway, but included for simulation of high temperature exposure. The model managed to reproduce the experimental profiles with good agreement.

Feng et al. (2015a) developed a model to describe thermal profile of a large format LIB during short-circuit. The abrupt rise in battery temperature during separator meltdown at 260^{o}C was described as exponential. The rate of heat release by each heat source at different time and temperature was studied. The model was expanded to include heat transfer modelling in order to simulate thermal runaway propagation in a battery module. The simulation results were in good agreement with the experimental data.

Lopez et al. (2015a) simulated LIB thermal behaviour during abuse by constant power heating at ambient temperature and constant elevated ambient temperature. The effect of inclusion of electrolyte decomposition reaction in the modelling was

studied. It was found that the inclusion was not necessary for conventional oven test, but for constant power heating, ignoring the reaction produced significant deviation from the experimental data.

Coman et al. (2016) included the effect of electrolyte venting and battery content expulsion in their thermal runaway model to describe the failure behaviour of cylindrical LIB under adiabatic-like condition. The authors combined the modelling of exothermic reactions that lead to thermal runaway as reported by Kim et al. (2007) and isentropic flow equations. Their model was validated against experimental work by Golubkov et al. (2014).

Kim et al. (2014) compared thermal runaway features of large format prismatic and 18650 cylindrical LIBs. The onset of thermal runaway was delayed in the cylindrical with lower peak temperature due to the larger surface area-to-volume ratio, compared to the large format prismatic battery. No experimental validation was provided.

3.4 Thermal Runaway Propagation in Large Scale Battery Pack

Studies on the hazards of LIBs have been concentrated on the detrimental consequences of failure of individual cells. The trend is driven by the current practice where vast amount of LIBs are usually found in small-scale applications. In this situation, the probability for abusive conditions is low. In case of failure, the impact is minor and the consequences would not reach beyond the devices and the end-users.

Superior energy characteristics of LIBs make them a potential candidate for large-scale applications such as electromobility and stationary energy storage. Insufficiency of single cells to meet the high-energy demand requires the assembly of battery packs. The integration of single cells into large capacity and high voltage battery pack has been discussed in Section 2.3. Vast amount of single cells are electrically connected by either series or parallel, or combination of both according to the desired capacity and voltage, and packed together in a single enclosure.

This situation necessitates for the understanding of the hazards posed by the large battery assembly during failure. The potential of cascade failure and thermal runaway propagation inflicted by a single cell in a battery pack should not be disregarded. The heat transfer process from the cell undergoing thermal runaway causes the temperature of the adjacent cells to increase and consequently triggering cell-to-cell chain reactions.

3.4.1 Heat Transfer from Faulty Cell to Adjacent Cells Leads to Cascade Failure in Battery Modules

The compact design of the battery pack, with less than 1 mm available inter-cells spacing, is driven by the demand for high energy density battery pack. This design, while meeting the high energy density requirement, nevertheless provides a favourable network for heat transport process. The heat transferred from the hot cell will heat the neighbouring cells gradually and eventually induce the heat-activated exothermic reactions in the neighbouring cells, leading to detrimental thermal runaway propagation.

Previous work by Jhu et al. (2011a) discovered that a single cylindrical cell can reach up to 900 ^{o}C during thermal runaway. The massive amount of heat associated with the high temperature hike can be transferred to the nearby cells by three modes of heat transport (Kim and Pesaran, 2007).

1. Radiation: heat is transferred at long distance from the defective cell through electromagnetic wave emission or absorption at cell surfaces.
2. Convection: heat is transferred from the hot cell by bulk motion of heat transfer medium.
3. Conduction: heat is diffused from the hot spot through solid medium such as electric connector.

In addition, the expelled hot content carries a significant amount of thermal energy that may promote thermal runaway propagation to the surrounding cells. The erratic hot content ejection and the subsequent combustion of the flammable content make thermal runaway propagation hardly predictable due to the intricate nature of the heat quantification process (Wilke et al., 2017).

Despite potential catastrophic aftermath of cascade failure inflicted by thermal runaway propagation, systematic study in this area is still scarce, irrespective of the failure initiation modes. Some of the studies as reported in literature are compiled in Table 3.7.

Table 3.7: Some of the works reported in literature pertaining to thermal runaway propagation.

Reference	**Battery Specification**	**Battery Active Materials**	**Failure Initiation Technique**
Spotnitz et al. (2007)	Hypothetic	Hypothetic	Hypothetic
Lopez et al. (2015b)	Cylindrical 18650 (2.8 Ah, 4.35 V) Pouch (5.3 Ah, 4.2 V)	Not made available by authors	Heating
Lamb et al. (2015)	Panasonic CGR18650CG 2.2 Ah AA Portable Power Corp 7035130-10C 3.0 Ah pouch	$LiCoO_2$ cathode and graphite anode $LiCoO_2$ cathode and graphite anode	Nail penetration
Feng et al. (2015b)	25 Ah, 3.8 V	$LiNi_xCo_yMn_zO_2$ cathode and graphite anode	Nail penetration

Feng et al. (2015a)	25 Ah, 3.8 V	$LiNi_xCo_yMn_zO_2$ cathode and graphite anode	Nail penetration
Wilke et al. (2017)	18650 cylindrical (2.85 Ah, 3.62 V)	$LiNi_xCo_yMn_zO_2$ cathode and graphite anode	Nail penetration
Feng et al. (2016)	25 Ah, 3.8 V	$LiNi_xCo_yMn_zO_2$ cathode and graphite anode	Nail penetration

3.4.2 Factors Affecting Thermal Runaway Propagation in Battery Modules

3.4.2.1 Thermal Properties of Cell Interstitial Medium

Initial work in thermal runaway propagation was pioneered by Spotnitz et al. (2007). A model was developed to investigate the effect of heat transfer coefficient and the relative position of the defective cell on propagation of thermal runaway in a laptop battery pack comprised of eight cylindrical 18650 cells. The model was developed based on the assumption that the rate of temperature rise caused by thermal runaway followed the standard normal curve and the initial mode of failure that lead to this catastrophic event was not specified. The simulation indicated that thermal runaway could propagate from the affected cell to the neighbouring cells, inducing exothermic reactions in the surrounding cells and leading to a detrimental cascade failure. In addition, it was found that heat transfer coefficients and close proximity of the neighbouring cells to the faulty cell had significant impact on the spread of thermal runaway. No experimental validation was performed to support the model.

Wilke et al. (2017) demonstrated that a considerable level of safety improvement can be achieved by embedding phase change composite (PCC) material around individual cells in a battery module. The large amount of heat generated by short-circuit was absorbed as latent heat during phase transition of the PCC material from

solid to liquid, preventing the cell temperature from soaring to a dangerous level and consequently deterring thermal runaway from destructing the whole pack.

3.4.2.2 Electrical Connection

For a configuration with limited physical contact such as triangular matrix constructed from cylindrical 18650 cells, the electrical connection plays a vital role in spreading thermal runaway to the neighbouring cells. The effect of electrical connection on thermal runaway propagation has been studied by Lamb et al. (2015). For a small triangular battery module fully connected in series, it was discovered that thermal runaway was not observed in any other cells than the induced cell. Fire was observed due to the burning of the leaked electrolyte. At the end of the test, the battery pack remained undamaged. The initiation of thermal runaway in the cell generated massive amounts of thermal energy but the heat transport process was retarded by the significant air gap between the cells. The inadequate heat transfer to the neighbouring cells will not be able to trigger the exothermic reactions in the cells and subsequently arrest thermal runaway from propagating.

While the module geometry remained unchanged, the module constructed in full parallel recorded a violent behaviour. The failure rapidly propagated to the adjacent cells and consequently consumed the whole module. The faulty cell triggered the chain electrolyte venting and leaking, which was subsequently being ignited, and instigated a sustained flame.

The significant difference in the battery module failure behaviour was brought by the different electrical connections. The series configuration provides limited electrical pathway to the cells directly attached to before and after the trigger cell. A rupture in the bus bar will in turn disconnect the cells. On the other hand, parallel electrical connection provides multiple pathways for current flow out of the trigger cell. At the point of failure initiation process, nail penetration induces short-circuit in the trigger cell and subsequently inflicts electrical shorting throughout the whole module.

In a different study, Lopez et al. (2015b) investigated the effect of inter-cell connection design on thermal runaway propagation. Figure 3.3 illustrates the two different tab configurations explored in the study.

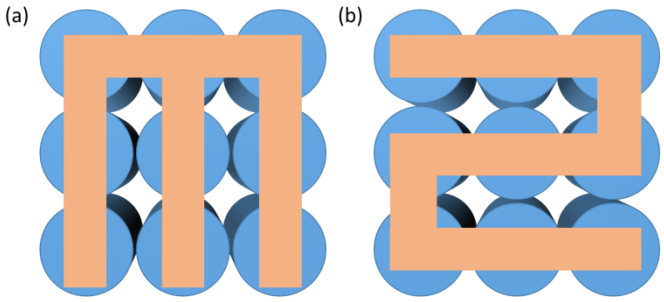

Figure 3.3: Two electrical connection designs (a) branched and (b) serpentine. Adapted from Lopez et al. (2015b).

The effect is pronounced, where serpentine configuration exhibited a more violent behaviour during thermal runaway propagation. Higher maximum temperature was recorded and electrical energy from all cells was completely drained, as indicated by zero open circuit voltage at the end of the tests.

3.4.2.3 Contact Surface Area

In geometries where contact surface area is abundant, a massive amount of heat generated by batteries experiencing thermal runaway is transferred through the inter-cells contact surface. Lamb et al. (2015) observed rapid propagation of thermal runaway in a battery module comprised of stacked pouch cells. Varying the inter-cells electrical connection appeared to have minimum impact on the severity and reactivity of thermal runaway spread. Thermal runaway propagated serially from the triggered cell, leading to total consumption of the whole module. A good thermal contact over the largest surface area promoted the heat transfer process from the defective cell to its neighbours.

Heat dissipation got more difficult as thermal runaway propagated throughout the module, inflicted an increase in maximum temperature of the cells. This observation reflects that assigning more cells in a single module not only increases the energy involved in the mishap, but also aggravates the severity of the failure. It was observed that initiation of thermal runaway in the middle cell produced a more rapid thermal runaway propagation and led to quick complete destruction of the

whole battery module, compared to the end cell due to the shorter thermal pathway for heat transfer.

Feng et al. (2015b) investigated thermal runaway propagation in a large format prismatic battery module. In general, the development of battery temperature within the module demonstrated the same pattern as observed by Lamb et al. (2015). Heat-activated exothermic reactions in the neighbouring cells were induced by gradual heating caused by the heat transfer from the hot cell. Upon separator meltdown at 260 ^{o}C, a surge in temperature was observed due to short-circuit, where the stored electrical energy was descended to thermal energy.

A model was developed by Feng et al. (2015a) in a separate work to simulate the propagation pattern by combining chemical reactions and heat transfer modelling. The model was developed based on assumption that the only way that the adjacent cells were brought into thermal runaway was by transfer of heat through the battery largest surface area. All components that contributed to thermal resistance were taken into account. The developed model was in good agreement with the experimental data. The work was further expanded into three-dimensions using the finite volume method by Feng et al. (2016). The structure was however assumed to be homogeneous blocks of solid where detailed components that made the battery have been left out. Empirical equations were introduced to describe the heat release caused by exothermic reactions that led to thermal runaway.

3.4.2.4 Miscellaneous

In a large format battery module, multiple pathways for heat transfer that may lead to thermal runaway propagation are available. Quantification of the heat transfer process through the pole connector, battery shell and fire scorching has been performed by Feng et al. (2015b). The analysis found that the heat transport through the battery shell dominated the heat transfer process. Heat transport due to fire scorching was negligible for thermal runaway propagation but may cause significant damage on the accessories located above the battery module. The same conclusion was drawn in the study by Lamb et al. (2015). Large contact surface between cells dominated the heat transfer process even though electrical connection appeared to be impactful for cells with limited surface area.

3.5 Summary

A review on the technique of evaluation of lithium-ion battery hazards was conducted. Batteries are subjected to thermal, mechanical and electrical off-nominal conditions to gain valuable insight into the probability and severity of thermal runaway under various situations. The five most common techniques are short-circuit, overcharge, nail penetration, crush and oven heating.

In addition, custom-designed and purpose-built equipment is used to quantify thermal runaway and fire hazards stem from intrinsic reactivity of the cell components and combustible materials of the battery assembly. Some of the tools are based on oxygen depletion method that come with various names, nevertheless, all the equipment in use principally comprises of two main components, which are the sample ignition and gas detection systems.

Moreover, a number of calorimeters and reactors are used to drive LIBs into thermal runaway and the resulting failure profiles are comprehensively studied for safety assessment. Hazards originating from the intrinsic reactivity and instability of battery components can be well quantified using those methods.

Most of the works reported in literature related to evaluation of lithium-ion battery hazards are concentrated on the impact and aftermath of failure of a single cell. A comparison between the available lithium-ion chemistries indicates that $LiCoO_2$ batteries produce the most severe consequences during failure. The failure behaviour gets more violent at higher SOC due to the higher electrical energy content.

The kinetic study of thermal decomposition of the reactive electrodes and flammable electrolyte was discussed. Thermal runaway of lithium-ion battery can be simulated by modelling the thermal kinetics of the pertinent chemical reactions. A further inclusion of heat transfer modelling with the thermal kinetic model allows the simulation of thermal runaway propagation in a battery pack.

Chapter 4: Development of a Numerical Model for Simulation of Lithium-ion Battery Thermal Runaway

Hazards of lithium-ion batteries have been discussed in the previous chapters. Thermal runaway has been identified as the prevalent failure mode of lithium-ion batteries, which is in most cases, is instigated by applications outside the manufacturer specifications. Current techniques for battery hazard assessment and evaluation have been presented. It is imperative to have a reliable model for prediction of battery thermal runaway hazard due to the capital-intensive and time-consuming nature of experimental assessment. This chapter describes the development of thermal runaway model for cylindrical lithium-ion battery with lithium cobalt oxide cathode and graphite anode. A prediction of battery thermal runaway behaviour under thermally abusive environments and impact-induced short-circuit is presented.

In addition, the model is further expanded to simulate the propagation of thermal runaway in a battery module consists of nine cylindrical cells. There are two major steps involved: (1) establishing the thermal kinetic modelling of reactions involved during thermal runaway in a single cell, and (2) coupling the thermal runaway model of the single cell with heat transfer modelling.

4.1 Battery Specifications

The study attempts to develop a model to simulate thermal behaviour of cylindrical 18650 LIB under abusive environments. The specifications of the battery are presented in Table 4.1.

Table 4.1: Cell specifications.

Specification	Value
Form Factor	Cylindrical 18650
Diameter (mm)	18
Length (mm)	65
Nominal voltage (V)	3.7
Maximum voltage (V)	4.2
Minimum voltage (V)	2.8
Chemistry	Lithium cobalt oxide cathode
	Graphite anode

4.2 Battery Physical and Thermal Properties

Thermal properties of the cell canister and volumetric mass of the battery components as collected from literature are presented in Table 4.2.

Table 4.2: Battery physical parameters for thermal runaway modelling.

Property	Value	Reference
Total mass, M (kg)	0.048	Measured
Specific heat capacity, C_p (J/kg.K)	830	Hatchard et al. (2001)
Volumetric mass of cathode (kg/m^3)	1.221×10^3	Kim et al. (2007)
Volumetric mass of anode (kg/m^3)	6.104×10^2	Kim et al. (2007)
Volumetric mass of electrolyte (kg/m^3)	4.069×10^2	Kim et al. (2007)
Thermal emissivity, ε	0.8	Hatchard et al. (2001)

4.3 Development of Thermal Runaway Model

4.3.1 Assumptions Made in Thermal Runaway Model Development

1. The battery is composed of jellyroll active materials packed inside the cylindrical stainless steel casing.
2. The heat leads to thermal runaway originates from exothermic reactions in the active materials and electrolyte.
3. Thermal runaway reactions occur at the centre of the battery.
4. The amount of heat liberated by Joule heating during short-circuit is negligible for high temperature abuse tests.
5. The combustion of the flammable electrolyte and any combustible materials is not considered.
6. The heat is dissipated to the surrounding by convective and radiative heat transfer.
7. The Joule-Thompson cooling effect instigated by venting of gases and expulsion of battery content is not considered.
8. The heat is transmitted from the defective cell to the neighbouring cells by conduction and convection.
9. Thermal conductivity of the heat conducting materials is isotropic and constant. The battery specific heat capacity remains constant at any temperature.
10. The battery temperature is uniform and any temperature gradient is neglected. The low Biot number of 0.0179 as reported by Hatchard et al. (2001) warrants the use of lumped thermal model.

4.3.2 Heat Source Term

In this work, heat sources from active materials and electrolyte are considered, totalling to four exothermic reactions. There are two reactions at anode, which are the breakdown of solid electrolyte interphase (SEI), and anode-electrolyte reaction. Meanwhile, both cathode and electrolyte have one reaction. Each of the reaction possesses characteristic decomposition reaction model and parameters. The thermal decomposition kinetics of the battery components for thermal runaway modelling which are collected from literature are listed in Table 4.3.

4.3.3 Thermal Kinetic Parameters of Thermal Runaway Reactions

Table 4.3: Thermal kinetic parameters of thermal decomposition reactions required for thermal runaway modelling.

Symbol	Description	Value	Reference
H_{SEI}	Reaction enthalpy (J/g)	257	Hatchard et al. (2001)
H_{anode}		1714	Hatchard et al. (2001)
$H_{electrolyte}$		155	Kim et al. (2007)
$H_{cathode}$		314	Hatchard et al. (2001)
E_{SEI}	Reaction activation energy (J/mol)	1.3508×10^5	Kim et al. (2007)
E_{anode}		1.3508×10^5	Kim et al. (2007)
$E_{electrolyte}$		1.7×10^5	Kim et al. (2007)
$E_{cathode}$		1.1495×10^5	Kim et al. (2007)
A_{SEI}	Reaction frequency factor (1/s)	1.667×10^{15}	Kim et al. (2007)
A_{anode}		2.5×10^{13}	Kim et al. (2007)
$A_{electrolyte}$		3×10^{15}	Kim et al. (2007)
$A_{cathode}$		1.75×10^9	Kim et al. (2007)
$c_{SEI,0}$	Initial concentration	0.15	Kim et al. (2007)
$c_{anode,0}$		0.75	Kim et al. (2007)
$c_{electrolyte,0}$		1	Kim et al. (2007)

$\alpha_{,0}$		0.04	Kim et al. (2007)
z_0		0.033	Kim et al. (2007)
m_{SEI}	Reaction order	1	Kim et al. (2007)
m_{anode}		1	Kim et al. (2007)
$m_{electrolyte}$		1	Kim et al. (2007)
$m_{cathode}$		1	Kim et al. (2007)

4.3.4 Governing Equations

In a lumped thermal model, the rate of temperature change in the battery can be expressed as in Eq 4.1.

$$\frac{dT(t)}{dt} = \frac{Q(t)}{MC_p} \quad \text{(Eq 4.1)}$$

where T (K) is the battery temperature, t (s) is the time, Q (W) is the net rate of heat generation, M (kg) is the mass and C_p (J/kg.K) is the battery specific heat capacity.

The rate of battery temperature change is directly proportional to the battery internal heat accumulation, which is a balance between self-generated and dissipated heat.

The net rate of heat generation is expressed in Eq 4.2, where Q_{gen} is the rate of internal heat generation and $Q_{dissipation}$ is the rate of heat transferred from battery to the surrounding.

$$Q(t) = Q_{gen}(t) - Q_{dissipation}(t) \quad \text{(Eq 4.2)}$$

The $Q_{dissipation}$ term in Eq 4.2 is the rate of heat dissipation to the environment due to the convective and radiative heat transfer, as presented in Eq 4.3. The rate of heat dissipation can be calculated using Eq 4.3.

$$Q_{dissipation}(t) = Q_{radiative}(t) + Q_{convective}(t) \quad \text{(Eq 4.3)}$$

The rate of convective heat transfer is given in Eq 4.4.

$$Q_{convective}(t) = h\ A\ \left(T(t)-T_{amb}(t)\right) \quad \text{(Eq 4.4)}$$

where h ($W/m^2.K$) is the heat transfer coefficient, A (m^2) is the surface area for heat exchange, T (K) is the instantaneous battery temperature, t (s) is the time, and T_{amb} (K) is the ambient temperature.

The rate of radiative heat transfer is given in Eq 4.5.

$$Q_{radiative}(t) = \varepsilon\ \sigma\ A(T(t)^4 - T_{amb}(t)^4) \quad \text{(Eq 4.5)}$$

where ε is the battery surface emissivity, σ (W/m^2K^4) is the Stefan-Boltzmann constant, A (m^2) is the surface area for heat exchange, T (K) is the instantaneous battery temperature and T_{amb} (K) is the ambient temperature.

The rate of internal heat generation is expressed in Eq 4.6, which is a sum of rate of heat generation from chemical reactions, Q_{cr} and short-circuit, Q_{sc}.

$$Q_{gen}(t) = Q_{cr}(t) + Q_{sc}(t) \quad \text{(Eq 4.6)}$$

Q_{sc} in Eq 4.6 is the rate of heat generation from short-circuit and can be expressed as in Eq 4.7 (Feng et al., 2015a).

$$Q_{sc}(t) = \frac{1}{\Delta t}\left[\Delta H_{sc} - \int_0^t Q_{sc}(\tau)\ d\tau\right] \quad \text{(Eq 4.7)}$$

where Δt (s) is the duration of short-circuit, ΔH_{sc} (J) is the amount of electrical energy discharged into heat during short-circuit, t (s) is the instantaneous time and τ (s) is the time at the point of short-circuit.

The amount of heat generated from rapid discharge of electrical energy during short-circuit can be calculated using Eq 4.8 (Feng et al., 2015a).

$$\Delta H_{sc} = CV \quad \text{(Eq 4.8)}$$

where C (Ah) is the battery capacity and V (V) is the battery voltage.

Q_{cr} in Eq 4.6 is the total rate of heat generation from chemical reactions instigated by thermal instability of the battery components as expressed in 4.9.

$$Q_{cr} = Q_{SEI} + Q_{anode} + Q_{electrolyte} + Q_{cathode} \quad \text{(Eq 4.9)}$$

The rate of heat generation by each chemical reaction is proportionate to the rate of reactant consumption. In general, the rate of heat generation from the exothermic reactions can be expressed as in Eq 4.10.

$$Q_x(t) = \Delta H_x \, W_x \, \frac{dc_x(t)}{dt} \quad \text{(Eq 4.10)}$$

where ΔH_x (J/kg) is the reaction enthalpy, W_x (kg) is the mass of the reactant and c_x is the normalised reactant concentration.

The thermal decomposition models of the reactions involved in thermal runaway are described in the following section.

4.3.5 Modelling of Thermal Decomposition Kinetics

4.3.5.1 Solid electrolyte interface (SEI) breakdown

As described by Richard and Dahn (1999a), the reaction is first-order and the rate constant of this reaction can be expressed as in Eq 4.11.

$$R_{SEI} = A_{SEI} \exp\left[-\frac{E_{SEI}}{RT}\right] c_{SEI}^{m_{SEI}} \quad \text{(Eq 4.11)}$$

The rate of change in reacting species content during the reaction is presented in Eq 4.12.

$$\frac{dc_{SEI}}{dt} = -R_{SEI} \quad \text{(Eq 4.12)}$$

The rate of heat evolution from the reaction can be calculated using Eq 4.13.

$$Q_{SEI} = \Delta H_{SEI} \, W_{anode} \, R_{SEI} \quad \text{(Eq 4.13)}$$

where R_{SEI} (s^{-1}) is the rate constant of SEI decomposition reaction, ΔH_{SEI} (J/kg) is the reaction enthalpy, A_{SEI} (s^{-1}) and E_{SEI} (J/mol) are frequency factor and activation energy respectively, R (J/K.mol) is the gas constant, T (K) is the battery temperature, m_{SEI} is the reaction order, W_{anode} (kg) is the mass of carbon in anode, and c_{SEI} is the dimensionless amount of lithium-containing meta-stable species in the SEI.

4.3.5.2 Reaction between anode and solvent

The reaction between the solvent and the intercalated lithium within the anode will eventually form a secondary SEI layer. As described by Richard and Dahn (1999b), the reaction is first-order and the rate constant of this reaction can be expressed as in Eq 4.14.

$$R_{anode} = A_{anode} \exp\left[-\frac{E_{anode}}{RT}\right] \exp\left[-\frac{z}{z_0}\right] c_{anode}^{m_{anode}} \quad \text{(Eq 4.14)}$$

The rate of depletion in reacting species content during the reaction is presented in Eq 4.15.

$$\frac{dc_{anode}}{dt} = -R_{anode} \quad \text{(Eq 4.15)}$$

z is the SEI layer thickness and its temporal change is expressed in Eq 4.16.

$$\frac{dz}{dt} = R_{anode} \quad \text{(Eq 4.16)}$$

The rate of heat evolution from the reaction can be calculated using Eq 4.17.

$$Q_{anode} = \Delta H_{anode} \, W_{anode} \, R_{anode} \quad \text{(Eq 4.17)}$$

where R_{anode} (s^{-1}) is the rate constant of anode-solvent reaction, ΔH_{anode} (J/kg) is the reaction enthalpy, A_{anode} (s^{-1}) and E_{anode} (J/mol) are frequency factor and activation energy respectively, R (J/K.mol) is the gas constant, T (K) is the battery temperature, m_{anode} is the reaction order, W_{anode} (kg) is the mass of carbon in anode, z is the thickness of SEI layer, z_0 is the initial thickness of SEI layer and c_{anode} is the dimensionless amount of lithium intercalated within the carbon negative electrode.

4.3.5.3 Electrolyte decomposition

As described by Spotnitz and Franklin (2003), the reaction is first-order and the rate constant of this reaction can be expressed as in Eq 4.18.

$$R_{electrolyte} = A_{electrolyte} \exp\left[-\frac{E_{electrolyte}}{RT}\right] c_{electrolyte}^{m_{electrolyte}} \quad \text{(Eq 4.18)}$$

The rate of reacting species consumption during the reaction is presented in Eq 4.19.

$$\frac{dc_{electrolyte}}{dt} = -R_{electrolyte} \quad \text{(Eq 4.19)}$$

The rate of heat evolution from the reaction can be calculated using Eq 4.20.

$$Q_{electrolyte} = \Delta H_{electrolyte}\ W_{electrolyte}\ R_{electrolyte} \quad \text{(Eq 4.20)}$$

where $\Delta H_{electrolyte}$ (J/kg) is the reaction enthalpy, $A_{electrolyte}$ (s^{-1}) and $E_{electrolyte}$ (J/mol) are frequency factor and activation energy respectively, R (J/K.mol) is the gas constant, T (K) is the battery temperature, $m_{electrolyte}$ is the reaction order, $W_{electrolyte}$ (kg) is the mass of electrolyte and $c_{electrolyte}$ is the dimensionless electrolyte concentration.

4.3.5.4 Cathode breakdown

Cathode breakdown is an auto-catalytic reaction (MacNeil et al., 2000). The rate constant for the decomposition of positive active material reaction can be expressed as in Eq 4.21.

$$R_{cathode} = A_{cathode} \exp\left[-\frac{E_{cathode}}{RT}\right] \alpha^{m_{cathode}} (1-\alpha)^{m_{cathode}} \quad \text{(Eq 4.21)}$$

The extent of the reaction is changing according to the following rate, as presented in Eq 4.22.

$$\frac{d\alpha}{dt} = R_{cathode} \quad \text{(Eq 4.22)}$$

The rate of heat evolution from the reaction can be calculated using Eq 4.23.

$$Q_{cathode} = \Delta H_{cathode}\ W_{cathode}\ R_{cathode} \quad \text{(Eq 4.23)}$$

where $\Delta H_{cathode}$ (J/kg) is the reaction enthalpy, $A_{cathode}$ (s^{-1}) and $E_{cathode}$ (J/mol) are frequency factor and activation energy respectively, R (J/K.mol) is the gas constant, T (K) is the battery temperature, $m_{cathode}$ is the reaction order, $W_{cathode}$ (kg) is mass of the cathode and α is the extent of cathode decomposition reaction.

4.4 Development of Thermal Runaway Propagation Model

For a battery module with a layout as in Figure 4.1, the associated thermal node configuration and thermal resistance network are shown in Figure 4.2 and Figure 4.3 respectively.

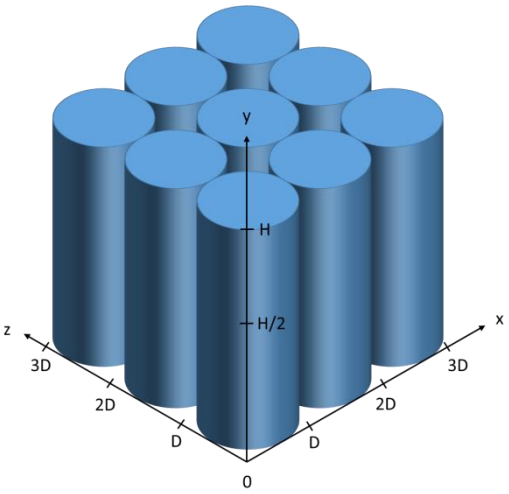

Figure 4.1: 3x3-matrix battery module assembled from nine unit of cylindrical cells.

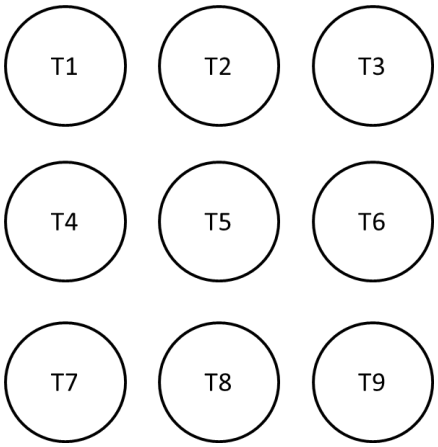

Figure 4.2: Thermal nodes in the battery matrix.

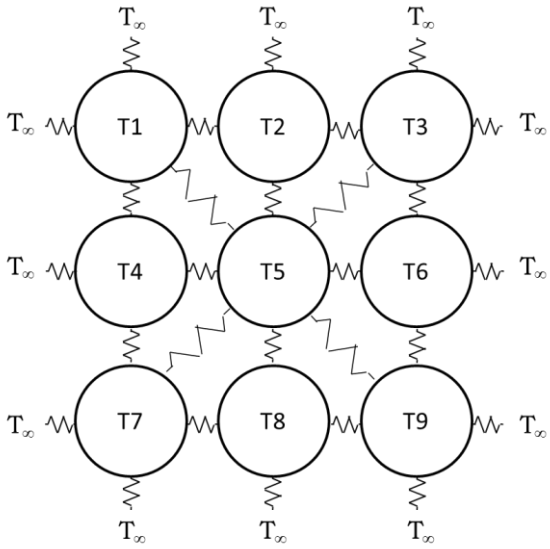

Figure 4.3: Thermal resistance network for heat transfer modelling.

For thermal node T5, the $Q_{dissipation}$ term in Eq 4.3 is further expanded as in Eq 4.24.

$$Q_{dissipation}(t)= \sum_{i=1}^{10} Q_{dissipation,i}\ (t) \qquad \text{(Eq 4.24)}$$

For thermal nodes T2, T4, T6 and T8, which are located directly adjacent to T5, the $Q_{dissipation}$ term in Eq 4.3 is further expanded as in Eq 4.25.

$$Q_{dissipation}(t)= \sum_{i=1}^{6} Q_{dissipation,i}\ (t) \qquad \text{(Eq 4.25)}$$

For T1, T3, T7 and T9 thermal nodes that are perpendicular to T5, the $Q_{dissipation}$ is expressed as in Eq 4.26.

$$Q_{dissipation}(t)= \sum_{i=7}^{7} Q_{dissipation,i}\ (t) \qquad \text{(Eq 4.26)}$$

Each $Q_{dissipation,i}$ term in Eq 4.24 - 4.26 can be calculated using Eq 4.27.

$$Q_{dissipation,i}=A_i \frac{T_n - T_{n-1}}{R_{total,\,i}} \quad \text{(Eq 4.27)}$$

where A_i is the surface area for heat exchange, $R_{total,\,i}$ is the total thermal resistance in any direction i and T_n is temperature of thermal node n.

The thermal resistance network within the battery module and single battery is illustrated in Figure 4.4 and Figure 4.5 respectively. The description and value of each thermal resistance involved in the simulation is listed in Table 4.4.

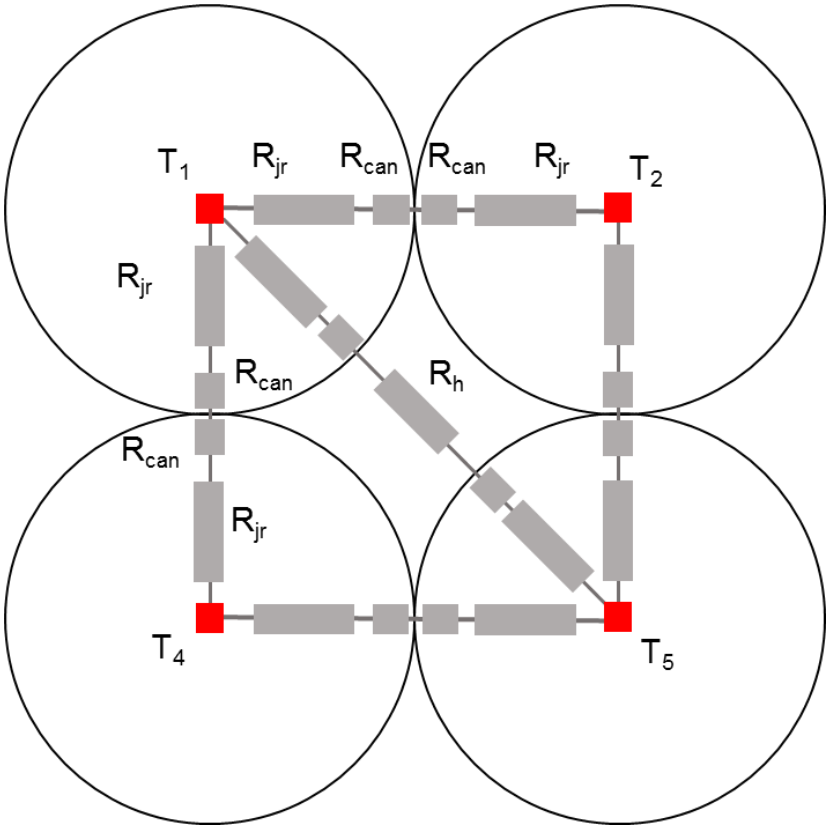

Figure 4.4: Heat transfer resistance network within the module.

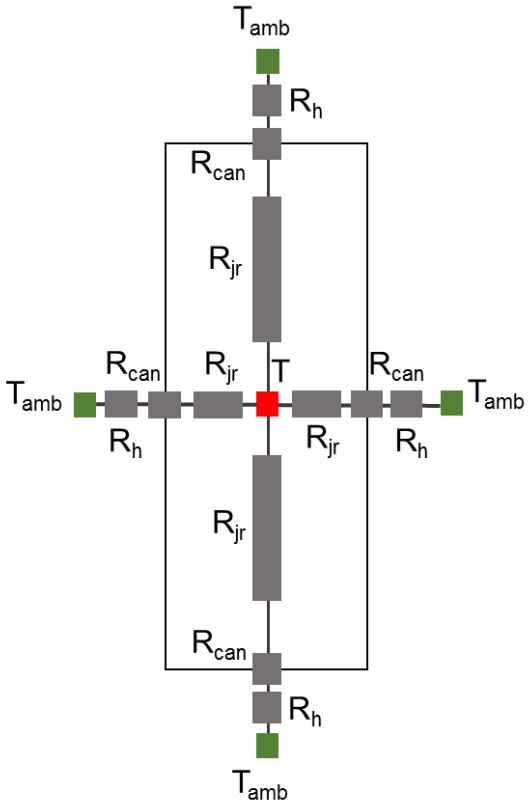

Figure 4.5: Heat transfer resistance network within the cylindrical cell.

Table 4.4: Description of all thermal resistances within the individual cell and battery module.

Thermal Resistance	Description	Thickness (m)	Thermal Conductivity (W/m.K)	Heat Transfer Coefficient ($W/m^2.K$)	Reference
R_{jr}	Jellyroll (Axial) (Radial)	0.0315 0.008	3.4	-	Hatchard et al. (2001)
R_{can}	Canister	0.001	14	-	Hatchard et al. (2001)
R_h	Convective heat transfer resistance	-	-	7.17	Hatchard et al. (2001)

4.5 Calculation Algorithm of Thermal Runaway Profile

4.5.1 Thermal Runaway at Constant High Ambient Temperature

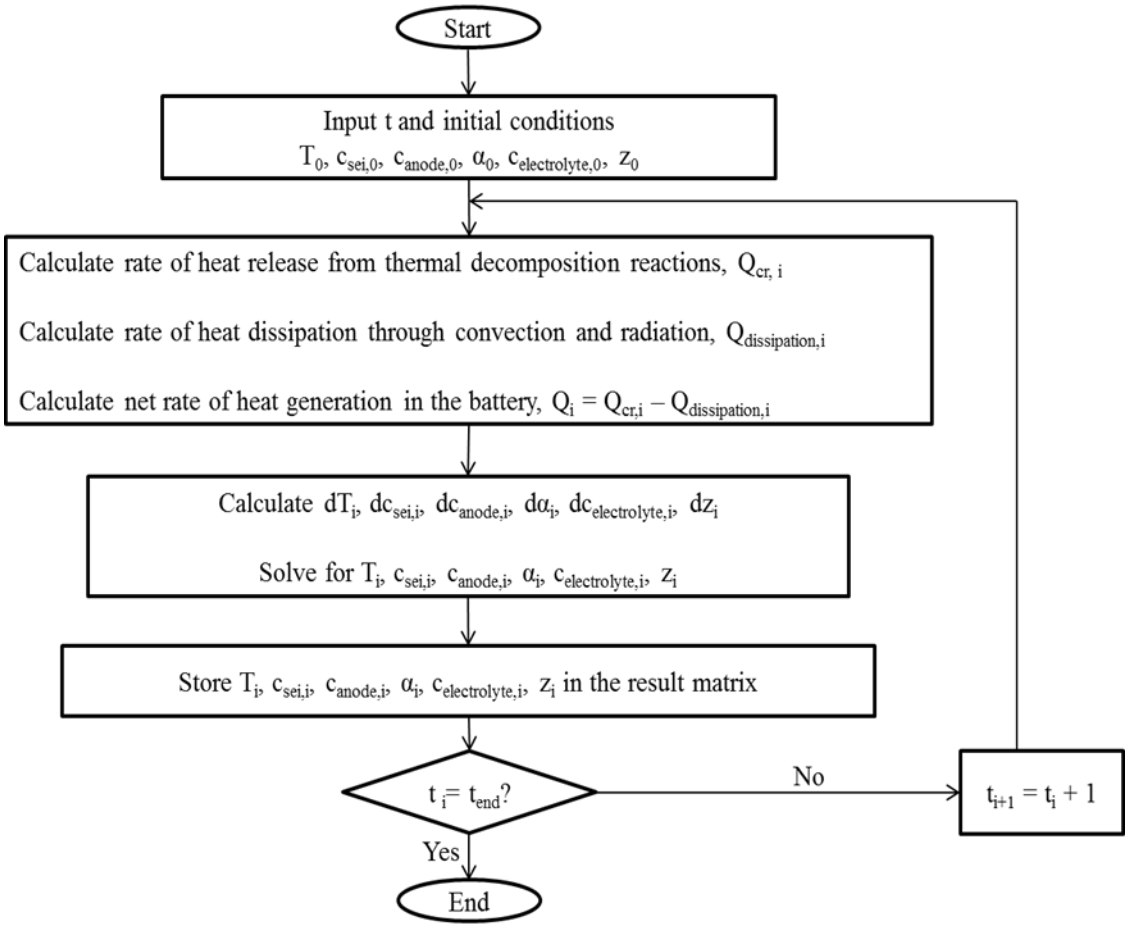

Figure 4.6: Calculation algorithm for solving thermal runaway profile at constant high temperature.

The calculation is conducted by using MATLAB. A function that contains all the relevant differential equations is written. A script is written to call the previously written function, specify the entire initial conditions and numerically solve the equations by using the built in solver in the MATLAB. In this calculation, trapezoidal rule and backward differentiation formula is used. This method is suitable for solving stiff differential equations but with low accuracy.

4.5.2 Thermal Runaway at Constant Heating Rate

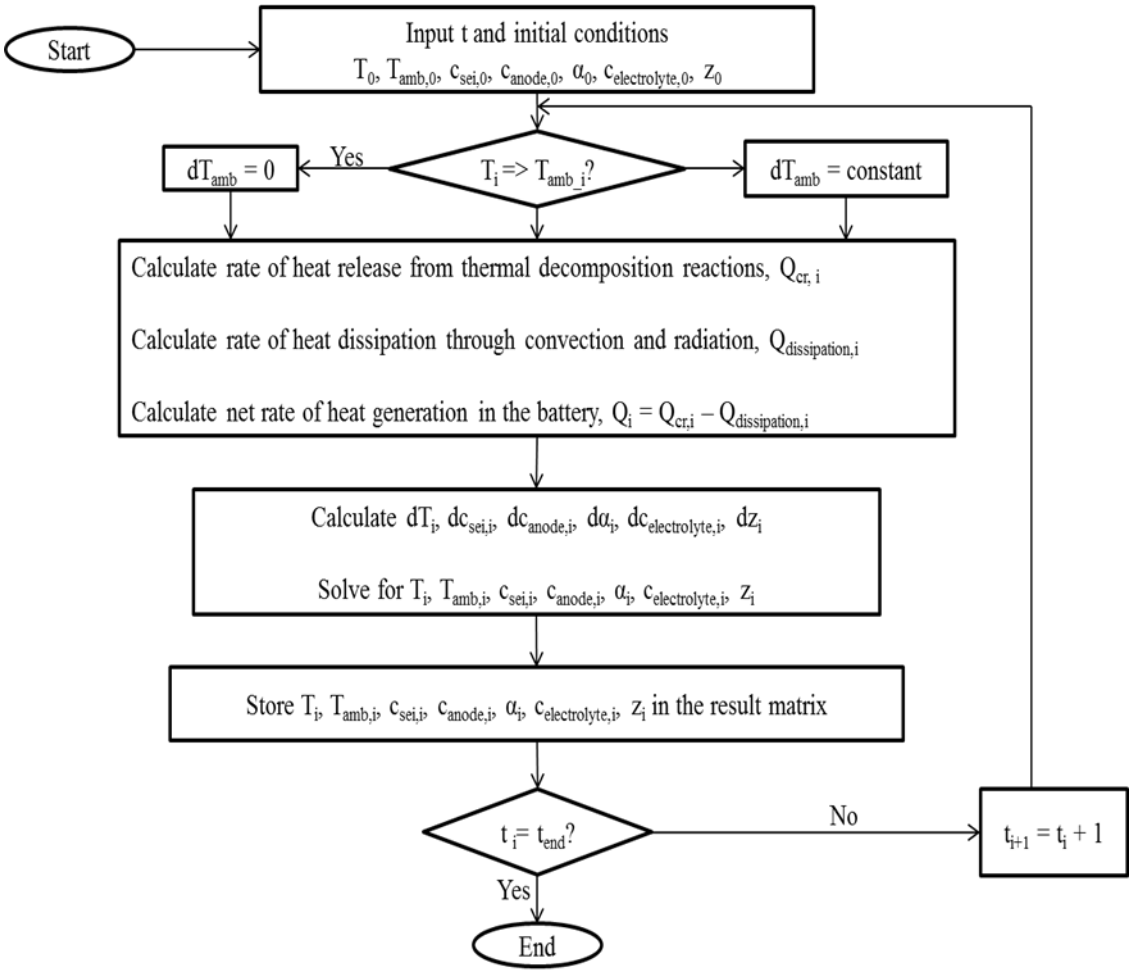

Figure 4.7: Calculation algorithm for solving thermal runaway profile at constant heating rate.

The calculation is conducted by using MATLAB. A function that contains all the relevant differential equations is written. A script is written to call the previously written function, specify the entire initial conditions and numerically solve the equations by using the built in solver in the MATLAB. In this calculation, trapezoidal rule and backward differentiation formula is used. This method is suitable for solving stiff differential equations but with low accuracy.

4.5.3 Thermal Runaway by Impact-Induced Short-Circuit

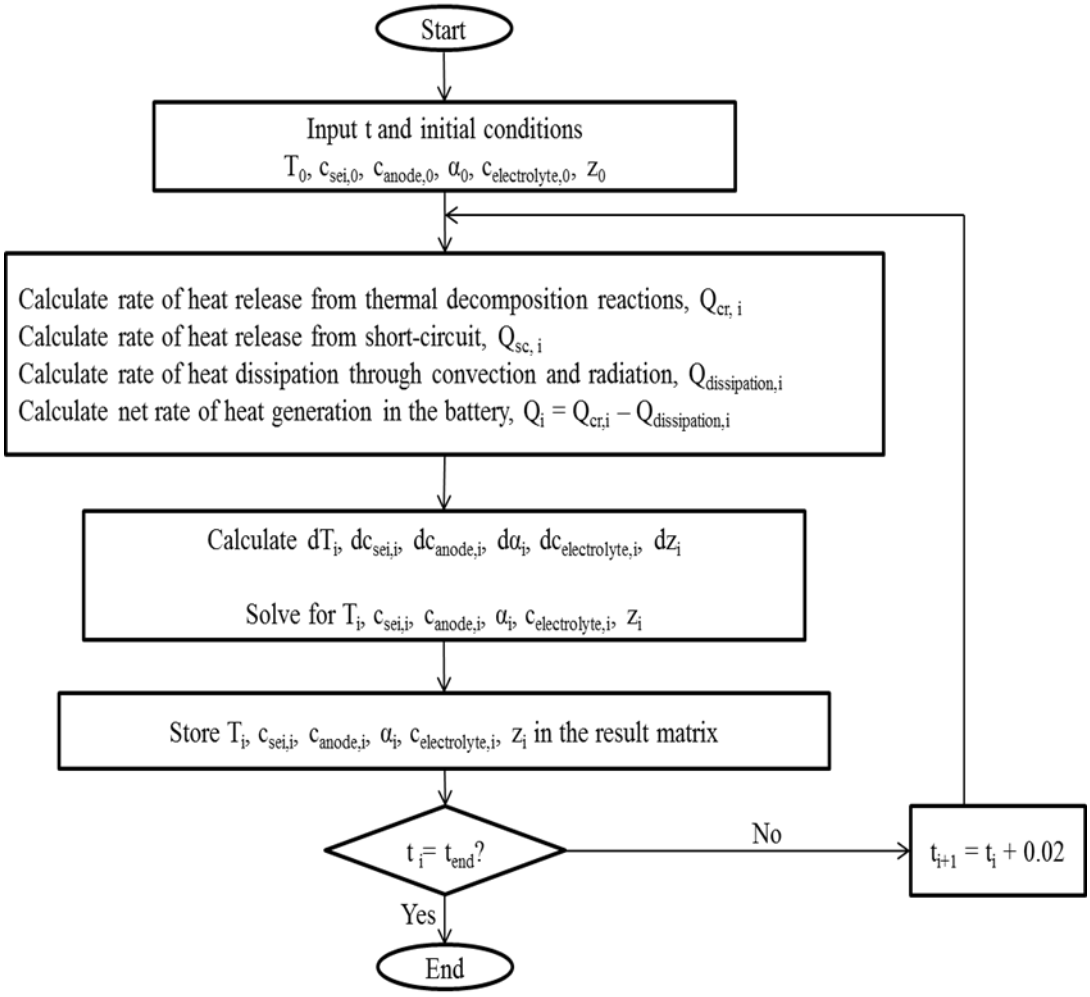

Figure 4.8: Calculation algorithm for solving thermal runaway profile during short-circuit.

The calculation is conducted by using MATLAB. A function that contains all the relevant differential equations is written. A script is written to call the previously written function, specify the entire initial conditions and numerically solve the equations by using the built in solver in the MATLAB. In this calculation, trapezoidal rule and backward differentiation formula is used. This method is suitable for solving stiff differential equations but with low accuracy.

4.5.4 Thermal Runaway Propagation in a Battery Module

The calculation process for the trigger cell follows the algorithm for solving thermal runaway profile during short-circuit as summarised in Figure 4.8. For other surrounding cells, the calculation of the temperature follows the algorithm for solving thermal runaway profile at constant heating temperature as summarised in Figure 4.6, but the ambient temperature is set to be at room temperature, which is 20 ^{o}C.

The calculation is conducted by using MATLAB. A function that contains all the relevant differential equations is written. A script is written to call the previously written function, specify the entire initial conditions and numerically solve the equations by using the built in solver in the MATLAB. In this calculation, trapezoidal rule is used. This method is suitable for solving stiff differential equations but with low accuracy.

4.6 Simulation Results and Discussion

4.6.1 Thermal Runaway at Constant High Ambient Temperature

A series of thermal abuse cases were developed at constant high ambient temperature of 150 ^{o}C, 155 ^{o}C and 160 ^{o}C. The heat exchange processes between the high ambient temperature and the battery occurred through convective and radiative heat transfer modes. The simulated thermal profiles are presented in Figure 4.9.

For low temperature thermal abuse test (150 ^{o}C), the condition did not lead to battery thermal runaway. The battery temperature increased gradually to the ambient temperature and no spike in temperature was observed. A small hump was detected at 110 minutes and the battery temperature remained unchanged at ambient temperature thereafter as the battery subsequently achieved thermal equilibrium with the environment where the rate of heat dissipation is equal to the rate of heat generation or supply.

At higher temperature, all the batteries suffered from thermal runaway and rapid temperature development was recorded. The temperature of the battery increased gradually to the ambient temperature before surged to higher than 200 ^{o}C. External thermal energy supplied by the hot environment triggered the heat-activated complex chemical reactions within the battery and caused the temperature to increase. From the simulation, the peak battery temperature reached was higher at higher ambient temperature. In addition, the battery recorded a narrower peak and a shorter thermal runaway period at a higher ambient temperature due to the higher rate of exothermic reactions and the associated heat release. Moreover, the battery overshoots the ambient temperature and reaches thermal runaway at a quicker rate a higher ambient temperature.

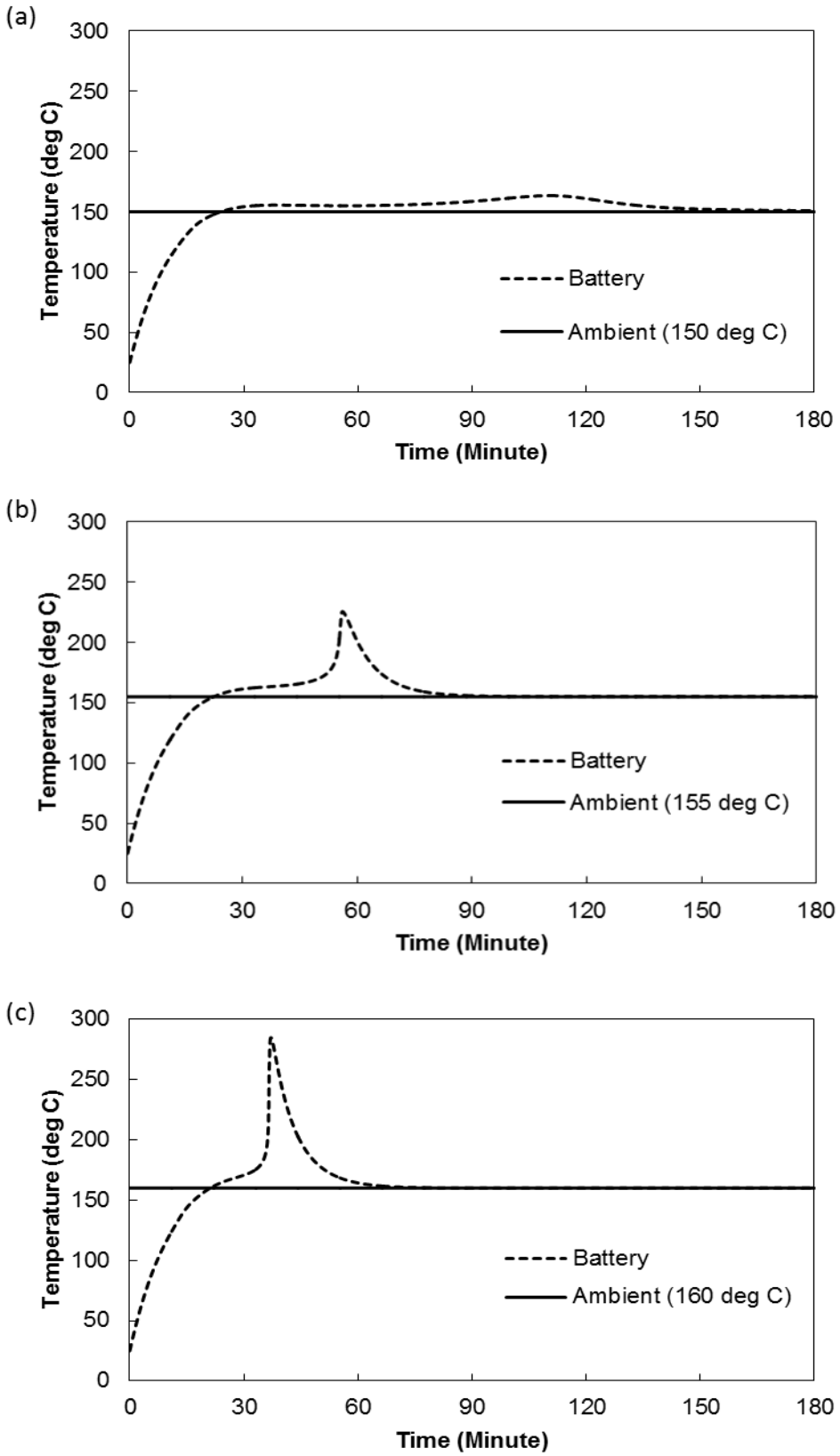

Figure 4.9: Temporal profile of the battery temperature during thermal abuse by constant high ambient temperature: (a) 150 (b) 155 and (c) 160 ^{o}C.

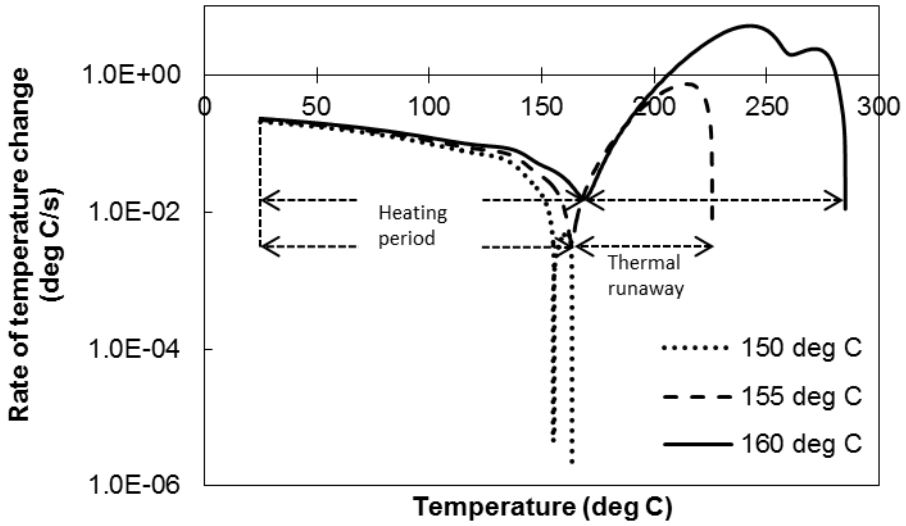

Figure 4.10: Rate of temperature increase profiles during thermal abuse by constant high ambient temperature.

Figure 4.10 presents the rate of temperature increase as the battery temperature changes to decipher the heat exchange process that contributes to the battery temperature increase. At lower temperature region prior to thermal runaway, the rate of heat increase is curvy, demonstrating a downward trend as the temperature increases which is due to the narrowing temperature difference between the battery and the environment. The initial change is identical for all ambient temperatures but the curves diverge as the temperature increases with higher rate is recorded for higher ambient temperature. The increase in battery temperature is instigated by a combination of self-generated heat by the reactive battery components and both conductive and radiative heat transfer between the high temperature environment and battery.

The point of thermal runaway is defined at the point of inflection between the decreasing curve and projectile of temperature increase rate. As thermal runaway is triggered, the amount of heat generated intensifies which leads to the peak of temperature increase rate. This is subsequently followed by the decreasing rate temperature rise until the maximum temperature is reached.

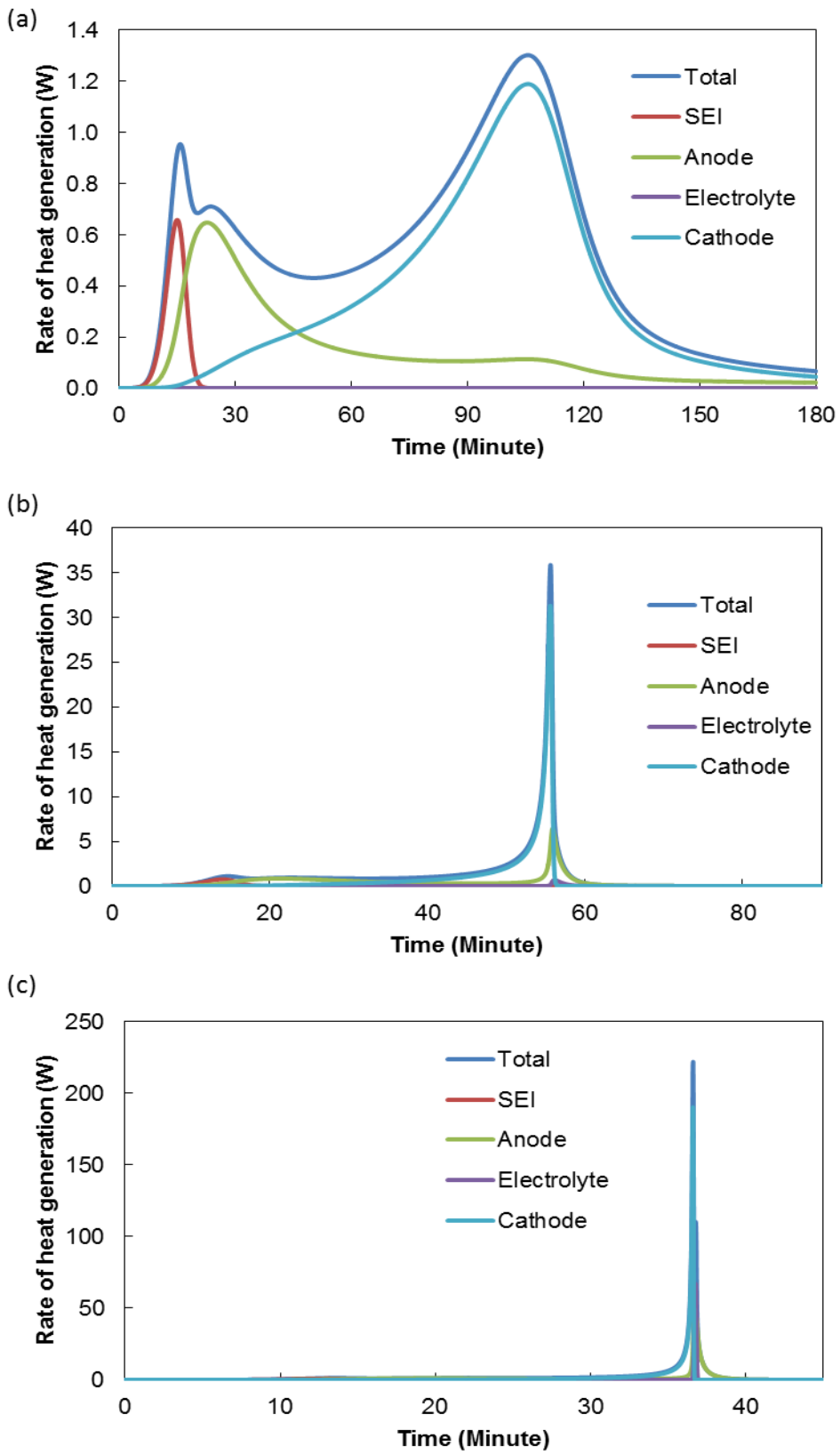

Figure 4.11: The rate of heat generation by exothermic reactions at battery components at ambient temperature of (a) 150 ^{o}C (b) 155 ^{o}C and (c) 160 ^{o}C.

The total rate of heat generation due to the exothermic reactions during thermal abuse is presented in Figure 4.11. The peak rate of heat generation increases while the period gets shorter as the ambient temperature increases. The amount of heat released by the chemical reactions can be obtained from area under the curve, which is summarised in Table 4.5.

Table 4.5: Total heat release and heat release rate under thermally abusive environments.

Temperature (^{o}C)	**150**	**155**	**160**
Peak heat release rate (W)	1.3021	35.88	221.8
Total heat release (J)	5.52×10^{3}	6.24×10^{3}	7.73×10^{3}
Total heat release by SEI reaction (J)	247.2	247.2	247.1
Total heat release by anode reaction (J)	1.515×10^{3}	2.06×10^{3}	2.96×10^{3}
Total heat release by electrolyte reaction (J)	0.174	69.95	663.6
Total heat release cathode reaction (J)	3.758×10^{3}	3.86×10^{3}	3.86×10^{3}

In general, a higher abusive temperature results in higher peak heat release rate (PHRR) and total heat release. The peak and spike in the rate of heat generation observed is instigated by cathode breakdown. As depicted in Figure 4.8, at an ambient temperature of 150 ^{o}C, the heat contribution by individual chemical reactions can be detected clearly but the patterns become obscure at higher abusive temperatures. The initial heat generation is caused by SEI breakdown, where the amount of heat released by the reaction remains almost identical for all abusive temperatures, followed by anode reaction and subsequently peaking by cathode decomposition. The amount of heat liberated from cathode reaction records an identical value at both 155 ^{o}C and 160 ^{o}C as the battery suffers from thermal runaway. Meanwhile, the amount of heat generation by electrolyte decomposition is initially negligible at 150 ^{o}C but escalates as the abusive temperature increases. A

similar pattern can be observed for anode reaction but the increment is not that abrupt.

At higher abusive temperatures that inflict thermal runaway, heat contribution by individual chemical reactions is not apparent and difficult to distinguish due to the domination by high rate heat generation of the cathode. To have a better illustration and understanding on the contribution of the chemical reactions involved to thermal runaway, the rate of heat generation for high-temperature study at 155 ^{o}C is depicted in Figure 4.12.

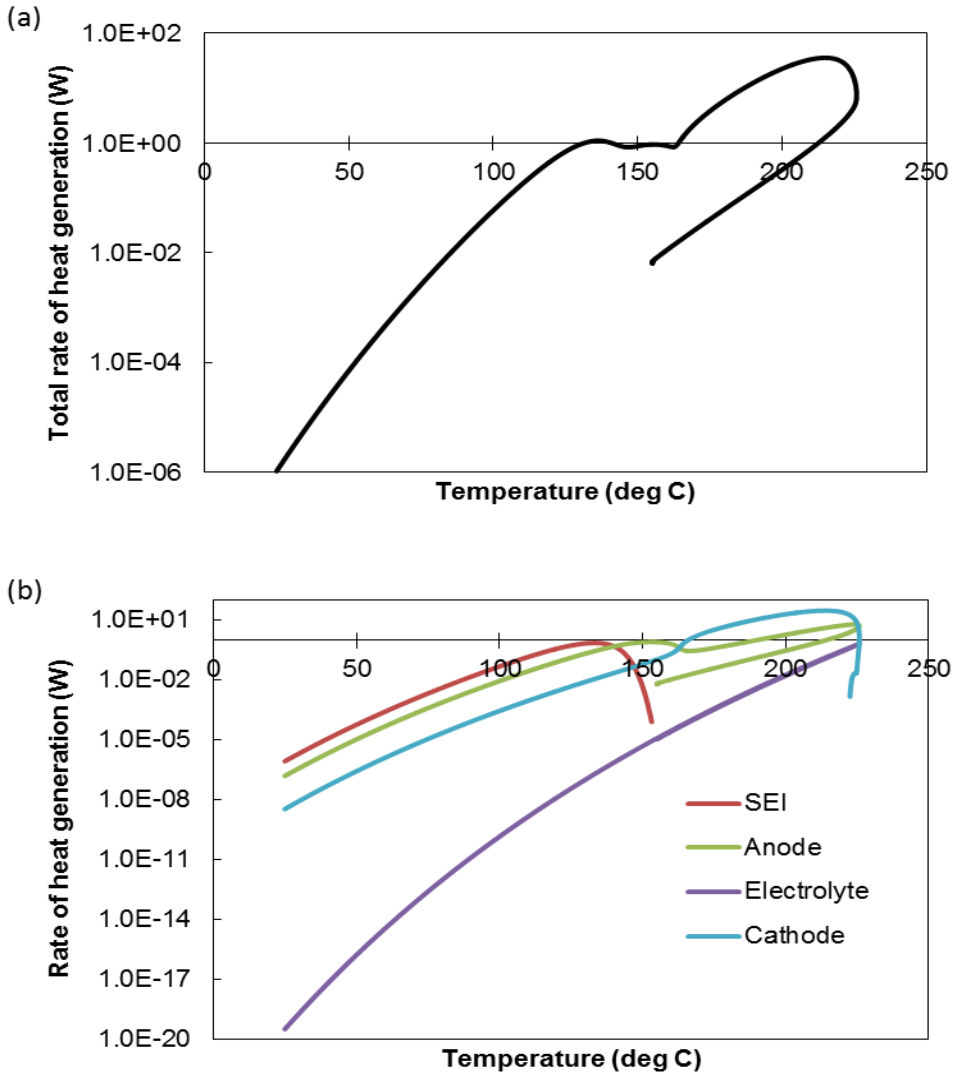

Figure 4.12: (a) Total rate of heat generation by chemical reactions at abusive temperature of 155 ^{o}C and (b) breakdown of the heat sources to its individual reactions.

The SEI decomposition plays an important role in thermal runaway, as this reaction is the bottleneck to the failure. The film acts as a protective layer to prevent further chemical reactions at the negative active material. SEI breakdown contributes the largest amount of power generation during the initial stage of thermal runaway. At higher temperature, cathode breakdown becomes the main heat source. The heat contributed by electrolyte decomposition reaction is not significant in the low temperature region but getting higher as the battery temperature increases.

The abuse temperature has a significant impact on the chemical reactions progress during thermal runaway. Figure 4.13 illustrates the dynamic of the chemical reaction progress at different temperatures. In general, the progress of the chemical reactions is more energetic at higher temperatures. In all simulated cases, the SEI decomposition reaction proceeds to completion. The same trend is observed for cathode conversion and the reaction is approaching completion at the ambient temperature of 150 ^{o}C.

In addition, the thermal energy supplied from 150 ^{o}C environment is not sufficient to trigger the heat-induced high-temperature electrolyte decomposition reaction. The reaction is fast that immediate depletion of the electrolyte concentration is observed provided that the ambient temperature is sufficiently high. An abrupt progress in the chemical reactions is observed in the spiking temperature region. After the highest temperature is reached, SEI thickness and lithium content in anode remain plateau, indicating a halt in the reaction progress.

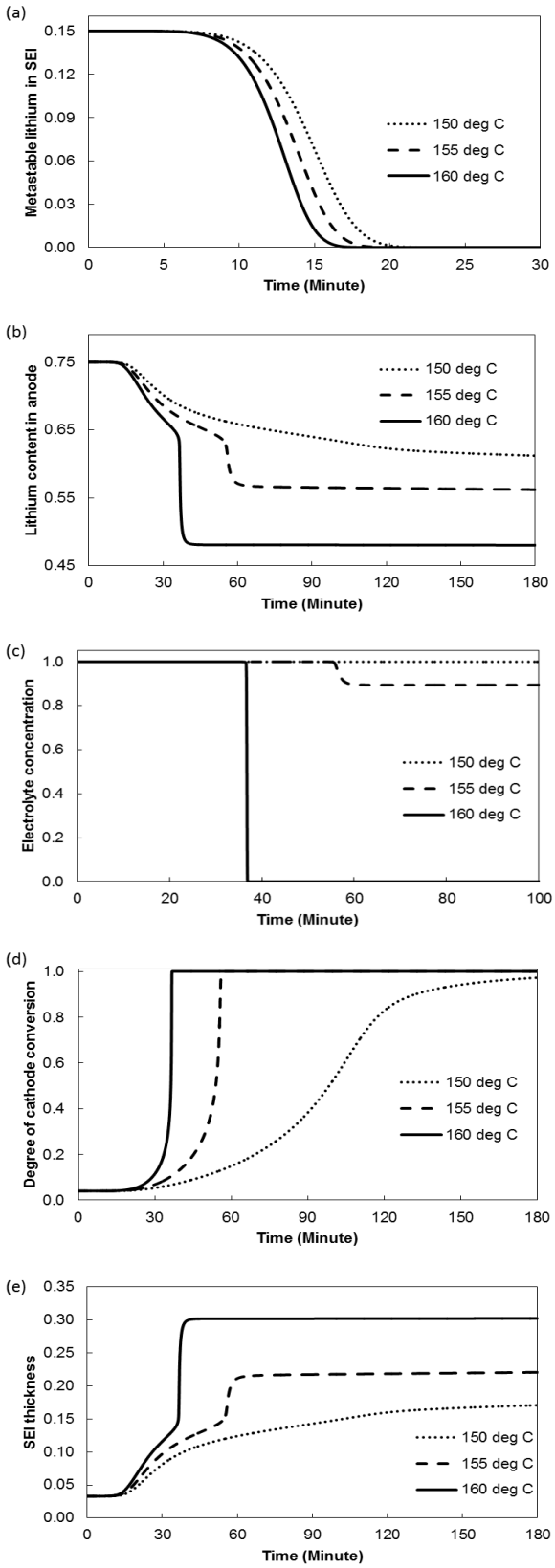

Figure 4.13: The progress of reaction (a) SEI (b) anode (c) electrolyte (d) cathode and (e) secondary SEI thickness, at different abusive temperatures.

4.6.2 Thermal Runaway at Constant Heating Rate

Thermal model for constant high ambient temperature is well reported in the literature. In this section, we demonstrate how the modelling of chemical reactions involved in thermal runaway can be used to simulate thermal profile of battery at continuously changing environment. Three cases were developed at constant thermal ramp of 1, 1.5 and 2 ^{o}C/minute up to the point where the battery temperature exceeded the ambient temperature and the ambient temperature was held constant thereafter. The simulated thermal profiles are presented in Figure 4.14.

In general, higher heating rate results in higher maximum temperature, less time to overshoot the ambient temperature and higher rapid thermal runaway temperature. The battery recorded a gradual temperature increase with widening temperature gradient between the battery and the ambient temperature before subsequently overshoot the ambient temperature due to the progressing local exothermic reactions. The battery temperature soared to higher than 300 ^{o}C as thermal runaway occurred and reduced to the ambient temperature thereafter. The battery temperature remained unchanged at ambient temperature thereafter as the battery subsequently achieved thermal equilibrium with the environment where the rate of heat dissipation is equal to the rate of heat generation or supply.

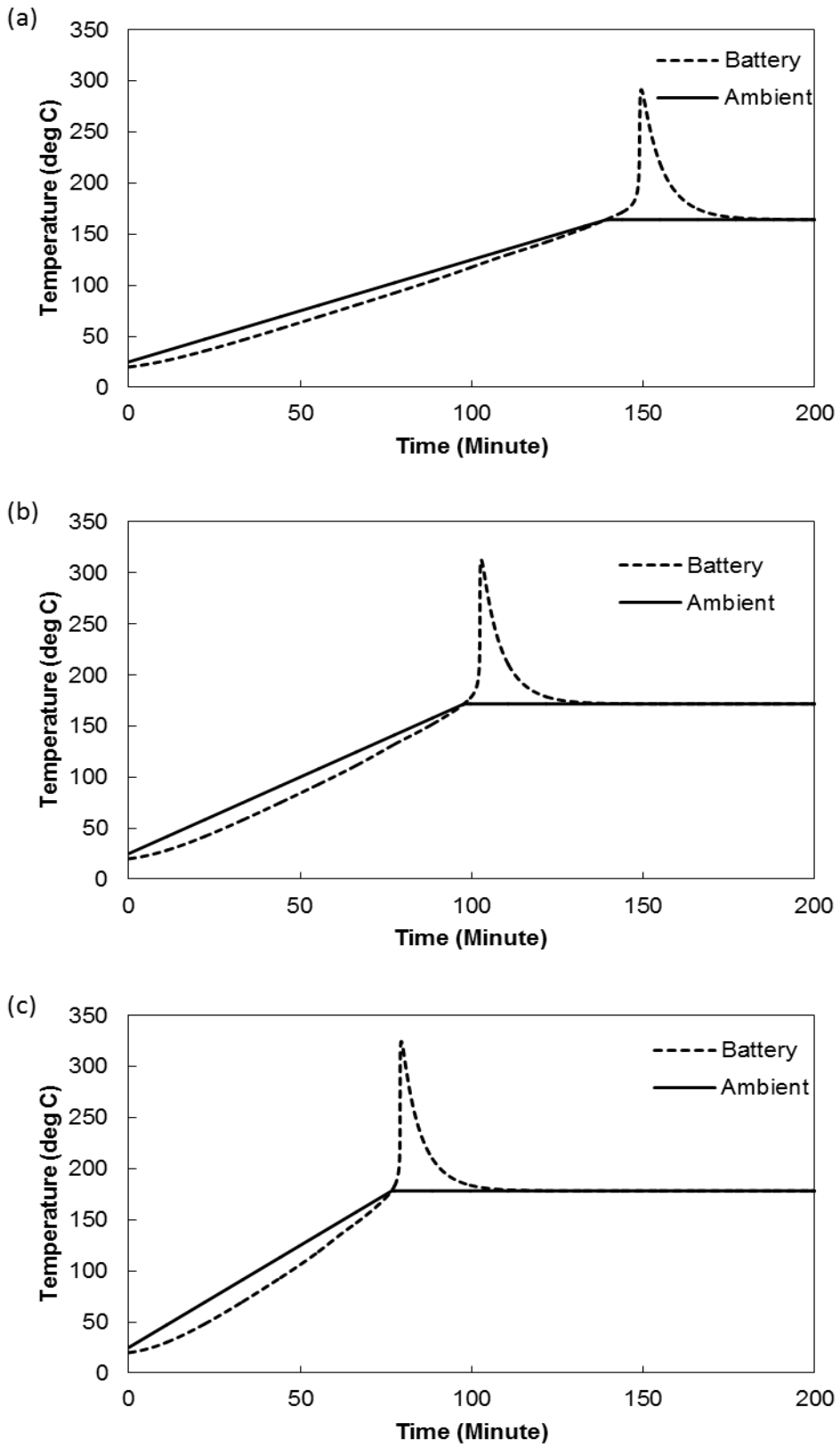

Figure 4.14: Battery temperature profile under continuously increasing ambient temperature at the rate of (a) 1 ^{o}C/min (b) 1.5 ^{o}C/min and (c) 2 ^{o}C/min.

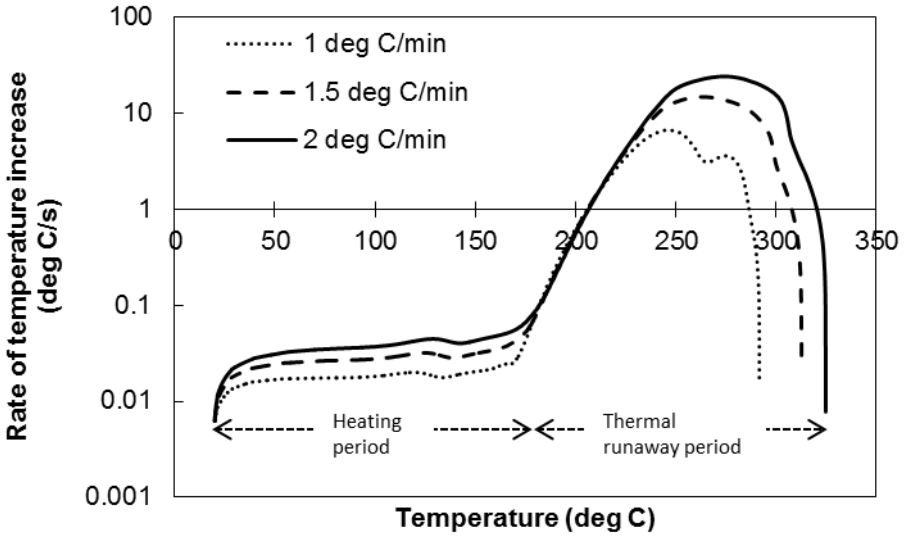

Figure 4.15: Rate of temperature increase profiles during thermal abuse by constant heating rate.

Figure 4.15 presents the rate of temperature increase as the battery temperature changes to decipher the heat exchange process that contributes to the battery temperature rise. At lower temperature region prior to thermal runaway, the rate of heat increase is curvy, demonstrating an upward trend as the temperature increases which is due to the widening temperature difference between the battery and the environment. Higher rate of temperature increase is recorded for higher heating rate and the curves converge as the temperature increases. The initial increase in battery temperature is instigated by a combination of self-generated heat by the reactive battery components and both conductive and radiative heat transfer between the high ambient temperature and battery. In comparison to constant high ambient temperature cases, wider projectile with higher peak is observed, reflecting higher maximum temperature during thermal spike and rate of temperature increase respectively.

The point of thermal runaway is defined at the point of inflection between the rising curve and projectile of temperature increase rate. As thermal runaway is triggered, the amount of heat generated intensifies which leads to peak of temperature increase rate. This is subsequently followed by decreasing rate temperature rise until the temperature spike is reached.

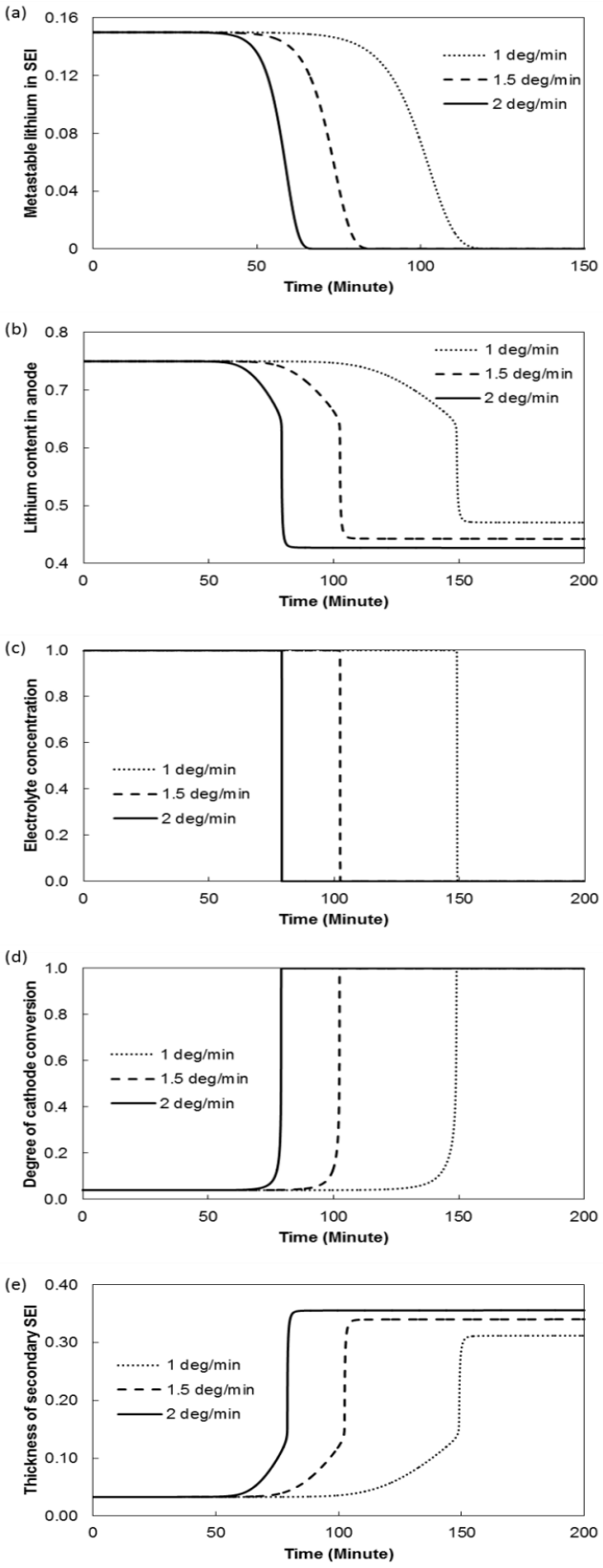

Figure 4.16: The progress of reaction (a) SEI (b) anode (c) electrolyte (d) cathode and (e) secondary SEI thickness, at varying heating rates.

The heating rate has a significant impact on the progress of chemical reactions during thermal runaway. Figure 4.16 illustrates the dynamic of the chemical reaction progress at varying heating rates. In general, the progress of the chemical reactions is more energetic at higher heating rate. In all simulated cases, all reactions proceed to completion except for the anode and the subsequent secondary SEI formation. An abrupt progress in the chemical reactions is observed at the spiking temperature region where the reactions at cathode and electrolyte reach immediate completion while anode is being consumed at a high rate.

The rate of heat generation by the chemical reactions at a heating rate of 2 ^{o}C/min is presented in Figure 4.17 to illustrate their exothermicity nature and heat contribution under constantly heated environment. The SEI, cathode and electrolyte stop generating heat after the thermal spike due to the complete consumption of the reactants, which in turn terminates the reactions entirely. The initial heat generation is caused by SEI breakdown. The rate of heat generation by electrolyte, cathode and anode peak at the thermal spike and the highest value is recorded by cathode. The precipitous depletion of the electrolyte concentration during thermal runaway entails a sharp spike in the rate of heat release. The reaction at anode continues to release heat for a short period after the thermal spike since the thermal environment cannot sustain the progress of the heat activated-reaction.

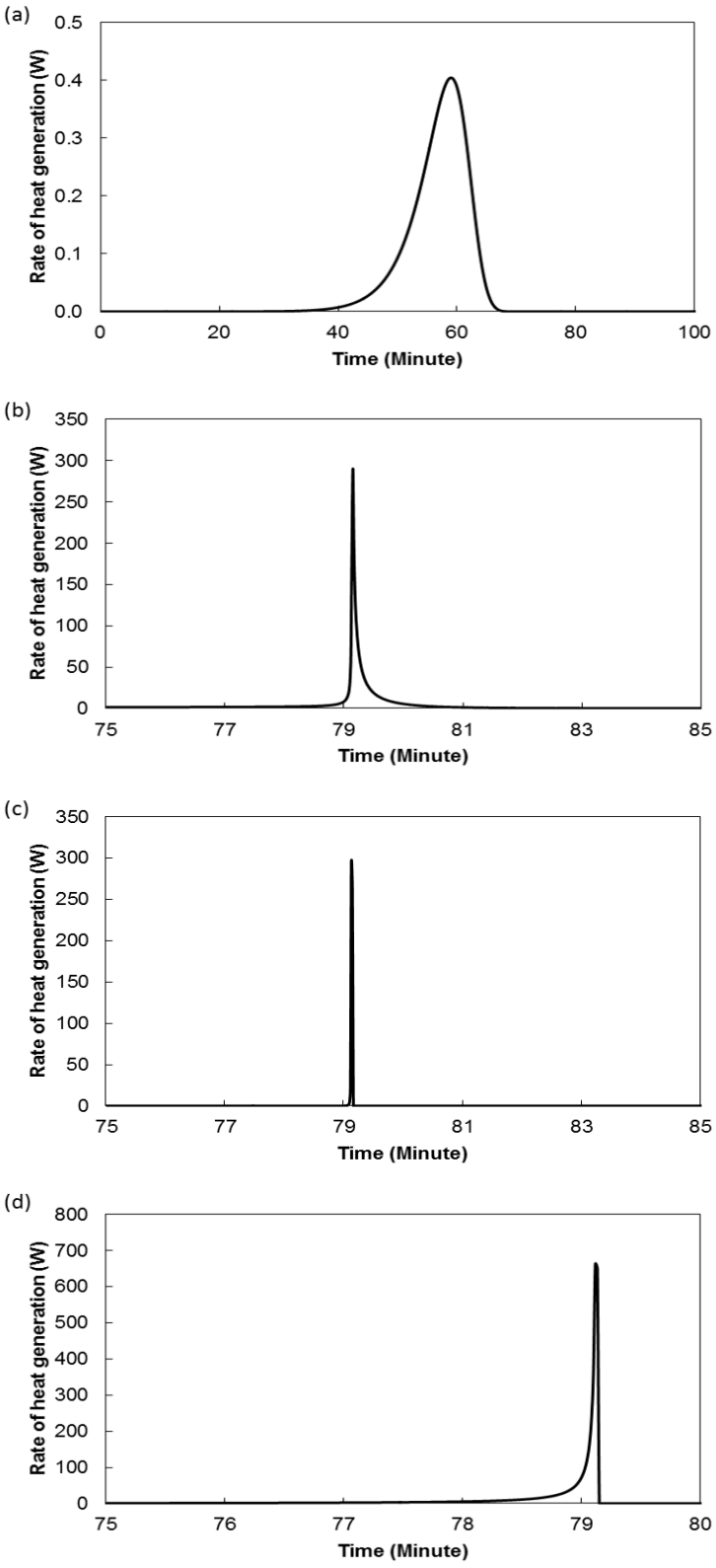

Figure 4.17: The rate of heat release by (a) SEI (b) anode (c) electrolyte and (d) cathode reactions, during thermal abuse at heating rate of 2 ^{o}C/min.

A comparison of total rate of heat generation at varying heating rate is given in Figure 4.18. The development in the rate of heat release is abrupt due to the exponential behaviour of the reaction rate and the associated heat release. A glance at the chart will only detect spike while the lower heat release rate that contribute to the temperature change is left unseen. The spike is stretched at lower heating rate with lower peak of heat release rate and gets narrower with higher peak as the heating rate increases.

The amount of heat released by the chemical reactions under linearly heated environment is summarised in Table 4.6.

Table 4.6: Total heat release and heat release rate under continuously changing thermal environments.

Temperature increment rate (^{o}C/min)	1.0	1.5	2.0
Peak heat release rate (W)	289.1	680.4	1129.4
Total heat release (J)	7.83×10^3	8.14×10^3	8.27×10^3
Total heat release by SEI reaction (J)	247.0	246.9	246.9
Total heat release by anode reaction (J)	3.06×10^3	3.37×10^3	3.55×10^3
Total heat release by electrolyte reaction (J)	663.5	664.1	579.5
Total heat release cathode reaction (J)	3.85×10^3	3.86×10^3	3.90×10^3

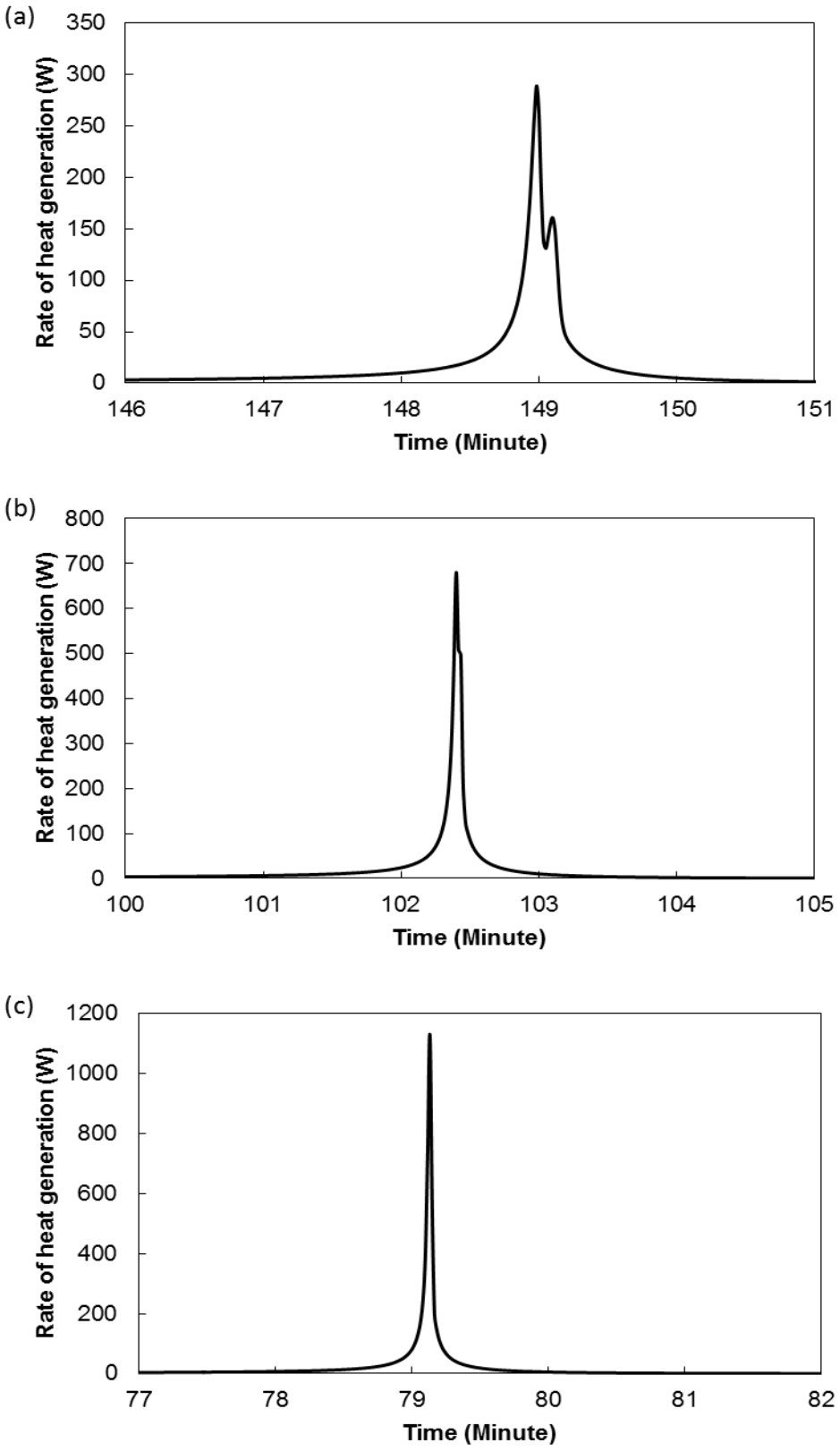

Figure 4.18: Total rate of heat generation in the battery at heating rate of (a) 1 (b) 1.5 and (c) 2 ^{o}C/min.

4.6.3 Thermal Runaway by Impact-Induced Short-Circuit

In a literature survey by Spotnitz and Franklin (2003), it has been determined that nail, short-circuit and crush are among the common methods used to assess abuse tolerance of lithium-ion cells. In general, these three techniques share the same feature. The battery releases a large amount of heat instantaneously upon failure, which is essentially due to short-circuit. The model developed in this work, being one-dimensional, is a rough approximation of a nail and crush test. The distribution of the heat released from the nail penetration is treated to be instantaneous and uniform in the plane perpendicular to the direction of nail penetration. In a real situation, a local hotspot will form because the heat dissipation from the nail puncture spot is not rapid. Three-dimensional modelling is necessary for better consideration of thermal gradient within the battery geometry. In a work done by Lamb and Orendorff (2014), the short-circuit induced by mechanical impact instigated the peak temperature of the cylindrical LIB with $LiCoO_2$ cathode to reach between 99 to 662 ^{o}C. The battery energetic response to the mechanical impact depends on the force and orientation of the impact, and the type of indentation used in the evaluation.

Short-circuit, despite being a different mode of failure, shares some general feature with thermal abuse behaviour. The simulated temperature profile for short-circuit is shown in Figure 4.19. In both thermal abuse and short-circuit, two apparent stages are observed. The surge and plunge patterns of the battery temporal behaviour due to short-circuit are comparable to thermal abuse. However, the temperature increment is not sharp and the temperature drop is gradual, as compared to the thermal abuse profile.

Figure 4.20 presents the rate of temperature increase as the battery temperature changes to decipher the heat exchange process that contributes to the battery temperature development. In comparison to thermal abuse cases, thermal runaway occurs straight away after the impact due to short-circuit. The initial temperature increment is brought by the instantaneous discharge of stored chemical energy and chemical reactions, which leads to thermal runaway. The chemical energy deposit that supposed to be converted into electrical energy during normal operation is descended as thermal energy instead via the Joule heating process.

The point of inflection between the declining curve and projectile of temperature increase rate marks the point when chemical energy becomes the dominant heat source during thermal runaway. The rate of temperature increase intensifies at higher temperature and plateaus at the intermediate temperature region. This is subsequently followed by decreasing rate temperature rise until the maximum temperature is reached.

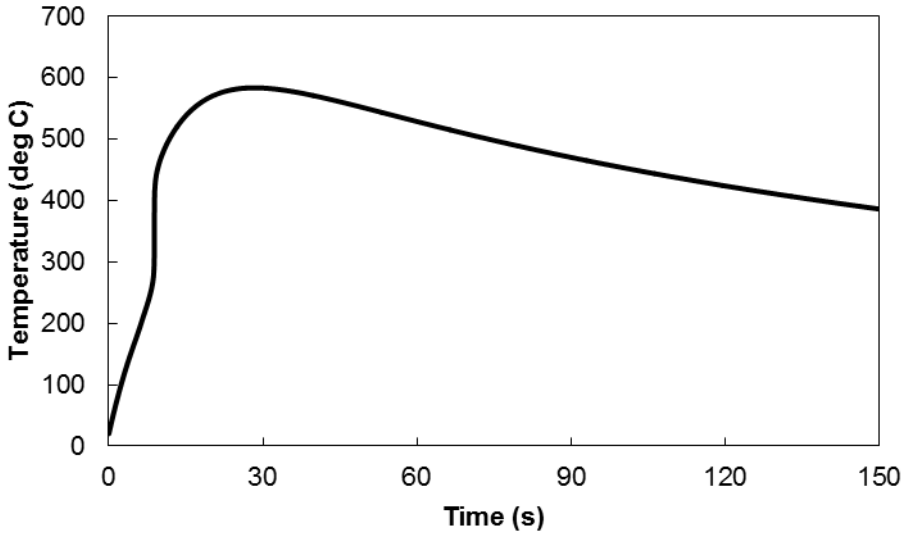

Figure 4.19: Thermal runaway profile of a short-circuited battery.

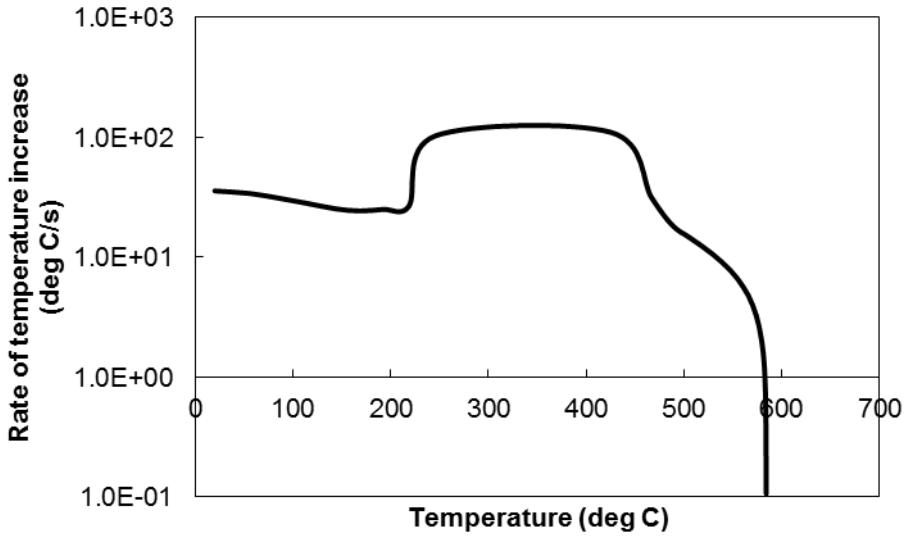

Figure 4.20: Rate of temperature increase profile during short-circuit.

To have a better illustration and understanding on the contribution of the chemical reactions involved and short-circuit to thermal runaway, the rate of heat generation of the respective sources is depicted in Figure 4.21.

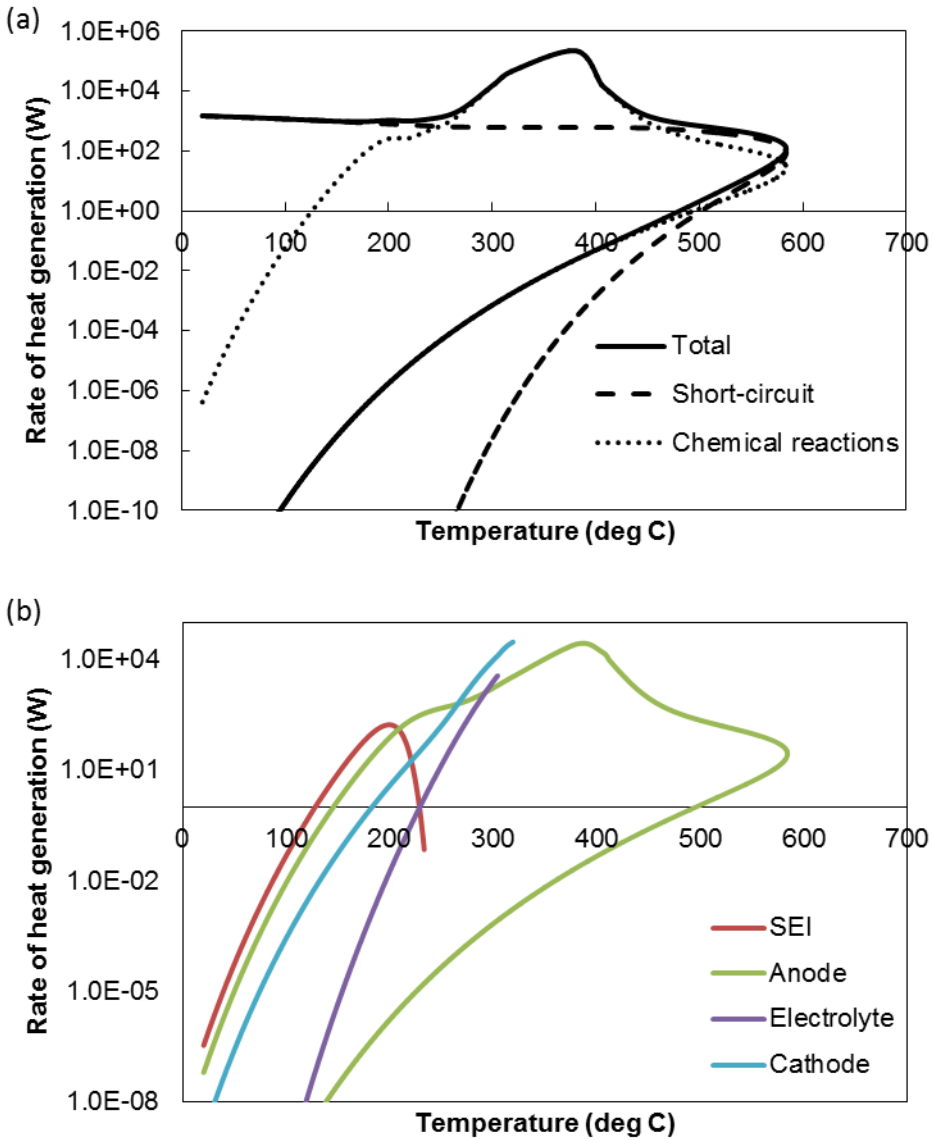

Figure 4.21: (a) Total rate of heat generation, which is a sum of heat released from short-circuit and chemical reactions (b) heat release rate by individual chemical reactions.

The heat generated in short-circuit case is contributed by a combination of both electrical and chemical energy. At the low temperature region, the amount of heat generated by chemical reactions is not significant where the initial heat generation is dominated by short-circuit. As the battery temperature increases, the exothermic reactions in the battery components proceed at a higher rate, which in turn enhance the amount of heat generated and render the dominant heat source in the intermediate temperature region.

The amount of reacting species depletes at high temperature that leads to reactions completion. The situation reduces the amount of heat generated by chemical reactions and makes short-circuit as the prevailing heat source at the high temperature region. The initial heat generation by chemical reactions is dominated by SEI breakdown. As most reactants are depleted as the battery temperature increases, the highest heat release rate at the intermediate and high temperature regions is contributed by the reaction at anode.

The progress of the individual reactions is presented in Figure 4.22. The intense amount of heat generated by short-circuit induces SEI, cathode and electrolyte reactions to completion within a short time. A sharp progress in the reactions is observed as the battery reaches peak temperature, which leads to completion of electrolyte and cathode reactions. SEI decomposition completes earlier since this reaction is the bottleneck to thermal runaway. After the highest temperature is reached, secondary SEI thickness and lithium content in anode remained plateau, indicating a halt in the reaction progress.

Figure 4.23 presents the total rate of heat release during short-circuit. A spike is observed as the battery temperature is sufficiently high to induce the heat-activated chemical reactions in the battery components. The rate reduces dramatically after complete depletion of most reacting species. Table 4.7 summaries the amount of heat released by chemical reactions and the rapid discharge of electrical energy into heat during short-circuit.

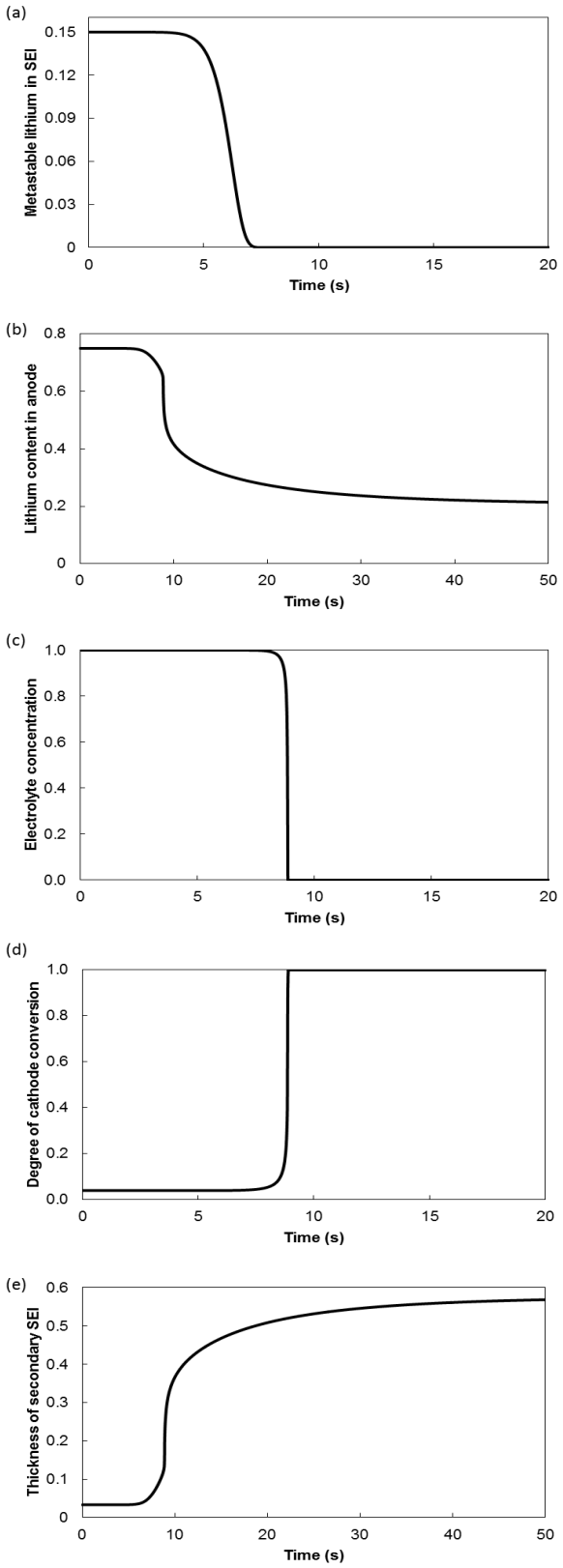

Figure 4.22: The progress of reaction (a) SEI (b) anode (c) electrolyte (d) cathode and (e) secondary SEI thickness, during short-circuit.

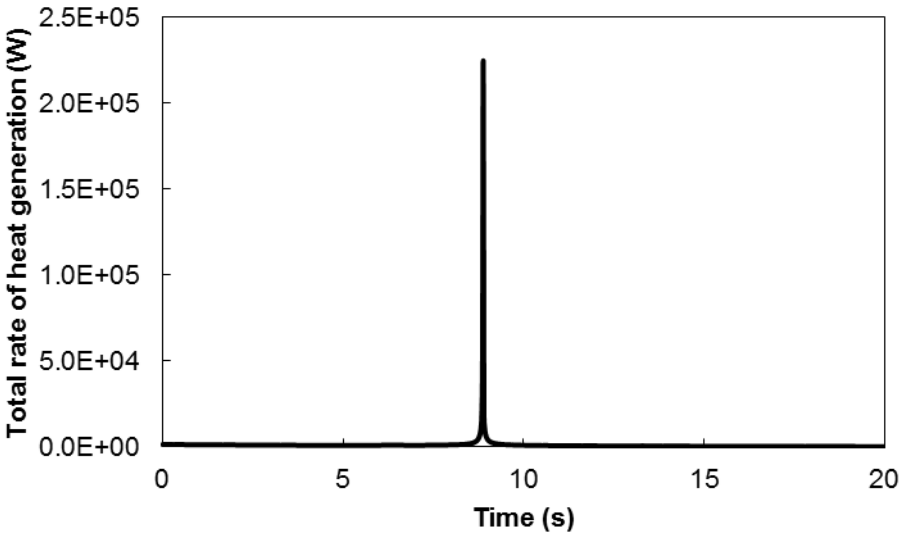

Figure 4.23: Total rate of heat generation in the battery during short-circuit.

Table 4.7: Total heat release and heat release rate during short-circuit.

Peak heat release rate (W)	2.25×10^5
Total heat release (J)	2.75×10^4
Total heat release during short-circuit (J)	1.5×10^4
Total heat release by SEI reaction (J)	247.1
Total heat release by anode reaction (J)	6.04×10^3
Total heat release by electrolyte reaction (J)	466.1
Total heat release cathode reaction (J)	5.76×10^3

4.6.4 Thermal Runaway Propagation in a Battery Module

The model in Section 4.6.3 was further expanded to include heat transfer modelling in order to investigate the propagation of thermal runaway in a battery module with 3x3 matrix configuration consisted of 9 cylindrical cells. Two thermal runaway propagation situations were developed at different positions of initial failure and the severity of the associated thermal hazard was compared. The cases were developed based on the assumption that the thermal runaway propagated from the initiated cell to the other surrounding cells by heat transfer. The effect of electrical connector that provides electrical pathway, which in turn might affect the propagation of thermal runaway in the whole module, was not considered.

4.6.4.1 Initiation of Thermal Runaway in the Middle Cell

In the first case, thermal runaway was assumed to be initiated by impact-induced short-circuit in Cell 5. The position of the failure initiation is marked in red, as illustrated in Figure 4.24.

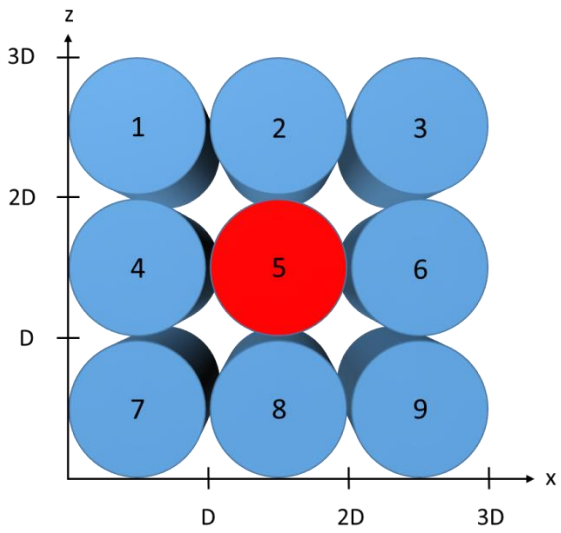

Figure 4.24: Thermal runaway initiation in the middle cell of the battery module.

The temperature development of the cells in the battery module is shown in Figure 4.25. Due to the symmetric nature of the 3x3 matrix configuration, all cells located at diagonals of the initiated cell, which are Cell 1, 3, 7 and 9, recorded the same temperature profile. In addition, identical temperature profiles can be observed for all cells directly adjacent to the initiated cell, which are Cell 2, 4, 6 and 8.

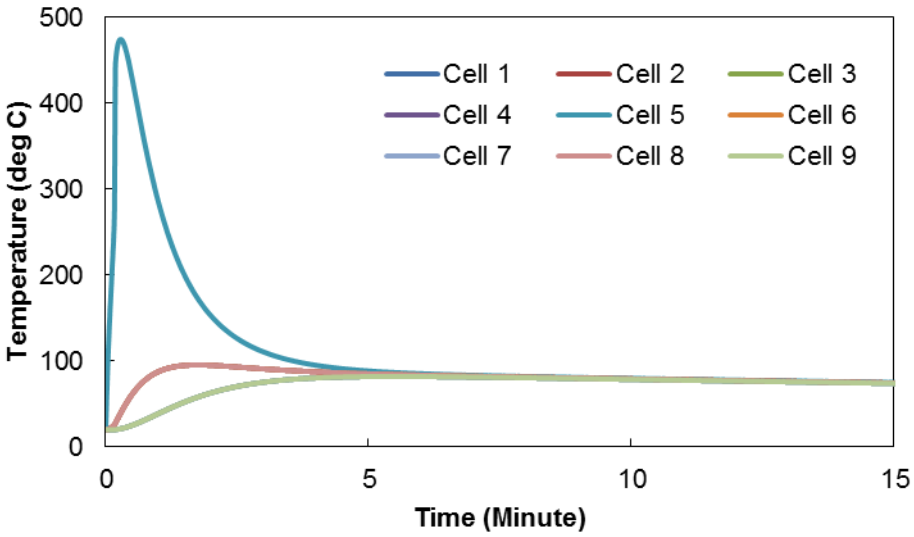

Figure 4.25: Temperature change of cells in the battery module.

The rapid heat release in the battery caused by short-circuit inflicts the temperature of Cell 5 to soar up to 500 ^{o}C. In general, all neighbouring cells recorded a temperature rise up to 100 ^{o}C. The close proximity and better surface contact of the directly adjacent cells (Cell 2, 4, 6 and 8) to the initiated cell caused the temperature to increase at a faster rate and reach a slightly higher peak compared to the cells located at the diagonals (Cell 1, 3, 7 and 9) of the battery module. All cells demonstrated an identical cooling profile after approximately 5 minutes of the failure initiation in Cell 5. The rise of temperature in the surrounding cells could be instigated by the heat transfer process from Cell 5, which might in turn induced the heat-activated exothermic reactions in the neighbouring batteries.

In order to inspect whether the heat transfer process from the defective cell managed to activate the exothermic reactions in the neighbouring cells, the progress of the reactions in all cells is shown in Figure 4.26 and Figure 4.27. Due to the slow progress of reactions in other cells compared to Cell 5, which might be difficult to notice, the information is presented in two separate figures.

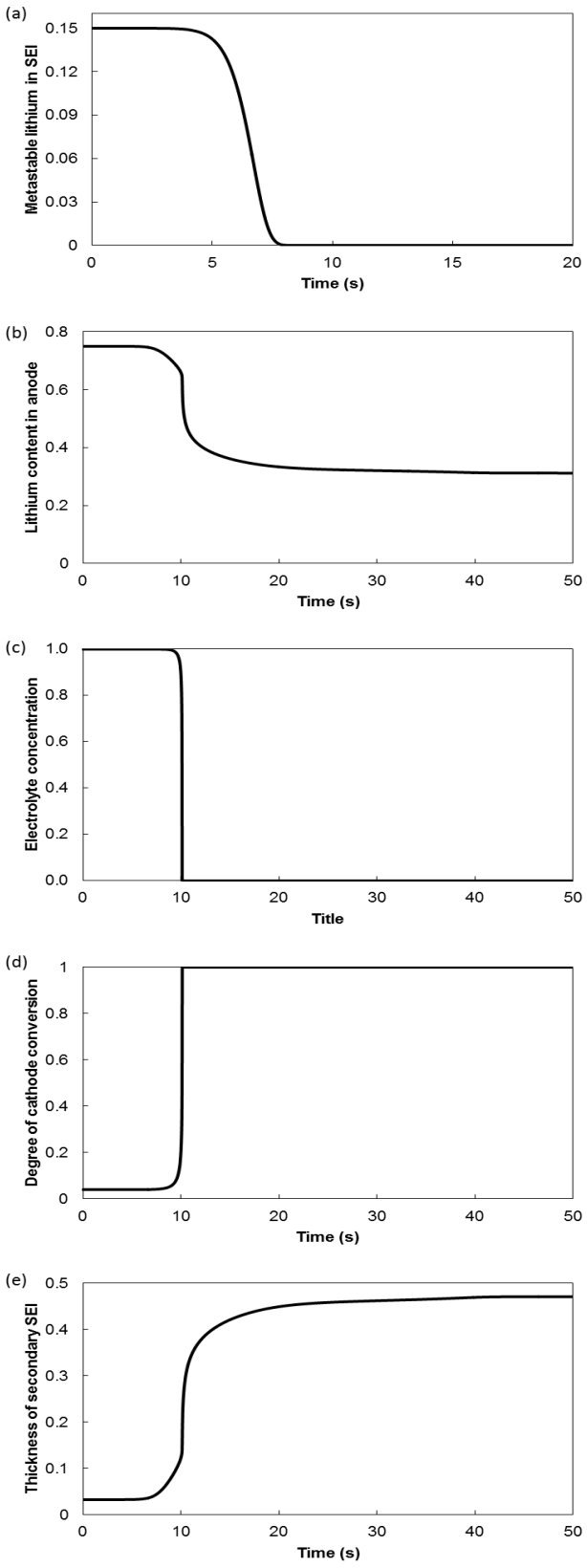

Figure 4.26: The progress of reaction (a) SEI (b) anode (c) electrolyte (d) cathode and (e) secondary SEI thickness, in Cell 5.

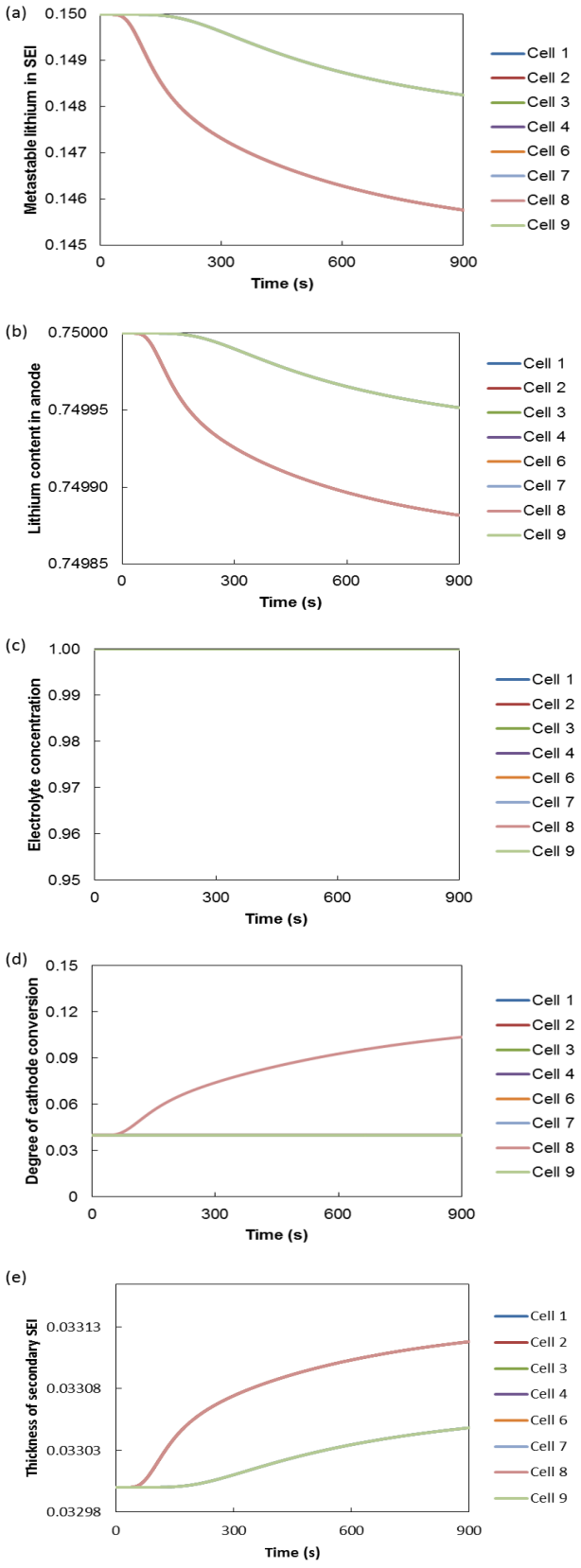

Figure 4.27: The progress of reaction (a) SEI (b) anode (c) electrolyte (d) cathode and (e) secondary SEI thickness, in all other cells in the battery module.

The pattern of reaction progress in Cell 5 is almost identical as observed in Section 4.6.3 due to the same method of failure initiation. The reactions in cathode, electrolyte and SEI are driven to completion in a short time span by the big amount of heat generated from short-circuit. The insufficient amount of heat after the peak temperature causes the reaction in anode and the subsequent secondary SEI layer film formation to cease.

In general, for all other cells in the battery module, the chemical reactions recorded a sluggish progress. A faster reaction progress can be observed for cells directly adjacent to the Cell 5. No reaction occurred at electrolyte since the reaction is a high temperature reaction. The progress of reactions in all neighbouring cells appears to be insignificant, implying the absence of thermal runaway and the temperature rise in the neighbouring cells is utterly caused by heat transfer from Cell 5.

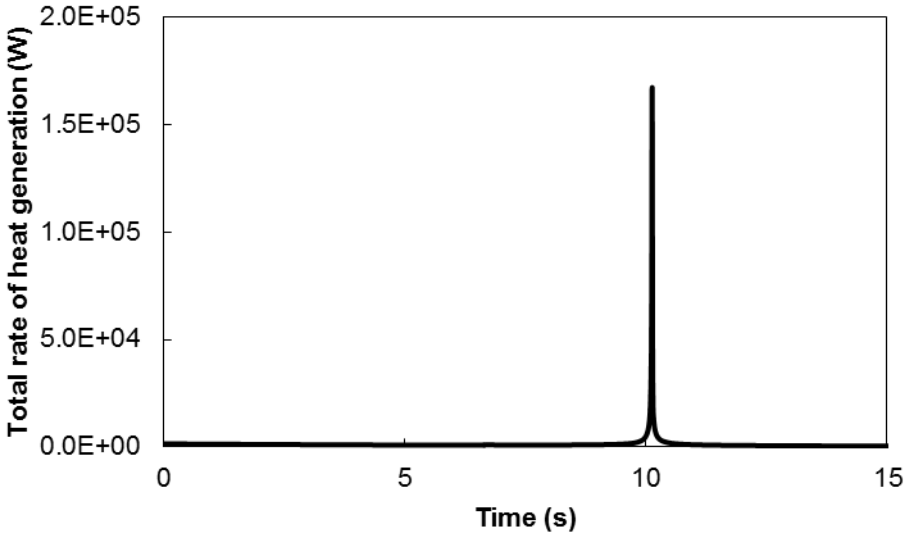

Figure 4.28: Rate of heat generation in the battery module.

Figure 4.28 presents the total rate of heat release in the battery module, indicating a peak of 167.1 kW. The heat generated in the module is sourced from a combination of both short-circuit and chemical reactions. A spike is observed as the battery temperature is sufficiently high to induce the heat-activated chemical reactions in the battery components. The rate reduces subsequently after complete depletion of

most reacting species. The total amount of heat liberated by this case, as calculated from the integration of the curve is determined to be 24.5 kJ.

4.6.4.2 Initiation of Thermal Runaway in Cell 1

In the second case, thermal runaway was assumed to be initiated by impact-induced short-circuit in Cell 1. The position of the failure initiation is marked in red, as illustrated in Figure 4.29.

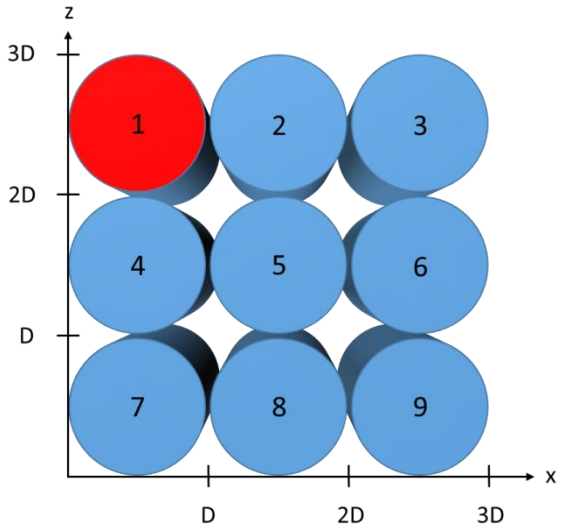

Figure 4.29: Thermal runaway initiation in the first cell of the battery module.

The temperature development of the cells in the battery module is shown in Figure 4.30. Due to the symmetric nature of the 3x3-matrix configuration, the following cells would have an identical temperature profile:

(a) Cell 2 and Cell 4
(b) Cell 3 and Cell 7
(c) Cell 6 and Cell 8

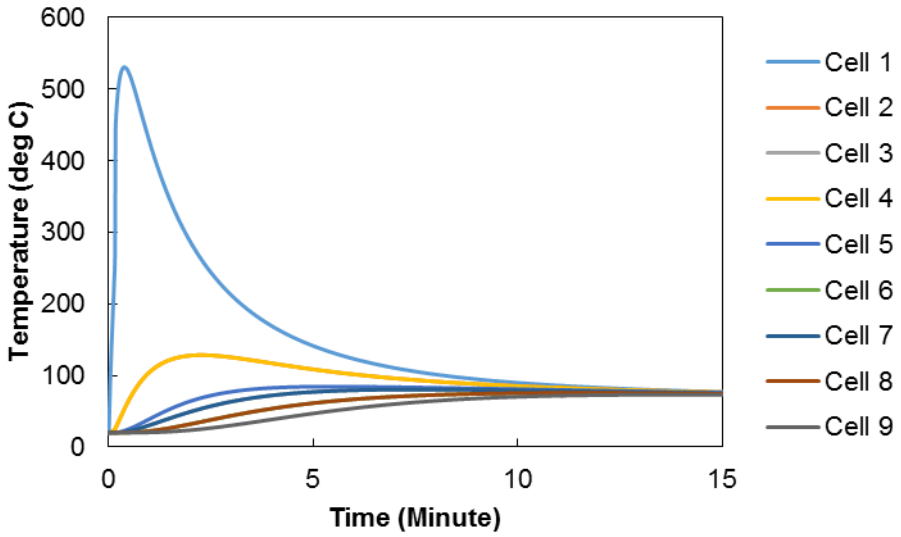

Figure 4.30: Temperature of cells in the battery module.

The rapid release of heat originating from conversion of electrical energy into thermal energy during short-circuit caused the temperature of Cell 1 to soar up to higher than 500 ^{o}C. In general, all neighbouring cells recorded a temperature rise up to 100 ^{o}C. Compared to all other neighbouring cells in the module, Cell 2 and Cell 4 recorded a higher and faster temperature development due to their relative position being directly adjacent to the defective cell. The temperature of all cells converged after approximately 13 minutes and exhibited a similar cooling profile. The rise of temperature in the surrounding cells could be instigated by the heat transfer process from Cell 1, which might in turn induced the heat-activated exothermic reactions in the neighbouring batteries. The progress of the reactions in all cells is shown in Figure 4.31 and Figure 4.32.

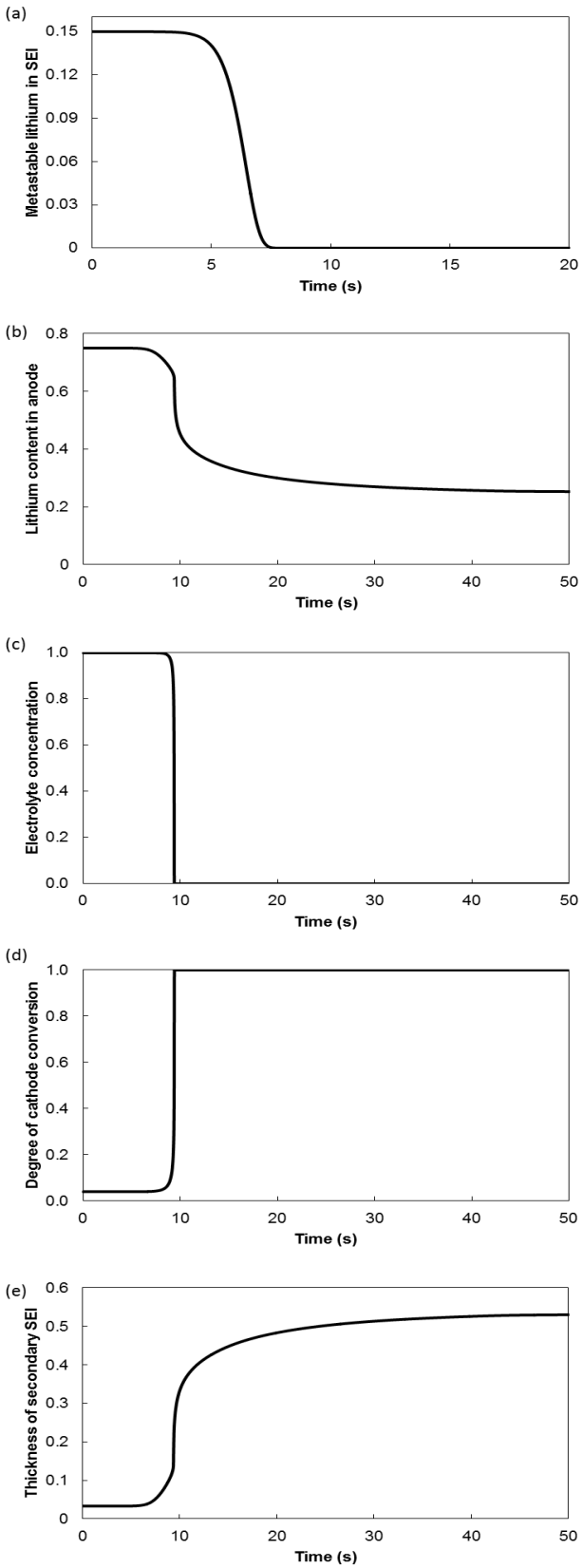

Figure 4.31: The progress of reaction (a) SEI (b) anode (c) electrolyte (d) cathode and (e) secondary SEI thickness, in Cell 1.

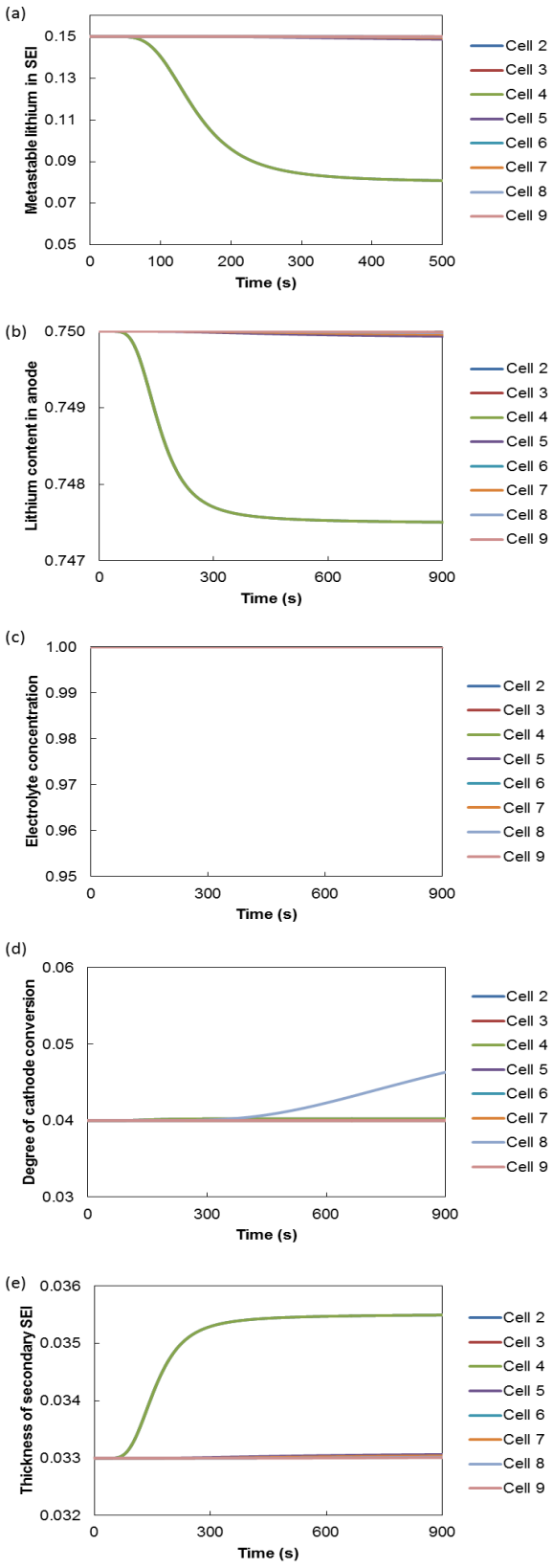

Figure 4.32: The progress of reaction (a) SEI (b) anode (c) electrolyte (d) cathode and (e) secondary SEI thickness, in all other cells in the battery module.

The pattern of reaction progress in Cell 1 is almost identical as observed in Section 4.6.3 and 4.6.4.2 due to the same method of failure initiation. The reactions in cathode, electrolyte and SEI are driven to completion in a short time span by the big amount of heat generated from short-circuit. Heat deficiency after the peak temperature retards the reaction in anode and the subsequent secondary SEI layer film formation.

In general, for all other cells in the battery module, the chemical reactions recorded a sluggish progress. A faster reaction progress can be observed for cells directly adjacent to the Cell 1. No reaction occurred at electrolyte since the reaction is a high temperature reaction. The heat transferred from the defective cell to the surrounding cells was not sufficient to induce thermal runaway propagation in the entire module.

Figure 4.33 presents the total rate of heat release in the battery module, with a peak of 211.9 kW. The total amount of heat liberated by this case, as calculated from the integration of the curve is determined to be 25.8 kJ.

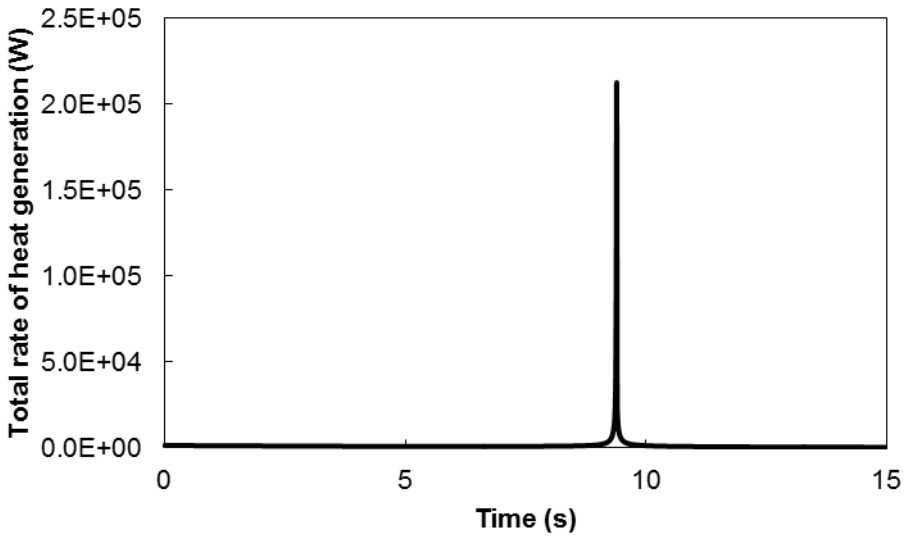

Figure 4.33: Total rate of heat generation in the battery module.

4.6.4.3 Discussion on the Effect of Thermal Runaway Initiation Location on Thermal Runaway Propagation

Two cases were developed where the effect of the location of failure initiation on thermal runaway propagation was investigated. In general, the simulated thermal behaviour of the battery module is qualitatively in agreement with the simulation work of Kim and Pesaran (2007) and experimental work of Wilke et al. (2017).

In both cases, thermal runaway propagation was not observed. Limited contact surface area retards the heat transfer process and deters the propagation of thermal runaway to the neighbouring cells. The small size of the cylindrical cells entails high surface area-to-volume ratio that promotes heat dissipation to the surrounding and prevents heat accumulation within the battery. A battery module consists of 9 cylindrical cells with 3x3 matrix configuration is a conductive thermal network. As a result, the initiation of failure in the centre of the module (Cell 5) results in less severe thermal runaway. The heat is conducted away from the defective cell through the thermal network and is being distributed evenly within the module. This situation in turn reduces the maximum rate of heat release and the subsequent peak temperature with delayed thermal runaway time.

In case where the failure was initiated in the edge (Cell 1), the defective cell recorded a higher and earlier peak rate of heat release and the ensuing temperature. Heat transfer by convection from the defective cell to the surrounding is not vigorous compared to conduction, which consequently slows down the heat dissipation process.

4.7 Summary

A numerical model was developed by combining thermal decomposition kinetics of battery components to simulate thermal runaway behaviour of high-capacity lithium-ion battery during thermal abuse and short-circuits. In addition, the model was further expanded to include heat transfer modelling to simulate thermal runaway propagation in a battery module.

From the modelling work, the findings are summarised as follow.

1. The modelling of thermal decomposition kinetics of battery components enables comprehensive understanding of relative contribution of the battery components towards thermal runaway.
2. Cathode reaction has been identified as the most reactive reaction during thermal runaway.
3. The consequence of battery thermal runaway is more severe at higher ambient temperature and higher heating rate. The situation is indicated by maximum temperature rise during thermal runaway.
4. The battery is more inclined towards thermal runaway at higher temperature and higher heating rate. The situation is indicated by thermal runaway induction time and time taken for the battery to overshoot ambient temperature.
5. Under thermally abusive environments, for both constant high ambient temperature and constant heating rate cases, thermal runaway does not occur instantaneously. Considerable amount of time is necessary to induce thermal runaway in the battery.
6. Impact-induced short-circuit, on the other hand, inflicts an immediate failure which in turn results in surge of the battery temperature.
7. A higher peak heat release rate is observed during short-circuit due to the combination of electrical and chemical energy that contributes to total thermal hazard.
8. For a battery module consists of 9 cylindrical 18650 cells, thermal runaway does not propagate. The small contact surface for the cylindrical geometry deters the heat transfer from the defective cell to the neighbouring cells.

Chapter 5: Experimental Characterisation of Lithium-ion Battery Thermal Runaway

Numerical modelling of battery thermal runaway has been discussed in Chapter 4. Battery thermal runaway under abusive conditions has been simulated by modelling thermal decomposition kinetics of the reactions involved. A further inclusion of heat transfer modelling in the numerical model allows the simulation of thermal runaway propagation in the battery module. This chapter details the experimental works done to validate and support the data obtained from numerical modelling.

5.1 Materials

The batteries used in the experimental work, as shown in Figure 5.1, are cylindrical with 18 mm diameter and 65 mm high. The specifications of the battery are presented in Table 5.1. Nickel strips of 8 mm wide and 1 mm thick are used to provide electrical connection, soldered at the terminals by SUNKO 788H spot welder.

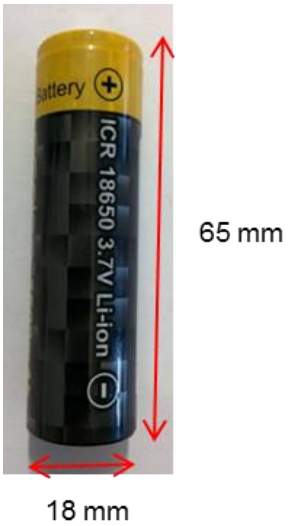

Figure 5.1: 18650 cylindrical lithium-ion cell used in the experimental work.

Table 5.1: Battery specifications.

Specification	Value
Form Factor	Cylindrical 18650
Mass (g)	48
Rated capacity (Ah)	2.5
Nominal voltage (V)	3.7
Maximum voltage (V)	4.2
Minimum voltage (V)	2.8
Cathode	Lithium cobalt oxide
Anode	Graphite

5.2 Experimental Programme

Four experimental programmes were conducted. First, the link between the battery charge state and voltage was established. Second, battery thermal runaway under non-adiabatic condition was characterised. Third, the features of thermal runaway under adiabatic condition were investigated. Four, thermal runaway behaviour during impact-induced short-circuit was explored.

5.2.1 Experimental Characterisation of Battery Discharge Curve

In the subsequent experimental programmes, the effects of state of charge on the severity of thermal runaway hazard are investigated. This initial work aims to establish the connection between the state of charge and the voltage of the cell. The state of charge is an expression of the present battery capacity as a percentage of maximum capacity, which cannot be measured instantaneously. Even though the capacity is proportionate to the battery voltage, the relationship is not linear. The discharge curve, which is a plot of voltage versus capacity, can serve as a guide to determine the state of charge at any particular voltage and vice versa.

5.2.1.1 Experimental Rig

The evaluation of the battery capacity was conducted by using fully automated and computerised MACCOR Series 4000. The testing equipment consists of a test cabinet, PC computer and test software. The test programme was coded using BuildTest software and the outcome was processed using MIMSClient. The equipment is shown in Figure 5.2.

Figure 5.2: Maccor Series 4000.

5.2.1.2 Experimental Procedures

The cell was left to rest for 6 hours to keep the temperature stabilised in the test cabinet prior to the cycling process. At the beginning of the cycling process, the battery was charged under constant current mode where the current was maintained at 1.25 A until the cell reached 4.2 V. Next, the cell was charged under constant voltage mode where the voltage was maintained at 4.2 V. After the completion of the charging process, the cell was discharged under constant current mode where the current was maintained at 1.25 A until the cell voltage dropped to 2.85 V. Lastly, the charging process was repeated once again. The current profile during the test procedures is presented in Figure 5.3.

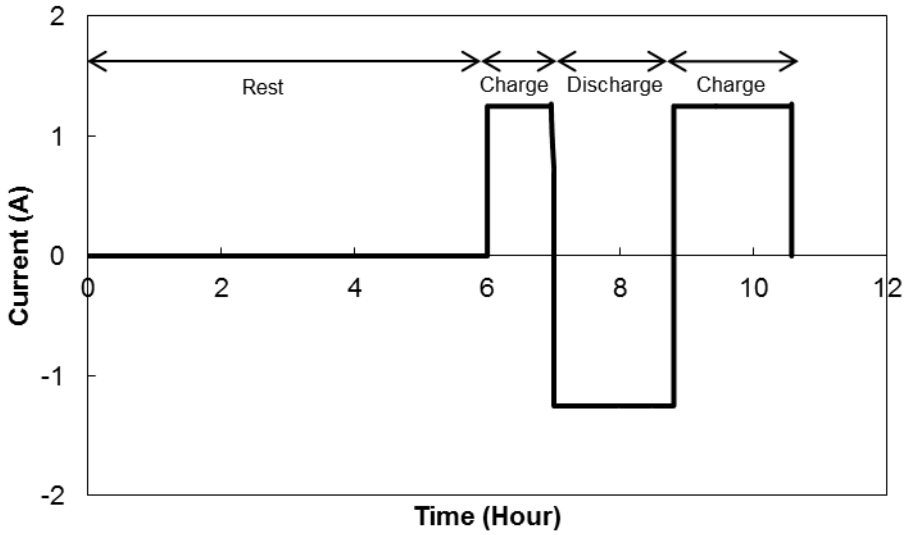

Figure 5.3: Current profile at different stages of test procedures.

5.2.2 Experimental Characterisation of Battery Thermal Runaway Using Oven Heating

This work aims to characterise battery thermal runaway under non-adiabatic and constant pressure conditions. Thermal runaway was induced by heating the battery from room temperature in an oven up to a preset temperature of 190 ^{o}C. The effects of varying battery mass and capacity on the severity of thermal runaway were examined.

5.2.2.1 Experimental Rig

Oven

Under non-adiabatic condition, the tests were conducted in a natural convection DRY-Line oven Model DL 53 supplied by VWR Collection. The oven is equipped with an electronic control with a maximum preset operational temperature of 220 ^{o}C. The built-in oven temperature measurement has an accuracy of $\pm$1 ^{o}C. The chamber of the oven is rectangular; holding a volume of 53 L with dimensions of 401 mm x 330 mm x 401 mm.

Sample Containment

The battery was contained inside two 100 ml oval flat-based ceramic pots and placed inside a lid-covered stainless steel holder. This dual-layer sample holder was necessary to contain any release from the battery from staining or damaging the oven chamber. The thermal and chemical resistant ceramic pot is 2.1 mm thick with 55 mm high and top opening of 60 mm. The stainless steel holder is a hollow cylinder with 70 mm diameter, 3 mm thick and 116 mm high, welded on the centre of a solid steel cylinder with 166.4 mm diameter and 21.1 mm high.

The top of the cylinder was covered with a steel sheet with dimensions of 135 mm x 105 mm x 1.5 mm, and overlaid with a 722 g mild steel cylinder on top. The whole sample containment was not completely sealed where the gases released throughout the experimental procedures could escape and preventing pressure build up, therefore this experimental arrangement can be classified as a constant pressure system. The experimental setup and thermocouple position is shown in Figure 5.4.

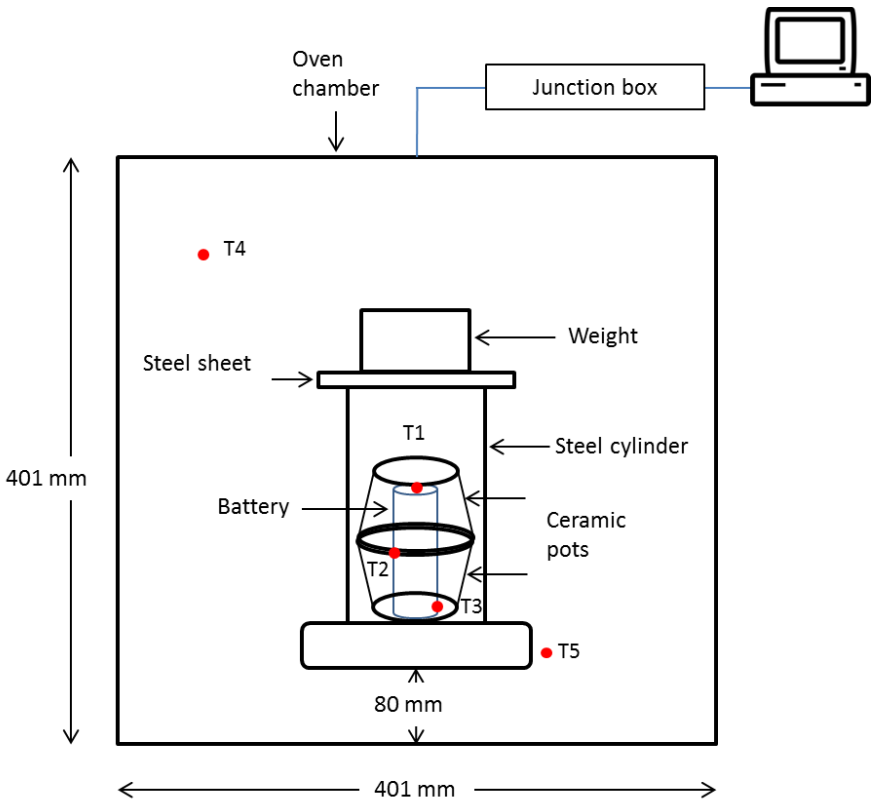

Figure 5.4: Schematic of the oven test experimental arrangement and thermocouple location.

Temperature Measurement

For measuring the temperature, type-K Inconel sheathed thermocouples were used. The data was recorded at a frequency of 1 Hz with a resolution of ± 0.001 ^{o}C by using Microlink 751 data logging interface and Windmill data acquisition software.

Five thermocouples were used in this experiment to measure the temperature at five different points. Three thermocouples, T1, T2 and T3 were positioned inside the ceramic pots to measure the temperature around the battery. Two thermocouples were placed outside the cylindrical steel holder to record the temperature of oven air, T4 and steel holder base, T5. The description of the thermocouple positions is given in Table 5.2.

Table 5.2: Arrangement of the thermocouples during oven tests.

Thermocouple	**Description**
T1	Battery positive terminal and vent
T2	Middle of the battery canister where reactive electrodes and flammable electrolytes are hosted
T3	Battery negative terminal
T4	Oven air temperature
T5	Sample container

5.2.2.2 Experimental Procedures

After complete placement of the battery and the thermocouples inside the oven chamber, the oven was heated from room temperature to 190 ^{o}C, a sufficiently high temperature for effective induction of thermal runaway. The oven was turned off and the data logging was stopped after all temperature readings stabilised after the completion of thermal runaway reactions. The details of the test programme and battery conditions are given in Table 5.3.

Table 5.3: Oven test experimental conditions.

Test	Description	State of charge	Number of battery	Total capacity (Ah)	Total voltage (V)	Total mass (g)
1	Full-charged single cell	100	1	2.50	4.19	48
2	Two unconnected full-charged cells	100	2	2.50	4.19	96
3	Two full-charged cells connected in parallel	100	2	5.00	4.23	96
4	Half-charged single cell	50	1	1.25	3.74	48
5	Zero-charged single cell	0	1	0	3.21	48

5.2.3 Experimental Characterisation of Battery Thermal Runaway Using Accelerating Rate Calorimeter

This work aims to characterise battery thermal runaway under adiabatic and constant volume conditions. Thermal runaway was induced in the battery by using Accelerating Rate Calorimeter under Heat-Wait-Seek mode. The effects of varying battery mass and capacity on the severity of thermal runaway were examined.

5.2.3.1 Experimental Rig

The evaluation of battery thermal hazard under adiabatic condition was conducted using Extended Volume+ Accelerating Rate Calorimeter provided by Thermal Hazard Technology. The testing equipment consists of a cylindrically-hollowed rectangular chamber confined within a containment vessel, desktop computer and computer software. The test programme was initialised using ARC-ES software and the outcome was processed using ARCCAL PLUS (Thermal Hazard Technology, 2013).

Calorimeter

The calorimeter consists of two main parts, which are the lid and the vessel. The calorimeter vessel is 55.3 L cylinder with 40 cm diameter and 44 cm depth, made from aluminium with a wall thickness of 1 cm, as shown in Figure 5.5. The near perfect adiabatic conditions are achieved by surrounding the calorimeter with a thick aluminium jacket containing a series of heaters and thermocouples, which are being positioned according to 2-4-2 configuration at three different zones. There are two heaters in the top zone, four equally spaced around the side zone and two in the base zone. Each zone is equipped with a thermocouple, which is intended for heater control during calorimeter operation. In addition, there is another thermocouple inside the bomb for measurement of battery temperature. The specifications of the thermocouples are given in Table 5.4.

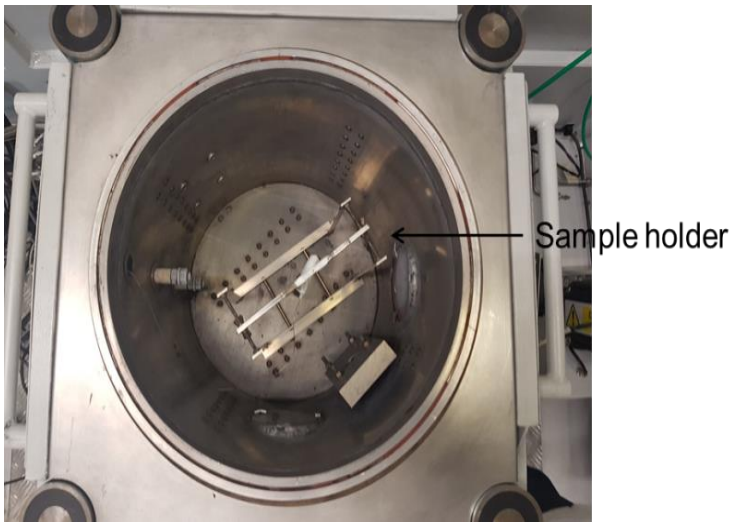

Figure 5.5: Cylindrical vessel with sample holder inside.

Table 5.4: Technical descriptions of thermocouples used in the calorimeter.

Type	Mineral insulated nisil-nicrosil (type N)
Resolution	0.001 ^{o}C
Precision	< 0.2%
Accuracy	0.7%

In order to provide additional protection from flying shrapnel and open flames in the event of fire and explosion, the calorimeter is further placed inside a containment vessel. The steel blast box is 5 mm thick with dimensions of 163 cm x 113 cm x 105 cm. The blast box is equipped with a pair of lids on the top and a pair of doors at the side, as shown in Figure 5.6. During the calorimeter operation, the lids are electronically locked. Besides that, the doors and the lids are mechanically locked using steel rods as part of additional safety features.

Figure 5.6: Blast box of the EV+ ARC.

A solenoid valve is installed at the back of the blast box. This valve controls the compressed air flow during the gas purge and cooling procedure. In addition, there is a vent at the side of the blast box, which is connected to the extraction system. The opening of motorised flap during the gas extraction allows air from the lab to flow into the blast box and assists the gas purging.

Sample Suspension

The heating process during the operation increases the temperature of the calorimeter to some extent. In order to prevent the calorimeter surfaces from conducting heat directly to the battery and interfere with the heating process, the battery is thermally isolated from any direct contact with the calorimeter base and sidewalls. An aluminium frame is used where the battery is suspended by using glass fibre tape. The arrangement of the battery for the ARC test is shown in Figure 5.7.

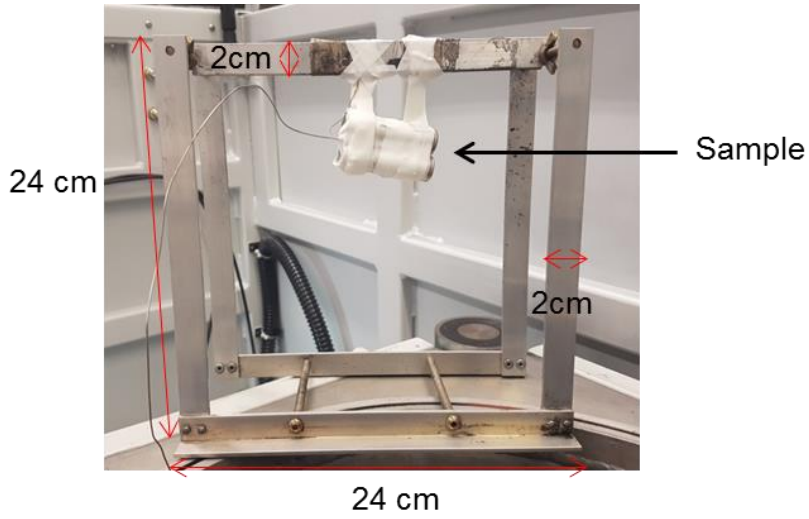

Figure 5.7: Battery with thermocouple attached being suspended in the aluminium frame for the test.

5.2.3.2 Experimental Procedures: Heat-Wait-Seek Method

The experiment was conducted under the Heat-Wait-Seek (HWS) mode. The battery was initially heated from the room temperature to the specified start temperature, followed by the first waiting period. The temperature of the bomb and the jacket heaters would reach thermal equilibrium and temperature difference between the two would reach zero during the waiting period. After stable adiabatic thermal environment was achieved, the calorimeter proceeded into the seek mode. During this period, the rate of temperature change was calculated and compared with the predetermined temperature rate sensitivity. If the rate of temperature change, also known as the self-heating rate exceeded the threshold temperature rate sensitivity during the seek period, the calorimeter would proceed into exotherm mode. Otherwise, the heating process would continue to increase the battery temperature with the predetermined temperature increment followed by another waiting and searching sessions. The HWS procedure was repeated according to the test programme until the self-heating rate reached the threshold temperature rate sensitivity or the test programme was terminated as the end temperature was reached. The cooling system was subsequently activated upon completion of the test programme.

The summary of the test procedures is illustrated in Figure 5.8. The setup for test initialisation is summarised in Table 5.5. The details of the test programme and battery conditions are given in Table 5.6.

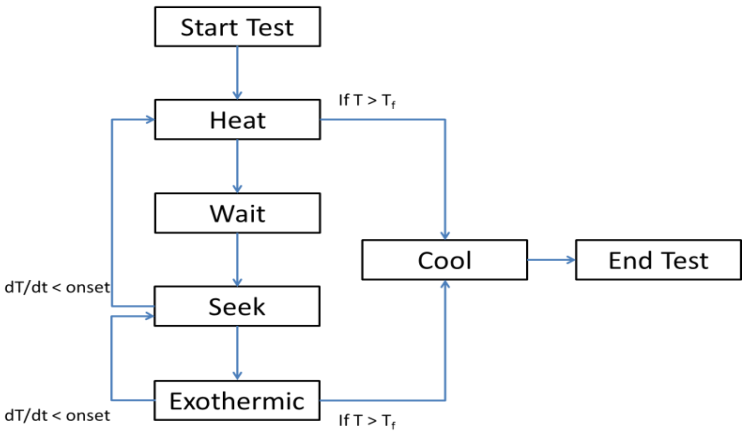

Figure 5.8: Algorithm of the ARC operation under Heat-Wait-Search mode.

Table 5.5: ARC setting.

Start Temperature (^{o}C)	50
End Temperature (^{o}C)	315
Temperature Step (^{o}C)	5
Temperature Rate Sensitivity (^{o}C/minute)	0.02
Waiting Time (Minute)	60
Driver Heater Power (%)	20

Table 5.6: ARC test experimental conditions.

Test	**Description**	**State of charge (%)**	**Number of battery**	**Total capacity (Ah)**	**Total voltage (V)**	**Total mass (g)**
1	Full-charged single cell	100	1	2.50	4.18	48
2	Two unconnected full-charged cells	100	2	2.50	4.23	96
3	Half-charged single cell	50	1	1.25	3.69	48
4	Zero-charged single cell	0	1	0	3.23	48

5.2.4 Experimental Characterisation of Impact-Induced Battery Thermal Runaway

This work aims to characterise thermal runaway initiated by impact induction method at ambient temperature. The effect of heat transfer in promoting thermal runaway propagation in a battery module with a 3x3-matrix configuration was investigated.

5.2.4.1 Experimental Rig

In this destructive test, high tensile rod is used to indent through the battery positive terminal where the safety vent is located. The intrusion of the rod into the battery canister causes both electrodes to collide with each other and consequently induces internal short-circuit. The schematic of the experimental rig for the impact tests is shown in Figure 5.9.

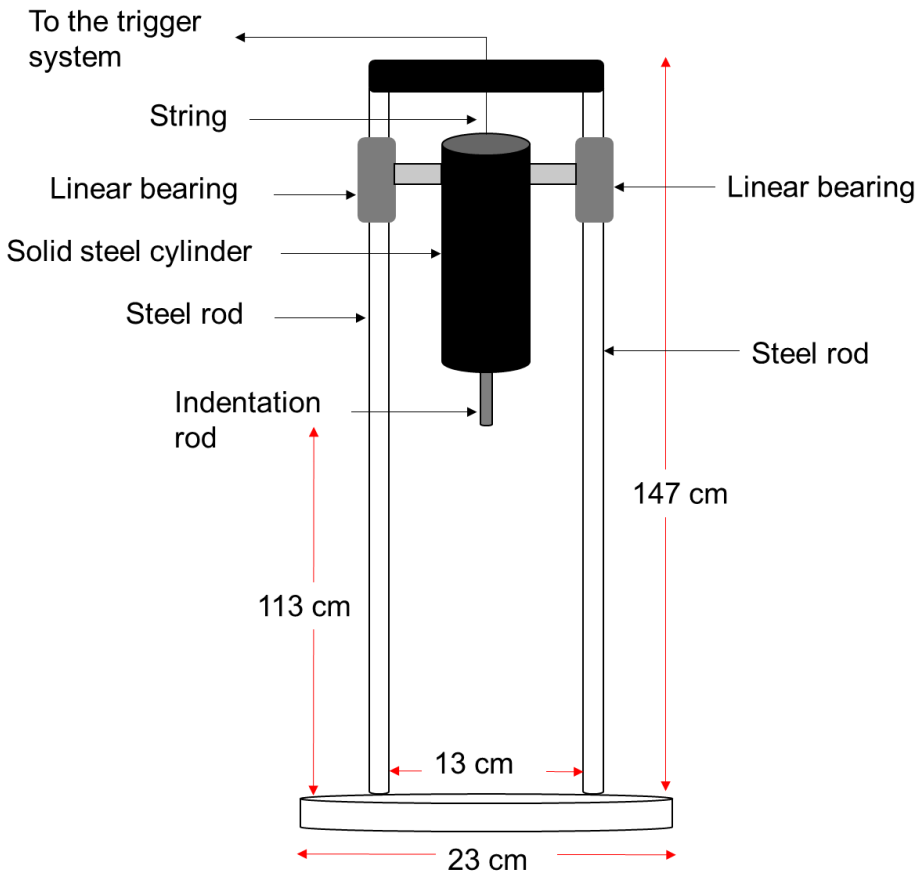

Figure 5.9: Schematic of the impact test experimental setup.

The high tensile rod for the indentation is 28 mm long with 4 mm diameter, produced by turning a high tensile grade 8.8 stainless steel bolt with an initial diameter of 5 mm in a lathe machine. The cylinder where the rod is mounted has a diameter of 51 mm and a length of 200 mm, made from mild steel. The steel cylinder is welded to two linear motion bearings that are installed to two steel rods, suspended at a high position by a string in the hook on top of the cylinder. As the trigger string is pulled, the heavy cylinder will slide off the steel rods and indent the battery with the mounted rod, triggering a short-circuit.

Sample Assembly

Tested batteries are held in place and gripped together with two adjustable steel fixtures to form the 3x3-matrix assembly. The battery assembly is further secured on a base made from Macor, a machinable thermal resistant glass-ceramic and bolted on the experimental rig base, as shown in Figure 5.10.

Since the steel fixtures and the sample base are designed to grip 9 identical cylindrical batteries, the single battery sample is assembled by positioning the battery in the middle of the 3x3-matrix and surrounded with hollow steel cylinders with identical dimensions to provide the necessary grip in the steel fixtures and Macor base. During the pack test, all hollow steel cylinders are replaced with batteries.

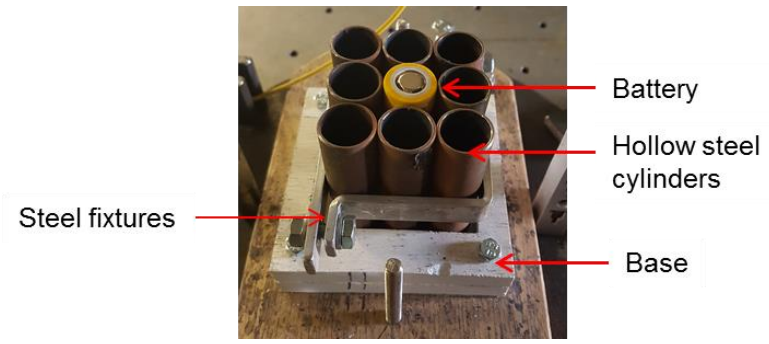

Figure 5.10: The assembly for destructive impact test of single battery.

Temperature Measurement

All temperature measurements were conducted by using type-K Inconel sheathed thermocouples. The data was recorded at a frequency of 1 Hz with a resolution of ± 0.001 ^{o}C by using Microlink 751 data logging interface and Windmill data acquisition software. The thermocouples were placed at the interstitial spaces in the 3x3-matrix assembly to avoid from obstructing the indentation during impact.

The coordinate of the thermocouples for single battery test is given in Table 5.7 and illustrated in Figure 5.11. For the battery pack test, the coordinate of the thermocouples is given in Table 5.8 and illustrated in Figure 5.12. Note that the letter 'D' in the aforementioned tables and figures represents battery diameter.

Table 5.7: Coordinate of thermocouples for single battery test.

Thermocouple	**Position**
T1	(2D, D)
T2	(D,D)
T3	(D, 2D)
T4	(2D, 2D)

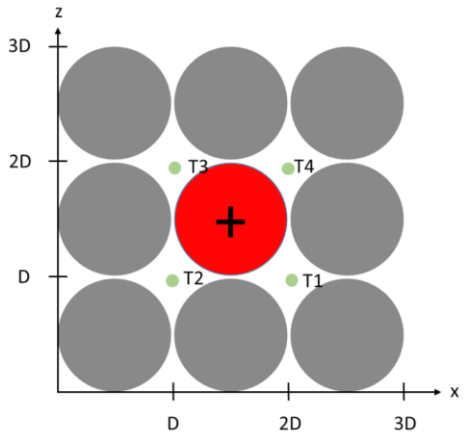

Figure 5.11: Arrangement of thermocouples for the single battery test. The grey circles represent hollow steel cylinders.

Table 5.8: Coordinate of thermocouples for 9-cells test.

Thermocouple	Position
T1	(2D, D)
T2	(D,D)
T3	(D, 2D)
T4	(2D, 2D)
T5	(0, D)
T6	(0, 2D)

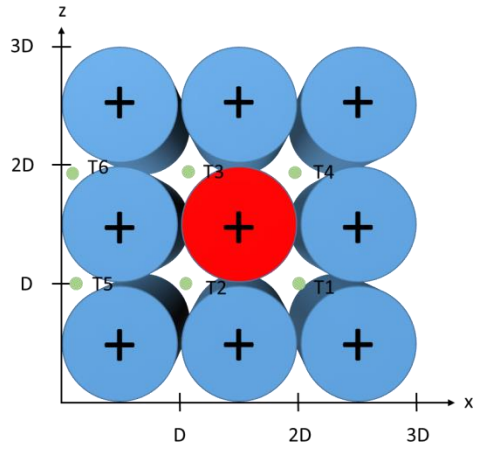

Figure 5.12: Arrangement of thermocouples for the 9-cells battery module test. Thermal runaway is induced in the middle battery as marked in red.

Visual Recording

Panasonic AG-AC90 Camcorder was used to record the experimental programme at 50 frames per second.

Thermal Imaging

FLIR SC650 thermal imaging camera was used to measure thermography of the batteries during destructive impact tests at a frequency of 30 Hz.

5.2.4.2 Experimental Procedures

Once the battery assembly is bolted in the test rig and the thermocouples are secured in the intended positions, the trigger string is pulled. Temperature measurement and visual recording are stopped once the flame extinguishes. The details of the test programme and battery conditions for impact tests are given in Table 5.9.

Table 5.9: Destructive impact test experimental conditions.

Test	**Description**	**Number of battery**	**State of charge**	**Capacity (Ah)**	**Voltage**
1	Full-charged single cell	1	100	2.50	4.2
2	Full-charged single cell	1	100	2.50	4.2
3	Nine full-charged cells packed together in a 3x3 matrix assembly	9	100	2.50	4.2

5.3 Results and Discussion

5.3.1 Results of Characterisation of Battery Discharge Curve

The battery voltage during the charge and discharge procedures is shown in Figure 5.13. The cell discharge curve is depicted in Figure 5.14.

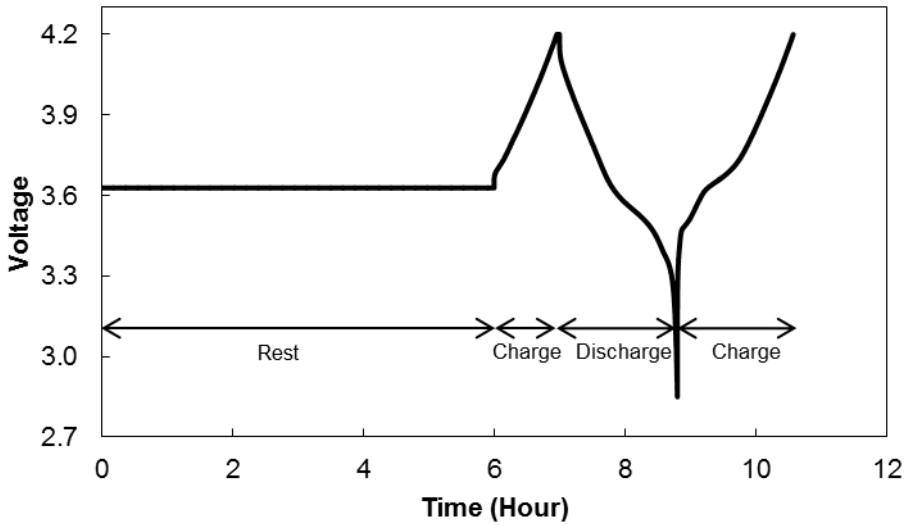

Figure 5.13: Cell voltage at different stages of test procedures.

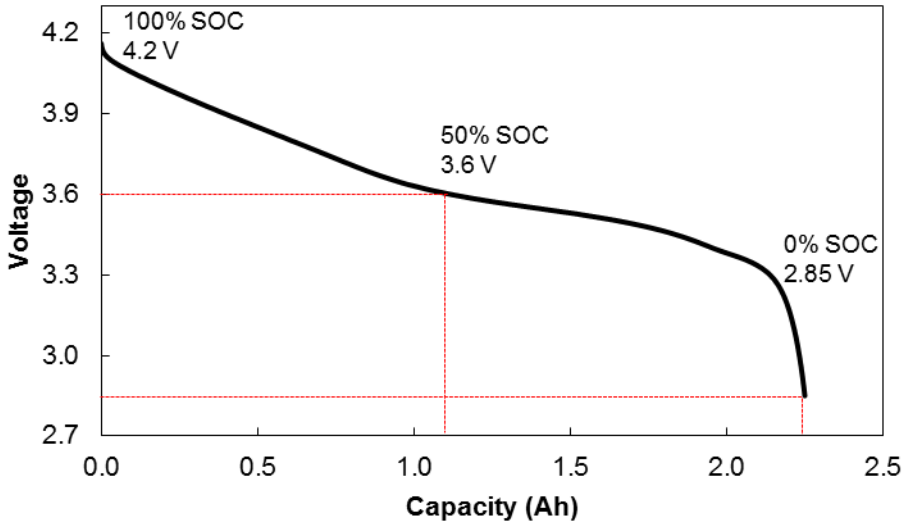

Figure 5.14: Voltage-capacity curve during discharge cycle.

The manufacturer specifies that the battery capacity is 2.5 Ah. In practice, the battery capacity is determined by the C-rate. As previously mentioned in Section 2.2, the C-rate is a measure of the battery capacity discharge rate relative to the battery maximum capacity. 1 C implies that the discharge rate will drain the whole battery capacity in one hour. The deliverable maximum battery capacity is reduced at a higher C-rate.

During the test procedures, the chosen discharge rate was 0.5 C and the corresponding discharge current was 1.25 A. The result indicated that at a constant discharge current of 1.25 A, the cell recorded a total capacity of 2.3 Ah and the battery completed each charge and discharge cycles in 2.2 hours. The measured capacity appears to be consistent with the manufacturer specification. In practise, there is some deviation between the rated capacity and the actual capacity, despite being produced by the same manufacturer with the identical battery chemistry. In the subsequent sections in the thesis, it is assumed that the capacity of the battery is similar to the manufacturer specification.

The change in the battery voltage as the battery is being discharged is depicted in Figure 5.14. The battery exhibited a slow voltage drop during the initial discharge process, the decrement was getting slower in the middle before exhibited a sharp drop to completely discharged state at the end of the cycle.

From the discharge curve, it can be established that for a discharge rate of 0.5 C, full capacity or 100% SOC is achieved at 4.2 V, half capacity or 50% SOC is achieved at 3.6 V and zero capacity or 0% SOC is achieved at 2.85 V.

In preparing the batteries for the energetic tests, the established guideline was used. Slight variation in the voltage value is acceptable since precise control of the charge and discharge processes using consumer charger is difficult. In addition, the current and the corresponding discharge rate used were different.

5.3.2 Results of Battery Thermal Runaway Characterisation Using Oven

5.3.2.1 Results of Oven Test 1 for Full-Charged Single Cell

In this test, thermal runaway of a single battery at 100% SOC was characterised. Under full-charged condition, the capacity and the voltage of the battery were 2.5 Ah and 4.19 V respectively. The findings are shown in Figure 5.15.

The oven air reached the preset temperature of 190 ^{o}C after 53 minutes and subsequently increased to and remained at 195 ^{o}C thereafter. The presence of the steel cylinder and ceramic pots around the battery provided a significant heat transfer resistance for battery heating. The rise of battery temperature inside the ceramic pot was delayed by 74 minutes and reached 182 ^{o}C after 127 minute. This situation was subsequently followed by a violent thermal runaway, instigating battery temperature inside the ceramic pots to spike to 738 ^{o}C. A close-up analysis of temperature measurement around the battery showed that the highest temperature was recorded at the battery central body, indicating that the chemical reactions are the most intense at that particular position.

The intense heat release by battery thermal runaway was also detected outside the steel holder as both thermocouples located outside recorded a soar in temperature to higher than 200 ^{o}C. After the completion of thermal runaway reactions, the temperature of the battery inside the ceramic pots reduced to the oven air temperature and remained unchanged thereafter as the battery subsequently achieved thermal equilibrium with the environment where the rate of heat dissipation is equal to the rate of heat generation or supply.

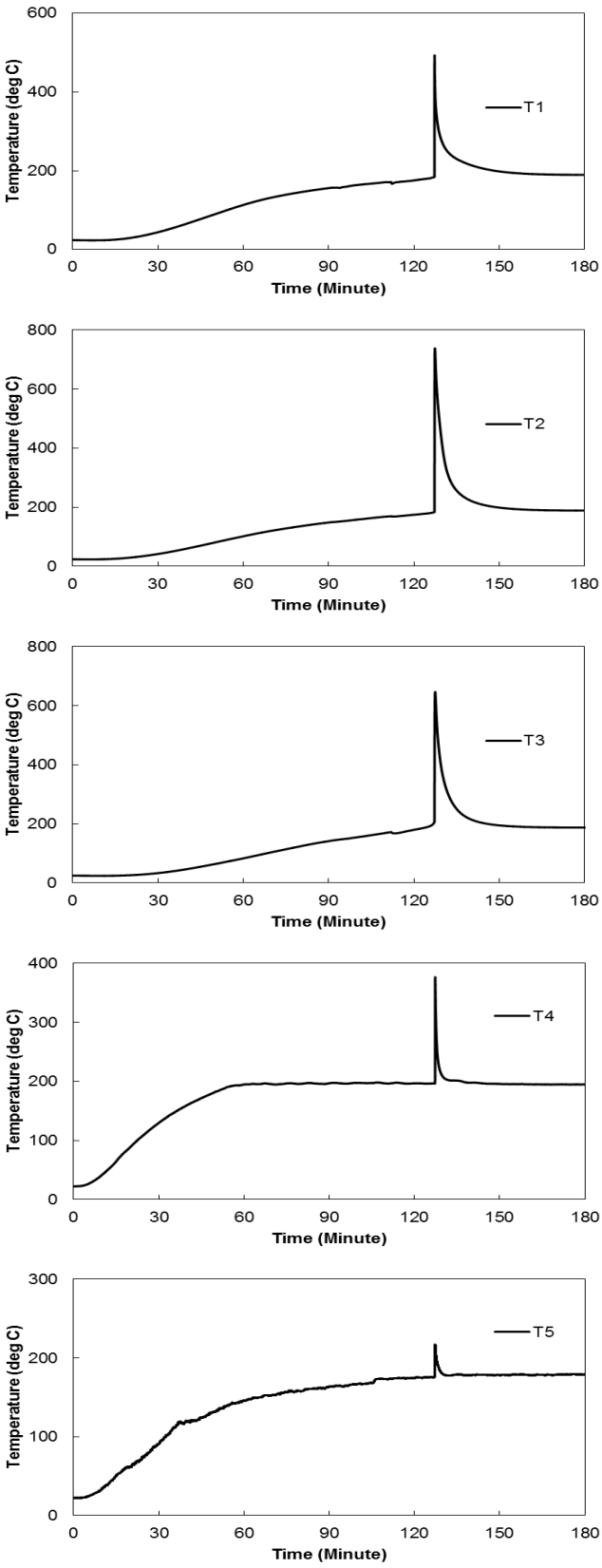

Figure 5.15: Temperature profiles from oven heating of a single full-charged battery.

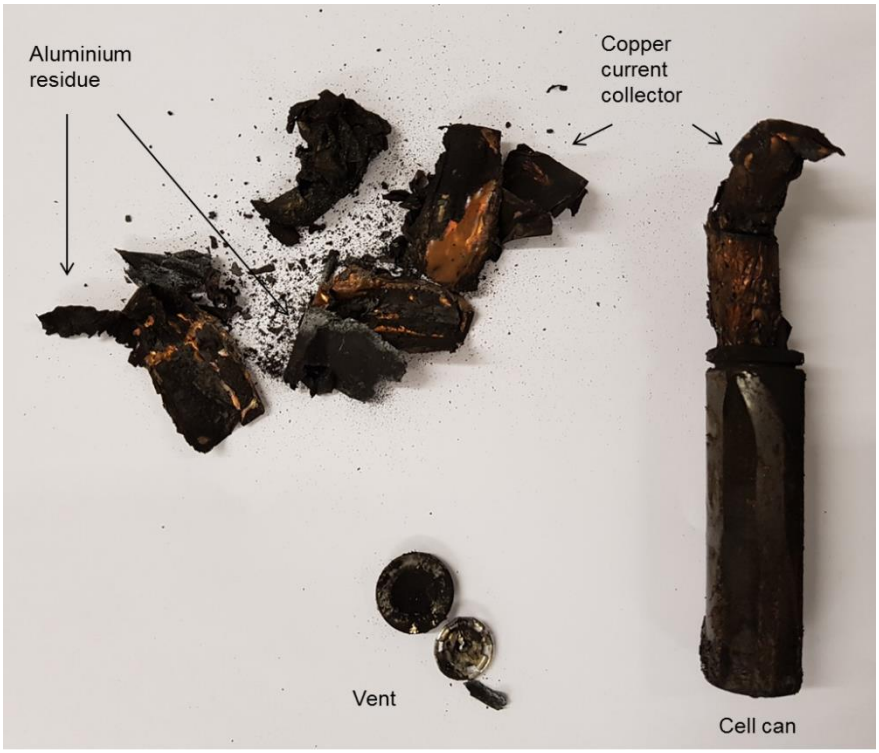

Figure 5.16: Remnant of single full-charged battery after the oven test.

Figure 5.16 shows the aftermath of battery thermal runaway at 100% SOC. From inspection of the residues, it can be seen that the mechanical integrity of the cell canister remained intact. However, safety vent equipped on top of the canister was detached which might be due to violent expulsion of battery contents. The sight of aluminium current collector ash and the presence of unburnt copper current collector in the residues indicated that the battery internal temperature reached a point higher than 659 ^{o}C, which is the aluminium melting temperature but lower than 1083 ^{o}C, which is the copper melting point. Temperature measurement around the battery exterior recorded the highest temperature of 738 ^{o}C, which appears to be consistent with the observation. The high temperature reached destroyed the external wrap covering the canister exterior surface.

5.3.2.2 Results of Oven Test 2 for Two Full-Charged Cells Not Electrically Connected

In this test, thermal runaway of two batteries at 100% SOC was characterised, which was aimed to investigate the effects of doubling the reactant mass. The batteries were fastened together with a steel wire but they are not electrically connected. Under this test condition, the batteries total voltage and capacity remained the same as single battery, which were 4.19 V and 2.5 Ah respectively, only the mass of batteries was doubled to 96 g. The findings are shown in Figure 5.17.

As shown by T1 – T3 in Figure 5.17, the increment of battery temperature is slower in comparison to oven air and sample containment. The presence of multilayer sample containment served as thermal resistance to the batteries and therefore retarded the battery heating process. The catastrophic thermal runaway occurred as the battery temperature reached 183 ^{o}C at 115 minute after the experiment commenced where the temperature spiked to 783 ^{o}C. Despite the multilayer sample containment, the abrupt heat release during thermal runaway can be detected outside the containment as a surge in temperature was recorded in T4 and T5. All temperature readings subsequently reduced to and remained at the oven preset temperature after the completion of thermal runaway reactions.

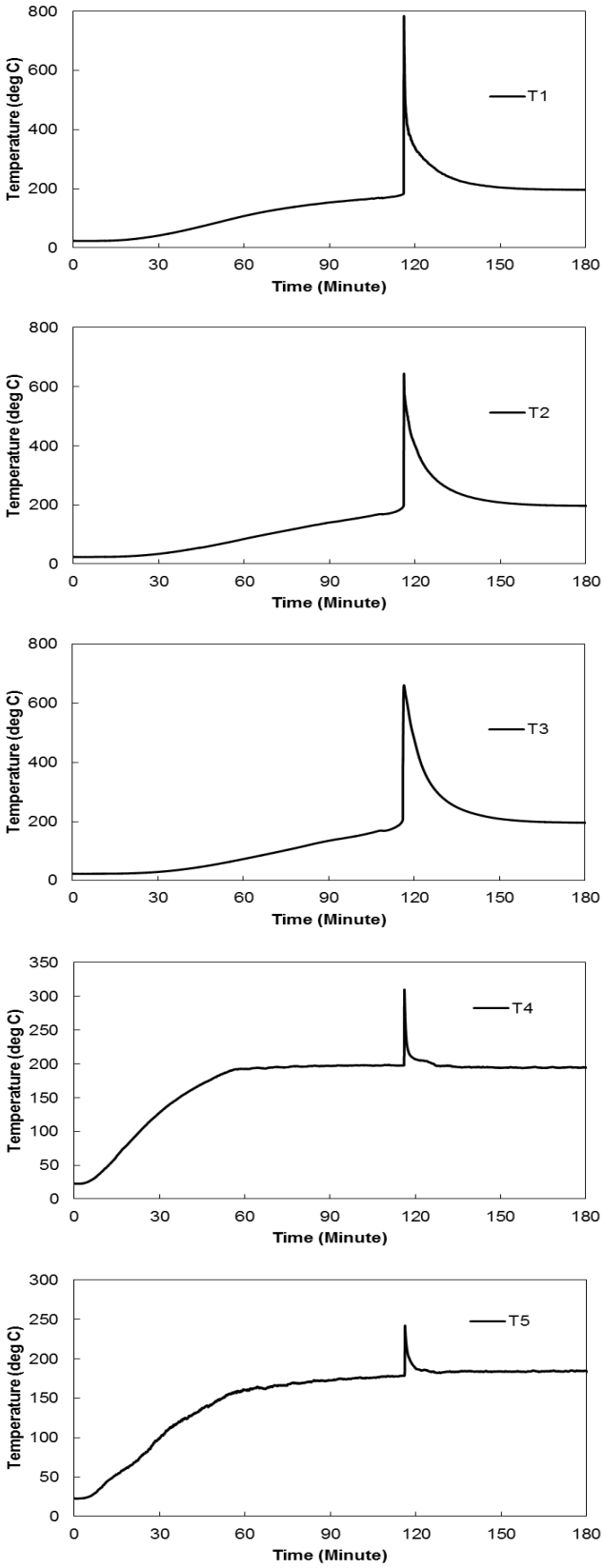

Figure 5.17: Temperature profiles from oven heating of two unconnected full-charged batteries.

Figure 5.18: Aftermath of two-cell thermal runaway.

Figure 5.18 shows thermal runaway aftermath of two full-charged batteries. It can be seen that the mechanical integrity of the cell canister remained intact. No disintegration of any of battery components that made the unit cell was detected. The presence of fine black powders, which might be carbon ashes or cobalt powders that were vented out through the safety vent was observed with no expulsion of battery contents such as jellyroll.

5.3.2.3 Results of Oven Test 3 for Two Full-Charged Cells Connected in Parallel

In this test, thermal runaway of two batteries at 100% SOC was characterised, which was aimed to investigate the effects of doubling the reactant mass and electrical capacity. Nickel strips were used to connect the battery terminals and form the intended parallel electrical connection. Under this test condition, the total voltage remained the same as single cell, which was 4.23 V, but the capacity and mass were doubled to 5.0 Ah and 96 g respectively. The outcomes of the test are shown in Figure 5.19.

The thermocouple used to measure the temperature at point T1, which is around battery positive terminal was damaged during the test. Hence, the reading was left out. In general, the same qualitative features can be observed in the temperature development. Thermal runaway was induced in the battery after 107 minute of heating process. At that juncture, the temperature around the negative terminal surged to 420 ^{o}C from 173 ^{o}C, while the battery central body recorded a rapid increment from 197 ^{o}C up to 756 ^{o}C.

The presence of multilayer sample containment was not able to prevent the thermocouples outside the sample containment from detecting the massive heat release during thermal runaway. After the completion of thermal runaway reactions, the temperature of the battery inside the ceramic pots reduced to the oven air temperature and remained unchanged thereafter.

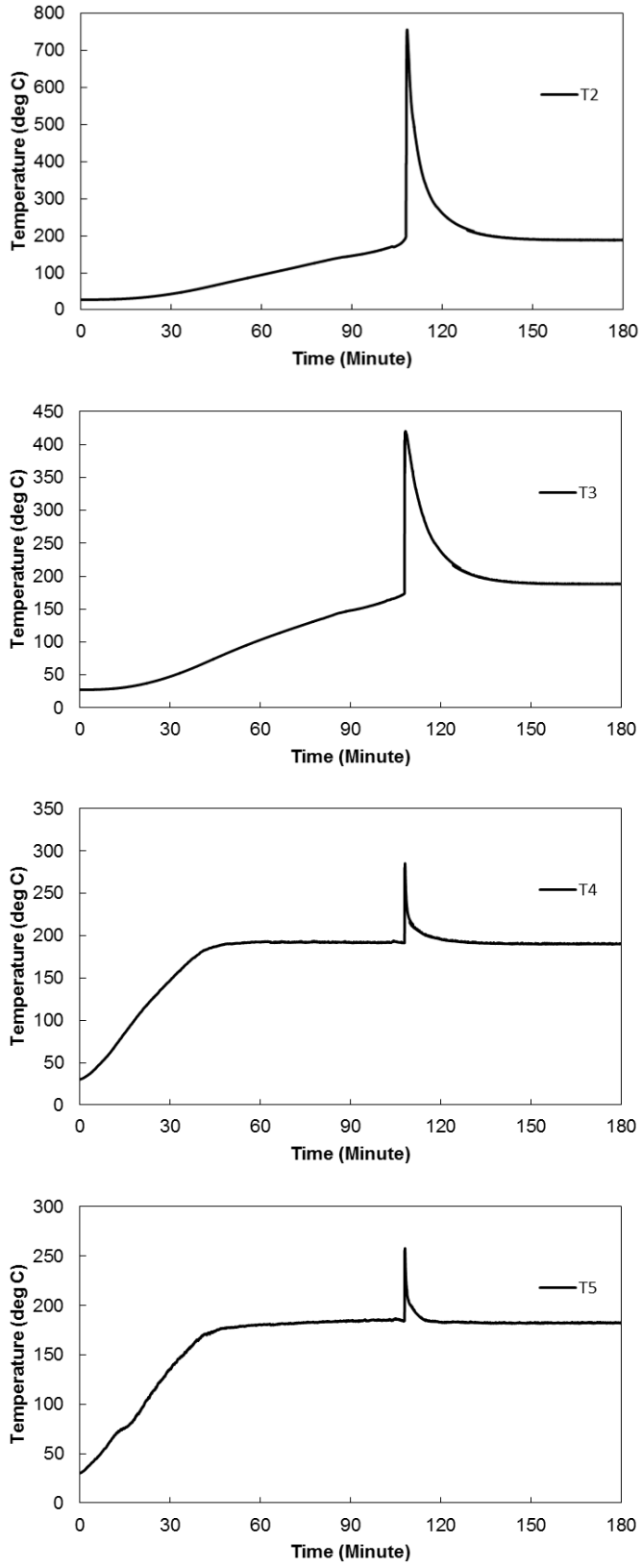

Figure 5.19: Temperature profiles from oven heating of two full-charged batteries connected in parallel.

Figure 5.20: Aftermath of thermal runaway of two full-charged batteries connected in parallel.

Figure 5.20 shows the aftermath of two full-charged batteries thermal runaway. Black powder that heavily stained the battery canisters was observed, which might be carbon ashes or cobalt powders that vented out during thermal runaway. Violent venting of the battery contents during thermal runaway caused the nickel strip at the positive terminals to break into two parts and disconnected the batteries while maintaining the adhesion on the surface of the terminals. On the other hand, no significant deformation was observed at the nickel strip at the battery negative terminals. The mechanical integrity of the batteries remained intact and no disintegration of any of battery components that made the unit cell was detected.

5.3.2.4 Results of Oven Test 4 for Half-Charged Single Cell

In this test, thermal runaway of a single battery at 50% SOC was characterised. Under half-charged condition, the battery has a capacity and a voltage of 1.25 Ah and 3.74 V respectively. The findings are presented in Figure 5.21.

After approximately six hours of heating, no thermal runaway was observed. Quick temperature drops were recorded inside the ceramic pot at 90 to 110 minutes, which was caused by gradual gas venting that entailed cooling effect due to the Joule-Thompson effect. At half-charge, the exothermic reactions that involved in thermal runaway took place at a slow rate. The slow heat release caused the battery temperature to overshoot the oven air temperature at 250 minute for a prolonged period, which led to the presence of thermal hump. A close look into the thermal hump is given in Figure 5.22. The temperature overshoot was too small to cause temperature increment in the oven air and steel holder base.

Figure 5.23 shows the aftermath of half-charged cell after the oven test. Apart than minor fragments that were collected from the cell holder, no ejection of battery contents was observed. High oven chamber temperature caused the canister wrap to melt and smudged the battery surface.

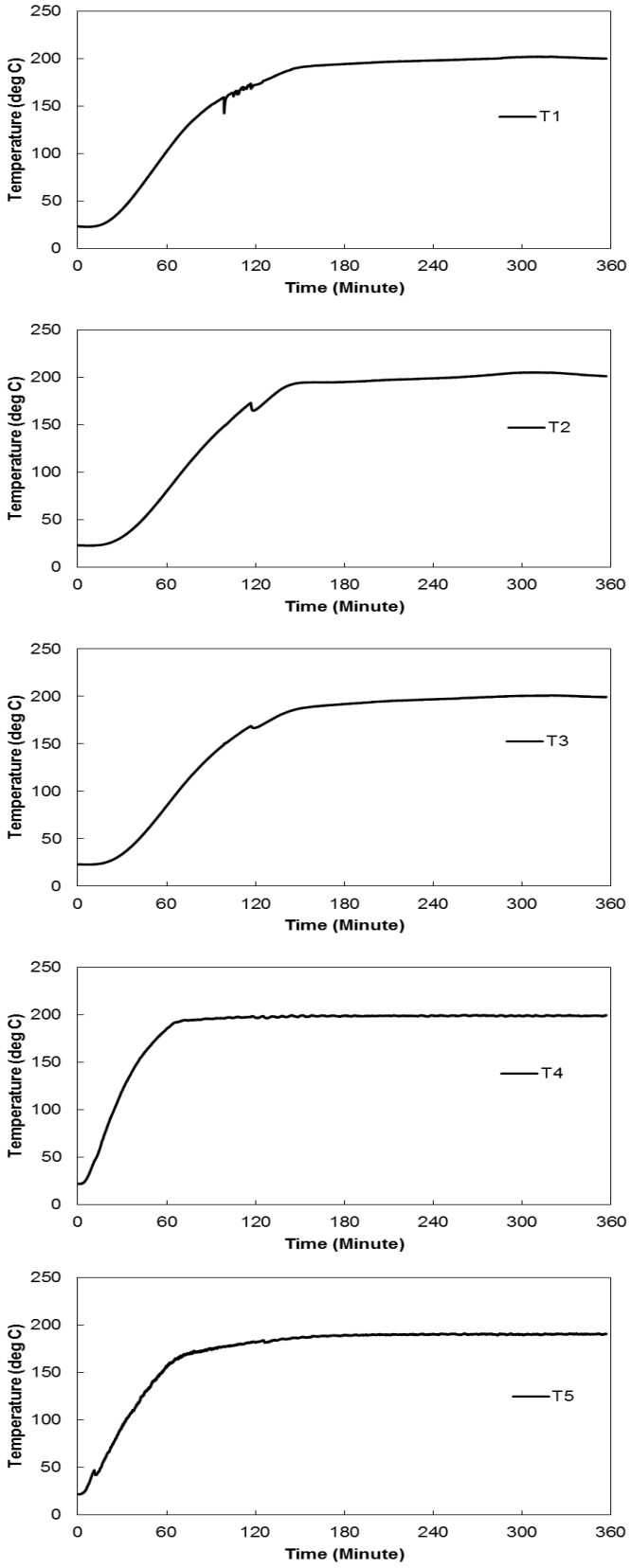

Figure 5.21: Temperature profiles from oven heating of single half-charged battery.

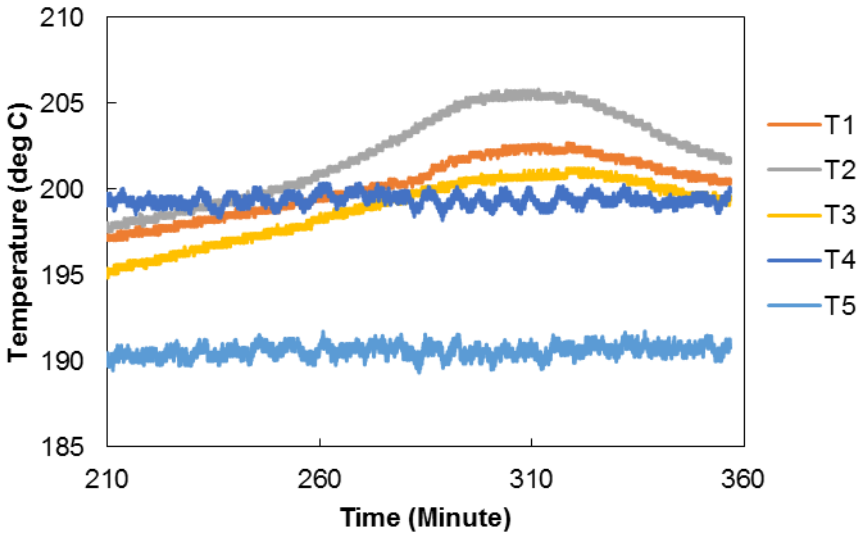

Figure 5.22: Temperature overshoot in the ceramic pots.

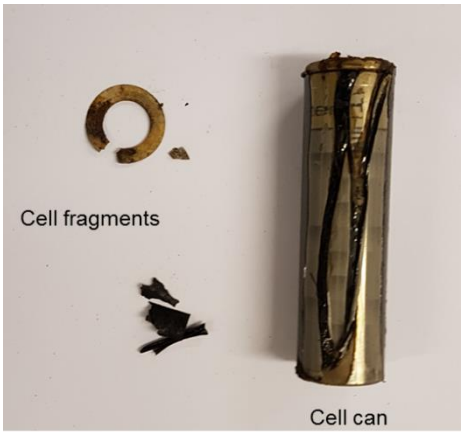

Figure 5.23: Remnant of half-charged battery after the oven test.

5.3.2.5 Results of Oven Test 5 for Zero-Charged Single Cell

In this test, thermal runaway of a single battery at 0% SOC was characterised. Under zero-charged condition, the battery has a capacity and a voltage of 0 Ah and 3.21 V respectively. The aftermath of the oven test is shown in Figure 5.24. The recorded temperatures are presented in Figure 5.25.

Figure 5.24: Remnant of the drained battery after the oven test.

The venting of cell contents as part of the battery integral hazard mitigation caused a temperature drop after 125 minutes. No thermal runaway was observed and the experiment was terminated after no indicators or signs of exothermic reactions were detected. The battery reached and plateaued at the oven air temperature as it reached thermal equilibrium with the oven air temperature. As shown in Figure 5.24, no significant blemish is spotted on the cell external canister.

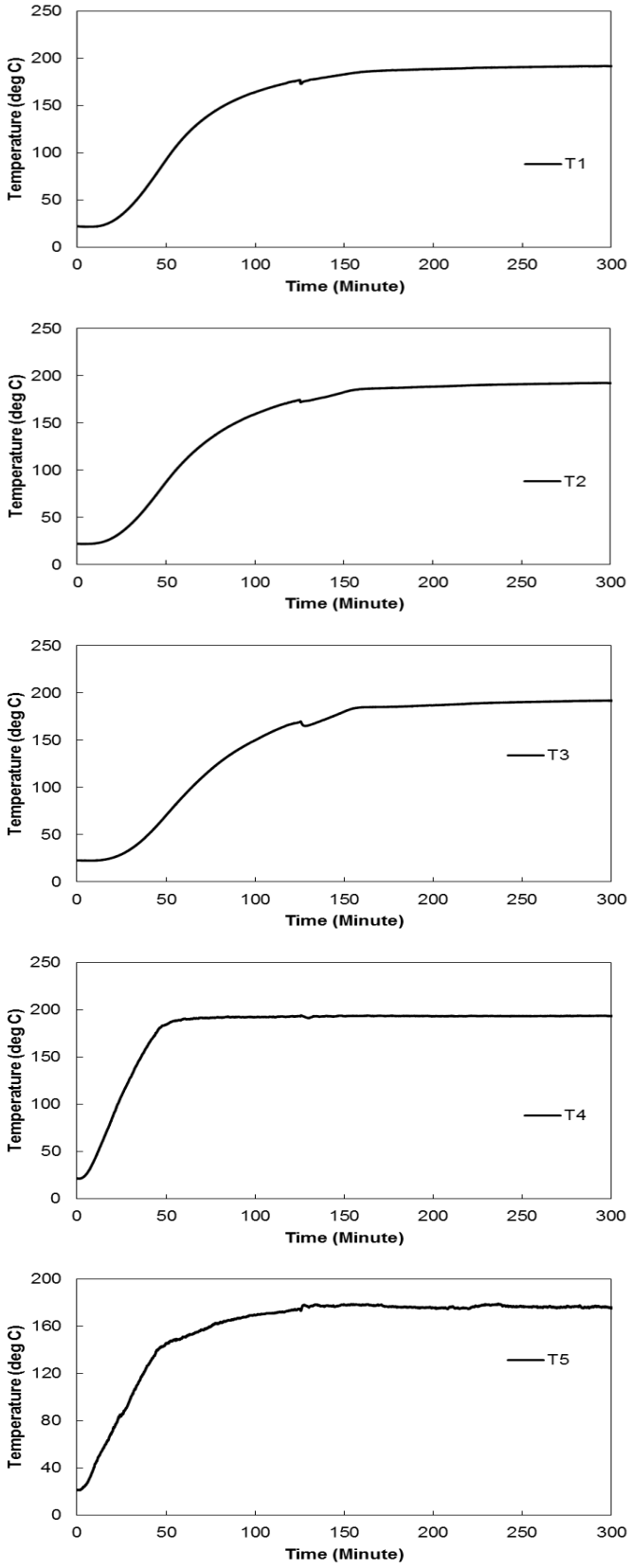

Figure 5.25: Temperature profiles from oven heating of single zero-charged battery.

5.3.3 Results of Battery Thermal Runaway Characterisation Using Accelerating Rate Calorimeter (ARC)

5.3.3.1 Results of ARC Test 1 for Single Full-Charged Cell

In this test, thermal runaway of a single battery at 100% SOC was characterised using ARC. Under full-charged condition, the capacity and the voltage of the battery were 2.5 Ah and 4.18 V respectively. Figure 5.26 presents the battery temperature during the ARC test. The associated self-heating rate is depicted in Figure 5.27. The key findings are summarised in Table 5.10.

Table 5.10: Thermal runaway characteristics of single full-charged battery from ARC test.

Exotherm onset temperature (^{o}C)	81.666
Exotherm onset time (Minute)	712.001
Thermal runaway temperature (^{o}C)	163.070
Thermal runaway induction time (Minute)	2046.893
Maximum temperature (^{o}C)	428.533
Maximum self-heating rate (^{o}C/min)	8677.259

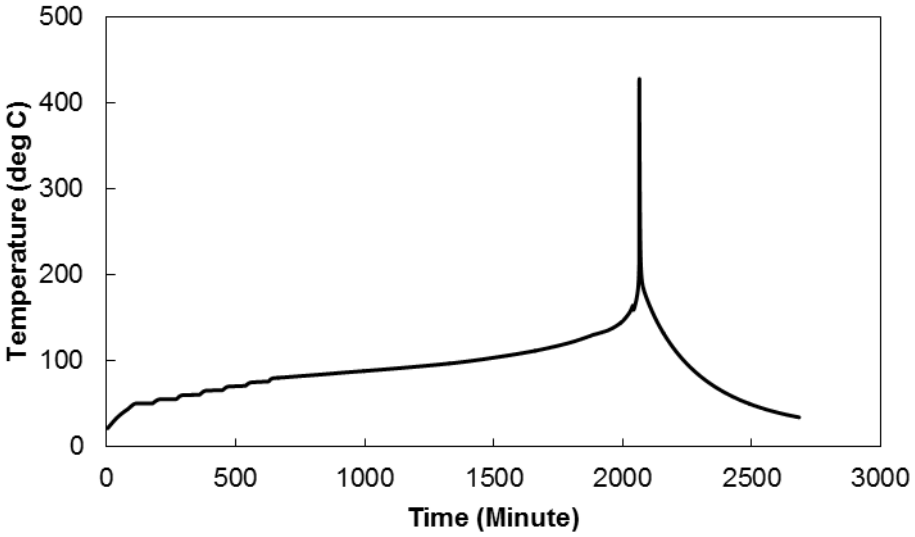

Figure 5.26: Temperature of single full-charged battery from ARC test.

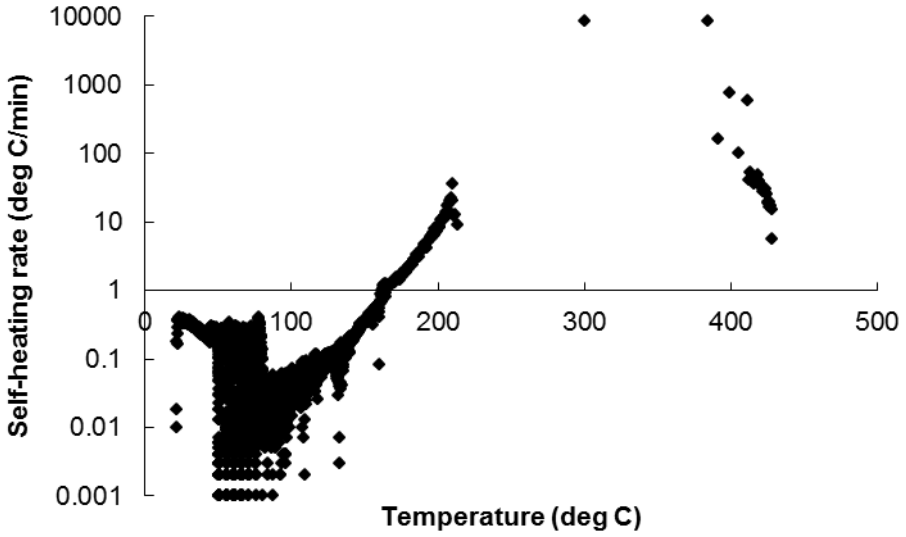

Figure 5.27: Self-heating rate of single full-charged battery from ARC test.

5.3.3.2 Results of ARC Test 2 for Two Full-Charged Cells

In this test, thermal runaway of two batteries at 100% SOC was characterised using ARC, which was aimed to investigate the effects of doubling the reactant mass. The batteries were fastened together with a fibre glass tape and there was no electrical connection present. Under this test condition, the batteries total voltage and capacity remained the same as single battery, which were 4.23 V and 2.5 Ah respectively, only the mass of batteries was doubled to 96 g. The recorded temperature is presented in Figure 5.28. The associated self-heating rate is depicted in Figure 5.29. The key findings are summarised in Table 5.11.

Table 5.11: Thermal runaway characteristics of two full-charged batteries from ARC test.

Exotherm onset temperature (^{o}C)	76.552
Exotherm onset time (Minute)	669.521
Thermal runaway temperature (^{o}C)	134.116
Thermal runaway induction time (Minute)	1752.027
Maximum temperature (^{o}C)	522.204
Maximum self-heating rate (^{o}C/min)	1795.02

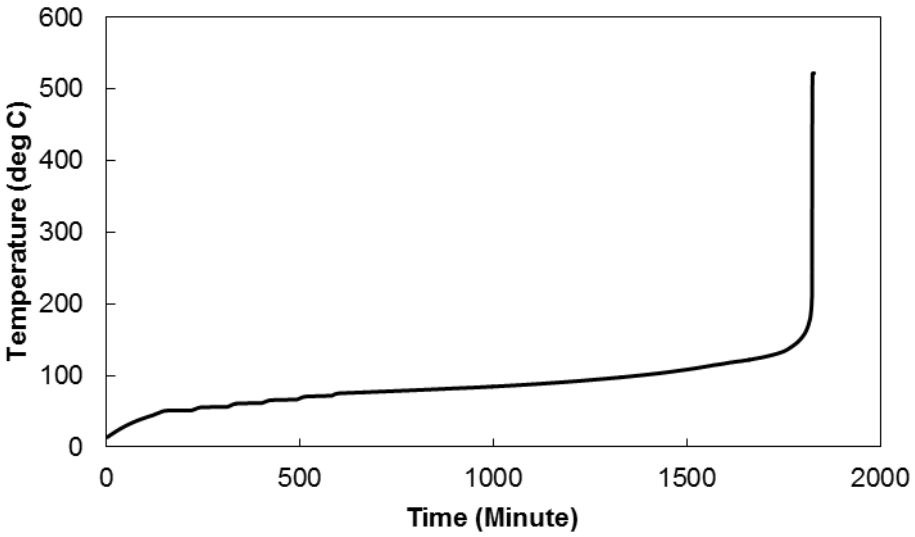

Figure 5.28: Temperature of two full-charged batteries from ARC test.

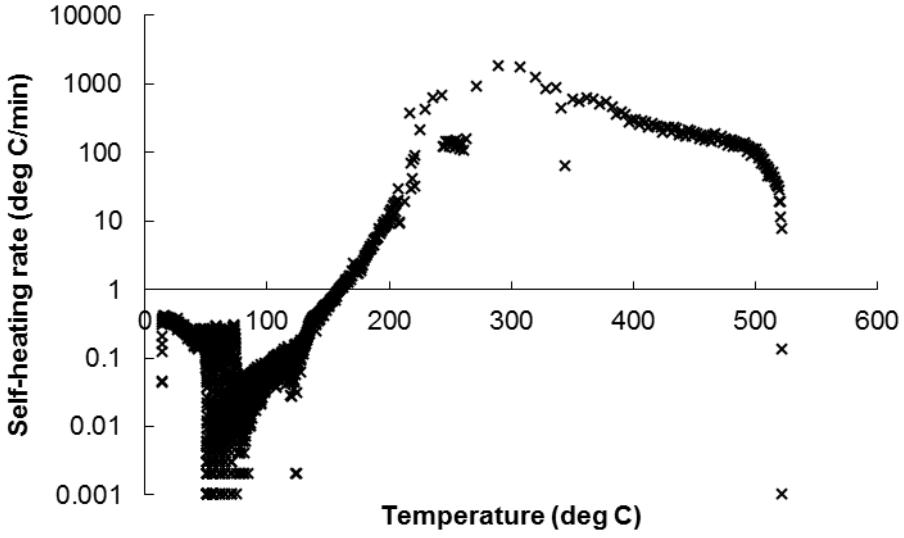

Figure 5.29: Self-heating rate of two full-charged batteries from ARC test.

5.3.3.3 Results of ARC Test 3 for Single Half-Charged Cell

In this test, thermal runaway of a single battery at 50% SOC was characterised. Under half-charged condition, the battery has a capacity and a voltage of 1.25 Ah and 3.69 V respectively. The recorded temperature is presented in Figure 5.30. The associated self-heating rate is depicted in Figure 5.31. The key findings are summarised in Table 5.12.

Table 5.12: Thermal runaway characteristics of single half-charged battery from ARC test.

Exotherm onset temperature (^{o}C)	101.534
Exotherm onset time (Minute)	1099.505
Thermal runaway temperature (^{o}C)	207.033
Thermal runaway induction time (Minute)	2507.342
Maximum temperature (^{o}C)	404.662
Maximum self-heating rate (^{o}C/min)	3189.066

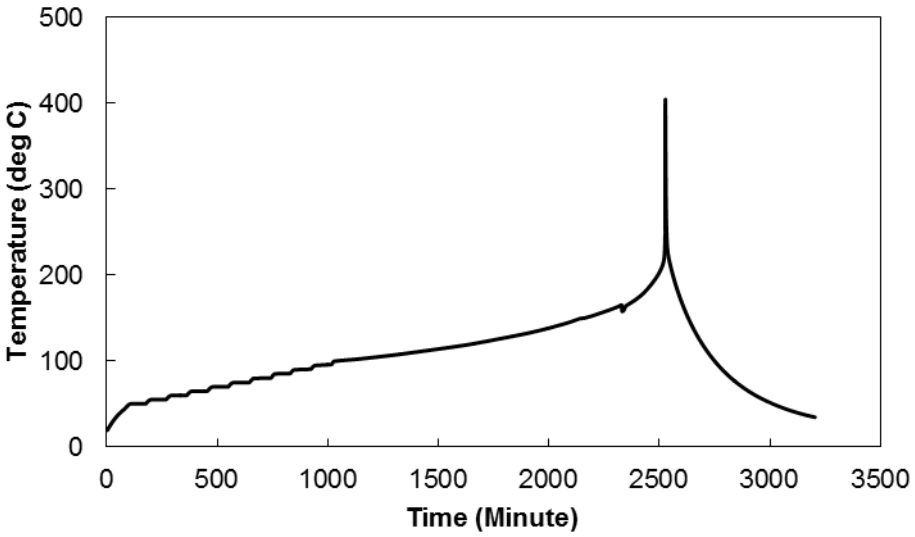

Figure 5.30: Temperature of single half-charged battery from ARC test.

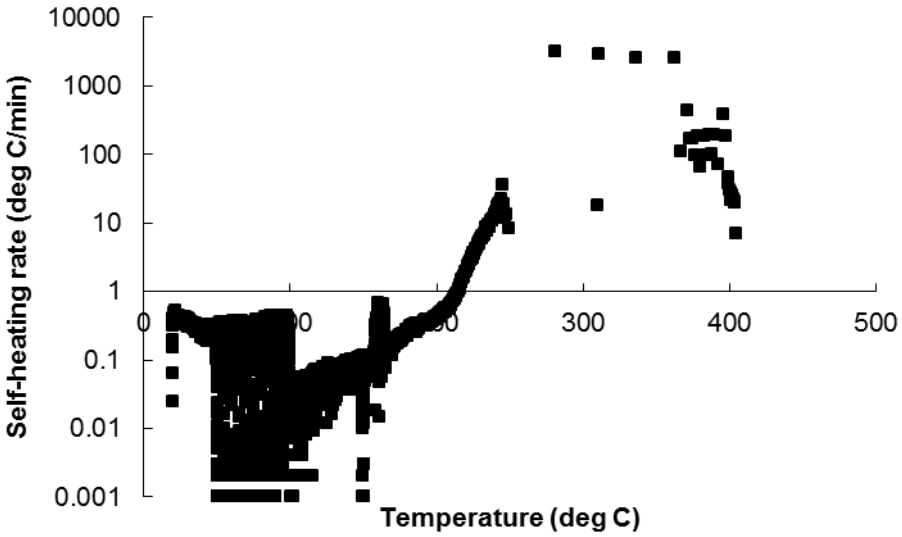

Figure 5.31: Self-heating rate of single half-charged battery from ARC test.

5.3.3.4 Results of ARC Test 4 for Single Zero-Charged Cell

In this test, thermal runaway of a single battery at 0% SOC was characterised using ARC. Under zero-charged condition, the battery has a capacity and a voltage of 0 Ah and 3.23 V respectively. The recorded temperature is presented in Figure 5.32. The associated self-heating rate is depicted in Figure 5.33. The key findings are summarised in Table 5.13.

Table 5.13: Thermal runaway characteristics of single zero-charged battery from ARC test.

Exotherm onset temperature (^{o}C)	91.377
Exotherm onset time (Minute)	827.001
Thermal runaway temperature (^{o}C)	Not observed
Thermal runaway induction time (Minute)	Not observed
Maximum temperature (^{o}C)	315.084
Maximum self-heating rate (^{o}C/min)	0.696

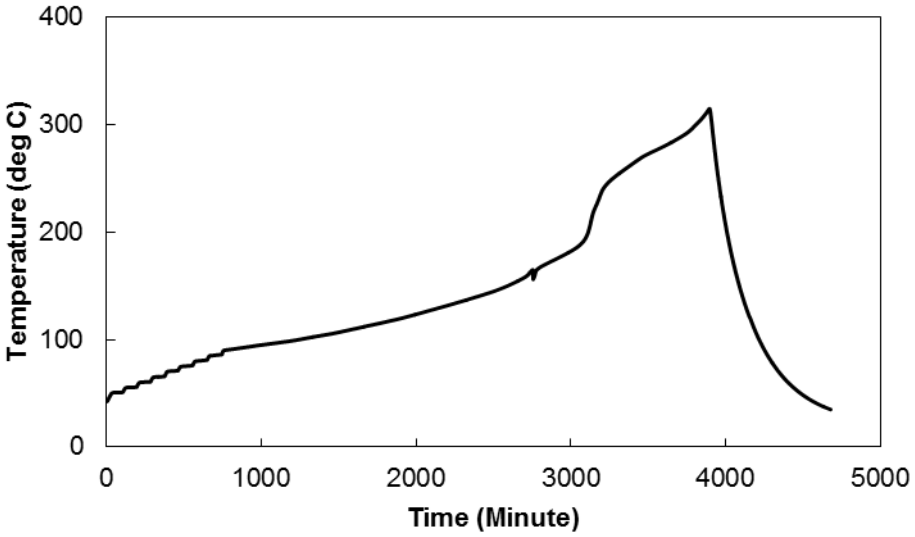

Figure 5.32: Temperature of single zero-charged battery from ARC test.

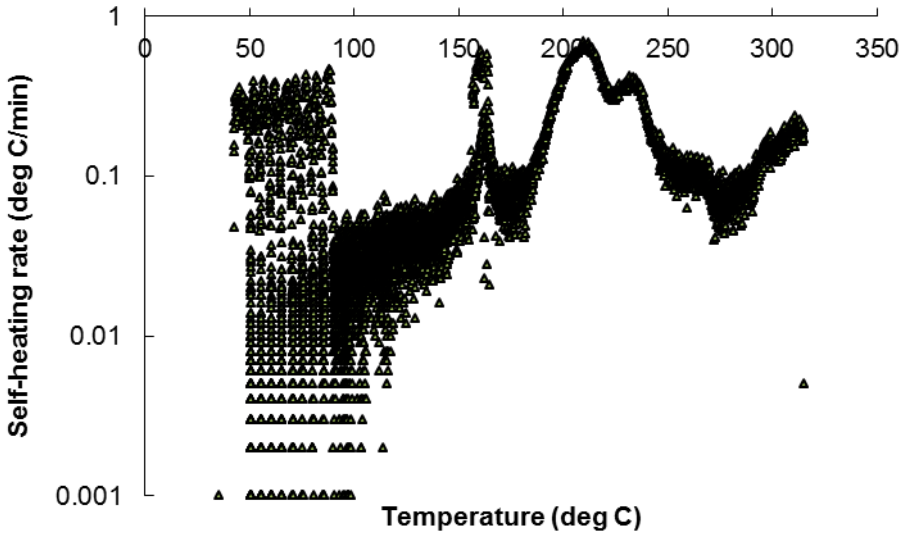

Figure 5.33: Self-heating rate of single zero-charged battery from ARC test.

5.3.4 Results of Impact-Initiated Battery Thermal Runaway

5.3.4.1 Results of Impact Test 1 for Full-Charged Single Cell

The recorded temperature during the impact test on single battery is shown in Figure 5.34. The failure caused by direct impact to the battery positive terminal caused an almost immediate failure. Upon indented by the steel rod, the temperature as recorded by thermocouples increased slightly from room temperature to 34 ^{o}C and appeared to plateau for 9 seconds before surging to 250 ^{o}C. The temperature dropped after completion of thermal runaway reactions.

The impact from the rod indentation was sufficient to damage the battery vent and penetrate through the cell canister. However, the impact was inadequate to force cathode and anode to collide with each other in the canister to cause a massive short-circuit. Boiling electrolyte was observed gushing through the deformed vent after the impact, indicating that heat was generated in the battery. An attempt to move the rod from the deformed battery agitated the battery components and resulted in collision between the electrodes. The heat generated from the massive short-circuit ignited the flammable particles in the battery and produced fire sparks, which was followed by fierce burning of the gases generated. Important events during the fire development are shown in Figure 5.35 – Figure 5.37.

Thermography from the first impact test is shown in Figure 5.38 – 5.39. It is shown that the battery temperature reached 81 ^{o}C prior to the flame eruption. At some point during the test, the flame and the ejected battery content reached 521 ^{o}C.

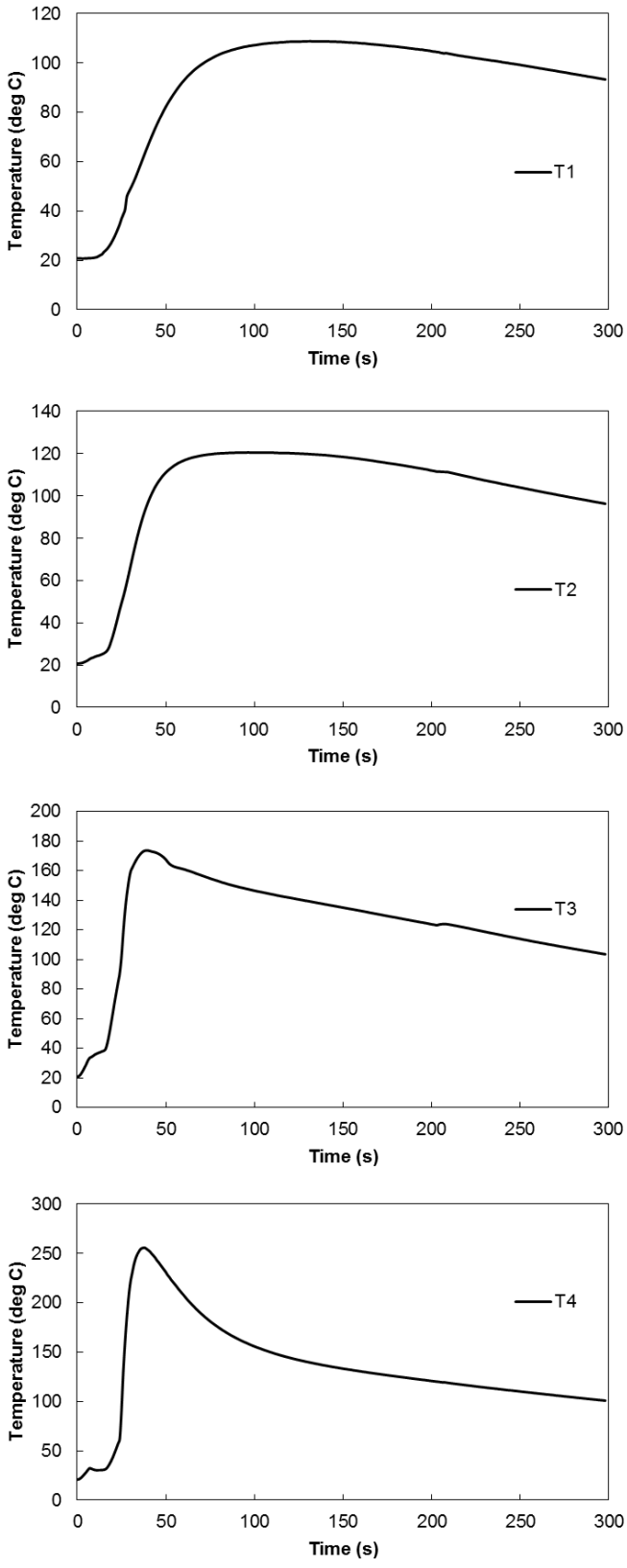

Figure 5.34: Thermocouple measurement during the first impact test.

Figure 5.35: Fire sparks and smoke plume were observed after an attempt was made to dislodge the rod from the indented battery.

Figure 5.36: Fierce burning of the ejected gases.

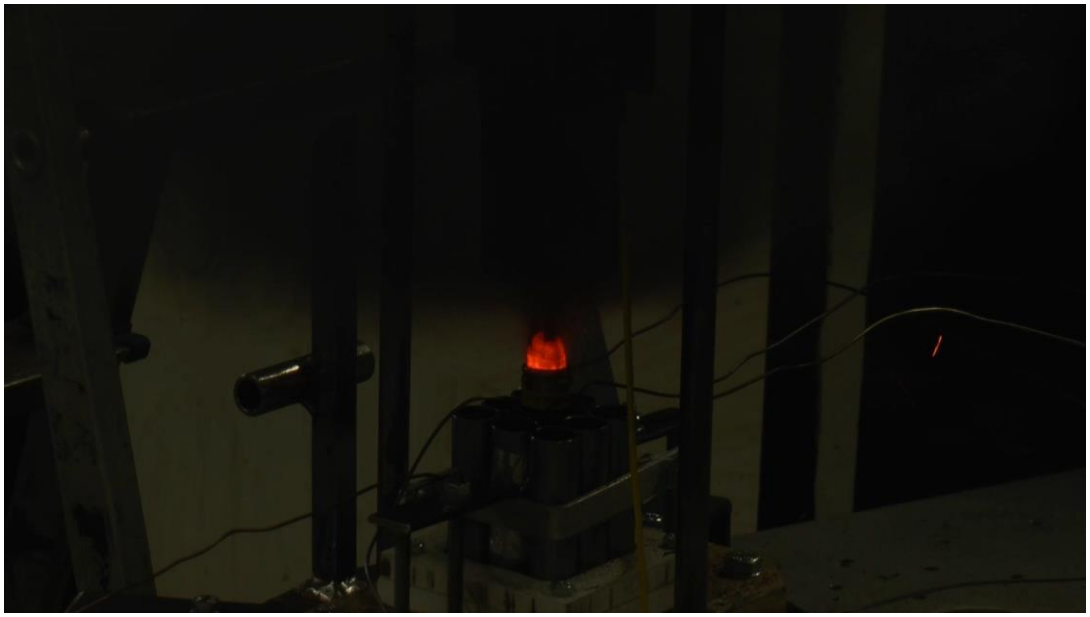

Figure 5.37: Expulsion of hot battery contents and release of smoke in between the flames.

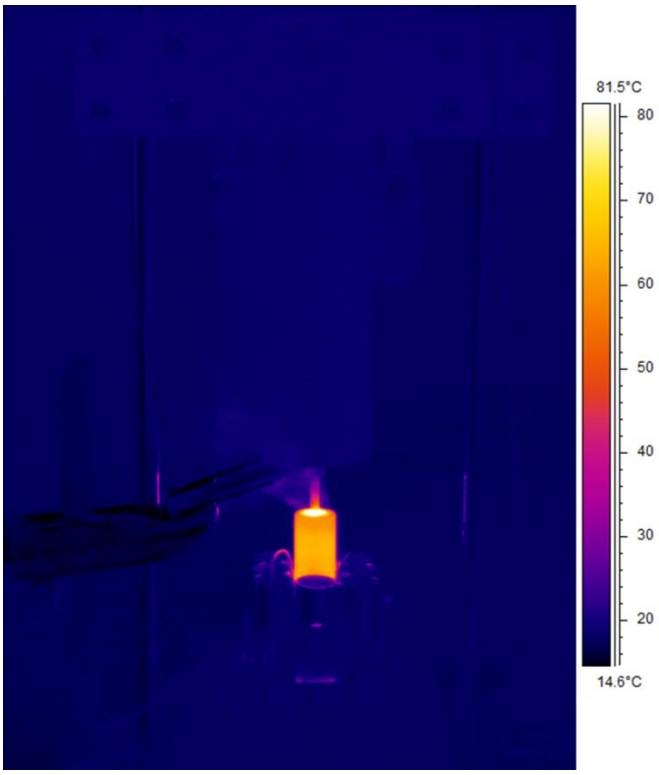

Figure 5.38: Thermography of the battery temperature before flame eruption.

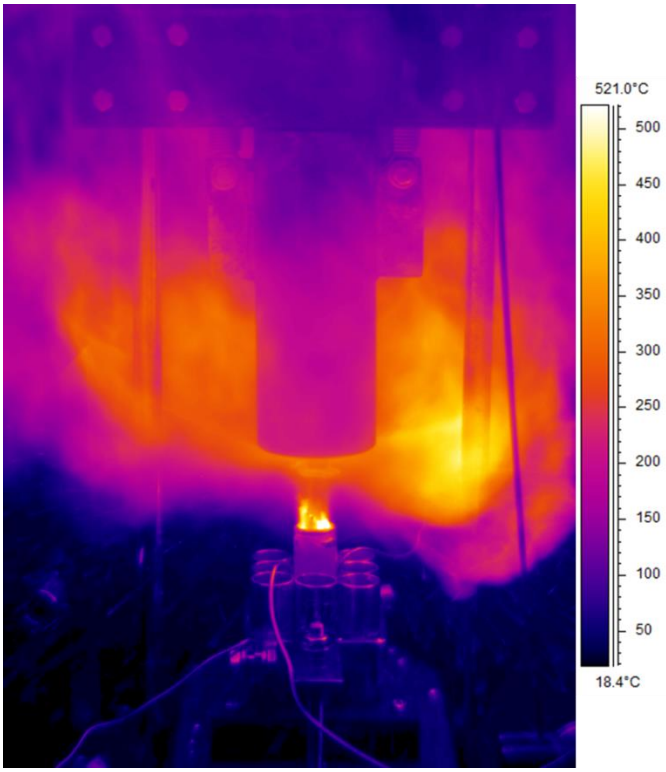

Figure 5.39: Thermography of the flame and ejected battery content temperature in the first impact test.

5.3.4.2 Results of Impact Test 2 for Full-Charged Single Cell

This time, the impact caused an immediate destruction to the battery. The temperature of the ejected battery content and the flames developed in the impact is shown in thermography in Figure 5.40. The temperature as recorded by thermocouples is shown in Figure 5.41.

The impact from the rod indentation was sufficient to damage the battery vent and penetrate through the cell canister. In addition, the impact was adequate to force cathode and anode to collide with each other in the canister and consequently leads to a massive short-circuit. The developments of fire at every second after the impact are shown in Figure 5.42 – Figure 5.46 and summarised in Table 5.14.

Table 5.14: Summary of fire development in the impact test.

Stage	Time after impact (s)	Description
1	1	Smoke plume
2	2	Fire sparks
3	3 – 5	Jet flames
4	6 – 8	Sustained flames
5	9 – 22	Flame weakening – orange flame
6	23 – 29	Flame weakening – blue flame
7	30	Flame extinguish

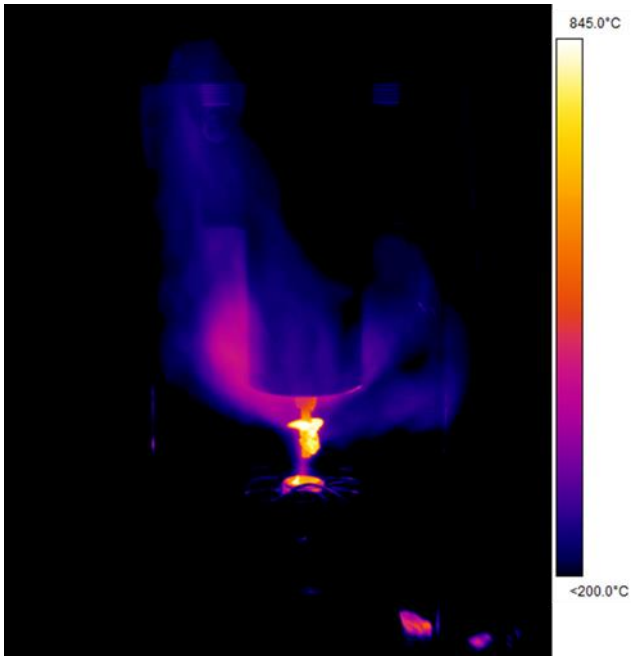

Figure 5.40: Thermography of the ejected battery content and the surrounding flames temperature.

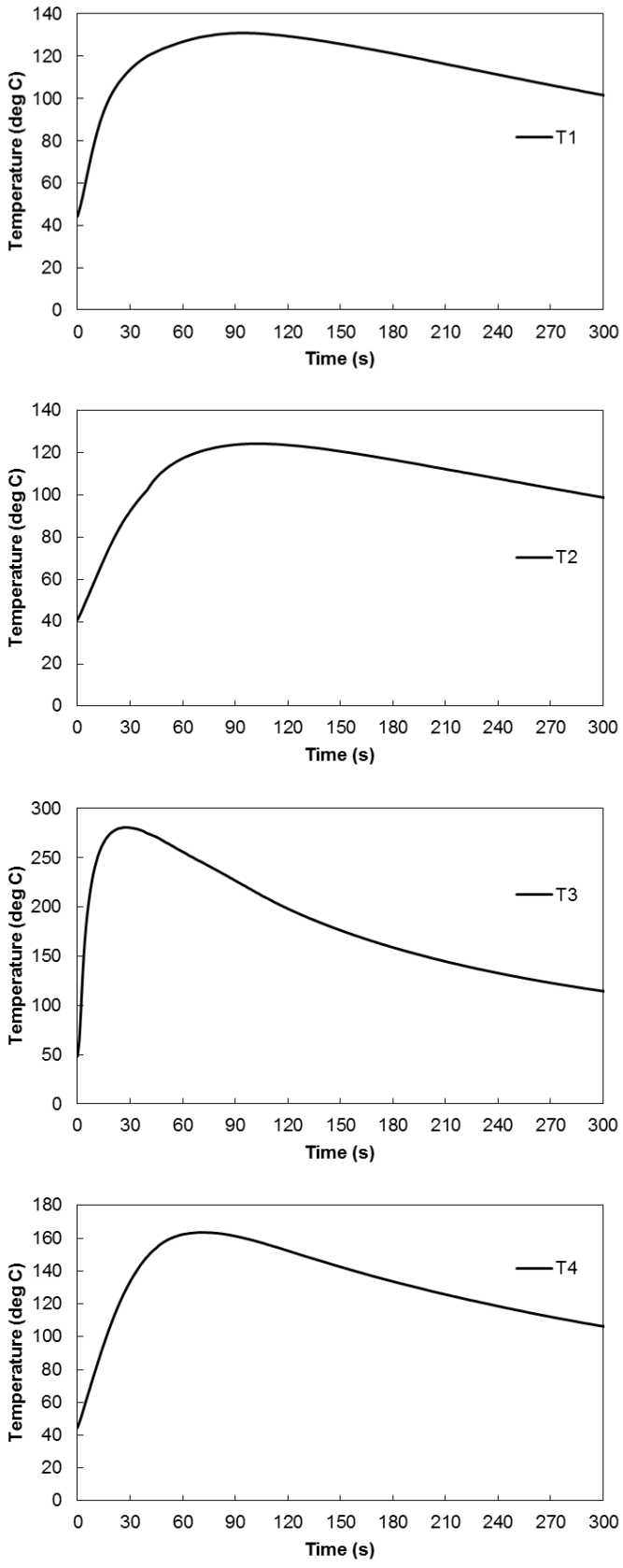

Figure 5.41: Thermocouple measurement during the second impact test.

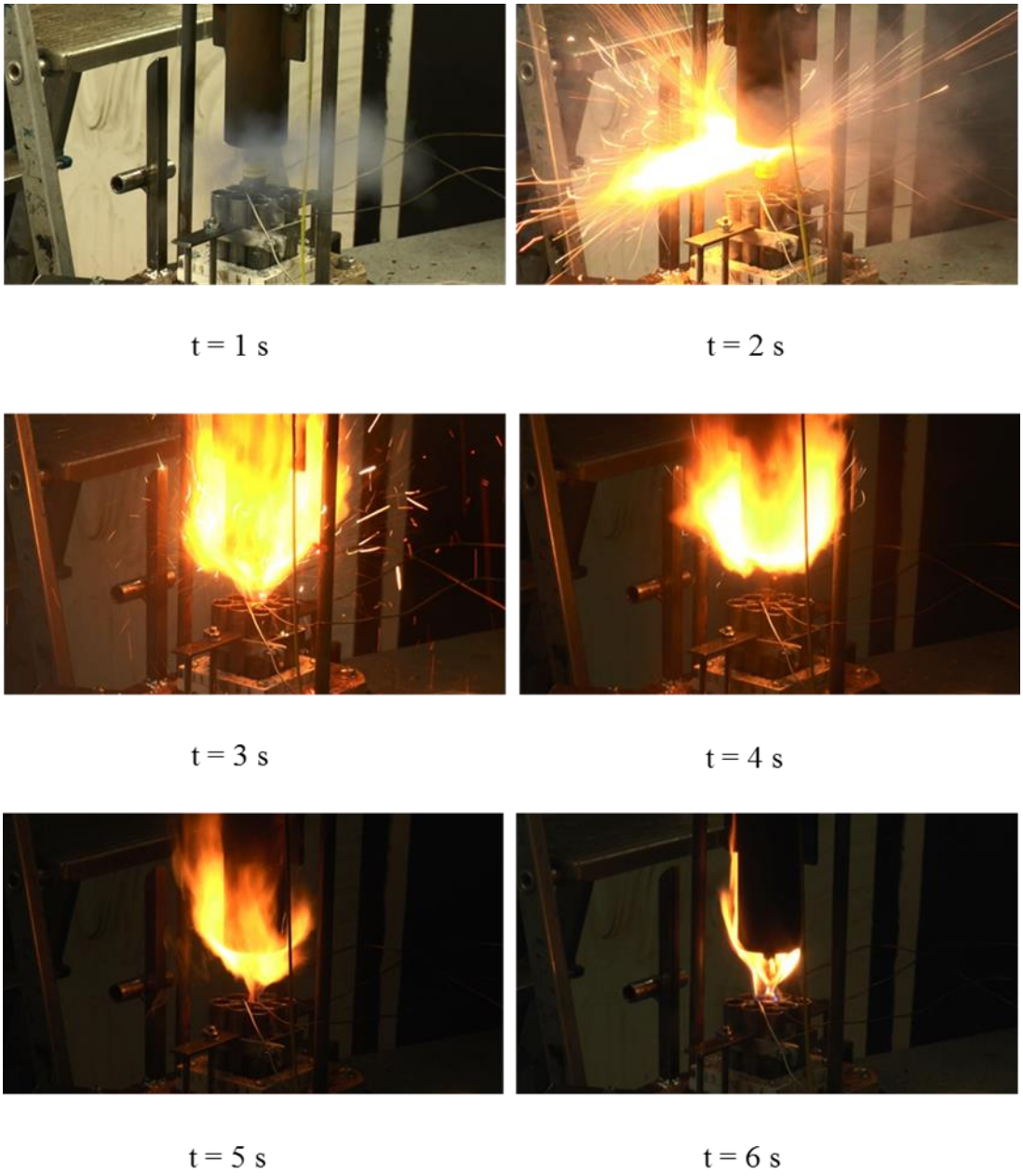

Figure 5.42: Screenshots corresponding to 1 to 6 seconds after the indentation showing the development of fire from the impact test.

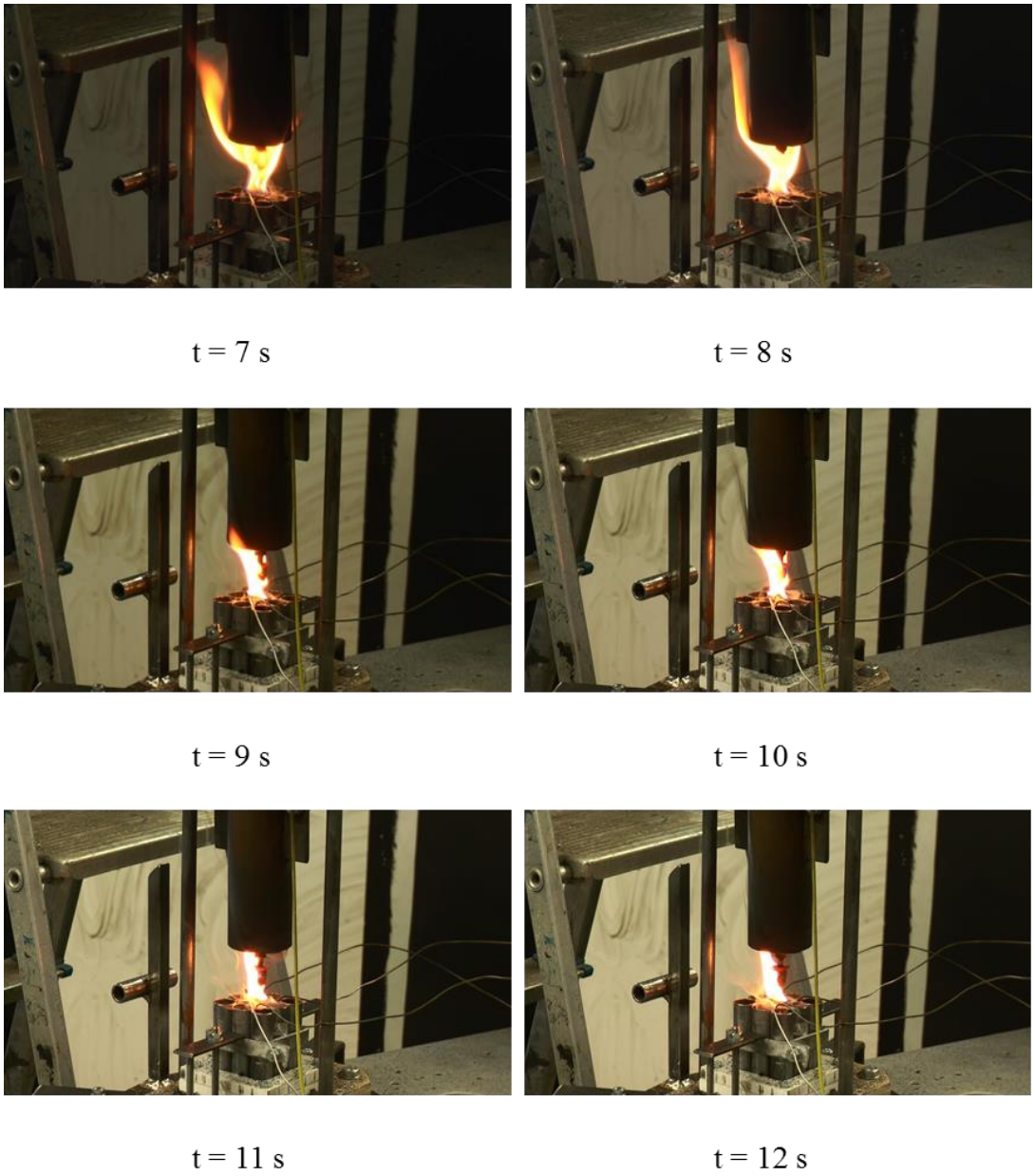

Figure 5.43: Screenshots corresponding to 7 to 12 seconds after the indentation showing the development of fire from the impact test.

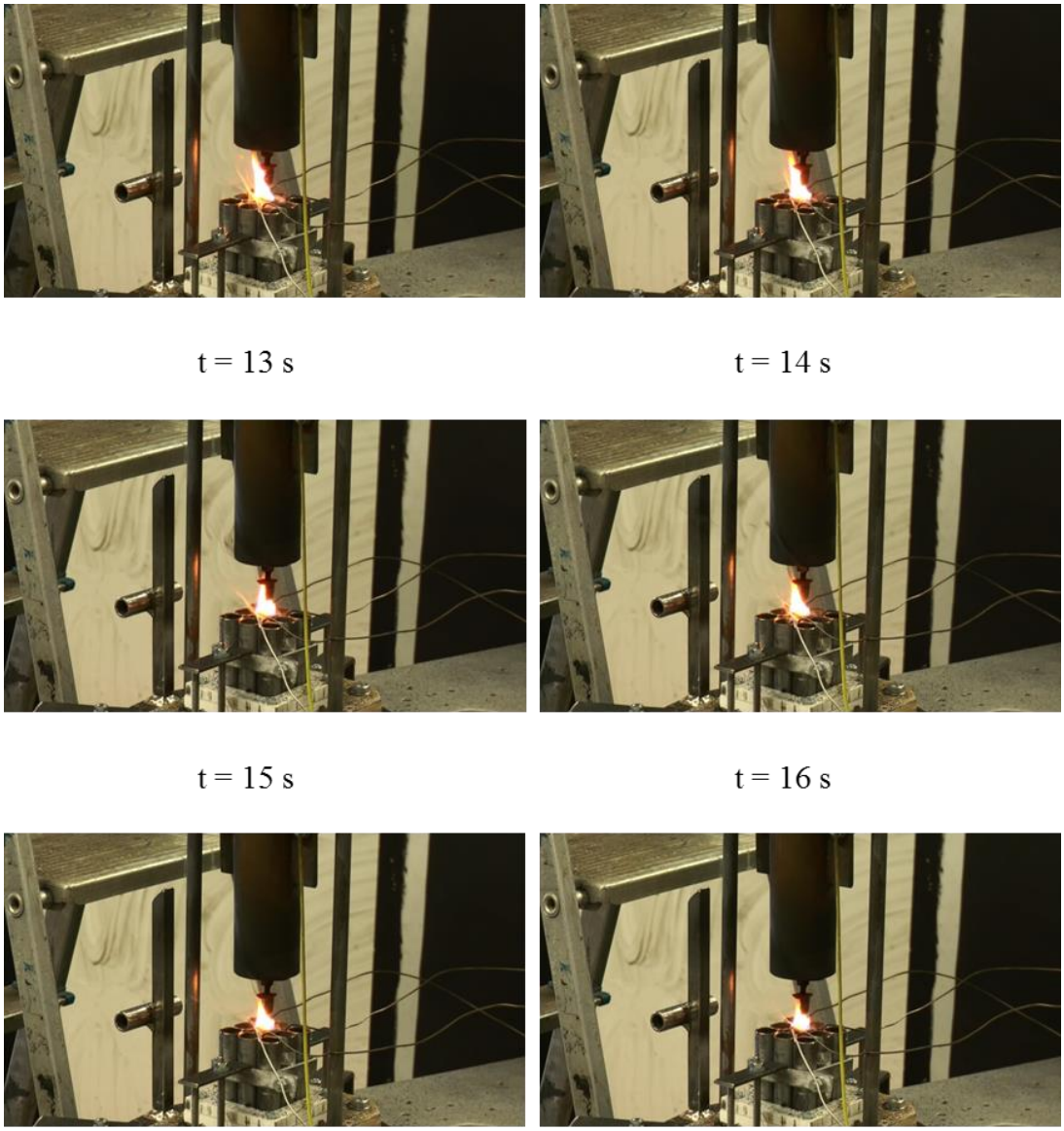

Figure 5.44: Screenshots corresponding to 13 to 18 seconds after the indentation showing the development of fire from the impact test.

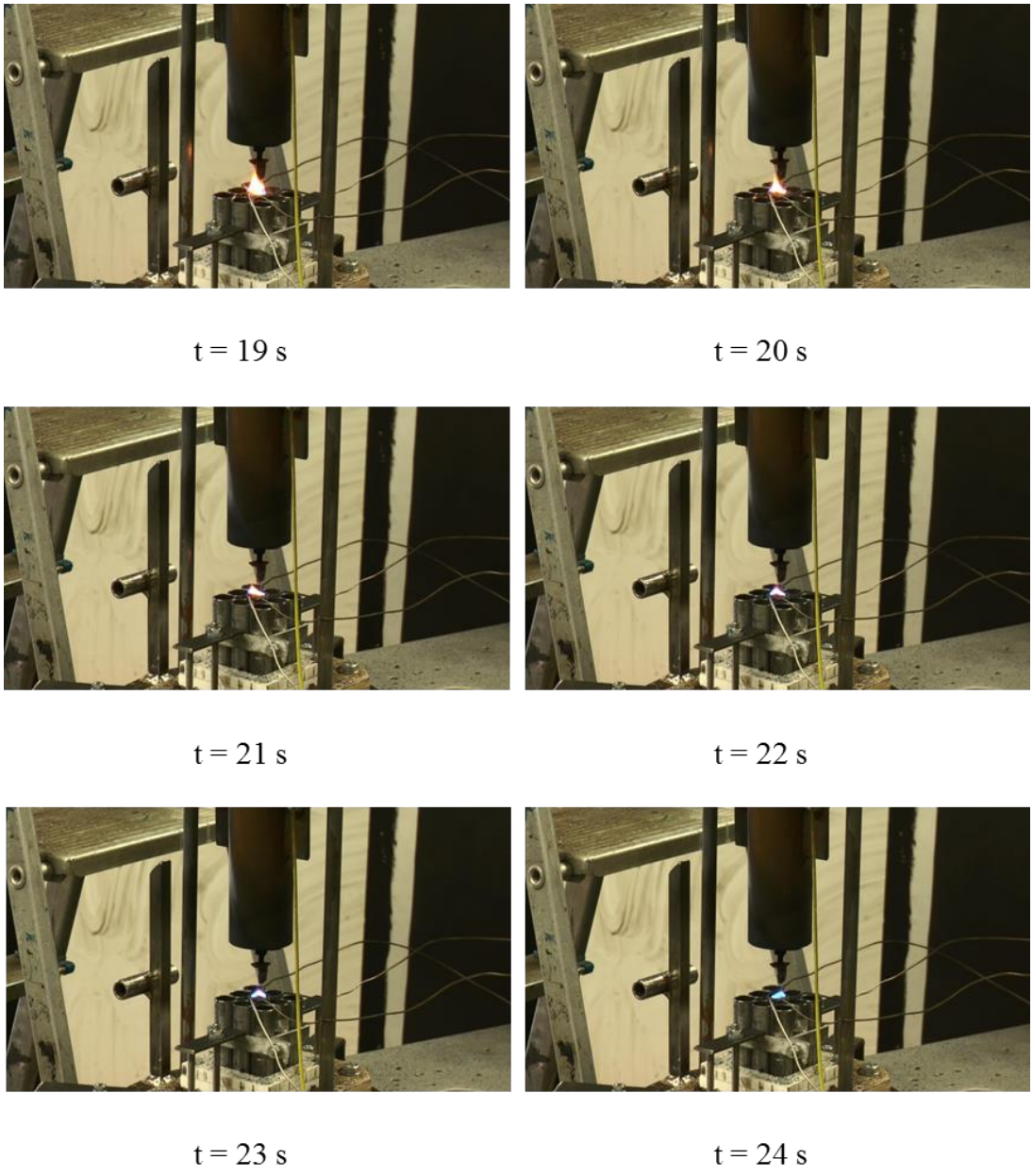

Figure 5.45: Screenshots corresponding to 19 to 24 seconds after the indentation showing the development of fire from the impact test.

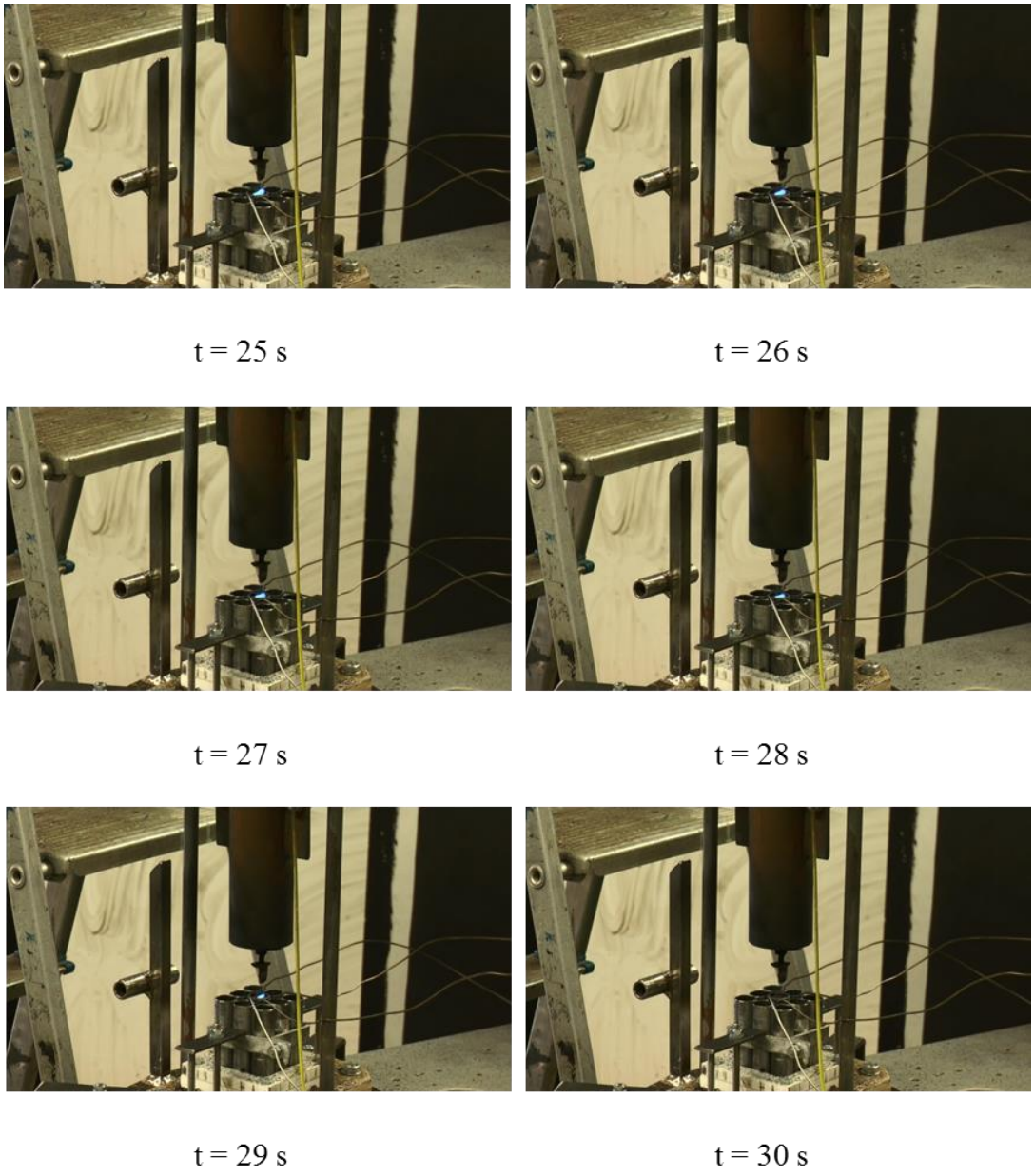

Figure 5.46: Screenshots corresponding to 25 to 30 seconds after the indentation showing the development of fire from the impact test.

5.3.4.3 Results of Impact Test 3 for Full-Charged 9 Cells Battery Module

Impact tests on single battery have demonstrated a violent and energetic response to the abusive situation. Fire sparks, sustained flames and expulsion of hot battery contents were observed. In addition to conductive, convective and radiative heat transfer processes from the hot cell canister, these fires could serve as heat transfer agents and consequently promote thermal runaway to other batteries in the assembly. Therefore, a test on a battery module was conducted to investigate the propagation of thermal runaway from the induced battery to the neighbouring batteries in the module.

The temperature during the test as recorded by thermocouples is shown in Figure 5.47. The impact caused an immediate destruction on the indented battery and led to rapid temperature rise to higher than 260 ^{o}C. Temperature drop was recorded after complete consumption of thermal runaway reactants. No significant differences were observed in the recorded temperature in comparison to the single battery tests conducted previously.

The initiation of thermal runaway in the indented cell generated a massive amount of thermal energy but the heat transport process was retarded by the significant air gap between the cells. The inadequate heat transfer to the neighbouring cells will not be able to trigger the exothermic reactions in the cells and subsequently arrest thermal runaway from propagating to other batteries in the assembly.

Important events during the fire development are shown in Figure 5.48 – Figure 5.49. Thermography of the battery module after the flame extinguished is shown in Figure 5.50. At that point, the content of the impacted battery showed a temperature of 548 ^{o}C while others maintained at room temperature, showing no sign of thermal runaway propagation.

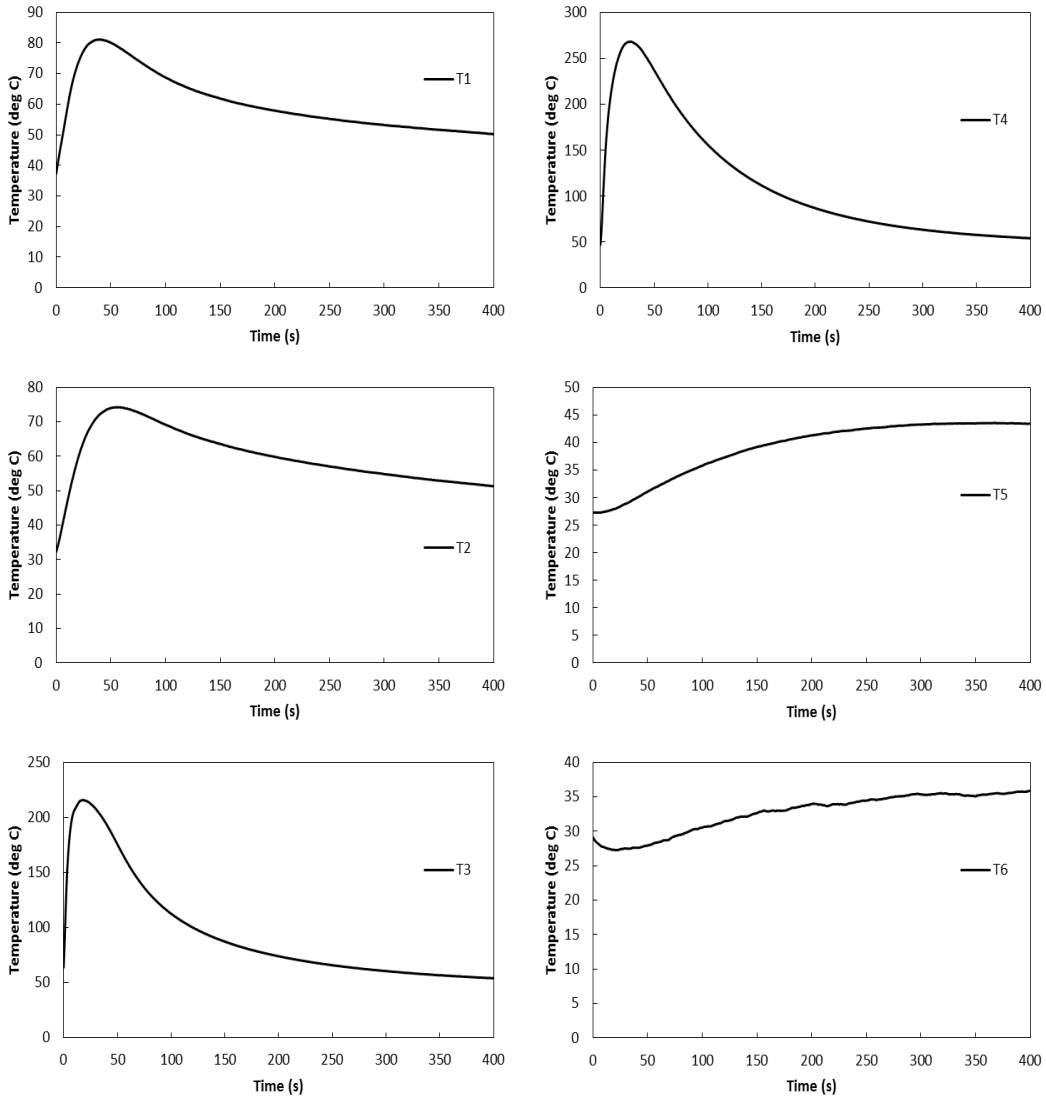

Figure 5.47: Temperature profiles in the battery assembly.

Figure 5.48: Fire sparks were produced after the impact.

Figure 5.49: The cylinder was engulfed in fire.

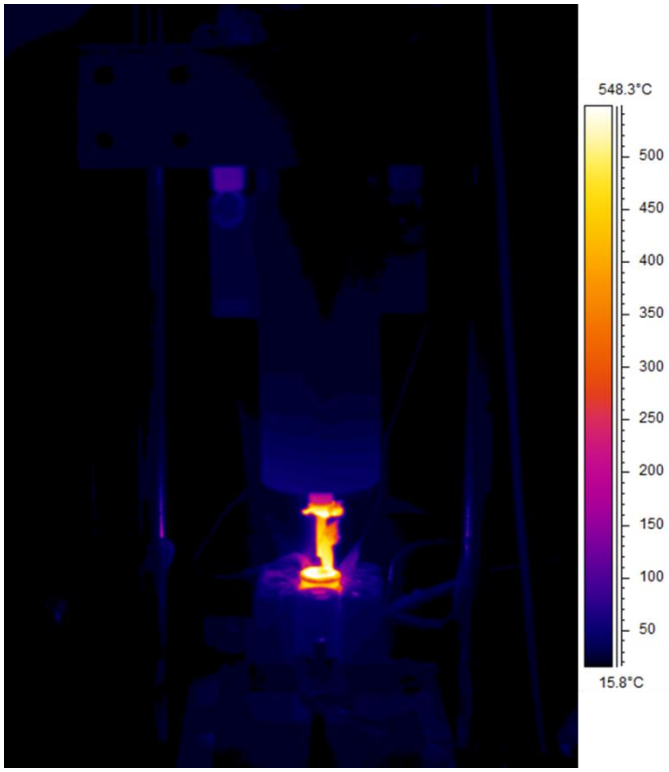

Figure 5.50: Thermography of the battery module after flame extinguished.

5.4 Summary

Experimental works were conducted to characterise thermal runaway of lithium-ion battery. Batteries were subjected to thermally abusive environments under both adiabatic and non-adiabatic conditions and the kinetics of thermal runaway were studied. In addition, destructive impact tests were conducted to investigate the effect of mechanical impact on battery thermal runaway. The summary of the key findings from the experimental works is given below.

1. During oven tests, only full-charged batteries suffered from thermal runaway. The period of the heating process during oven test at a preset temperature of 190 ^{o}C appeared to be insufficient to induce the heat-activated exothermic reactions in batteries at SOC of 0% and 50%.
2. During the adiabatic test using ARC, all batteries, even the zero-charged battery demonstrated a self-heating behaviour. The prolonged experimental period was able to induce the heat-activated exothermic reactions in the batteries.
3. Venting of the cell volatile contents was observed at a temperature range of 154 ^{o}C to 170 ^{o}C.
4. The mechanical integrity of the cell canister was able to withstand the internal pressure. The equipped safety vent appeared to deliver the intended purpose of protecting the canister from catastrophic rupture.
5. The effect of SOC on battery thermal runaway is profound, where battery with higher SOC demonstrated a higher tendency to experience thermal runaway, with shorter time span to induce the heat-activated exothermic reactions and resulted with a more severe response, as indicated by the maximum temperature achieved.
6. Impact-induced short-circuit inflicts an immediate failure which in turn results in surge of the battery temperature and development of flame.
7. The battery temperature can reach higher than 800 ^{o}C during impact as recorded by thermal imaging equipment. Despite showing a violent response to abuse, propagation of thermal runaway in a battery module was not observed.

Chapter 6: Discussions of the Experimental Results and Validation of the Numerical Models

Both experimental techniques and numerical modelling conducted in this research work have been discussed in the preceding chapters. This chapter is aimed to compare and discuss the findings from both methods and to evaluate the suitability of the previously developed model for prediction of battery thermal runaway temperature. There are three main parameters of thermal runaway as studied in both numerical modelling and experimental validation:

1. Thermal runaway temperature
2. Thermal runaway induction time
3. Maximum temperature rise

The point of thermal runaway is defined at the inflection point in the rate of temperature increase where the battery starts to experience a rising pattern in the rate of temperature increase which reflecting accelerating reaction rates.

6.1 Modelling of Thermal Reaction Kinetics for Simulation of Battery Thermal Runaway

Thermal runaway hazard of lithium-ion battery originates from the reactive metallic electrodes and the flammable electrolyte that form the cell components. These components are thermally unstable at high temperature and involve in intricate exothermic reactions that lead to thermal runaway. Each of the reactions possesses their own characteristic kinetic parameters and decomposition model to mathematically describe the progress of the reactions. A numerical model was developed to simulate thermal runaway of lithium-ion batteries during failure by

combining the kinetics of the pertinent chemical reactions. The work was concentrated on full-charged cylindrical lithium-ion battery with lithium cobalt oxide cathode and graphite anode.

From the thermal kinetic model, a range of thermal runaway situations was predicted. Three cases were developed to investigate thermal runaway characteristics at high constant temperature of 150 ^{o}C, 155 ^{o}C and 160 ^{o}C, assuming the battery was initially at room temperature. The simulation results indicate that prolonged exposure to high constant temperature would induce thermal runaway. However, the temperature needs to be sufficiently high to overcome the activation energy of the heat-activated chemical reactions in the battery.

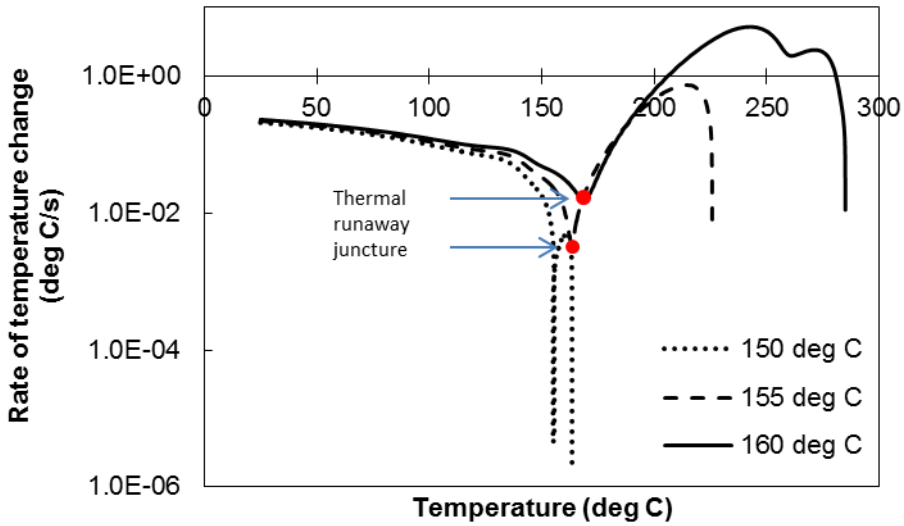

Figure 6.1: Rate of battery temperature change during prolonged exposure to constant high temperature. Thermal runaway points are marked in red.

While thermal runaway was not induced in 150 ^{o}C case, a small temperature overshoot was observed indicating the occurrence of local exothermic reactions at a sluggish rate. Prolonged exposure to both 155 ^{o}C and 160 ^{o}C resulted in thermal runaway, which was observed at 163 ^{o}C and 169 ^{o}C respectively. The increase in temperature results in shorter induction time to overshoot the ambient temperature and the subsequent thermal runaway. The temperature increment also led to a more severe consequence, as reflected by a higher maximum temperature rise.

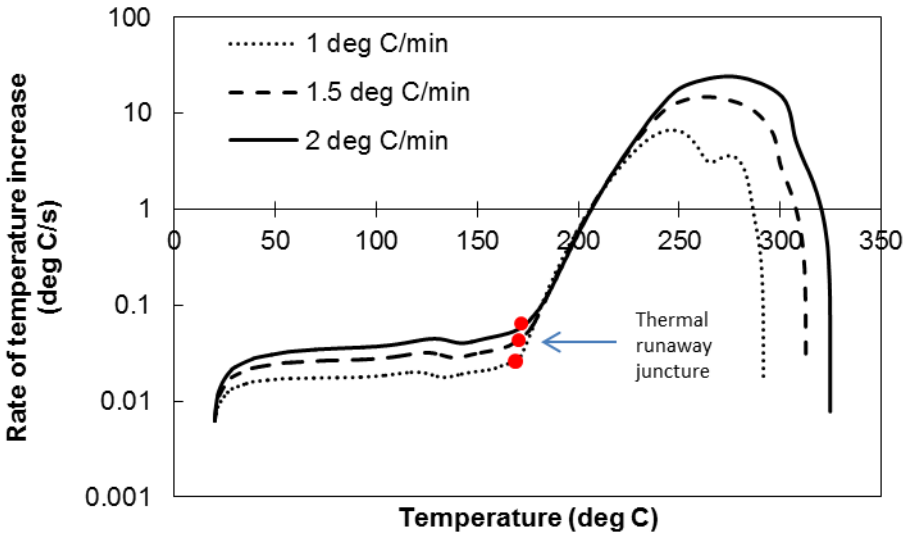

Figure 6.2: Rate of battery temperature change at constant heating rate. Thermal runaway points are marked in red.

In addition, the effect of constant heating rate to the characteristics of thermal runaway was further investigated. Three cases were developed at heating rates of 1, 1.5 and 2 ^{o}C/min. The simulation results show that the battery temperature overshoots the ambient temperature at 164, 171 and 178 ^{o}C under linear heating rate of 1, 1.5 and 2 ^{o}C/min respectively. In general, a higher heating rate results in shorter time to exceed the ambient temperature. Thermal runaway temperature for the 1 ^{o}C/min case can be determined clearly at 166 ^{o}C from the inflection point in Under both constant temperature and constant heating conditions, the model indicates that rapid thermal runaway is observed when significant progress in cathode reaction is observed at a temperature higher than 160 ^{o}C. The cathode reaction is the most energetic reaction during thermal runaway and will become the dominant heat source once activated. The characteristics of a full-charged battery thermal runaway as determined from numerical modelling are summarised in Table 6.1.

Table 6.1: Summary of thermal runaway characteristics of a single full-charged lithium-ion battery from numerical modelling.

Condition	**Thermal runaway induction time (Minute)**	**Thermal runaway temperature (^{o}C)**	**Maximum temperature rise (^{o}C)**
Constant temperature of 150 ^{o}C	Not observed	Not observed	163.417
Constant temperature of 155 ^{o}C	35.500	162.992	225.708
Constant temperature of 160 ^{o}C	28.117	168.897	284.880
Constant heating rate of 1.0 ^{o}C/min	140.300	166.004	291.667
Constant heating rate of 1.5 ^{o}C/min	97.400	170.724	312.687
Constant heating rate of 2.0 ^{o}C/min	75.933	175.338	324.751

6.2 Experimental Validation of Thermal Runaway Model

In order to validate the previously developed model, experimental programme was conducted by using two different approaches. The study of thermal runaway characteristics was performed under both adiabatic and non-adiabatic conditions by using Accelerating Rate Calorimeter and oven respectively. The characteristics of full-charged battery thermal runaway as determined from experimental programmes are summarised in Table 6.2.

Table 6.2: Summary of battery thermal runaway characteristics from experimental programmes.

Test	**Battery capacity (Ah)**	**SOC (%)**	**Number of battery**	**Thermal runaway induction time (Minute)**	**Thermal runaway temperature (^oC)**	**Maximum temperature rise (^oC)**
Oven 1	2.5	100	1	126.917	182.506	738.245
Oven 2	2.5	100	2	115.983	183.064	783.089
Oven 3	5.0	100	2	107.717	173.063	756.679
ARC 1	2.5	100	1	2046.893	163.070	428.533
ARC 2	2.5	100	2	1752.027	134.116	522.204
ARC 3	1.25	50	1	2507.342	207.033	404.662
ARC 4	0	0	1	Not observed	Not observed	315.084

In the first approach, a series of tests was performed on single batteries at varying state of charge by using oven. As previously mentioned, battery thermal runaway hazard originates from reactive metallic electrodes and flammable electrolytes that form the battery main components. The effects of doubling the amount of these reactants on thermal runaway characteristics were investigated by studying two full-charged batteries. In addition, parallel electrical connection was further formed on the two-full charged batteries to explore the effects of doubling the electrical capacity.

The simulation indicates that to thermally induce rapid thermal runaway in a full-charged cylindrical lithium-ion battery with lithium cobalt oxide cathode and graphite anode, the ambient temperature needs to be at least 155 ^{o}C while the occurrence of rapid thermal runaway will be at a higher temperature. Therefore, the oven tests were conducted at 190 ^{o}C, a preset temperature way higher from the one determined from the simulation to ensure effective induction of thermal runaway.

The oven used is not designed to contain any fire and explosion hazards caused by battery thermal runaway and therefore cannot be left unattended. Due to the limitation of the equipment available, the experimental programme needs to be terminated at the end of the day to prevent any undesirable safety issues. The major setback from this situation is that this technique hinders the study of thermal runaway characteristics of half-charged and zero-charged batteries since prolonged uninterrupted heating is required for this purpose.

At the end of the experimental programme, it was noticed that the weight-supported lid covering the cylindrical steel holder was displaced; indicating its inability to withstand the pressure build-up caused by the gases released during battery thermal runaway. Nevertheless, no pressure measurement was conducted to quantify the actual pressure within the sample holder. The release of the gases from the containment arrangement relieved the internal pressure build-up. Hence, this experimental arrangement can be considered as a constant pressure system.

Thermal runaway characteristics of full-charged batteries at varying mass and capacity from oven tests are shown in Figure 6.3. The corresponding rate of temperature change is depicted in Figure 6.4.

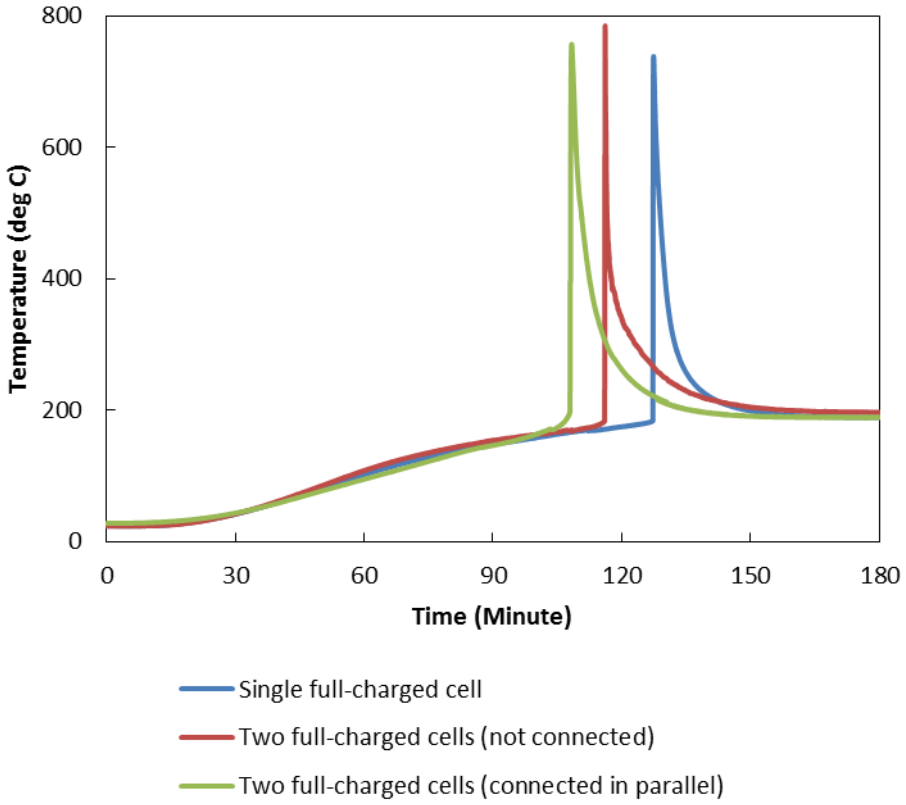

Figure 6.3: Full-charged battery thermal runaway characteristics from oven tests.

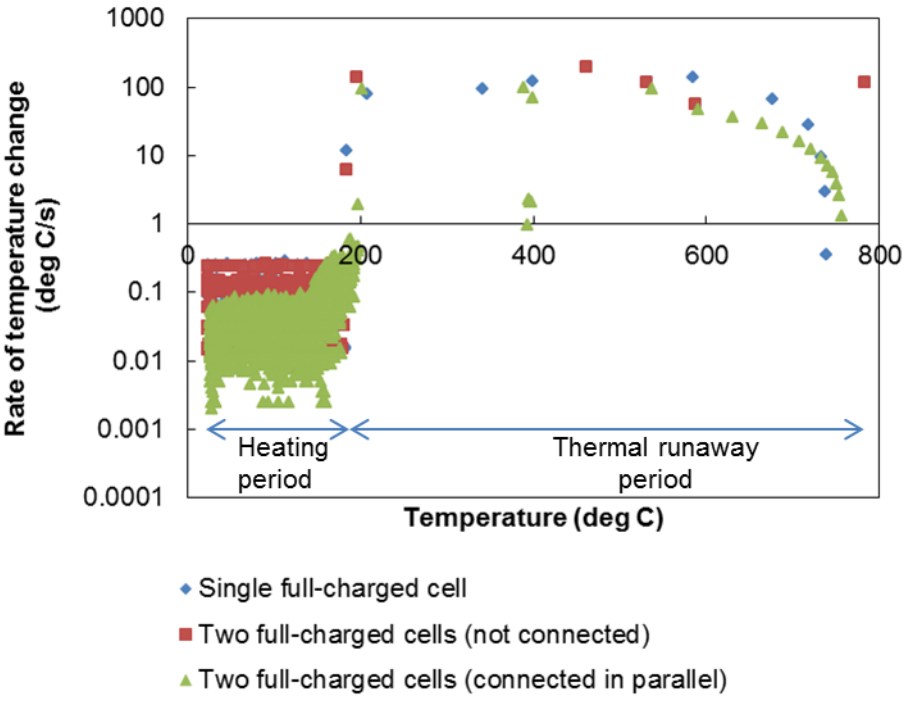

Figure 6.4: Rate of battery temperature change during oven tests.

Increasing the amount of battery which directly increased the amount of reactants involved in thermal runaway reactions did result in the rise of the maximum temperature reached. Thermal runaway of a single battery resulted in a maximum temperature of 738 ^{o}C. The value increased to 783 ^{o}C as one more battery was added to double the amount of reactants involved in thermal runaway. Two batteries with parallel electrical connection that doubled both electrical capacity and reactant mass resulted in a maximum temperature of 756 ^{o}C. Since the difference is not so significant in comparison to the single battery, it can be concluded that the effects of increasing the reactant mass on the maximum temperature rise are not apparent.

However, it should be noted that two batteries are more inclined towards thermal runaway in comparison to the single battery. A single battery recorded a thermal runaway induction time of 126.92 minute. The time is reduced by 8.6% to 115.98 minute as two batteries were present in the oven. The presence of parallel electrical connection that increased the total capacity by 100% to 5.0 Ah resulted in a further inclined towards thermal runaway by 15% to 107.72 minute.

In the second approach, Accelerating Rate Calorimeter (ARC) was used. The calorimeter is well-sealed where the gases released from thermal runaway reactions are confined within the chamber and consequently leads to pressure increase. Hence, the experimental setup can be considered as a constant volume system. The operation of ARC under Heat-Wait-Seek mode allows the detection of exothermicity onset point and the subsequent enthalpy quantification. Exothermicity onset point is the point where the battery temperature increase due to the local reactions surpasses 0.02 ^{o}C/minute and the calorimeter shifts the operation to exotherm mode. The presence of thick aluminium jackets with a series of heaters and thermocouples around the calorimeter maintains the adiabaticity of the calorimeter operation under exotherm mode.

The integrated safety features provided by the ARC allows unattended prolonged experimental programme and which in turn permits thermal runaway characterisation of half-charged and zero-charged lithium-ion batteries. As previously mentioned in Section 5.2.3, the calorimeter is placed in a blast box to provide additional protection from flying debris and open flames in case of fire and

explosion events. The blast box is electronically locked during operation that prohibits any access and supported with mechanical locks at the doors and lids using steel rods.

Thermal runaway characteristics of batteries at varying mass and capacity from ARC tests are shown in Figure 6.5. The corresponding rate of battery temperature change is shown in Figure 6.6. The effects of electrical capacity on battery thermal runaway are profound, where battery with higher capacity demonstrated a higher tendency to experience thermal runaway with shorter time span to induce the heat-activated exothermic reactions. A further reduction in induction time is observed as the amount of battery is doubled. A single full-charged battery recorded a thermal runaway induction time of 2046.89 minute. The time is reduced by 14.4% to 1752.0 minute as two batteries were present in the ARC chamber. Meanwhile, reducing the available battery capacity to half resulted in an increment of induction time by 22.5% to 2507.34 minute. As the battery capacity is further reduced to zero, no thermal runaway was observed. The findings indicate that battery with less electrical capacity is safer.

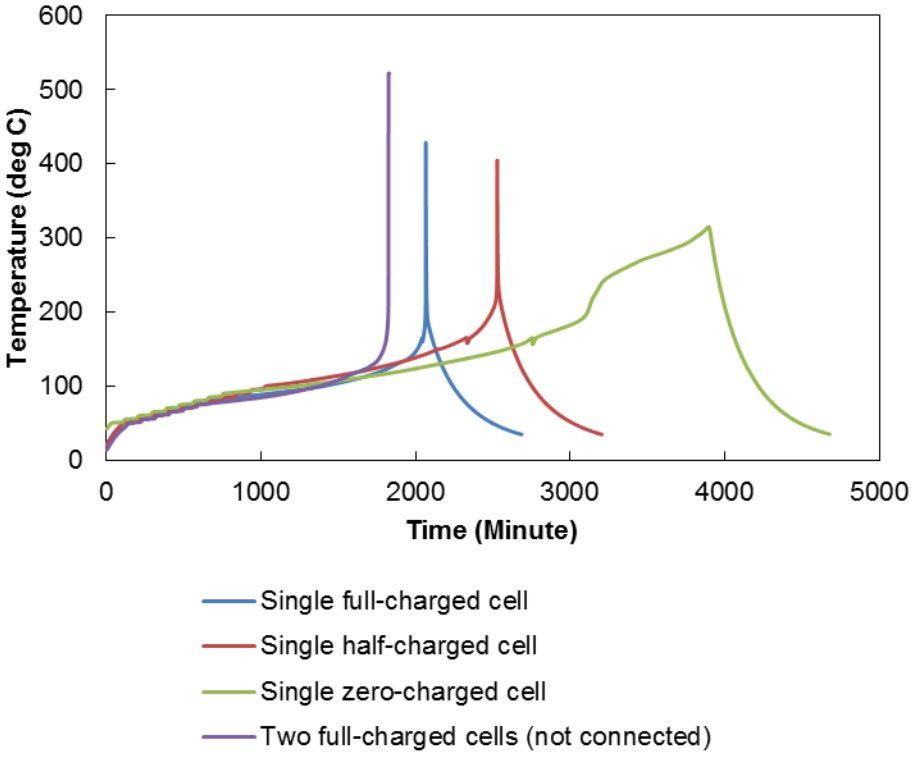

Figure 6.5: Battery thermal runaway characteristics at varying charge states from ARC tests.

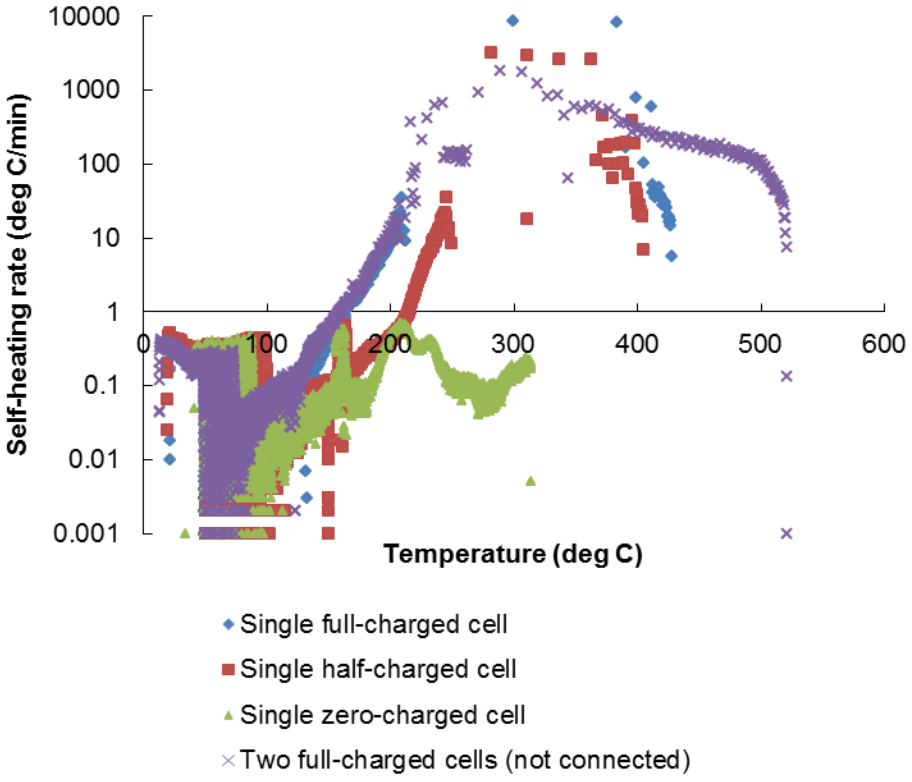

Figure 6.6: Battery self-heating rate at varying electrical capacity and mass.

The rate of temperature change as presented in Figure 6.6 gives a clear idea of the kinetic and exothermicity of the reactions involved in thermal runaway. The pattern of initial heating curves prior to self-generated heating and the subsequent exotherm mode were almost identical for all batteries irrespective of the battery's electrical capacity or number of batteries. Zero-charged cell demonstrated a fluctuating self-heating rate below 1 ^{o}C/min throughout the test programme. Meanwhile, other batteries experienced an increasing self-heating rate at higher temperature and exceeded 1 ^{o}C/min. Full-charged batteries, both single and two batteries recorded an overlapped pattern up to 210 ^{o}C and subsequently diverged at higher temperature where single-battery sample demonstrated a higher self-heating rate while two-battery sample reached a higher maximum temperature at a lower self-heating rate. Half-charged cell on the other hand recorded a lower self-heating rate compared to full-charged cells but indicated an identical increasing pattern as the temperature increased.

Even though thermal runaway was not observed in zero-charged cell, the battery was able to progress into exotherm mode as the recorded self-heating surpassed the predetermined temperature rate sensitivity. The local exothermic reactions in the battery sample proceeded at a sluggish rate and released a small amount of thermal energy that eventually increased the sample temperature slowly. The process of heat release from the exothermic reactions, despite being slow, was sufficient to sustain the calorimeter operation in exotherm mode up to the point of experiment termination since the rate of temperature increment in the sample was higher than the preset temperature rate sensitivity. The highest self-heating recorded was below than 1 ^{o}C/min that occurred at temperature of 200 ^{o}C where a steep increase in the temperature can be observed. The experimental programme was terminated as the battery temperature reached 315 ^{o}C and was cooled down thereafter.

6.3 Thermal Runaway of Impact-Induced Short-Circuit

The battery canister has an important role of hosting and protecting the active materials that form the battery components. In the event of impact, a rupture in the mechanical integrity of the battery canister will result in collision between the positive and negative electrodes. The situation leads to a short-circuit where the electrical energy content is converted into a massive amount of heat.

The failure induced by impact is immediate where a rapid temperature increment is observed. In addition, the heat generated from short-circuit will induce and accelerate the heat-activated exothermic reactions and further exacerbate the situation. In some reactions, the release of heat is accompanied by the generation of flammable gases. Even the first and bottleneck chemical reactions to thermal runaway, the decomposition of solid electrolyte interphase (SEI) do produce flammable gases. According to Yang et al. (2006), the reactions produce flammable ethylene gases and proceed according to the following mechanisms.

$$(CH_2OCO_2Li)_2 \rightarrow Li_2CO_3 + C_2H_4 + CO_2 + 0.5O_2 \quad \text{(Eq 6.1)}$$

$$2Li + (CH_2OCO_2Li)_2 \rightarrow 2Li_2CO_3 + C_2H_4 \quad \text{(Eq 6.2)}$$

The rupture of SEI layer leaves the anode surface unprotected and exposed to reactions with electrolyte. These reactions produce flammable gases such as ethylene, ethane and propene. The mechanisms of the reactions between anode and electrolytes as reported by Lopez et al. (2015a) are shown below.

$$2Li + C_3H_4O_3\ (EC) \rightarrow Li_2CO_3 + C_2H_4 \quad \text{(Eq 6.3)}$$

$$2Li + C_3H_6O_3\ (DMC) \rightarrow Li_2CO_3 + C_2H_6 \quad \text{(Eq 6.4)}$$

$$2Li + C_4H_6O_3\ (PC) \rightarrow Li_2CO_3 + C_3H_6 \quad \text{(Eq 6.5)}$$

The destructive impact tests were conducted to simulate the loss of mechanical integrity of the battery structure. Since the tests were done in open air where the oxygen was abundant, the outcome was devastating where fire was developed. The massive amount of heat produced by short-circuit induced the generation of the flammable gases and provided ignition source required for flame production.

In the destructive impact tests, thermocouples were used for temperature measurement. It should be noted that thermocouples only provided measurement of battery skin temperature while thermal runaway reactions occurred inside the cell canister. The slow response of thermocouples renders this tool less suitable for rapid temperature measurement as in the impact test. Despite being able to capture the qualitative behaviour of temperature development during the impact and in good agreement with the model developed previously, temperature measurement by using thermocouples is far from accurate for representation of thermal runaway hazard under this condition. The thermocouples were not placed near the flame since this will obstruct the steel rod movement and the indentation process. Due to the limitation of thermocouples for fast temperature recording, the measurement of temperature was supported by using thermal imaging technique.

There are two main hazards from impact-induced short-circuit. The first hazard originates from the reactive metallic electrodes that reached a very high temperature as a result of short-circuit and thermal runaway. Thermography of the aftermath showed that the battery content reached a temperature higher than 800 ^{o}C. The second hazard is the flame erupted due to the ignition of flammable electrolytes and combustible gases produced by battery components. As shown by thermography, the flame temperature can be higher than 500 ^{o}C. Even though violent failure behaviour was observed from the impact test, the large amount of heat was unable to induce thermal runaway reactions in the neighbouring cells. Thermography showed that all the surrounding cells remained at room temperature after the impact.

6.4 Summary

A comparison of the numerical modelling results and experimental validations was conducted. The experimental results indicate that the numerical model was able to predict thermal runaway temperature as reflected by the agreeable value between both numerical modelling and experimental results, validating the model as a reliable tool for simulation of thermal runaway.

The results from numerical model, and supported by the experimental works show that considerable amount of time is required to induce thermal runaway by heating. The exothermic reactions involved in thermal runaway are heat-activated where considerable heating time is necessary for catastrophic failure to occur. Impact-induced short-circuit, on the other hand, inflicts an immediate failure which in turn results in surge of the battery temperature. The massive amount of heat generated during short-circuit accelerates the production of flammable gases and subsequently ignites the gases, leads to the flame eruption.

In addition, thermal runaway characteristics of lithium-ion batteries are dependent on environmental temperature, heating rate and electrical capacity. The presence of higher amount of electrical energy at higher capacity makes the reactive materials thermally unstable as reflected by thermal runaway induction time and results in severe response, as indicated by the maximum temperature achieved. The severity is further intensified as the amount of reactants involved in thermal runaway reactions is doubled in two batteries.

Chapter 7: Conclusions

This chapter presents the conclusions drawn from this research project. The limitations of the study are discussed and suggestions for further improvement for the next stage of research programme in this area are made.

Conclusions

- Thermal runaway is the common failure mode in lithium-ion batteries, with the potential to cause fire and explosion.
- Thermal runaway hazard of lithium-ion batteries stems from its components where a combination of highly reactive electrodes and flammable organic electrolytes is present.
- There are multiple exothermic reactions during thermal runaway. All of them are heat-activated where energetic or high temperature environments are required to overcome the associated activation energy and therefore induce the thermal reactions.
- Cathode breakdown is the most energetic reaction during thermal runaway with the highest rate of heat release. The reaction produces oxygen, which may lead to the combustion of organic electrolyte in the battery.

<u>Numerical Modelling of Thermal Runaway Behaviour</u>

- Thermal runaway model for a cylindrical lithium-ion battery with lithium cobalt oxide cathode and graphite anode was developed. Battery thermal runaway behaviour under thermally abusive conditions and impact-induced short-circuit was predicted.
- The modelling of the thermal kinetics of pertinent chemical reactions enables comprehensive understanding of relative contribution of the battery components towards thermal runaway.

- Under thermally abusive conditions, for both constant high ambient temperature and constant heating rate cases, thermal runaway does not occur instantaneously. Considerable amount of time is necessary to induce thermal runaway in the battery.
- Impact-induced short-circuit, on the other hand, inflicts an immediate failure which in turn results in rapid increment of battery temperature.
- Simulation results show that thermal runaway characteristics are dependent on the heating temperature and heating rate. Higher heating temperature and heating rate result in higher maximum temperature rise, higher thermal runaway temperature and shorter induction time. The simulated results indicate that thermal runaway temperature for a full-charged lithium-ion battery falls within the range of 162 ^{o}C – 175 ^{o}C.
- Thermal runaway model of the single cell was further expanded to include heat transfer modelling to simulate the propagation of thermal runaway in a battery pack consisted of 9 identical cylindrical cells. Two different failure initiation locations were investigated, which both showed no thermal runaway propagation.

Experimental Study of Thermal Runaway Characteristics

- The numerical model was experimentally validated by using oven heating and ARC. The experimental results indicate that thermal runaway temperature for a full-charged battery falls within the range of 163 ^{o}C – 183 ^{o}C.
- Oven test was able to capture thermal runaway characteristics of full-charged batteries only. The short heating time of a few hours was insufficient to induce thermal runaway in half-charged and zero-charged batteries. Meanwhile, ARC was able to induce thermal runaway in half-charged battery due to its longer heating process.
- The effects of battery electrical capacity on battery thermal runaway are profound, where battery with higher capacity demonstrated a higher tendency to experience thermal runaway, with shorter time span to induce

the heat-activated exothermic reactions and resulted with a more severe response, as indicated by the maximum temperature rise.

- In comparison to heating, thermal runaway induced by impact led to immediate failure. The massive amount of heat produced by short-circuit accelerated the generation of flammable gases and provided ignition source required for flame production.

Validation of Numerical Model by Experimental Study

- The experimental results indicate that the numerical model was able to predict thermal runaway temperature as reflected by the agreeable value between both numerical modelling and experimental work, validating the model as a reliable tool for simulation of thermal runaway behaviour.

Limitations and Suggested Future Works

- Thermal decomposition kinetics pertaining to thermal runaway of lithium-ion battery with lithium cobalt oxide cathode are well established with an account of publications can be found in the scientific literature. A range of chemistries of lithium-ion battery is available that entails significant variation in the electrochemical properties and thermal stability that determines its safety behaviour. Modelling of thermal decomposition kinetics has been proven to be a flexible and convenient way for simulation of thermal runaway and the subsequent hazard quantification. Therefore, it would be beneficial to develop thermal kinetics of other lithium-ion battery chemistries as well.
- High capacity battery pack is usually constructed by electrically connecting individual cells. The charge state of the individual cells is regulated to be uniform throughout the battery pack by electronic control. An assembly of batteries, even not at full-charged condition does lead to capacity increase. Therefore, it is suggested to study how the hazard would change in a high capacity battery pack under varying charge state.
- A range of lithium-ion batteries is available with varying size and geometry, which entails significant difference in surface area for heat transfer. Due to this reason, it is recommended to study the effects of the cell geometry on propagation of thermal runaway in a battery pack.
- Venting of the cell volatile contents has been observed at 150 ^{o}C to 170 ^{o}C during oven and ARC tests. As the cylindrical battery structure is hollow in the middle with sufficient size for drilling which may facilitate the placement of pressure line, it is recommended to measure the development of pressure inside the cell canister to investigate the pressure of vent activation.
- The chamber of the ARC used in the adiabatic tests is a fixed-volume closed-system and the gases released during the tests are contained within the vessel. Therefore, it is suggested that the gases should be collected and analysed to determine the toxicity and flammability of the gases released. In addition, it is recommended to evaluate how the gas contents mutate at

higher capacity and number of cells in the future. Also, the release of gases in the system will lead to pressure increase. Thus, it is recommended to measure the development of the pressure profile within the chamber.

- The experimental study related to propagation of thermal runaway in a battery pack has been conducted by inducing short-circuit and the subsequent thermal runaway in a cell by nail penetration. Since there is a range of abusive environments that can trigger thermal runaway, it is suggested to diversify the failure initiation techniques to investigate its effect on propagation of thermal runaway.
- It was observed that the steel rod used in the impact test was stuck into the battery body during the experiment. The rod was detached from the battery upon violent flame eruption. This situation obstructed the flame from developing to its maximum height. It is suggested that the retraction system is improved in the future to prevent the rod from sticking inside the battery and able to suspend the rod at a higher position so that full fire development can be observed.

References

Abada, S., Marlair, G., Lecocq, A., Petit, M., Sauvant-Moynot, V. & Huet, F. 2016. Safety focused modeling of lithium-ion batteries: A review. *Journal of Power Sources,* 306**,** 178-192.

Abraham, D. P., Roth, E. P., Kostecki, R., Mccarthy, K., Maclaren, S. & Doughty, D. H. 2006. Diagnostic examination of thermally abused high-power lithium-ion cells. *Journal of Power Sources,* 161**,** 648-657.

Armand, M. & Tarascon, J. M. 2008. Building better batteries. *Nature,* 451**,** 652-657.

Aurbach, D., Levi, M. D., Levi, E. & Schechter, A. 1997. Failure and Stabilization Mechanisms of Graphite Electrodes. *J. Phys. Chem.,* B**,** 2195-2206.

Aurbach, D., Markovsky, B., Shechter, A. & Ein-Eli, Y. 1996. A Comparative Study of Synthetic Graphite and Li Electrodes in Electrolyte Solutions Based on Ethylene Carbonate-Dimethyl Carbonate Mixtures. *J. Electrochem. Soc.,* 143**,** 3809-3820.

Bandhauer, T. M., Garimella, S. & Fullerb, T. F. 2011. A Critical Review of Thermal Issues in Lithium-Ion Batteries. *Journal of The Electrochemical Society,* 158**,** R1-R25.

Bbcnews. 2013. *Boeing 787 Dreamliner: NTSB details battery fire* [Online]. Available: http://www.bbc.co.uk/news/business-21710577 [Accessed 29 April 2014].

Belov, D. & Yang, M.-H. 2008. Failure mechanism of Li-ion battery at overcharge conditions. *Journal of Solid State Electrochemistry,* 12**,** 885-894.

Biensan, P., Simon, B., Pérès, J. P., De Guibert, A., Broussely, M., Bodet, J. M. & Perton, F. 1999. On safety of lithium-ion cells. *Journal of Power Sources,* 81–82**,** 906-912.

Biteau, H., Steinhaus, T., Schemel, C., Simeoni, A., Marlair, G., Bal, N. & Torero, J. L. 2008. Calculation Methods for the Heat Release Rate of Materials of Unknown Composition. *Fire Safety Science - Proceedings of the Ninth International Symposium*

University of Karlsruhe.

Brett, D. 2011. *Another cargo aircraft carrying batteries crashes – off South Korea* [Online]. Available: http://www.airportwatch.org.uk/another-cargo-aircraft-carrying-batteries-crashes-off-south-korea/ [Accessed 13 November 2014].

Cao, J. & Fenner, R. 2016. *Samsung's Lithium-Ion Battery Headache Gets Worse: QuickTake Q&A* [Online]. Bloomberg. Available:

https://www.bloomberg.com/news/articles/2016-09-18/quicktake-q-a-samsung-and-its-lithium-ion-battery-headache [Accessed 22 January 2017].

Cbcnews. 2009. *Trail battery-recycling fire leaves questions* [Online]. Available: http://www.cbc.ca/news/canada/british-columbia/trail-battery-recycling-fire-leaves-questions-1.805780 [Accessed 31 May 2014].

Chen, M., Zhou, D., Chen, X., Zhang, W., Liu, J., Yuen, R. & Wang, J. 2015. Investigation on the thermal hazards of 18650 lithium ion batteries by fire calorimeter. *Journal of Thermal Analysis and Calorimetry***,** 1-9.

Chen, W.-C., Wang, Y.-W. & Shu, C.-M. 2016. Adiabatic calorimetry test of the reaction kinetics and self-heating model for 18650 Li-ion cells in various states of charge. *Journal of Power Sources,* 318**,** 200-209.

Coman, P. T., Rayman, S. & White, R. E. 2016. A lumped model of venting during thermal runaway in a cylindrical Lithium Cobalt Oxide lithium-ion cell. *Journal of Power Sources,* 307**,** 56-62.

Cpsc. 2014. *United States Consumer Product Safety Commission* [Online]. Available: http://www.cpsc.gov/ [Accessed 13 April 2014 2014].

Dahn, J. R., Fuller, E. W., Obrovac, M. & Von Sacken, U. 1994. Thermal stability of LixCoO2, LixNiO2 and λ-MnO2 and consequences for the safety of Li-ion cells. *Solid State Ionics,* 69**,** 265-270.

Dos Santos, R. G., Vidal Vargas, J. A. & Trevisan, O. V. 2014. Thermal Analysis and Combustion Kinetic of Heavy Oils and Their Asphaltene and Maltene Fractions Using Accelerating Rate Calorimetry. *Energy & Fuels,* 28**,** 7140-7148.

Doughty, D. & Roth, E. P. 2012. A General Discussion of Li Ion Battery Safety. *The Electrochemical Society Interface***,** 37 - 44.

Doughty, D. H. 2011. Battery Safety and Abuse Tolerance. *In:* DANIEL, C. & BESENHARD, J. O. (eds.) *Handbook of Battery Materials.*

Doughty, D. H., Butler, P. C., Jungst, R. G. & Roth, E. P. 2002. Lithium battery thermal models. *Journal of Power Sources,* 110**,** 357-363.

Doughty, D. H. & Pesaran, A. A. 2012. Vehicle Battery Safety Roadmap Guidance. National Renewable Energy Laboratory.

Dubaniewicz, T. H. & Ducarme, J. P. 2014. Further study of the intrinsic safety of internally shorted lithium and lithium-ion cells within methane-air. *Journal of Loss Prevention in the Process Industries,* 32**,** 165-173.

Edström, K., Herstedt, M. & Abraham, D. P. 2006. A new look at the solid electrolyte interphase on graphite anodes in Li-ion batteries. *Journal of Power Sources,* 153**,** 380-384.

Eshetu, G. G., Grugeon, S., Laruelle, S., Boyanov, S., Lecocq, A., Bertrand, J.-P. & Marlair, G. 2013. In-depth safety-focused analysis of solvents used in electrolytes for large scale lithium ion batteries. *Physical Chemistry Chemical Physics,* 15**,** 9145-9155.

Feng, X., Fang, M., He, X., Ouyang, M., Lu, L., Wang, H. & Zhang, M. 2014. Thermal runaway features of large format prismatic lithium ion battery using extended volume accelerating rate calorimetry. *Journal of Power Sources,* 255**,** 294-301.

Feng, X., He, X., Ouyang, M., Lu, L., Wu, P., Kulp, C. & Prasser, S. 2015a. Thermal runaway propagation model for designing a safer battery pack with 25 Ah LiNixCoyMnzO2 large format lithium ion battery. *Applied Energy,* 154**,** 74-91.

Feng, X., Lu, L., Ouyang, M., Li, J. & He, X. 2016. A 3D thermal runaway propagation model for a large format lithium ion battery module. *Energy,* 115**,** 194-208.

Feng, X., Sun, J., Ouyang, M., Wang, F., He, X., Lu, L. & Peng, H. 2015b. Characterization of penetration induced thermal runaway propagation process within a large format lithium ion battery module. *Journal of Power Sources,* 275**,** 261-273.

Freed, J. 2014. *Boeing confirms new 787 battery incident* [Online]. Available: http://www.usatoday.com/story/todayinthesky/2014/01/15/boeing-confirms-new-787-battery-incident/4494157/ [Accessed 31 May 2014].

Fu, Y., Lu, S., Li, K., Liu, C., Cheng, X. & Zhang, H. 2015. An experimental study on burning behaviors of 18650 lithium ion batteries using a cone calorimeter. *Journal of Power Sources,* 273**,** 216-222.

Garthwaite, J. 2011. *Lithium Ion Batteries Faulted for Jet Crash* [Online]. Available: https://gigaom.com/2011/04/04/lithium-ion-batteries-faulted-for-jet-crash/ [Accessed 15 November 2014].

Golubkov, A. W., Fuchs, D., Wagner, J., Wiltsche, H., Stangl, C., Fauler, G., Voitic, G., Thaler, A. & Hacker, V. 2014. Thermal-runaway experiments on consumer Li-ion batteries with metal-oxide and olivin-type cathodes. *RSC Advances,* 4**,** 3633-3642.

Golubkov, A. W., Scheikl, S., Planteu, R., Voitic, G., Wiltsche, H., Stangl, C., Fauler, G., Thaler, A. & Hacker, V. 2015. Thermal runaway of commercial 18650 Li-ion batteries with LFP and NCA cathodes - impact of state of charge and overcharge. *RSC Advances,* 5**,** 57171-57186.

Goodenough, J. B. & Kim, Y. 2009. Challenges for Rechargeable Li Batteries. *Chemistry of Materials,* 22**,** 587-603.

Hales, P. 2006. *Dell laptop explodes at Japanese conference* [Online]. Available: http://www.theinquirer.net/inquirer/news/1042700/dell-laptop-explodes-japanese-conference [Accessed 24 May 2014].

Hatchard, T. D., Macneil, D. D., Basu, A. & Dahn, J. R. 2001. Thermal Model of Cylindrical and Prismatic Lithium-Ion Cells. *Journal of The Electrochemical Society,* 148**,** A755-A761.

Hse. 2009. *Company fined £150,000 over major Preston chemical fire* [Online]. Available: http://www.hse.gov.uk/press/2009/coinw001veolia09.htm [Accessed 31 May 2014].

Hsieh, T.-Y., Duh, Y.-S. & Kao, C.-S. 2014. Evaluation of thermal hazard for commercial 14500 lithium-ion batteries. *Journal of Thermal Analysis and Calorimetry,* 116**,** 1491-1495.

Huria, T. 2012. *Rechargeable lithium battery energy storage systems for vehicular applications.* Ph.D, Universita Di Pisa.

Ishikawa, H., Mendoza, O., Sone, Y. & Umeda, M. 2012. Study of thermal deterioration of lithium-ion secondary cell using an accelerated rate calorimeter (ARC) and AC impedance method. *Journal of Power Sources,* 198**,** 236-242.

Jhu, C.-Y., Wang, Y.-W., Shu, C.-M., Chang, J.-C. & Wu, H.-C. 2011a. Thermal explosion hazards on 18650 lithium ion batteries with a VSP2 adiabatic calorimeter. *Journal of Hazardous Materials,* 192**,** 99-107.

Jhu, C.-Y., Wang, Y.-W., Wen, C.-Y. & Shu, C.-M. 2012. Thermal runaway potential of LiCoO2 and Li(Ni1/3Co1/3Mn1/3)O2 batteries determined with adiabatic calorimetry methodology. *Applied Energy,* 100**,** 127-131.

Jhu, C. Y., Wang, Y. W., Wen, C. Y., Chiang, C. C. & Shu, C. M. 2011b. Self-reactive rating of thermal runaway hazards on 18650 lithium-ion batteries. *Journal of Thermal Analysis and Calorimetry,* 106**,** 159-163.

Kelion, L. 2014. Panasonic recalls laptop and tablet batteries. *BBC News*.

Kim, G.-H. & Pesaran, A. 2007. Analysis of Heat Dissipation in Li-Ion Cells & Modules for Modeling of Thermal Runaway. *The 3rd International Symposium on Large Lithium Ion Battery Technology and Application.* Long Beach, California.

Kim, G.-H., Pesaran, A. & Smith, K. 2008. Thermal Abuse Modeling of Li-Ion Cells and Propagation in Modules. *The 4th International Symposium on Large Lithium Ion Battery Technology and Application.* Tampa, Florida.

Kim, G.-H., Pesaran, A. & Spotnitz, R. 2007. A three-dimensional thermal abuse model for lithium-ion cells. *Journal of Power Sources,* 170**,** 476-489.

Kim, S. U., Albertus, P., Cook, D., Monroe, C. W. & Christensen, J. 2014. Thermoelectrochemical simulations of performance and abuse in 50-Ah automotive cells. *Journal of Power Sources,* 268**,** 625-633.

Kitoh, K. & Nemoto, H. 1999. 100 Wh Large size Li-ion batteries and safety tests. *Journal of Power Sources,* 81–82**,** 887-890.

Kossoy, A. & Koludarova, E. 1995. Specific features of kinetics evaluation in calorimetric studies of runaway reactions. *Journal of Loss Prevention in the Process Industries,* 8**,** 229-235.

Lamb, J. & Orendorff, C. J. 2014. Evaluation of mechanical abuse techniques in lithium ion batteries. *Journal of Power Sources,* 247**,** 189-196.

Lamb, J., Orendorff, C. J., Steele, L. a. M. & Spangler, S. W. 2015. Failure propagation in multi-cell lithium ion batteries. *Journal of Power Sources,* 283**,** 517-523.

Lancasteronline. 2014. *Exploding laptop battery sparks apartment fire in New Holland* [Online]. Available: http://lancasteronline.com/news/local/exploding-laptop-battery-sparks-apartment-fire-in-new-holland/article_ffbf110c-b2ea-11e3-9c1d-0017a43b2370.html [Accessed 1 June 2014 2014].

Larsson, F., Andersson, P., Blomqvist, P., Lorén, A. & Mellander, B.-E. 2014. Characteristics of lithium-ion batteries during fire tests. *Journal of Power Sources,* 271**,** 414-420.

Larsson, F. & Mellander, B.-E. 2012. Energy storage system safety in electrified vehicles. *Poster presented at Second International Conference on Fires in Vehicles.* Chicago, USA.

Larsson, F. & Mellander, B.-E. 2014. Abuse by External Heating, Overcharge and Short Circuiting of Commercial Lithium-Ion Battery Cells. *Journal of The Electrochemical Society,* 161**,** A1611-A1617.

Lee, C. H., Bae, S. J. & Jang, M. 2015. A study on effect of lithium ion battery design variables upon features of thermal-runaway using mathematical model and simulation. *Journal of Power Sources,* 293**,** 498-510.

Lee, Y. & Kim, S. 2016. *Samsung Kills Off Note 7 After Second Round of Battery Fires* [Online]. Available: https://www.bloomberg.com/news/articles/2016-10-11/samsung-ends-production-of-note-7-after-global-recall-new-fires [Accessed 22 January 2017].

Leising, R. A., Palazzo, M. J., Takeuchi, E. S. & Takeuchib, K. J. 2001. Abuse Testing of Lithium-Ion Batteries Characterization of the Overcharge Reaction of LiCoO2ÕGraphite Cells. *Journal of The Electrochemical Society,* 148**,** A838-A844.

Levy, S. C. & Bro, P. 1994. *Battery Hazards and Accident Prevention*, Springer.

Linden, D. 2001. Basic Concepts. *In:* LINDEN, D. & REDDY, T. B. (eds.) *Linden's Handbook of Batteries.* Third ed.: McGraw Hill Professional, Access Engineering.

Lisbona, D. & Snee, T. 2011. A review of hazards associated with primary lithium and lithium-ion batteries. *Process Safety and Environmental Protection*, 89**,** 434-442.

Lopez, C. F., Jeevarajan, J. A. & Mukherjee, P. P. 2015a. Characterization of Lithium-Ion Battery Thermal Abuse Behavior Using Experimental and Computational Analysis. *Journal of The Electrochemical Society*, 162**,** A2163-A2173.

Lopez, C. F., Jeevarajan, J. A. & Mukherjee, P. P. 2015b. Experimental Analysis of Thermal Runaway and Propagation in Lithium-Ion Battery Modules. *Journal of The Electrochemical Society*, 162**,** A1905-A1915.

Lowy, J. 2010. *Hazard of lithium batteries on planes sparks debate* [Online]. Available: http://www.nbcnews.com/id/39852461/ns/travel-news/t/hazard-lithium-batteries-planes-sparks-debate/#.VGTV5_msVfA [Accessed 15 November 2014].

Lowy, J. & Freed, J. 2013. *Boeing 787 battery fire was difficult to control through intense smoke, documents show* [Online]. Available: http://www.huffingtonpost.ca/2013/03/07/boeing-787-battery-fire-w_n_2831956.html?utm_hp_ref=canada-business [Accessed 5 May 2014].

Lu, L., Han, X., Li, J., Hua, J. & Ouyang, M. 2013a. A review on the key issues for lithium-ion battery management in electric vehicles. *Journal of Power Sources*, 226**,** 272-288.

Lu, T.-Y., Chiang, C.-C., Wu, S.-H., Chen, K.-C., Lin, S.-J., Wen, C.-Y. & Shu, C.-M. 2013b. Thermal hazard evaluations of 18650 lithium-ion batteries by an adiabatic calorimeter. *Journal of Thermal Analysis and Calorimetry*, 114**,** 1083-1088.

Lyon, R. E. & Walters, R. N. 2016. Energetics of lithium ion battery failure. *Journal of Hazardous Materials*, 318**,** 164-172.

Macneil, D. D., Christensen, L., Landucci, J., Paulsen, J. M. & Dahn, J. R. 2000. An Autocatalytic Mechanism for the Reaction of Li x CoO2 in Electrolyte at Elevated Temperature. *Journal of The Electrochemical Society*, 147**,** 970-979.

Macneil, D. D. & Dahn, J. R. 2001. Test of Reaction Kinetics Using Both Differential Scanning and Accelerating Rate Calorimetries As Applied to the Reaction of LixCoO2 in Non-aqueous Electrolyte. *The Journal of Physical Chemistry A*, 105**,** 4430-4439.

Maleki, H., Deng, G., Anani, A. & Howard, J. 1999. Thermal Stability Studies of Li-Ion Cells and Components. *Journal of The Electrochemical Society,* 146**,** 3224 - 3229.

Maloney, T. 2016. Lithium Battery Thermal Runaway Vent Gas Analysis. U.S. Department of Transportation.

Mendoza-Hernandez, O. S., Ishikawa, H., Nishikawa, Y., Maruyama, Y. & Umeda, M. 2015. Cathode material comparison of thermal runaway behavior of Li-ion cells at different state of charges including over charge. *Journal of Power Sources,* 280**,** 499-504.

Mikolajczak, C., Kahn, M., White, K. & Long, R. T. 2011. Lithium-Ion Batteries Hazard and Use Assessment. Massachusetts, United States: Exponent Failure Analysis Associates, Inc.

Mit Electric Vehicle Team. 2008. *A Guide to Understanding Battery Specifications* [Online]. Available: http://web.mit.edu/evt/summary_battery_specifications.pdf [Accessed 2 March 2015].

Nishi, Y. 2001. The development of lithium ion secondary batteries. *The Chemical Record,* 1**,** 406-413.

Ohsaki, T., Kishi, T., Kuboki, T., Takami, N., Shimura, N., Sato, Y., Sekino, M. & Satoh, A. 2005. Overcharge reaction of lithium-ion batteries. *Journal of Power Sources,* 146**,** 97-100.

Pasquier, A. D., Disma, F., Bowmer, T., Gozdz, A. S., Amatucci, G. & Tarascon, J.-M. 1998. Differential Scanning Calorimetry Study of the Reactivity of Carbon Anodes in Plastic Li-Ion Batteries. *J. Electrochem. Soc.,* 145**,** 472-477.

Ping, P., Wang, Q., Huang, P., Li, K., Sun, J., Kong, D. & Chen, C. 2015. Study of the fire behavior of high-energy lithium-ion batteries with full-scale burning test. *Journal of Power Sources,* 285**,** 80-89.

Ping, P., Wang, Q., Huang, P., Sun, J. & Chen, C. 2014. Thermal behaviour analysis of lithium-ion battery at elevated temperature using deconvolution method. *Applied Energy,* 129**,** 261-273.

R.E.A. 2015. Energy Storage in the UK - An Overview. London: Renewable Energy Association.

Randall, M. 2017. *Tesla Flips the Switch on the Gigafactory* [Online]. Bloomberg. Available: https://www.bloomberg.com/news/articles/2017-01-04/tesla-flips-the-switch-on-the-gigafactory?cmpid=socialflow-facebook-business&utm_content=business&utm_campaign=socialflow-organic&utm_source=facebook&utm_medium=social [Accessed 14 January 2017].

Randall, T. 2016. *Here's How Electric Cars Will Cause the Next Oil Crisis* [Online]. Bloomberg. Available: http://www.bloomberg.com/features/2016-ev-oil-crisis/ [Accessed 1 March 2016].

Rezvanizaniani, S. M., Liu, Z., Chen, Y. & Lee, J. 2014. Review and recent advances in battery health monitoring and prognostics technologies for electric vehicle (EV) safety and mobility. *Journal of Power Sources,* 256**,** 110-124.

Ribiere, P., Grugeon, S., Morcrette, M., Boyanov, S., Laruelle, S. & Marlair, G. 2012. Investigation on the fire-induced hazards of Li-ion battery cells by fire calorimetry. *Energy & Environmental Science,* 5**,** 5271-5280.

Richard, M. N. & Dahn, J. R. 1999a. Accelerating Rate Calorimetry Study on the Thermal Stability of Lithium Intercalated Graphite in Electrolyte. *Journal of The Electrochemical Society,* 146**,** 2068-2077.

Richard, M. N. & Dahn, J. R. 1999b. Accelerating Rate Calorimetry Study on the Thermal Stability of Lithium Intercalated Graphite in Electrolyte. II. Modeling the Results and Predicting Differential Scanning Calorimeter Curves. *Journal of The Electrochemical Society,* 146**,** 2078-2084.

Richard, M. N. & Dahn, J. R. 1999c. Predicting electrical and thermal abuse behaviours of practical lithium-ion cells from accelerating rate calorimeter studies on small samples in electrolyte. *Journal of Power Sources,* 79**,** 135-142.

Robbins, J. 2007. *Clean Harbors continues to operate; Company says it has no plans to reopen battery recycling operations in Thorold* [Online]. Available: http://www.wellandtribune.ca/2007/12/28/clean-harbors-continues-to-operate-company-says-it-has-no-plans-to-reopen-battery-recycling-operations-in-thorold [Accessed 18 April 2014].

Roth, E. P. & Doughty, D. H. 2004. Thermal abuse performance of high-power 18650 Li-ion cells. *Journal of Power Sources,* 128**,** 308-318.

Roth, E. P. & Nagasubramanian, G. 2000. Thermal Stability of Electrodes in Lithium-Ion Cells. Sandia National Laboratories.

Sato, N. 2001. Thermal behavior analysis of lithium-ion batteries for electric and hybrid vehicles. *Journal of Power Sources,* 99**,** 70-77.

Saw, L. H., Ye, Y. & Tay, A. a. O. 2016. Integration issues of lithium-ion battery into electric vehicles battery pack. *Journal of Cleaner Production,* 113**,** 1032-1045.

Scrosati, B. & Garche, J. 2010. Lithium batteries: Status, prospects and future. *Journal of Power Sources,* 195**,** 2419-2430.

Sin, B. 2016. *Samsung Knew Note 7 Had A Dangerous Design, But Took The Risk Anyway, Say Analysts* [Online]. Forbes. Available: http://www.forbes.com/sites/bensin/2016/12/04/samsung-knew-note-7-had-a-dangerous-design-but-took-the-risk-anyway-say-analysts/?utm_source=FBPAGE&utm_medium=social&utm_term=InstantArticle&utm_content=704236161&utm_campaign=sprinklrForbesMainFB#48aa5d664995 [Accessed 22 January 2017].

Somandepalli, V., Marr, K. C. & Horn, Q. 2013. Explosion Hazards Due to Failures of Lithium-Ion Batteries. *9th Global Congress on Process Safety.* Texas.

Spotnitz, R. & Franklin, J. 2003. Abuse behavior of high-power, lithium-ion cells. *Journal of Power Sources,* 113**,** 81-100.

Spotnitz, R. M., Weaver, J., Yeduvaka, G., Doughty, D. H. & Roth, E. P. 2007. Simulation of abuse tolerance of lithium-ion battery packs. *Journal of Power Sources,* 163**,** 1080-1086.

Stull, D. R. 1977. *Fundamentals of fire and explosion,* New York, American Institute of Chemical Engineers.

Thermal Hazard Technology 2013. *The Accelerating Rate Calorimeter EV+ ARC Operations Manual*.

Tmtv Bctv 2009. Explosions and fire at battery recycling plant in Trail, BC - TMTV News.

Tobishima, S.-I. & Yamaki, J.-I. 1999. A consideration of lithium cell safety. *Journal of Power Sources,* 81–82**,** 882-886.

Torabi, F. & Esfahanian, V. 2011. Study of Thermal–Runaway in Batteries I. Theoretical Study and Formulation. *Journal of The Electrochemical Society,* 158**,** A850-A858.

Townsend, D. I. & Tou, J. C. 1980. Thermal hazard evaluation by an accelerating rate calorimeter. *Thermochimica Acta,* 37**,** 1-30.

Väyrynen, A. & Salminen, J. 2012. Lithium ion battery production. *The Journal of Chemical Thermodynamics,* 46**,** 80-85.

Venugopal, G. 2001. Characterization of thermal cut-off mechanisms in prismatic lithium-ion batteries. *Journal of Power Sources,* 101**,** 231-237.

Verma, P., Maire, P. & Novák, P. 2010. A review of the features and analyses of the solid electrolyte interphase in Li-ion batteries. *Electrochimica Acta,* 55**,** 6332-6341.

Vetter, M. & Rohr, L. 2014. Lithium-Ion Batteries for Storage of Renewable Energies and Electric Grid Backup. *In:* PISTOIA, G. (ed.) *Lithium-Ion Batteries: Advances and Applications.* First ed. Amsterdam: Elsevier.

Von Sacken, U., Nodwell, E., Sundler, A. & Dahn, J. R. 1994. Comparative thermal stability of carbon intercalation anodes and lithium metal anodes for rechargeable lithium batteries. *Solid State Ionics,* 69**,** 284-290.

Wald, M. L. 2014. Safety Agency Says New Tests Are Needed on Boeing Battery. *New York Times,* 2014 May 23.

Wang, Q., Ping, P., Sun, J. & Chen, C. 2011. The effect of mass ratio of electrolyte and electrodes on the thermal stabilities of electrodes used in lithium ion battery. *Thermochimica Acta,* 517**,** 16-23.

Wang, Q., Ping, P., Zhao, X., Chu, G., Sun, J. & Chen, C. 2012. Thermal runaway caused fire and explosion of lithium ion battery. *Journal of Power Sources,* 208**,** 210-224.

Wang, Q., Sun, J. & Chen, C. 2009. Effects of solvents and salt on the thermal stability of lithiated graphite used in lithium ion battery. *Journal of Hazardous Materials,* 167**,** 1209-1214.

Wang, Q., Sun, J., Yao, X. & Chen, C. 2006. Thermal Behavior of Lithiated Graphite with Electrolyte in Lithium-Ion Batteries. *Journal of The Electrochemical Society,* 153**,** A329 - A333.

Wen, C.-Y., Jhu, C.-Y., Wang, Y.-W., Chiang, C.-C. & Shu, C.-M. 2012. Thermal runaway features of 18650 lithium-ion batteries for LiFePO4 cathode material by DSC and VSP2. *Journal of Thermal Analysis and Calorimetry,* 109**,** 1297-1302.

Wilke, S., Schweitzer, B., Khateeb, S. & Al-Hallaj, S. 2017. Preventing thermal runaway propagation in lithium ion battery packs using a phase change composite material: An experimental study. *Journal of Power Sources,* 340**,** 51-59.

Yang, H., Amiruddin, S., Bang, H. J., Sun, Y.-K. & Prakash, J. 2006. A Review of Li-Ion Cell Chemistries and Their Potential Use in Hybrid Electric Vehicles. *Journal of Industrial and Engineering Chemistry,* 12**,** 12-38.

Young, A. 2013. *Watch This Video Of A Tesla Model S Fire In The City Of Merida, Yucatan State, Mexico* [Online]. International Business Times. Available: http://www.ibtimes.com/watch-video-tesla-model-s-fire-city-merida-yucatan-state-mexico-1444006 [Accessed 23 January 2017].

Zhang, Z., Fouchard, D. & Rea, J. R. 1998. Differential scanning calorimetry material studies: implications for the safety of lithium-ion cells. *Journal of Power Sources,* 70**,** 16-20.

Appendix I: Numerical Model Direct Verification

Direct verification of our model was conducted and compared against simulation results by Kim et al. (2007) to ensure the consistency of the results produced.

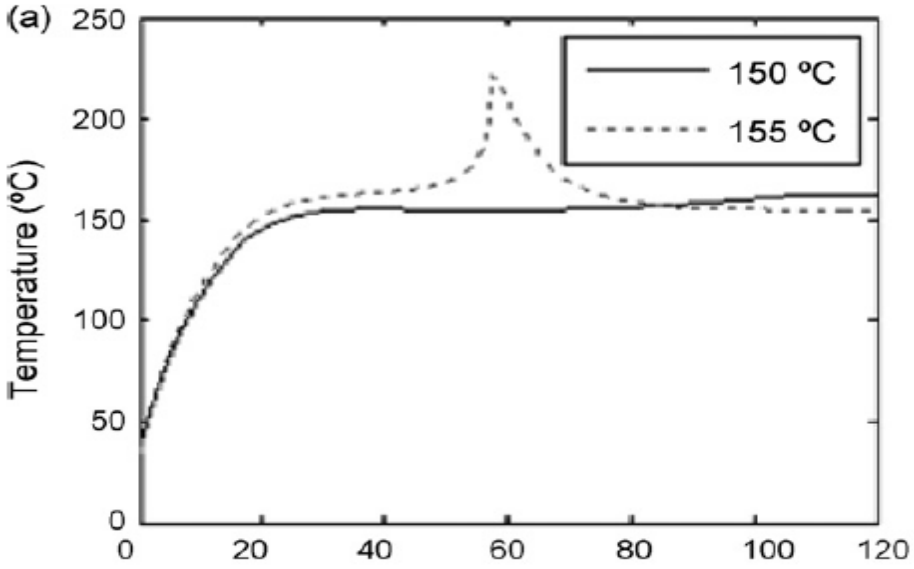

Simulated temperature profile at constant temperature abuse of 150 ^{o}C and 155 ^{o}C as reported by Kim et al. (2007).

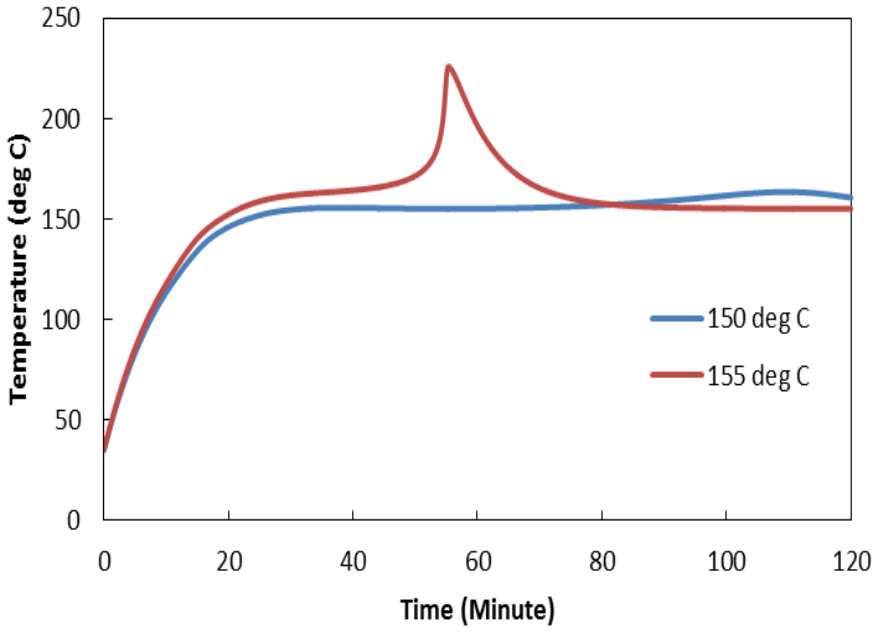

Simulated temperature profile at constant temperature abuse of 150 ^{o}C and 155 ^{o}C from our model.